Design Principles for High Power Linear Accelerators

Ciprian Plostinar

Trinity College, Oxford

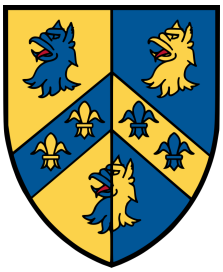

Thesis submitted in fulfilment of the requirements for the degree of Doctor of Philosophy at the University of Oxford

Trinity Term, 2015

Abstract

The demand for high power proton beams is at an all time high. The global community has identified many applications ranging from spallation sources, material irradiation facilities and secondary beams factories to accelerator driven systems for energy production, transmutation of waste or production of tritium.

The typical path to high power beams involves the use of a linac at least in the lower energy stages. For high intensity, high power operation, significant developments are needed particularly in the linac section and the front end of the machine. Consequently, this thesis brings original contributions in tackling several limiting aspects to do with two major pillars of high power operation in linacs: energy and intensity.

One of the major decisions in any linac design concerns the choice of normal accelerating structures. The general aim of every designer is to find the optimal path to the final energy without compromising the beam quality or increasing excessively the structure complexity. In the absence of a much needed comparative assessment of accelerating cavities, this choice was often made based on available local expertise rather than solid reasoning. This problem is tackled at length in two chapters of this thesis in which a framework is created for a methodical examination of available structures. The result is the first systematic analysis of normal conducting structures for proton acceleration which includes beam dynamics, electromagnetic, mechanical, thermal and vacuum aspects of cavity design.

On the intensity side, several innovative developments have arisen through involvement in the Front End Test Stand Project (FETS) and the ISIS linac upgrade efforts. Beam dynamics studies for the Medium Energy Beam Transport line (MEBT) of FETS, as well as an analysis of several other MEBT designs for existing international projects, highlighted the difficulty in reducing beam loss and emittance growth in high current MEBT lines incorporating beam choppers. Through end-to-end tracking studies, it was shown that the initial beam quality produced in the MEBT will heavily influence the emittance evolution, halo development and beam loss in subsequent structures. As a result, a novel distributed MEBT design is proposed as an alternative, allowing better matching and chopping as well as higher intensity, lossless operation.

Further downstream, the beam quality is not only affected by initial mismatch and MEBT beam quality, but by the choice of operating points as well. Theoretical work developed over the last two decades indicate that safe tunes outside conventional equipartitioning limits can be found, but the lack of experimental verification remains a problem. This problem was tackled through an experimental campaign at J-PARC, where for the first time emittance exchange driven by the $k_z/k_t = 2$ resonance was measured in a linac with emittance ratios close to 1.

Finally, these principles are applied to the design of a future upgrade of the ISIS linac. Three linac options have been developed accelerating the beam to 100, 180 and 800 MeV opening the possibility of MW-level operation in ISIS.

To my mother, whose unbridled love and humble generosity has shaped not only my life, but that of many others.

Acknowledgements

Like most people of their generation, my parents, who both come from essentially agrarian backgrounds, valued education more than anything. My dad had an impressive book collection which included poetry, history and classical philosophy, a rather unusual choice for someone proficient at handling the plough and the scythe. The contrast between his large, overworked, rough palms and the thin, soft pages of the books he read only became obvious to me well into my teenage years. I remember being told from an early age that getting a good education was paramount for an "easier" life with fewer hardships and a nice air-conditioned office. And after each long, hot day of summer, stacking hay in the Transylvanian mountains, the prospect of a "cool office" was even more enticing. My mother, who has a remarkable mind, was key at translating this aversion of heat, rakes and sheep-herding into a love of pencils, books and equations. She spent so much time reading and working with me that for the first few years of school I was convinced that all my end-of-year awards and laurel wreaths were completely underserved. It is therefore my pleasure to thank my parents Dan and Mia for everything they have given me and for all the sacrifices they have made, of which I am well aware. I would also like to show my gratitude to my extended family, in particular my late grandfather Iulius Ilea (Ticu).

Naming every person who has contributed in one way or another to my development, and ultimately, to the very existence of this thesis is an almost impossible exercise. I'm most likely going to leave someone out and for that I would like to apologise in advance. I do, however, want to express my gratitude to several people who have played a bigger role that they will ever know in my early formation years, in particular my teachers and mentors Ecaterina Negruța, Paraschiva Botar, Elena Moșilă and Dorin Groza. I still think of you fondly and cherish our brief encounters.

From the Physics Department at Babeș-Bolyai University, I would like to show my appreciation to Professors Constantin Cosma, Decebal-Radu Ciurchea, who have encouraged me to follow my interest in high energy physics despite the fact that I was studying in an environment with a strong tradition in solid state physics and magnetic materials. It was with their kind recommendation letters and the help of several lorry drivers that I arrived in Geneva on a cold winter day for the Joint Universities Accelerator School (JUAS), a move that has marked my career ever since. During my time at JUAS I met many people, including some fantastic tutors like Joël Le Duff and Nicolas Pichoff, who have introduced me to linac beam dynamics. This introduction was taken to the next stage soon after, when as an Erasmus exchange student at Joseph Fourier University and Laboratoire de Physique Subatomique et de Cosmologie (LPSC), I had the privilege to work with Jean-Marie De Conto, a charismatic opera lover-mathematician turned accelerator physicist, with a booming baritone voice. It was during my year in France that I learned that the success of a scientific talk is directly proportional with the amplitude of the presenter's voice. Through Jean-Marie I was then

introduced to several accelerator physicists like Frank Gerigk and Maurizio Vretenar from CERN. I have learned a lot from them and I still appreciate our professional and personal friendship.

After I moved to Oxford, taking a position at the Rutherford Appleton Laboratory in the ASTeC's Intense Beams Group, I came in contact with some fantastic people. I was always fascinated that on any odd day one could just walk down the corridor and bump into the unassuming world expert on charge exchange injection or H^- ion sources. My gratitude goes to my Rutherford supervisor, Chris Prior, the Intense Beams group leader and emeritus tutor at Trinity College, Oxford, who has shaped not only my career, but my very identity in a rather irreversible way. When on a recent visit home I was told by my father that I have now become irreversibly Anglicised, I remember thinking that that's by and large Chris's work. I have learned from Chris the power of independent thinking, the ability to remain composed and unruffled even in the most stressful situations, as well as the importance of a precise attention to detail, even in something as "trivial" as split infinitives. I cannot thank him enough for all the opportunities that have arisen from working with the most prestigious beam dynamics group in the UK.

I have learned a lot from people from ISIS and ASTeC, but in particular I would like to mention Grahame Rees, Mike Clarke-Gayther, Alan Letchford and Shinji Machida, who had the patience to not only teach me, but the wisdom to overlook the inexperience of my youth, while encouraging my naïve exuberance. In addition I would like to thank several colleagues here in the Intense Beams group, as well as in the ISIS and Rutherford lab for their support and camaraderie: Dan Faircloth, David Kelliher, Ben Pine, Chris Rogers, Suzie Sheehy, the late Christoph Gabor, as well as many others. Further afield, I would like to thank colleagues from the FETS project and collaborators from BNL, CEA, CERN, ESS, MSU, as well as from J-PARC and KEK, in particular Stephen Brooks, Masanori Ikegami, Jean-Michel Lagniel, Yong Liu, Jim Stovall and Didier Uriot.

I would also like to thank another gentleman with a booming voice, my Oxford supervisor, Professor Ken Peach, who made this thesis possible and together with Chris Prior saw the need for an addition to the field of high power accelerators. I am deeply indebted to Ken for his vision, support and guidance. I would also like to extend my appreciation to the Physics Department at Oxford and the John Adams Institute, in particular Professors Andrei Seryi and Emmanuel Tsesmelis, who have given me the opportunity to teach graduate students as well as co-supervise student accelerator projects for several years. I am also thankful to the staff and academics at Trinity College, in particular the College President, Sir Ivor Roberts, who has taken time for many personal meetings throughout the years.

On a personal level, I would like to thank my many friends at Oxford who have made me feel I belong here, who have overlooked my (by now proverbial) 15 minute-tardiness and who have accepted and celebrated my obsession with watermelons. In no particular order, I thank my new-found brother Dave Gasca-Tucker for the midnight misty strolls down Queen's Lane, for the constant stream of advice and for teaching me the power of an idiomatic phrase such as "at this stage". Dragos Cirstea, Daniel Costa, Jacqui Crawford, Tudor Popescu, Lillian Spearing as well as many others have been part of my life and have made these years here such an unforgettable experience. I would also like to mention the friends I left behind back in Romania who still welcome me as if I have never left: Erzsi Boico, Cristian Bontoiu, Erik Csergezan, Aurel Hojda, Ioan Petrovai, Vali Stoi, Adrian Toader, to name just a few, are the people I admire and try to emulate.

And finally, I want to thank my wonderful wife Georgiana and our two little boys, Theo and Alex, for their love and care and for adding so much flavour and colour to my life. Going through a DPhil programme is hard enough, but trying to raise a young family at the same time is virtually impossible without constant support and understanding. I apologise for the many occasions I was "caught-up at work", for the many trips abroad and for often being absent-minded. I'm hoping that a lifetime supply of dark chocolate, lovage and some long train journeys, preferably with steam locomotives, would go some way towards paying for these sins. And to paraphrase a celebrated contemporary song, without you, all this is a waste of time.

Having now spent a good part of my life in an academic environment, the very cradle of education my parents so much value, I can assure them there is no such thing as an "easy life" and that hard-work is crucial in almost every walk of life. Yes, my office is air-conditioned, but rather ironically, these days, I mostly dream of rakes, hay and the hills and mountains of Transylvania.

Contents

Chapter 1

Introduction

The ultimate purpose of this thesis is to produce a new linac design for upgrading the ISIS Spallation Neutron Source. This will open several routes for achieving MW-level beam power operation. Tough design requirements have to be met both in terms of minimising beam loss and mitigating high intensity effects as well as in choosing the optimum acceleration path for an efficient and cost effective machine. It is essential that these aspects are analysed in depth and tackled before a final linac design is produced. In this introductory chapter the stage is set for defining the context and the goals of this thesis. Over the last century, particle accelerators have evolved from obscure machines in research laboratories to devices that affect our daily lives in the most remarkable ways. While we track this historical progress, we observe the rise and fall of various machine types and the ever-changing set of accelerator requirements and applications. Attention is paid in particular to proton linear accelerator (linac) developments from the early Alvarez Drift Tube Linac to the most ambitious current proposals like ESS and MYRRHA. While the aim of early machines was to achieve higher beam energies, as the technology matured, for many applications the focus has shifted to higher beam powers. The aim of this thesis is to analyse and propose solutions for high power operation in hadron linacs while targeting two major bottlenecks: energy and intensity limitations.

In 1676 in a letter to Robert Hooke, Sir Isaac Newton made perhaps one of his most famous statements: "*If I have seen further it is by standing on the shoulders of Giants*" [1]. Adapted from the works of Bernard of Chartres, a 12th century scholar, this single phrase, "*nos esse quasi nanos gigantum humeris insidentes*", encapsulates the very spirit of scientific progress [2]. Across centuries, the history of science is a long list of existing concepts being amended, challenged and improved, of experiments being repeated, upgraded and perfected and of theories ever-evolving, ever-changing, ever-refining.

Accelerator science is no different and this process of building on existing ideas is continuous and dynamic. The first electrostatic accelerators were invented out of the need to replace limited natural radioactive sources for subatomic physics experiments. As higher and higher energies were achieved so was the upper limit of these machines. New methods of acceleration had to be found and with strong foundations set, a series of machines were invented ranging from cyclotrons, betatrons and FFAGs to linacs, synchrotrons and today's super-colliders. This is made possible by progress not just in accelerator science, but also in engineering, technology and computing. It took several more decades from the dawn of the first accelerators until scientists from other fields noticed the potential of such machines for material science, biology or medicine. Today, synchrotron radiation sources, spallation neutron sources or cancer therapy accelerators, are key tools for a wide-ranging set of applications.

It is widely accepted that the accelerator age started with two emblematic experiments performed over 100 years ago: J.J. Thomson's discovery of the electron in 1897 and E. Rutherford's scattering experiment in 1909. The idea that charged particles exist and that they can be controlled by electromagnetic fields still is the cornerstone of accelerator physics. With the advent of quantum mechanics, it became clear that in the pursuit of seeing smaller scales and heavier particles, more energetic beams were needed. Consequently, most of the first half of accelerator science history is defined by the drive for higher and higher energies [3]. This has led to the invention of electrostatic accelerators, linacs, cyclotrons, synchrotrons and FFAGs as well as concepts like phase stability and strong focussing, which are still at the core of accelerator physics today.

1.1 High Power Hadron Accelerators

In 1962, M.S. Livingstone plotted on a logarithmic scale the beam energy of every major accelerator built, against the year of entering operation. He noticed an order of magnitude increase in the beam energy every seven years. Since then, the plot has been updated many times, with continued exponential growth, although arguably at a slightly slower rate.

However, the middle of the last century signalled the beginning of a paradigm shift.

While the energy of a machine was an important parameter for potential discoveries, other factors started to play a central role. Beam intensity and machine duty cycle were important aspects for particular applications, but also for any experiment where statistical significance is paramount. The beam loss in the accelerator limited the maintenance capabilities and therefore the machine availability. Additionally, operational and practical aspects ranging from reliability and costs to specific application requirements could not be overlooked. This has led to several parallel developments, one of them being towards high power hadron accelerators.

The definition of high power machines is quite broad and includes a wide variety of accelerators with average beam powers extending from 100 kW to tens of MW. Although difficult to classify, in general, it is acknowledged that depending on the application, four different accelerator types can generally been employed, either as single machines or in a staged approach: linacs, cyclotrons, synchrotrons and FFAGs. Beam energies vary from hundreds of MeV to tens of GeV [4]. Equation 1.1 shows that the main beam power (P) ingredients are beam energy (E) and beam intensity (I_{avg}) and as we shall see, in the drive for higher powers these two components must be optimised (N_p is the number of particles and f_{rep} is the duty cycle).

$$P = E \times I_{avg} = E \times N_p q f_{rep}. \tag{1.1}$$

The initial demand for high beam powers came from particle and nuclear physics and the most notable historical developments have been the 800 MeV proton linac at Los Alamos National Laboratory (LANL) and the 590 MeV proton cyclotron at Paul Scherrer Institute (PSI). At 1 and 1.3 MW, the LANL linac and the PSI cyclotron, still are some of the most powerful accelerators in the world. One of the driving factors for development has been the demand for high beam power for spallation neutron sources.

1.1.1 Spallation Neutron Sources

Spallation is one of the most effective neutron production methods and is based on a simple principle: an energetic proton beam hits a heavy nucleus target. This interaction leads to

neutrons being emitted at different energies, which are further captured, moderated and used in neutron scattering experiments for which high neutron flux is a dominant requirement.

Spallation sources are complex facilities consisting of many subsystems: accelerator, target, moderators, instruments, etc. Depending on the target material, the optimal energy of the incoming proton beam for high neutron yield is at GeV level and therefore, for a given energy the neutron flux increases with beam intensity, leading to high beam power requirements for the accelerator design.

Generally, spallation neutron sources are classified based on the pulse length as short pulse, long pulse or continuous. Short pulse sources usually employ synchrotrons or compressor rings to deliver beam pulses a few μs long, long pulses of ms level can be obtained with linacs, while continuous beams are produced using cyclotrons as well as linacs [5].

The **short pulse** development started with the ZING-P prototype, built at Argonne National Laboratory (ANL) in 1974 using recycled components from the defunct ZGS accelerator. Its success lead to a second prototype ZING-P$'$ and eventually to the Intense Pulse Neutron Source (IPNS), a full-scale facility. At 450 MeV, IPNS used a linac and a rapid cycling synchrotron (RCS) operating at 30 Hz, to produce beams of 6.4 kW. It operated until 2008 [6]. A similar development was done at KEK in Tsukuba, where the KENS facility produced 500 MeV protons at 3.5 kW, using a 20 Hz RCS. However, it was the ISIS facility at Rutherford Appleton Laboratory in the UK that tested the power frontier. The ISIS machine consists of a 70 MeV linac and an 800 MeV RCS operating at 50 Hz to produce a nominal beam power of $\sim$200 kW and for nearly two decades was the most powerful, pulsed spallation neutron source in the world [7].

The success of ISIS in terms of scientific output has been tremendous and has triggered further global developments. At Oak Ridge in USA, the SNS facility started operation in 2007. It uses a superconducting linac and a compressor ring approach. The linac accelerates the beam to 1 GeV when it is injected into the ring. The ring compresses the 1 ms long pulse to less than 1 μs. The machine operates at 60 Hz and the nominal beam power is 1.4 MW, although a 30% lower power is used in normal operation. Potential upgrade options up to 3 MW are available [8].

In Japan at Tokai, the J-PARC facility started operation in 2008. J-PARC is a multipurpose machine and for spallation, a linac-RCS approach is used. A 180 MeV linac injects the beam into a 3 GeV RCS. At 25 Hz, beam powers of 500 kW have been attained, although not in production. Recently, the machine has been upgraded with the aim of reaching 1 MW. The linac energy has been increased to 400 MeV, while higher beam current operation is being tested [9].

In terms of future machines, the Chinese Spallation Neutron Source (CSNS) is currently being built. It consists of an 80 MeV linac and a 1.6 GeV, 25 Hz RCS. The goal is to reach 100 kW. Like J-PARC, CSNS uses a staged upgrade approach to obtain beam powers up 500 kW [10].

The **long pulse** source development started with the 800 MeV normal conducting linac, commissioned at LAMPF (now LANSCE) in 1972. With an initial power of 0.8 MW, the linac was originally intended for meson physics and weapons research, but the potential for neutron scattering experiments was soon realised. The facility is still operational and remains at the higher end of proton linac beam power [11].

Due soon to start construction is the European Spallation Source (ESS), a long pulse facility in Lund, Sweden. Building on the experience from all operational facilities, ESS aims at delivering a record 5 MW beam. In the baseline design, a normal conducting linac is envisaged up to 90 MeV, followed by a superconducting linac up to 2 GeV. Operating at 14 Hz, 62.5 mA and 2.86 ms pulse lengths, ESS is the most ambitious and challenging neutron spallation source project to date and maintains options for future power upgrades [12].

The accelerator choice for **continuous** sources has been the cyclotron, a well understood machine type with a long history. The PSI multipurpose facility in Switzerland uses a 72 MeV injector cyclotron followed by a 590 MeV main cyclotron to accelerate a 2.2 mA proton beam. The beam power currently delivered is 1.3 MW, a world record and potential upgrades are currently analysed. The SINQ spallation source at PSI uses 0.86 MW. While a cyclotron approach to neutron production can be elegant, several issues limit the wider use, including beam loss, clean extraction, high intensity operation concerns, as well as the dimensions and complexity of magnets [13].

There are several advances in accelerator science that have made the development of high intensity, high power beams possible. Some of the most evident contributions include improvements to the front-end and in particular the invention of the radiofrequency quadrupole (RFQ), the development of normal and superconducting linac technology, higher beam loss control as well as low loss injection into rings. A better understanding of beam dynamics as well as the development of rapid cycling synchrotrons (RCS), cyclotrons and FFAGs are also major contributing factors. The evolution as well as the current status of worldwide high power accelerators is illustrated in Figure 1.1. The 0.1, 1 and 10 MW power levels are clearly marked by diagonal lines. The tendency for higher power is evident for accelerators currently under construction (ESS) as well as in the study stage (ADS, IFMIF, etc).

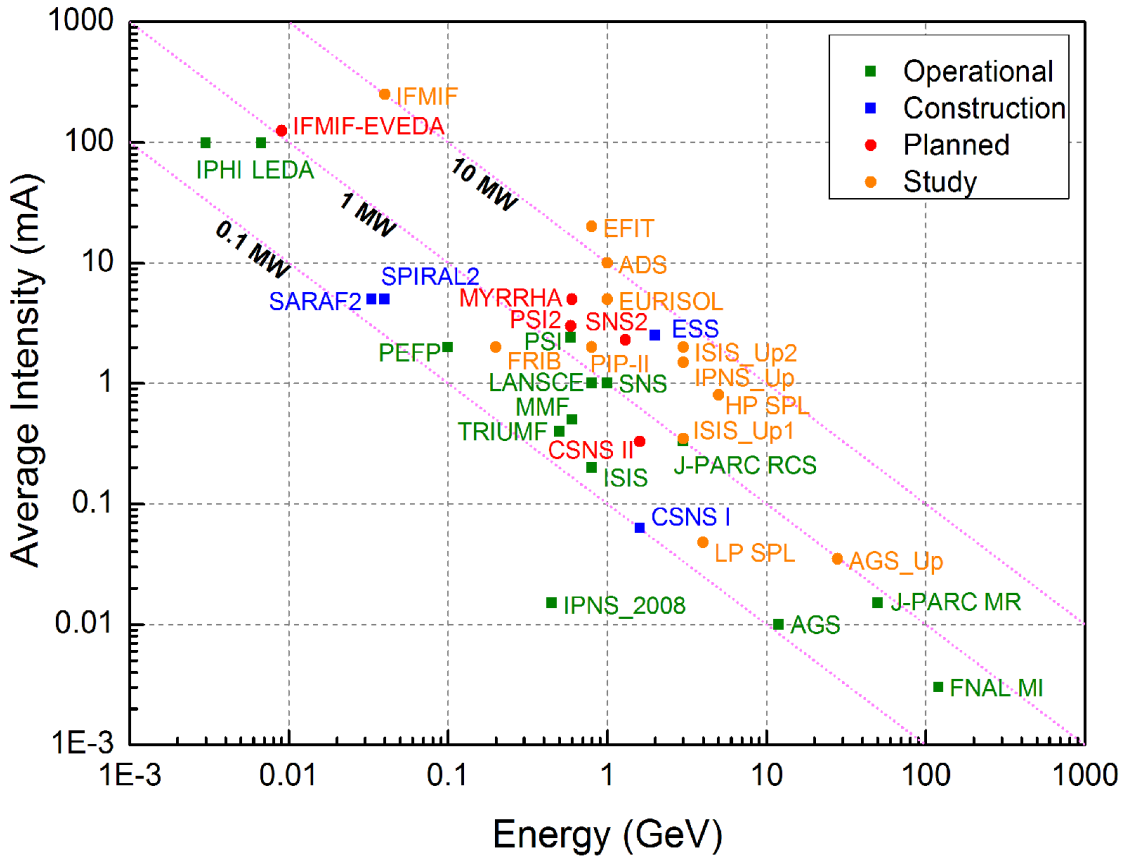

Figure 1.1: Average beam power of several major accelerator projects. Compiled in part from [14], [15] and E. Laface (private communication).

1.2 Proton Linac Development

In terms of proton linac development, there are several historically significant milestones. The first proof of principle linac with only three drift tubes was built in 1928 by R. Widerøe who was developing an original idea by G. Ising. The concept was further developed by D. Sloan and E. O. Lawrence who in 1931 built a linac with 30 drift tubes accelerating Hg ions to 1.25 MeV. A few years later, by adding several more tubes and increasing the voltage, energies of 2.5 MeV were achieved. However, by then the cyclotron attracted much more interest and showed greater potential due to some inherent limitations in linacs. To maintain synchronicity between the radiofrequency field and the particles, the distance between each gap had to be $\beta\lambda$ long and therefore it increased gradually with energy (β is the ratio of velocity to the speed of light and λ is the RF wavelength). This requirement led to longer drift tubes, which for high energies became impractical, as high frequency RF sources were not available.

However, interest in linacs was reignited after the Second World War mainly due to technological progress made in radar technology. With high frequency RF sources available, in 1946 L. Alvarez built a 32 MeV proton Drift Tube Linac (DTL). The accelerator used Widerøe's concept but the drift tubes were enclosed in a conducting cylindrical structure. The resulting structure was an RF cavity in which accelerating modes could be excited. The DTL is operated in the TM_{010} mode and the drift tubes ensure it functions in a similar way to Widerøe's accelerator: the particles are accelerated in the gap, and shielded in the drift tubes while the fields point in the wrong direction. A schematic figure showing a DTL section can be seen in Figure 1.2.

The early DTLs although employing phase stability, did not make use of strong focussing elements for transverse beam control, as the principle was not known at the time. Instead, grids were added at the entrance of each drift tube such that the electric fields were distorted in order to provide radial focussing. The obvious disadvantage of this was the inevitable radioactivation and beam loss, which although small at each drift tube, was significant over the entire length of the linac. Additional difficulties were also found with the mechanical structure of the large cavities. The technology at the time was not capable of delivering large

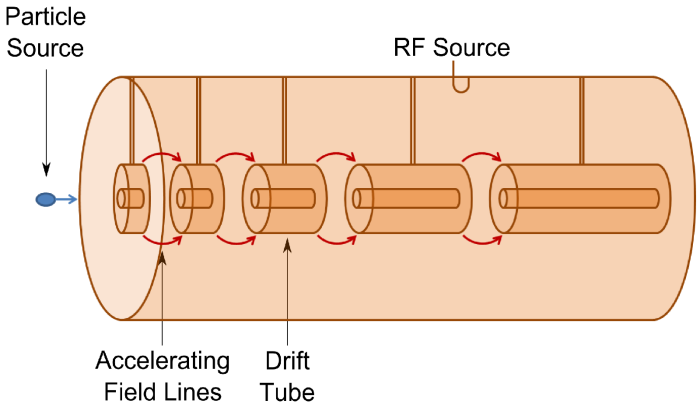

Figure 1.2: Schematic drawing showing the principle of an Alvarez Drift Tube Linac (DTL).

copper tubes sufficiently rigid to maintain the vacuum levels required. As a result, a thin conducting tank was normally placed in a larger vacuum tank made of steel. The thin RF structure was however affected by dissipated heat leading to cavity detuning and operational difficulties. These machines have been called the first generation DTLs.

The success in delivering the first DTL made Alvarez's name synonymous with the structure and soon other machines using the new accelerator were being designed. The second generation DTLs had several key improvements. One major milestone has been the addition of electromagnetic quadrupoles for transverse focussing which improved transmission greatly. The mechanical structure was now sufficiently robust mainly due to progress in copper plating technology and as a result the vacuum and the RF tanks were now identical. These improvements were largely the indirect result of the Material Testing Accelerator (MTA) project, a military DTL intended at accelerating up to 1 A of deuterons at 100% duty cycle, with the aim of producing fissile uranium, an objective eventually abandoned [16], [17].

With the development of synchrotrons, it was realised that injection at a suitable intermediate energy was required and soon proton linacs were also being built as injectors rather than standalone machines. These DTLs had multiple tanks that allowed an improved power management from the RF amplifiers as well as a better control of the electric field flatness along the length of the DTL. Some notable machines built in the 1950s and operating at 50 MeV have been the Bevatron Injector, the CERN Linac1, the BNL AGS Injector and the RAL Nimrod Injector. Two of the tanks from the Nimrod Injector are still operational today in ISIS [18].

The rapid expansion of proton linacs seen in just a decade after the construction of the first DTL has been made possible by the development of high frequency, high power RF amplifiers. The frequency of ∼200 MHz, although originally inherited from radar amplifiers, has been accepted as suitable and is still in use today in many accelerators.

The third generation DTLs that followed showed additional, but smaller improvements. With computers starting to become available, more refined and optimised designs were being proposed, with improved beam dynamics and more precise RF calculations. Small developments were being added on the mechanical design side as well, most notably the introduction of the post-coupler, an insertion aimed at stabilising and flattening the accelerating field profile. The fourth generation DTLs being constructed today employ a rather holistic design approach making full use of the computing power and codes available. A better understanding of the effects of space-charge, emittance and halo growth is now an essential design step. Additionally, the development of compact permanent magnet quadrupoles has allowed more design freedom in optimising the linac for higher efficiency.

Demand for higher energy machines exposed one major limitation of DTLs. At higher energies, the very long drift tubes required, made them very inefficient and therefore alternative structures were necessary. The 800 MeV high power proton linac at Los Alamos (LANL) started operation in 1972. It used a DTL up to 100 MeV, followed by the newly invented cell (side) coupled structure (CCL) to accelerate the beam to the final energy. CCLs have alternating accelerating and coupling cells operating in π mode. However, the coupling cells are placed off-axis, thus allowing the design of the accelerating cells to be optimised for efficiency. CCLs are normally operating at higher frequencies with an additional efficiency gain. Since their invention, CCLs or additional variants have been employed in many linacs.

Alternatives to DTLs have also been proposed, mainly TE-type (H-mode) structures. These cavities have a transverse electric field, which is bent by small drift tubes such that it provides acceleration. The H-mode structures are generally more efficient than DTLs at lower energies and are being used in a number of applications.

At very low energies (up to several MeVs), linacs have also gained from the invention of the radio-frequency quadrupole (RFQ), a revolutionary accelerator proposed by Kapchinsky and Teplyakov in 1970. An RFQ accelerates, focusses and bunches the beam using four

electrodes with periodic radial modulations. It is operated in a quadrupole mode TE_{210} and since its invention has largely replaced all low energy electrostatic injectors, due to the increased reliability and transmission efficiency [19].

1.2.1 Superconducting Linacs

Technological advancements in superconducting technology made possible the development of a new class of accelerators: superconducting linacs. The aim was to provide complementary and alternative solutions to overcome some of the limitations of normal conducting structures, in particular to do with achieving high accelerating gradients, low dissipated power and large cavity apertures for low loss operation. It should be noted that fundamental critical field limitations strictly restrict the maximum achievable accelerating gradient in superconducting structures and for projects requiring extremely high gradients, a combination of high frequency and normal conducting technology is preferable as in the case of the proposed CLIC project [20].

The Argonne Tandem Linac Accelerator System (ATLAS) was the first linac operating in CW mode to use independently phased superconducting cavities to accelerate ion species from hydrogen to uranium to energies up to 17 MeV/u. Since then many other superconducting machines have been built. However, the choice between normal conducting and superconducting structures has to be weighed carefully and it depends on many factors like application type, electric field gradient, duty cycle or beam current [21].

One of the main advantages of superconducting cavities is the high field gradients achievable which lead to higher energy gains per metre and potential overall cost savings. Gradients in excess of 50 MV/m have been demonstrated. Q values of superconducting cavities (10^{10}) are much higher than for normal conducting cavities (10^4) due to almost negligible surface losses. However, a large Q also implies large stored energy and therefore long cavity filling times. This requires the RF pulse to be much longer than the beam pulse therefore reducing the overall efficiency. Additional cryogenics costs also have to be taken into account [22].

In general, for pulsed linac applications, superconducting cavities can be paired with normal conducting cavities, with the superconducting linac section employed at the higher

energy end and a frequency jump between the two. The transition energy between the normal conducting and superconducting sections has to be decided for each individual application. For high duty factor machines the transition energy tends to be lower as superconducting cavities are likely to be more efficient. Similarly for high beam currents, higher transition energies are preferred. The high power SNS facility in the USA operating at 6% duty cycle, uses normal conducting structures up to 186 MeV (a DTL up to 87 MeV, followed by a CCL) and superconducting cavities up to 1 GeV.

In designing superconducting cavities a different approach is normally taken than with normal conducting structures. With high gradients and low surface losses a given, the structures are not optimised for high shunt impedance, but for low peak electric and magnetic fields for a given gradient. The results are elliptically shaped structures with large apertures, a desirable feature if beam loss is to be avoided. Several elliptical structures (cells) are coupled together to form multi-cell cavities, which are then placed in dedicated cryostats.

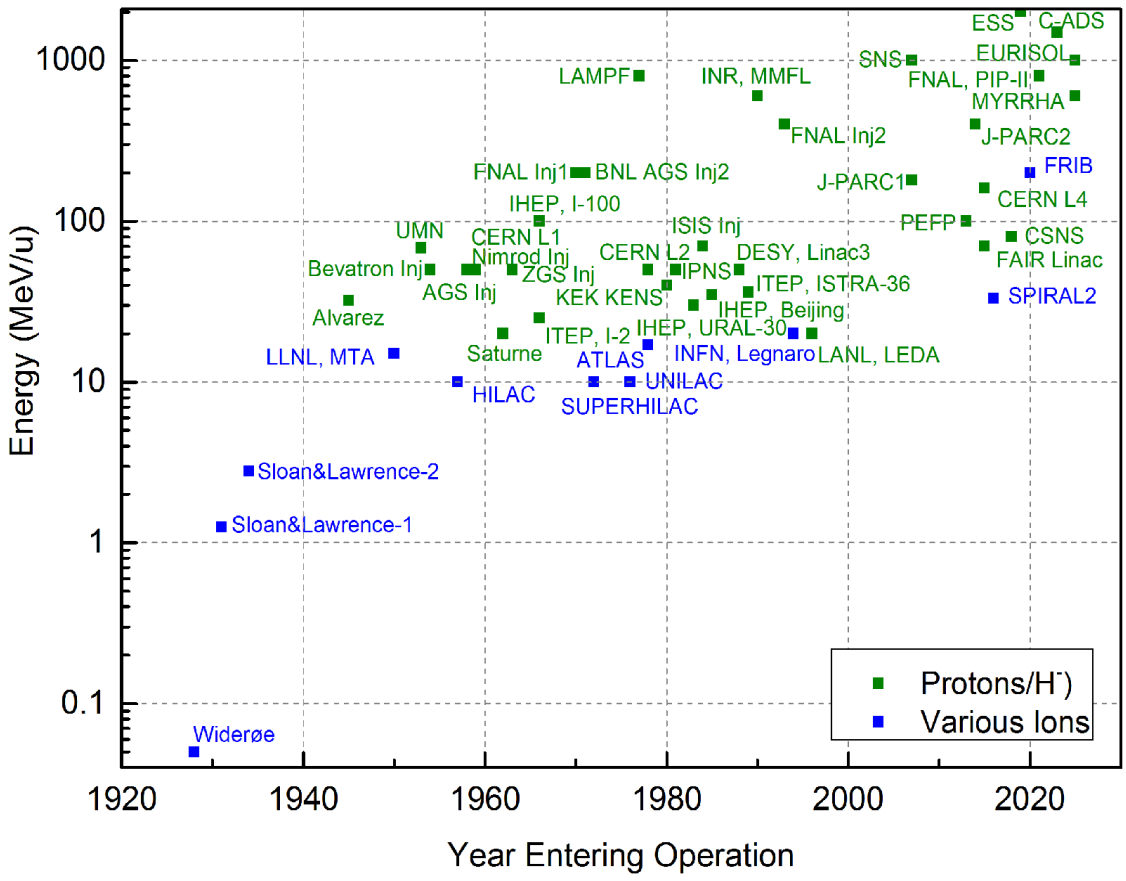

Figure 1.3: Historical development and evolution of major proton/ion linear accelerator projects.

Elliptical cavities are operated in the π mode (mode TM_{010} is excited). The length and the number of cells in each cavity is normally the subject of further optimisation taking into account the necessity for transverse focussing elements between cavities, the total power available from the klystron, etc. For non-relativistic linacs covering a wide energy range, several cavity families are normally chosen with different lengths (geometric relativistic β), a compromise between acceleration efficiency and cost.

Alternative structures are also being investigated like quarter-wave and half-wave resonators. A different, more recent proposal that could be employed at lower energies is the spoke-type cavity. Spokes are stacked half-wave resonators operated in a TE mode. Several proposed projects are aiming to employ them for low and intermediate energies, including the European Spallation Source (90 - 216 MeV).

In recent years, with the superconducting accelerator technology reaching maturity, more projects aim to use superconducting structures at intermediate to lower energies. Superconducting cavities require less RF power and smaller amplifiers, have large apertures, are stable and have fewer thermal problems. On the other hand, the cavities are more sensitive, beam loss can be a problem, the technology is complex and additional cryogenics infrastructure is required. The general consensus is that normal conducting structures are preferred for low energy, low duty cycle and high power applications, while superconducting structures are more suitable for high energy, high duty cycle and low power applications [23].

Figure 1.3 shows a Livingstone type plot with the historical development of proton and ion linacs. It is interesting to note that the interest for linacs is at an all time high, with major projects like ESS, MYRRHA, PIP-II and ADSRs planned for the next decade.

1.3 The Need for High Power Proton Injectors

The global community has identified many high power accelerator applications, ranging from spallation sources to accelerator driven systems. Systematic reviews of high power, high intensity accelerators by G. Rees [4] and C. Prior [14] have classified existing and proposed facilities in several categories.

- **Spallation Neutron Sources (SNS).** There are several existing dedicated neutron

production facilities: ISIS (UK), SINQ@PSI (CH) and SNS (USA). Some other neutron sources are part of larger multipurpose facilities (J-PARC (JP), LANSCE (USA)), while others are currently under construction (CSNS (CN), ESS (SE)). In terms of accelerator architecture, cyclotrons, linacs or linacs and synchrotrons/accumulator rings are being used, offering cw, short pulse or long pulse beams.

- **Radioactive Ion Beams (RIB)** are generally being used for nuclear matter studies exploring the limits of the nuclei stability chart while searching for rare isotopes. Globally, there are several facilities (operational, proposed or under construction): FAIR@GSI (multipurpose facility in DE), FRIB (USA), EURISOL (Europe), ISOLDE (CH), RIKEN (JP), SPIRAL2 (FR), SPES (IT), SARAF (IL).

- **Material Irradiation Facilities (MIF)** are especially relevant in the context of future fusion reactors (ITER) and used as a test bed for advanced materials under extreme radiation conditions: IFMIF-EVEDA, IFMIF and FAFNIR(Global effort).

- **Secondary Beams (Neutrino/Muon/Kaon Factories).** High power hadron accelerators are also needed for secondary beams production. The machines are usually envisaged as part of multipurpose facilities like Linac4/SPL at CERN and PIP-II at Fermilab offering additional options for neutrino physics, beta-beams, neutrino superbeams, muon colliders, neutrino and kaon factories. For a neutrino factory a combination of pulsed H^- linac and proton rings is normally needed to produce the necessary intense muon beam (IDS-NF (Global effort), UKNF (UK)). A similar accelerator arrangement is needed to generate intense μ^+ and μ^- beams for a muon collider.

- **Accelerator Driven Subcritical Reactors (ADSR).** Using spallation produced neutrons to drive a sub-critical reactor is another application with potentially wide implications in energy production and emissions reduction. There are several initiatives worldwide to generate continuous or pulsed high power proton beams (10 MW) using high reliability accelerators: ADS (CN), MYRRHA (BE), ThorEA (UK).

- **Accelerator Driven Transmutation of Radioactive Waste (ATW).** Equally high power as for ADSR is required for transmutation facilities, another application

with potentially wide implications. A linac only option operating at around 1 GeV is generally favoured due to its simplicity. The TRASCO project in Italy is envisaged to deliver a 30 MW cw beam.

- **Accelerator Production of Tritium (APT).** CW linacs are usually preferred. An APT study produced at LANL (USA) proposed a machine capable of delivering 170 MW of average beam power at 1.7 GeV.

At Rutherford Appleton Laboratory (RAL), the development of a next generation high power proton accelerator complex represents a priority and is mainly driven by two important factors: the requirement of a high intensity proton machine as the driver for a future neutrino factory and the necessity to upgrade the ageing ISIS Spallation neutron source [18].

1.3.1 Proton Drivers for Neutrino Production

The neutrino, although one of the most abundant particles in the universe, has remained one of the most mysterious. With the relatively recent but compelling evidence suggesting that neutrinos have mass, efforts are underway to gain a deeper understanding of neutrino physics which could lead to a complete overhaul of the Standard Model. In particular, characterising neutrino flavours and oscillations from one type to another are significant physics milestones that have to be clarified. More specifically, a precise measurement of the mixing angles θ_{12}, θ_{13} and θ_{23} and of the mass splitting terms Δm^2_{ij} is essential in explaining neutrino mixing. For an in-depth description of neutrino oscillations, see [24].

Such measurements require intense controlled sources of neutrinos. One proposal is to use an accelerator based source, referred to as a "neutrino factory". Neutrinos are produced indirectly via intermediate particles. A high power, high energy, proton beam hits a high-Z target where pions are produced. Pions are further captured and will decay to muons ($\pi^+ \rightarrow \mu^+ + \nu_\mu$, $\pi^- \rightarrow \mu^- + \bar{\nu}_\mu$). A second accelerator chain will capture and accelerate the resulting muons to the required energy (tens of GeV). Finally, the muon decay ($\mu^+ \rightarrow e^+ + \nu_e + \bar{\nu}_\mu$, $\mu^- \rightarrow e^- + \bar{\nu}_e + \nu_\mu$) will produce a focussed neutrino beam directed at detectors placed at baseline length (hundreds to thousands of km). A possible outline for a neutrino factory is presented in Figure 1.4.

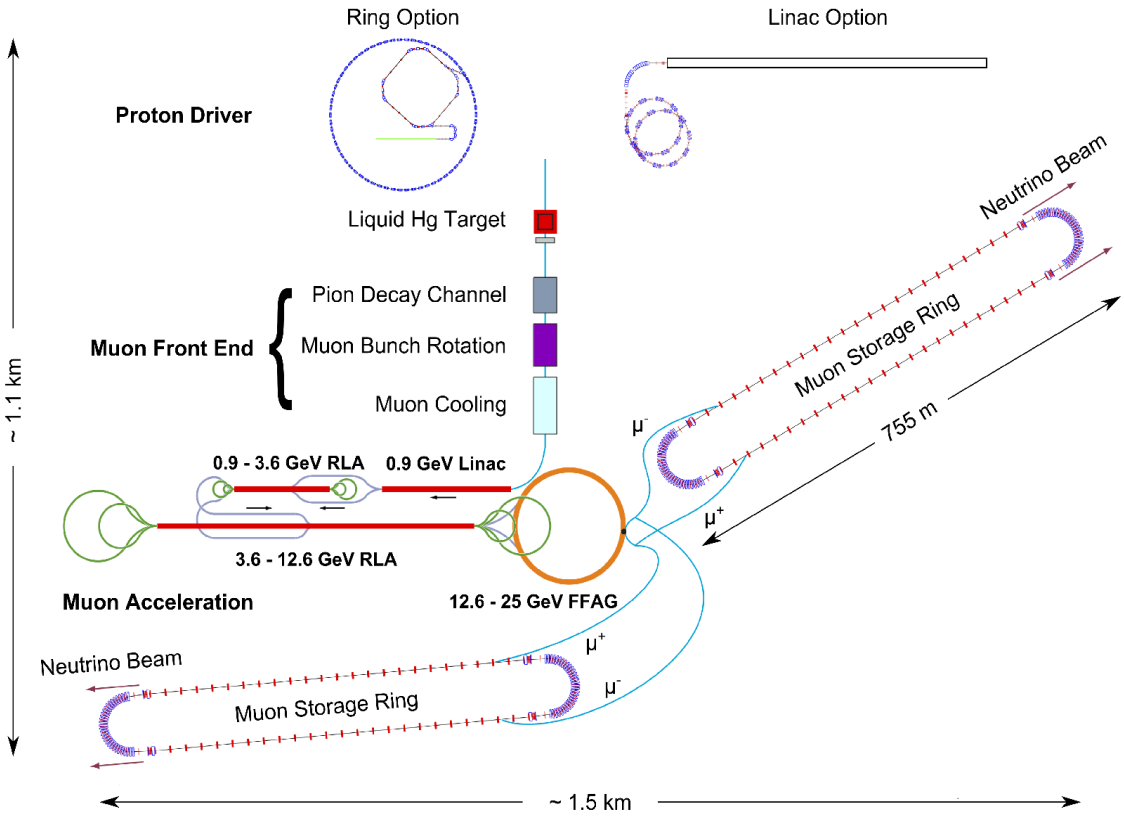

Figure 1.4: A possible layout for a neutrino factory. Courtesy of C. Prior.

This scheme poses several challenges. The highly statistical nature of mixing angles measurements, requires muon decay events in the region of 10^{21} per year. This high flux determines the specifications of the proton driver: a minimum average beam power of 4 MW, a proton kinetic energy of 5 - 15 GeV and the ability to produce high intensity short bunches of protons with time duration of 1 - 2 ns necessary for the muon capture systems [25]. For high power operation, high quality beams are essential. Significant technical development is necessary, especially at the front end of the accelerator where low energy (2.5 - 3 MeV) beam chopping at high duty cycle (1 - 10%) is required to minimise beam loss and the induced radioactivity at injection into downstream circular accelerators. Additionally, attention has to be paid to beam matching into the linac, as initial mismatch could lead to halo development, emittance growth and beam loss [26].

Figure 1.5 shows several alternative technical proposals for the proton driver involving high energy linacs, rapid cycling synchrotrons with stacked rings and FFAGs. As each design requires a linac front end, the drive to overcome existing linac limitations is fully justified. One ongoing development in this area is through the Front End Test Stand project

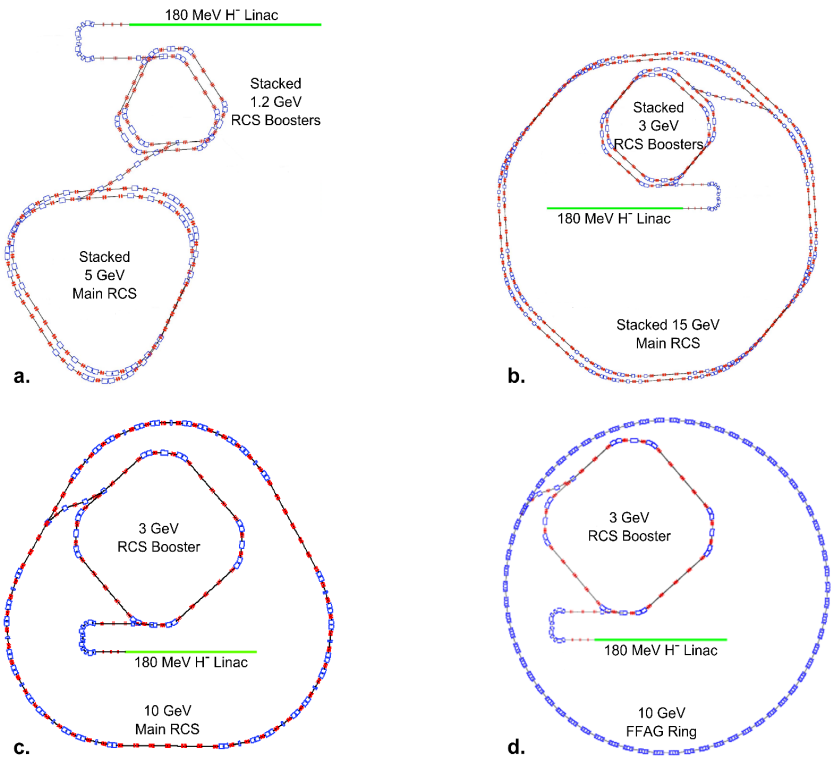

Figure 1.5: Alternative proposals for a high power proton driver for a neutrino factory. **a.** The accelerator consists of a 180 MeV H^- linac, followed by an achromat section for collimation and two stacked 1.2 GeV, 50 Hz, booster synchrotrons each accelerating 2 bunches of 2.5×10^{13} protons. Two further stacked synchrotrons operating at 25 Hz with 4 bunches in each ring accelerate the beam to 5 GeV. **b.** A similar 180 MeV H^- linac is used for injection into two stacked 3 GeV, 25 Hz booster synchrotrons with 3 bunches of 1.11×10^{13} protons in each ring. Two stacked, 15 GeV, 12.5 Hz main synchrotrons are further used, each accelerating 6 bunches. **c.** A 180 MeV H^- linac injects the beam into a 3 GeV RCS operating at 50 Hz. The beam is further accelerated up to 10 GeV in the main synchrotron. Beam intensities of $\sim 10^{14}$ protons will be achieved. **d.** A similar arrangement is proposed as in the previous scenario (**c.**), but the main synchrotron is replaced by a 10 GeV non-scaling FFAG. (Figure created from original proton driver layouts by C. Prior.)

(FETS) at RAL. FETS is a generic R&D effort showing the UK's commitment for high power accelerators. It is aimed at delivering a 3 MeV high intensity, high quality, chopped beam, thus meeting the stringent requirements for high power drivers.

1.3.2 ISIS Upgrades

A second factor driving the development of high power proton accelerators at RAL is the necessity to upgrade the ageing ISIS spallation neutron source. As already mentioned, ISIS uses a 70 MeV injector and an 800 MeV RCS to deliver a total of ~200 kW beam to 2 target stations: 160 kW to Target Station 1 (40 Hz) and 40 kW to the recently commissioned

Target Station 2 (10 Hz). While ISIS has been the most successful pulsed spallation source in the world, it is also the oldest, still operating source and the necessity for an upgrade has been made clear for some time. This involves not just maintaining or improving the current machine reliability, but also increasing the existing capabilities. With new facilities like the SNS in the USA now delivering MW level beams and J-PARC in Japan soon to achieve similar beam powers, a major power upgrade for ISIS has become a key strategic goal in the medium to long term.

Small machine upgrades are already taking place aimed mainly at improving the machine reliability. As one of the oldest part in the machine, the linac has seen most developments. A programme designed to improve the ion source lifetime, beam current, pulse length and reliability has been successfully taking place as part of the Front End Test Stand project. The old Cockcroft-Walton linac injector has been replaced with a 665 keV, 202.5 MHz RFQ, the structure of choice for most modern injectors. Also on the linac front, efforts are underway to replace the fourth DTL tank, a structure soon to celebrate its 60th anniversary. In terms of ring developments, the installation of a dual harmonic system has been taking place. By employing a combination of harmonic number 2 and 4 RF cavities, the stable area of the longitudinal phase space can be increased allowing more beam to be injected and accelerated, thus overcoming the old machine intensity space-charge limit of 2.5×10^{13} protons per pulse. Beam powers of $\sim$240 kW have already been demonstrated [27].

In terms of major upgrades, the addition of a second target station at the end of 2008, saw the machine capabilities and user base greatly expanded. However, in terms of power upgrades, the construction of new accelerators is necessary. There have been several proposals for a power increase. In general, a staged upgrade is preferred with minimal user disruption. Additionally, proposals exist for a multipurpose facility where a high power proton accelerator would be used both for a spallation source and as a driver for a neutrino factory as explained in Section 1.3.1. Summarised here are the major upgrade options leading to a significant increase in beam power for ISIS [28]:

- **A new 180 MeV linac** to replace the old 70 MeV injector. This potential upgrade has the benefit of replacing the oldest and most capricious part of the machine. By

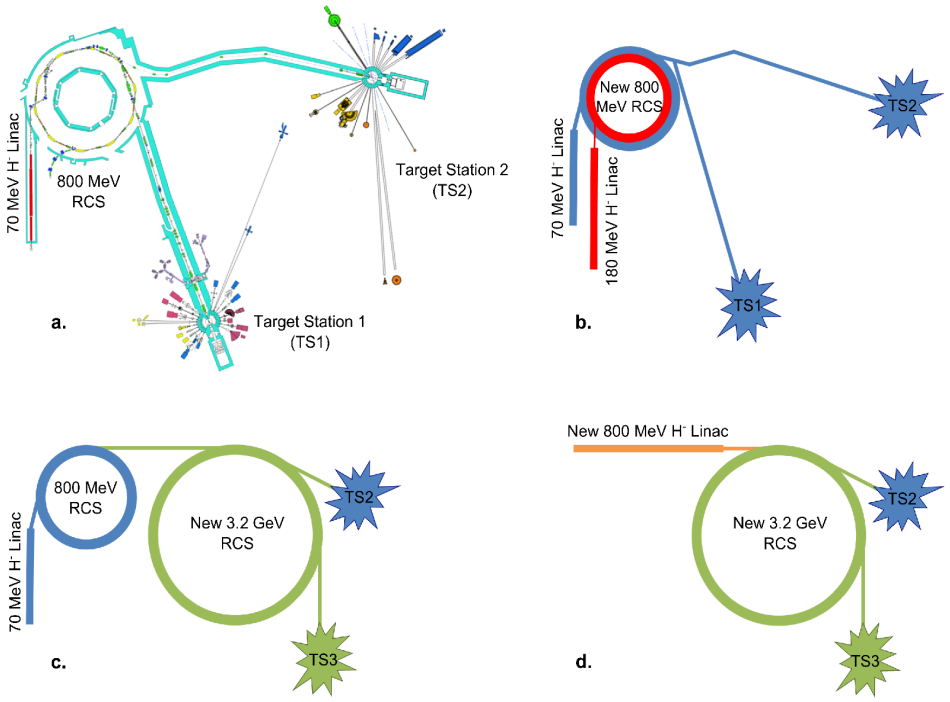

Figure 1.6: Schematic layout of alternative proposals for ISIS power upgrades. **a.** Current ISIS facility. **b.** Proposed upgrade to include a new 180 MeV linac and a new 800 MeV RCS. **c.** High power upgrade with the addition of a new 3.2 GeV RCS and a new target station. **d.** Further power increase can be by achieved by replacing the current ISIS machine with an 800 MeV superconducting linac injecting into the 3.2 GeV RCS.

injecting at a higher energy an increased ring intensity can be achieved, thus leading to an increase in beam power to ∼0.4 MW. Additionally, an upgrade scheme can be designed such that the disruption to ISIS operation is minimal (see Figure 1.6b).

- By adding **a new 800 MeV ring** identical to the current ISIS RCS, the beam intensity could be doubled by operating the two rings in parallel, thus providing beam powers in the region of ∼0.5 MW. This upgrade assumes that the current linac can run longer beam pulses with consecutive or alternate half cycles such that the repetition rate is doubled on target, but has obvious operational limitations. By combining the first two options (a new linac and a new ring), beam powers in the region of 0.9 MW could be achieved (see Figure 1.6b).

- Another proposed scheme is to add **a new 3.2 GeV 50 Hz RCS** that would use the current facility as an injector. This upgrade would lead to a 1 MW beam power and would most likely require the construction of a third target station, but it has the

advantage of minimum ISIS user operation disruption (see Figure 1.6c).

- As the previous option faces reliability risks from using ISIS as an injector, one proposal is to replace the entire injector chain with **a new 800 MeV linac**. This will also allow increased intensity through phase-space painting. By using the new linac and the new 3.2 GeV RCS, beam powers of up to 5 MW can be achieved (see Figure 1.6d).

- Finally, as building on an existing site poses several key design limitations, **green field solutions** are also investigated. One proposal is to use a new linac and synchrotron with several target stations maximising the number of beam lines and allowing a much higher flexibility for neutron experiments (variable proton energy, intensity, repetition rate, etc.). Megawatt level proton beam powers would be achievable.

It is interesting to note that most of the proposed upgrades involve either the replacement of the existing linac with a similar, but higher energy machine, or the construction of a new high energy linac as the main injector for an upgraded ISIS facility. Whatever upgrade path is chosen for ISIS or its replacement, an optimised linac will be needed as a front-end injector to enable the facility to meet the high beam power requirements. A general layout of the RAL site with the potential location of new machines in some of the upgrade scenarios discussed above is shown in Figure 1.7.

1.4 The Goals of This Thesis

In 2007 as part of the EU/FP6 HIPPI collaboration (High Intensity Pulsed Proton Injectors), I was asked to produce an up to date review of existing normal conducting (NC) accelerating structures for ion linacs. It soon became clear that the choice of accelerating cavities for many projects and in many research laboratories was not entirely based on their efficiency, suitability for a certain energy range or application. The justifications for the selection were often apocryphal, ranging from existing local expertise to alleged cost savings. In short, the proton linac community lacked a systematic analysis of available normal conducting structures. Through discussions with various colleagues including Frank Gerigk, Suitbert Ramberger and Maurizio Vretenar from CERN as well as Alan Letchford from RAL and

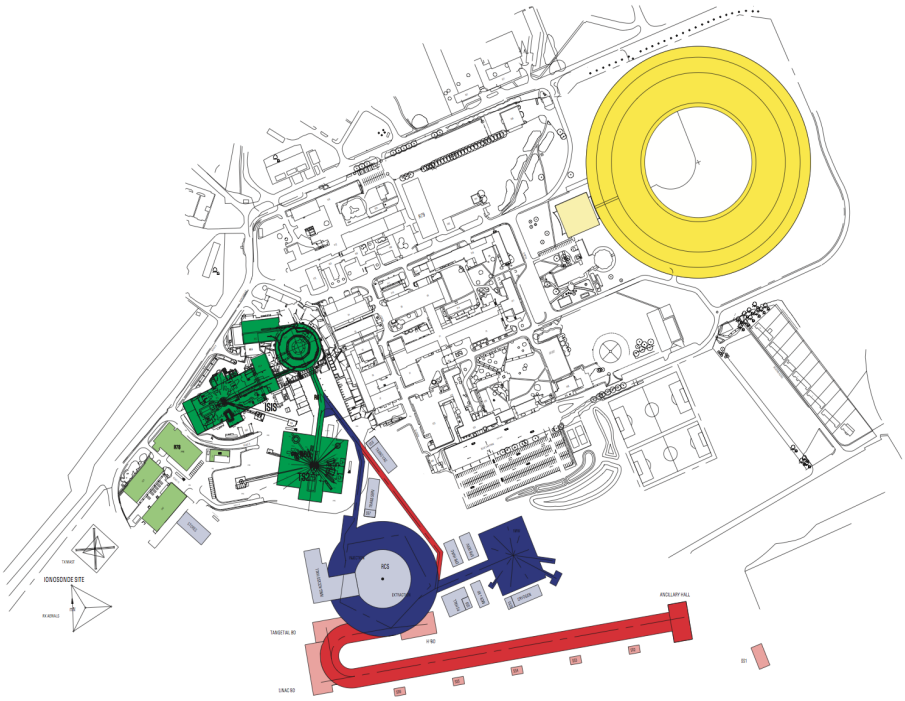

Figure 1.7: The Rutherford Appleton Laboratory site, showing the current accelerator facilities ISIS Neutron Source (green) and Diamond Light source (yellow), the 3.2 GeV RCS potential upgrade (blue) and a new 800 MeV linac (red). (Picture courtesy of J. Thomason.)

Jim Stovall from LANL, it was decided that a methodical examination of linac NC RF structures was urgent and essential. The study was structured in several sections: a first part where the design and comparison criteria were listed and explained, a second part containing a comprehensive assessment of each structure type including RF modelling and beam dynamics simulations and finally, an overall structure comparison and evaluation. In this process, reference plots and comparison tables were produced, a valuable addition to the RF linac design landscape. In addition, several novel tools for cavity design analysis were developed, allowing a better understanding of all the correlations between the different design choices available and various constraints and limitations. This work is summarised in Chapter 3 and 4.

At approximately the same time, I had started working on the Front End Test Stand project (FETS), mainly on beam dynamics and component design of the Medium Energy Beam Transport chopper line (MEBT). One major difficulty for the MEBT design was reducing the beam loss and emittance growth, which was made more complicated by the high beam intensity required for FETS. The difficulties with high intensity beams became

more evident when as part of the efforts to design a new linac for ISIS upgrades (180 MeV normal conducting and 800 MeV superconducting), end-to-end simulations were performed where the FETS beam was fed into the new linac structure. These studies indicated that the halo level and to a certain degree the beam loss in the downstream accelerator, were to a great extent correlated with the initial beam quality and the mismatch level at the beginning of the accelerator. Since the MEBT line was largely responsible for matching the RFQ beam into the DTL, through extensive discussions with my colleagues Shinji Machida and Grahame Rees, it was decided that a better MEBT design philosophy was needed. A systematic analysis of performance of all MEBT lines with choppers was therefore carried out highlighting their major limitation causes, with an emphasis on the FETS MEBT line. A novel MEBT with choppers was then proposed, allowing better matching and chopping as well as higher intensity, lossless operation. This work is summarised in Chapter 5.

While working on a new linac for ISIS, one early design choice was to use the equipartitioning rule to avoid space-charge driven emittance exchange between phase space planes. Equipartitioning simply means that the beam "temperatures" are equal in the longitudinal and transverse planes: $T_t/T_z \sim k_t\epsilon_t/k_z\epsilon_z = 1$, where k is the tune and ϵ is the beam emittance. This imposes some strict limits on the selection of the working points, leading to a potentially less optimised design in terms of RF and beam optics with probable repercussions on machine costs. However, over the last two decades or so, work done by Ingo Hofmann, Jean-Michel Lagniel, Bob Jameson and others, suggests that safe tunes can be found in the tune diagram, outside the equipartitioning limits. Tune stability charts (Hofmann diagrams) have been produced in an attempt to illuminate and ease the design procedure. While some new linacs are being designed with the stability charts in mind, the lack of experimental verification remains a problem. Knowing this, a collaboration study was started with Masanori Ikegami and others from J-PARC leading to an experimental campaign where for the first time emittance exchange driven by the $k_z/k_t = 2$ resonance was measured in a linac with emittance ratios close to 1. A summary of this work is presented in Chapter 6.

All these novel developments finally converge to produce the most optimised design to date for an ISIS upgrade linac both in terms of how the final energy is achieved and how well the beam quality is preserved. Three options have been fully developed and investigated,

accelerating the beam to 100, 180 and 800 MeV and offering for the first time realistic solutions for MW-level operation in ISIS. These designs not only outperform the existing ISIS linac, but are comparable or better than similar projects worldwide, a testament that the linac design principles explored and formulated here are not particular to a certain machine, but generic and universal. Furthermore these linac designs are sufficiently versatile such that they can also be incorporated with virtually no modifications in the proton driver design for future, long-term projects like the neutrino factory.

At last, the birth of this thesis was possible because of Shinji Machida, Ken Peach and Chris Prior who in the context of high power proton machines in general and ISIS upgrades in particular, saw the necessity of a consistent and coherent piece of work in which the above mentioned subjects converge. The purpose of this thesis is to tackle several limiting aspects to do with two major pillars of high power operation: energy and intensity.

Chapter 2

Basic Equations and Definitions

In this chapter, the physics foundations of proton linear accelerators are set in a rigorous mathematical manner. This exercise is necessary as it forms the basis for extensive discussions in subsequent chapters. Several key accelerator physics concepts are outlined, covering acceleration in RF linacs, longitudinal and transverse beam dynamics and multi-particle beam physics. Fundamental notions like phase stability, transfer matrixes, Twiss parameters, emittances and space-charge are explained.

2.1 Particle Acceleration in RF Linacs

2.1.1 RF Cavities

One of the key components in particle accelerator design is the accelerating cavity, the means by which the beam receives energy from an external source (i.e. the grid). This section will review the main concepts and equations necessary to understand the principles of particle acceleration in RF linacs. References [29] [30], [31] and [32] on which this short summary is based, as well as dedicated CERN Accelerator School lectures (CAS) and many other resources, offer a more extensive description.

An RF cavity is fundamentally an empty volume delimited by conducting boundaries. The electromagnetic fields in this volume are described by Maxwell's equations. In their

differential form in free space, the equations are:

$$\begin{aligned} \nabla \cdot \mathbf{E} &= \frac{\rho}{\epsilon_0} \\ \nabla \cdot \mathbf{B} &= 0 \\ \nabla \times \mathbf{E} &= -\frac{\partial \mathbf{B}}{\partial t} \\ \nabla \times \mathbf{B} &= \mu_0 \mathbf{J} + \frac{1}{c^2} \frac{\partial \mathbf{E}}{\partial t} \,. \end{aligned} \tag{2.1}$$

$\mu_0 = 4\pi \cdot 10^{-7}$ (T·m/A) - Vacuum Permeability (Magnetic Constant)

$\epsilon_0 = \frac{1}{\mu_0 c^2}$ (F/m) - Vacuum Permittivity (Electric Constant)

$c = 1/\sqrt{\mu_0 \epsilon_0} = 2.99792458 \cdot 10^8$ (m/s) - Speed of Light in Vacuum

The propagation of the electric and magnetic fields through a medium can be described by a well known second-order partial differential equation. The electromagnetic wave equation is derived from Maxwell's equations and in terms of the electric and magnetic fields in the absence of sources is written as:

$$\begin{aligned} \nabla^2 \mathbf{E} - \frac{1}{c^2} \frac{\partial \mathbf{E}}{\partial t^2} &= 0 \\ \nabla^2 \mathbf{B} - \frac{1}{c^2} \frac{\partial \mathbf{B}}{\partial t^2} &= 0 \,. \end{aligned} \tag{2.2}$$

To find a solution to these differential equations, the boundary conditions need to be included. They simply state that outside the conductor surface the tangential electric field component and the normal magnetic field component are zero ($\hat{n} \cdot \mathbf{E} = \frac{\Sigma}{\epsilon_0}, \hat{n} \cdot \mathbf{B} = \mathbf{0}, \hat{n} \times \mathbf{E} = \mathbf{0}, \hat{n} \times \mathbf{H} = \mathbf{K}$). As most accelerating cavities have cylindrical geometries, solutions to Maxwell's equations for this particular case will be further investigated. These solutions must satisfy the wave equation inside the cavity and the boundary conditions above. Proposing a solution of the form:

$$E_z(r, \theta, z, t) = E(r, \theta, z) e^{j\omega t} \tag{2.3}$$

and substituting it into the wave equation, one arrives at the Bessel equation of the zero order, for which analytical solutions exist, known as Bessel functions. Figure 2.1 plots the Bessel functions of the first kind for integer orders 0 to 5, which resemble a damped oscillation. Using these functions one can arrive at the general expression for the electric

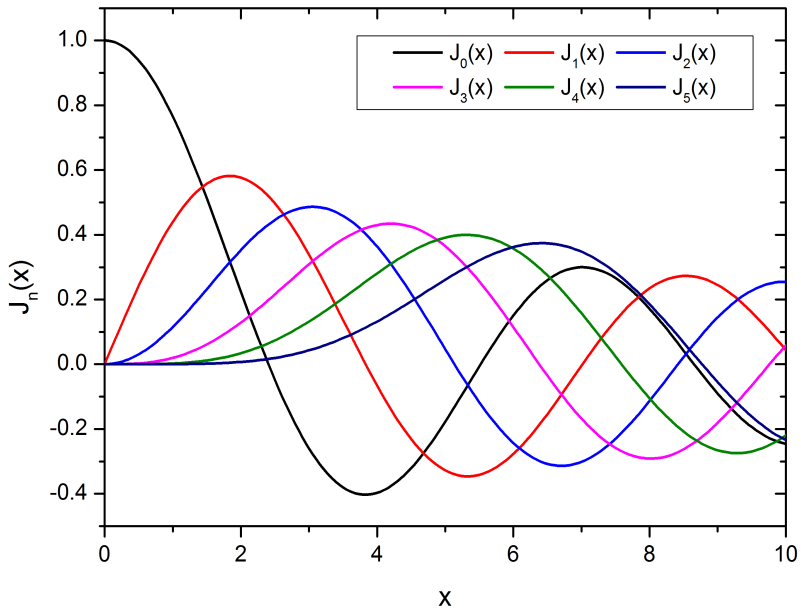

Figure 2.1: Plot of the Bessel function of the first kind for integer orders 0 to 5.

and magnetic field components in a cylindrical cavity:

$$
\begin{aligned}
E_z &= E_0 J_m(k_{mn} r)\cos(m\theta)\cos\frac{p\pi z}{l}e^{j\omega t} \\
E_r &= -\frac{p\pi}{l}\frac{a}{x_{mn}}E_0 J_m'(k_{mn} r)\cos(m\theta)\sin\frac{p\pi z}{l}e^{j\omega t} \\
E_\theta &= \frac{p\pi}{l}\frac{ma^2}{x_{mn}^2 r}E_0 J_m(k_{mn} r)\sin(m\theta)\sin\frac{p\pi z}{l}e^{j\omega t} \\
B_z &= 0 \\
B_r &= -j\omega\frac{ma^2}{x_{mn}^2 r c^2}E_0 J_m(k_{mn} r)\sin(m\theta)\cos\frac{p\pi z}{l}e^{j\omega t} \\
B_\theta &= -j\omega\frac{a}{x_{mn} c^2}E_0 J_m'(k_{mn} r)\cos(m\theta)\cos\frac{p\pi z}{l}e^{j\omega t}
\end{aligned}
\tag{2.4}
$$

$m,\ n,\ p$ - Integer numbers

a, l - Cavity radius and length

x_{mn} - Zeros of the Bessel functions $J_m(x)$

$\frac{x_{mn}^2}{a^2} = \frac{\omega^2}{c^2} - \left(\frac{p\pi}{l}\right)^2$ - Dispersion relation

In a cavity, the different field patterns that can occur are known generically as **cavity modes**. In the equations above, since the magnetic field has components only in the transverse direction while the z component is zero, these modes are known as **transverse-magnetic**, **TM modes** or **E modes**. Because of the non-zero longitudinal electric field,

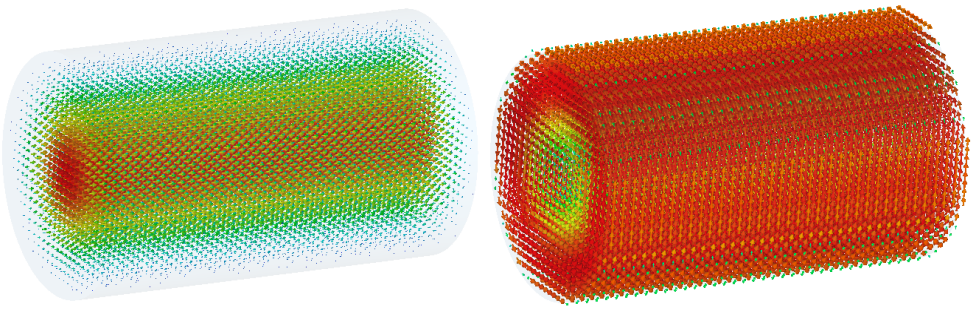

Figure 2.2: Electric (left) and magnetic fields (right) in a pillbox cavity operating at 324 MHz (from CST MicroWave Studio).

they are generally suitable for acceleration. Most linac accelerating structures to be discussed in Chapter 4 operate in a TM mode. To differentiate the various modes and allow an ordered classification, the convention generally accepted uses the $\mathrm{TM}_{\mathrm{mnp}}$ notation where:

- **m** is the number of full-period oscillations of the field components in the azimuthal direction (m=0,1,2,3...).
- **n** is the number of zero-crossings of the axial field components in the radial direction (n=0,1,2,3...).
- **p** is the number of half-period variations of the field components in the longitudinal direction (p=0,1,2,3...).

The simplest accelerating mode is the TM_{010} **mode**, which is the fundamental mode in a **pillbox cavity**. A pillbox cavity is essentially a cylinder with conducting boundaries. In this mode the longitudinal electric field is concentrated along the axis of the cavity while the magnetic field circles around it in the transverse direction as can be seen in Figure 2.2 where such a cavity was modelled using CST MicroWave Studio, a 3D EM simulation tool for high frequency components [33].

For the specific case of a pillbox cavity, the field components are now reduced to:

$$\begin{aligned} E_z &= E_0 J_0(k_r r)\cos(\omega t)\,, \\ B_\theta &= -\frac{E_0}{c} J_1(k_r r)\sin(\omega t)\,. \end{aligned} \tag{2.5}$$

It is interesting to note that the resonant frequency f_0 of a pillbox cavity is independent

of the cavity length and depends only on the cavity radius a:

$$\omega_0 = 2\pi f_0 = \frac{2.40483 \cdot c}{a} \,. \tag{2.6}$$

For completeness it should be also mentioned that in cylindrical cavities **transverse electric** or **TE-modes** can also be excited. Since the longitudinal component of the electric field is zero in this case, these modes cannot generally be used for acceleration. However, suitable solutions have been found and indeed a TE-mode linac cavity structure will be analysed in detail in Chapter 4.

In linacs, accelerating with single cell cavities is not efficient and instead multiple cells are coupled together to form chains of resonators. For optimum acceleration, the particles have to arrive in each gap close to the crest of the RF wave. However, as the particles become faster, the synchronicity with the accelerating field is quickly lost and therefore two different approaches can be adopted: adjust the phase ϕ of the accelerating field or increase the distance between consecutive accelerating cells. For practical reasons, the first solution is generally avoided as it would require individual power supplies for each accelerating cell at exorbitant costs and therefore it is only used in projects where flexibility is the overriding requirement for acceleration (i.e. accelerators for multiple ion species). Instead, a synchronicity condition is followed that relates the phase change $\Delta\phi$ between consecutive cells with the particle velocity β, the RF wavelength λ and the distance d between cells:

$$\frac{\Delta\phi}{d} = \frac{2\pi}{\beta\lambda} \,. \tag{2.7}$$

When multiple accelerating cells are coupled together to form chained resonators, **normal-modes** emerge, described by the relative phase difference of the field oscillation in neighbouring cells. These modes represent yet another taxonomic classification of accelerating cavities. Assuming a coupled-cavity system, the number of modes possible will depend on the number of cells and will be distributed on a dispersion curve between the lower frequency "0-mode" where the oscillations are in-phase and the higher frequency π-mode where the oscillations are in opposite phase. The modes are characterised by frequency, amplitude and

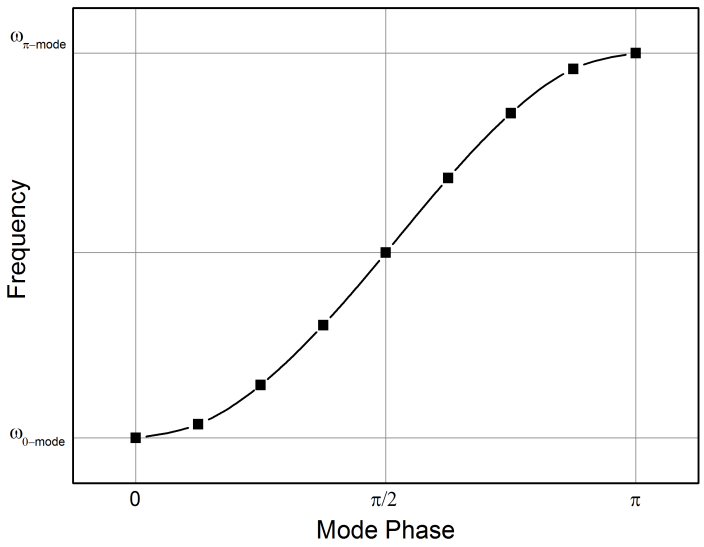

Figure 2.3: Dispersion curve for a multi-cell coupled cavity with nine cells.

phase. The dispersion relation is a sinusoidal curve given by the following equation:

$$\omega_q^2 = \frac{\omega_0^2}{1 + k\cos\Delta\phi} = \frac{\omega_0^2}{1 + k\cos\frac{\pi q}{N}}\,. \tag{2.8}$$

ω_q - Mode Frequency

ω_0 - Uncoupled single cell frequency

q - Mode Number

$\frac{\pi q}{N}$ - Mode Phase (N - Number of Cells)

k - Coupling Constant

The 0-mode and the π-mode frequencies are given by:

$$\begin{aligned} \omega_{0-mode} &= \frac{\omega_0}{\sqrt{1+k}}\,, \\ \omega_{\pi-mode} &= \frac{\omega_0}{\sqrt{1-k}}\,. \end{aligned} \tag{2.9}$$

Figure 2.3 shows the dispersion curve for a coupled cavity with nine cells, with the 0-mode, $\pi/2$-mode and π-mode highlighted, as these modes are generally useful for acceleration as it will be shown in Chapter 4. The accelerating field pattern in the three accelerating modes of interest is shown in Figure 2.4. Additional intermediate modes do exist and as more cells are added, more modes will appear. The synchronicity condition for these three

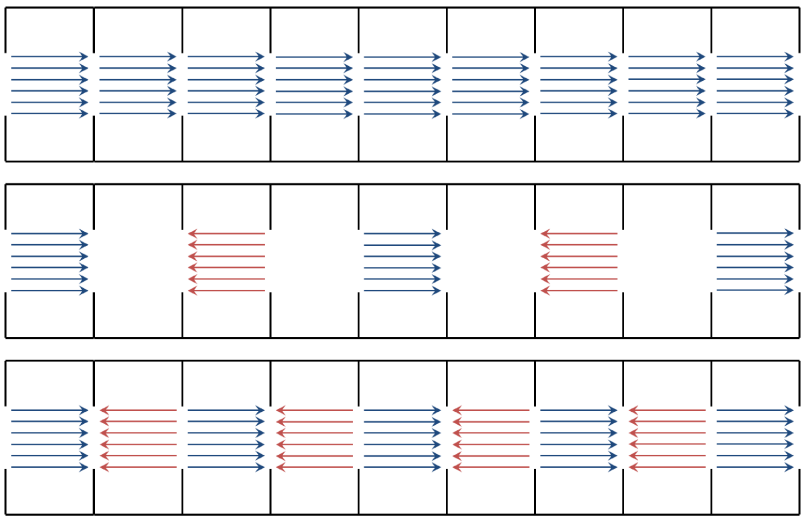

Figure 2.4: Normal modes in a multi-cell coupled cavity: 0-mode (top), $\pi/2$-mode (middle) and π-mode (bottom).

accelerating modes is given by:

$$\begin{aligned} &\text{0-mode} && d = \beta\lambda \\ &\frac{\pi}{2}\text{-mode} && d = \frac{\beta\lambda}{4} \\ &\pi\text{-mode} && d = \frac{\beta\lambda}{2} \end{aligned} \tag{2.10}$$

2.1.2 Energy Gain

Let us now consider a standing wave accelerating cavity of the type presented above (i.e. pillbox-type cavity) excited in the TM_{010} mode. The accelerating field along a cavity gap of length L is shown in Figure 2.5, while the electric field on axis ($r = 0$) can be expressed as already shown as:

$$E_z(z,t) = E(z)\cos(\omega t + \phi)\,. \tag{2.11}$$

where ϕ is the synchronous phase and will be described in further detail later in this chapter. For a particle of charge q crossing the gap along the axis, the energy gain will be given by:

$$\Delta W = q \int_{-L/2}^{L/2} E(z)\cos(\omega t(z) + \phi)\mathrm{d}z\,. \tag{2.12}$$

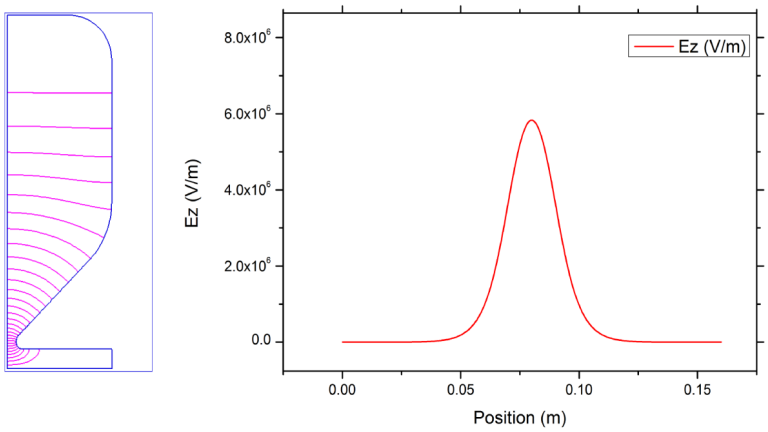

Figure 2.5: On-axis field distribution (right) along a pillbox-type cavity (left, half cell).

$$\Delta W = q \int_{-L/2}^{L/2} E(z)[\cos\omega t(z)\cos\phi - \sin\omega t(z)\sin\phi]\mathrm{d}z\,. \tag{2.13}$$

By choosing the origin to coincide with the centre of the gap ($z = 0$) such that the particle arrives at the centre at $t = 0$, the energy gain can be written as:

$$\Delta W = q\left[\int_{-L/2}^{L/2} E(z)\mathrm{d}z\right]\left[\frac{\int_{-L/2}^{L/2} E(z)\cos\omega t(z)\mathrm{d}z}{\int_{-L/2}^{L/2} E(z)\mathrm{d}z}\right]\cos\phi\,. \tag{2.14}$$

Defining a voltage V_0 and a transit-time factor T as:

$$\begin{aligned} V_0 &= \int_{-L/2}^{L/2} E(z)\mathrm{d}z\,, \\ T &= \frac{\int_{-L/2}^{L/2} E(z)\cos\omega t(z)\mathrm{d}z}{\int_{-L/2}^{L/2} E(z)\mathrm{d}z}\,. \end{aligned} \tag{2.15}$$

reduces equation 2.14 to well-known form:

$$\Delta W = qV_0T\cos\phi\,. \tag{2.16}$$

The transit-time factor T defined above is an important concept that takes into account

the fact that while the particle crosses the gap, it will see only a fraction of the peak field due to the time-varying nature of the fields in the cavity. It is a measure of the resulting reduction in energy gain. T can have a maximum value of 1, (the case of a static DC field) and changing the cavity design to maximise the transit-time factor is often an important optimisation driver. This involves reducing the gap length by introducing nose cones to concentrate the field in the centre.

2.2 Linac Beam Dynamics

This following section will concentrate on describing several linac beam dynamics concepts essential in the context of this thesis. While the extent of the subject of beam dynamics can be very wide, only necessary, fundamental aspects will be presented here [29], [30], [34], [35].

It was shown above that a charged particle motion through a linac is essentially a continuous interaction with electromagnetic fields created by external devices like accelerating cavities and magnets. The movement of a particle of charge q and velocity v is governed by the Lorentz equation:

$$\frac{d\mathbf{p}}{dt} = q\left(\mathbf{v} \times \mathbf{B} + \mathbf{E}\right) \tag{2.17}$$

By introducing the s variable denoting the linac path, it can be rewritten as:

$$\frac{d\mathbf{p}}{ds} = q\,\frac{\mathbf{v} \times \mathbf{B} + \mathbf{E}}{v_z}\,. \tag{2.18}$$

In Cartesian coordinates, the general equation of motion becomes:

$$\begin{aligned}
\frac{d(\gamma\beta_x)}{ds} &= \frac{q}{mc}\cdot\left(y'B_z - B_y + \frac{E_x}{v_z}\right) = \frac{d(\gamma\beta_z x')}{ds}\,,\\
\frac{d(\gamma\beta_y)}{ds} &= \frac{q}{mc}\cdot\left(B_x - x'B_z + \frac{E_y}{v_z}\right) = \frac{d(\gamma\beta_z y')}{ds}\,,\\
\frac{d(\gamma\beta_z)}{ds} &= \frac{q}{mc}\cdot\left(x'B_y - y'B_x + \frac{E_z}{v_z}\right).
\end{aligned} \tag{2.19}$$

where m is the rest mass. The general linac convention is that x and y denote the transverse

plane (horizontal and vertical) while z the longitudinal direction, with x' and y' defined as:

$$\begin{aligned} x' &= \frac{dx}{ds} = \frac{p_x}{p_z} = \frac{\beta_x}{\beta_z}\,, \\ y' &= \frac{dy}{ds} = \frac{p_y}{p_z} = \frac{\beta_y}{\beta_z}\,. \end{aligned} \tag{2.20}$$

From equation 2.19 it is obvious that the transverse and longitudinal particle movements are coupled. However, in general the two motions are treated independently by making several assumptions. The first is the paraxial approximation which simply assumes that $x'^2 + y'^2 \ll 1$ and therefore $\beta_z \simeq \beta$ while a second assumption considers the contribution of the transverse component of the electric field to the energy gain to be negligible and the longitudinal component to be independent of the radial position [30].

2.2.1 Longitudinal Dynamics

The entire longitudinal particle dynamics in proton linacs is based around the notion of synchronicity between the particle and the accelerating field. This requires the introduction of the concept of **synchronous particle**, a single ideal particle which is always synchronous with the accelerating field. The phase of this particle will be further referred to as the **synchronous phase**, ϕ_s, in linac convention defined with respect to the field crest where $\phi = 0$ (maximum acceleration). The other neighbouring particles will oscillate around the synchronous particle in phase and energy as they are being accelerated by a time varying electric field. The trajectories of these particles in phase-space will be briefly analysed below, but the concept of **phase stability** is explained in Figure 2.6. By choosing a synchronous phase not on the crest, but on the rising sector of the RF wave, particles arriving early will see a smaller amplitude accelerating field and therefore will gain slightly less energy, while particles arriving late will experience a higher energy gain than the synchronous particle. This results in a focussing effect in which particles will tend to cluster around the synchronous particle. Of course, there is only a limited stable region of phase stability.

Assuming the variables ϕ (absolute particle phase) and W (particle kinetic energy), the

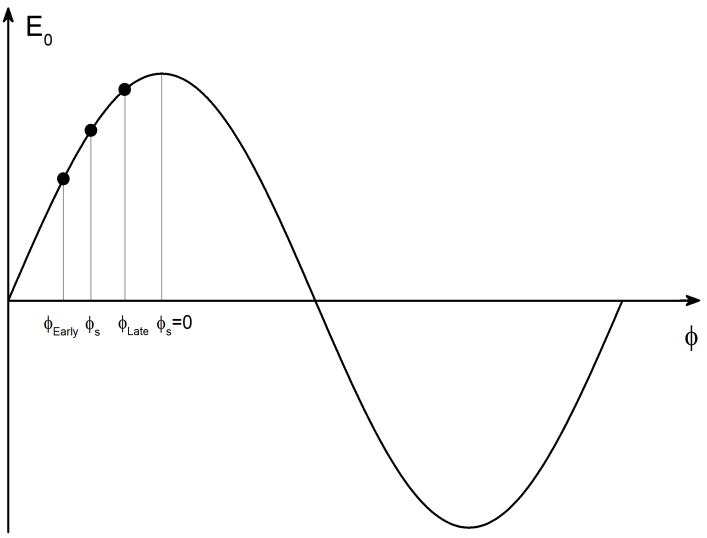

Figure 2.6: Phase stability diagram.

longitudinal equations of motion can be written as:

$$\begin{aligned} \frac{d\phi}{ds} &= \frac{\omega}{\beta_z c} = \frac{2\pi}{\beta\lambda \cdot \sqrt{1 - x'^2 - y'^2}}\,, \\ \frac{dW}{ds} &= q \cdot \left(x' E_x(s,\phi,r) + y' E_y(s,\phi,r) + E_z(s,\phi,r)\right). \end{aligned} \tag{2.21}$$

For the synchronous particle, these equations are simplified to:

$$\begin{aligned} \frac{d\phi_s}{ds} &= \frac{2\pi}{\beta_s \lambda}\,, \\ \frac{dW_s}{ds} &= q \cdot E_z(s,\phi_s,0)\,. \end{aligned} \tag{2.22}$$

Defining the variables $\varphi = \phi - \phi_s$ and $w = W - W_s$, assuming an accelerating field as described in 2.11 and applying the decoupling assumptions mentioned above results in:

$$\begin{aligned} \frac{d\varphi}{ds} &= \frac{2\pi}{\lambda}\left(\frac{1}{\beta(s)} - \frac{1}{\beta_s(s)}\right), \\ \frac{dw}{ds} &= -qE_0T\big(\cos\phi_s \cdot (1 - \cos\varphi) + \sin\phi_s \cdot \sin\varphi\big)\big)\,. \end{aligned} \tag{2.23}$$

For $\delta\beta \ll 1$,

$$\frac{1}{\beta} - \frac{1}{\beta_s} \simeq -\frac{\delta\beta}{\beta_s^2}\,. \tag{2.24}$$

and using

$$\delta\beta = \frac{w}{mc^2\gamma_s^3\beta_s}\,. \tag{2.25}$$

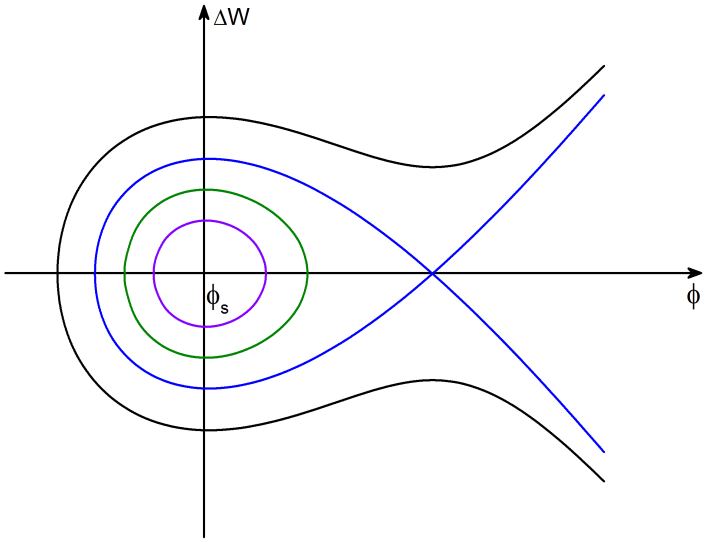

Figure 2.7: Longitudinal phase-space plot showing the separatrix (blue line) and stable (inside) and unstable (outside) trajectories.

simplifies equations 2.23 to:

$$\begin{aligned} \frac{d\varphi}{ds} &= -2\pi \cdot \frac{w}{(\beta_s\gamma_s)^3 mc^2\lambda} = \frac{\partial H}{\partial w}\,, \\ \frac{dw}{ds} &= -qE_0T\big(\cos\phi_s \cdot (1-\cos\varphi) + \sin\phi_s \cdot \sin\varphi\big) = -\frac{\partial H}{\partial \varphi}\,. \end{aligned} \tag{2.26}$$

In the above equations, H is recognised as the Hamiltonian, easily identified as:

$$H = -\frac{2\pi}{(\beta_s\gamma_s)^3 mc^2\lambda} \cdot \frac{w^2}{2} - qE_0T\big(\sin\phi_s(\cos\varphi - 1) + \cos\phi_s(\sin\varphi - \varphi)\big)\,. \tag{2.27}$$

Equation 2.27 is an important result, as it describes the longitudinal particle motion in the phase-energy phase space. Solving this equation numerically yields the trajectories shown in Figure 2.7 with particles following curves where H is constant. The stable area in phase space is called "the bucket" and is delimited by "the separatrix", or sometimes called "the fish" (the blue curve). Stable (green and purple curves) and unstable (black curve) trajectories can also be seen in Figure 2.7. In obtaining this plot, a constant velocity was assumed. When acceleration is taken into account, the shape of the separatrix changes to the well-known golf club.

2.2.2 Transverse Dynamics

This section outlines briefly several key transverse beam dynamics concepts. A more in-depth analysis can be found in references [36], [37], [29] as well as many others. Transverse beam motion in linacs is dictated primarily by magnetic focussing elements. In modern machines, these elements are the quadrupoles. The particular periodicity and arrangement of quadrupoles forms the machine **lattice**. The lattice choice for any accelerator is very significant as it dictates the magnet design, the machine aperture and the beam behaviour. All high power proton linac lattices employ the concept of strong focussing or alternating gradient.

The general approach is to split the problem of transverse dynamics in two parts such that one arrives at two distinct descriptions: the machine and the beam travelling in the machine. The transverse motion is dictated primarily by quadrupoles. In addition when crossing accelerating gaps, particles off axis will experience non-zero radial electric and azimuthal magnetic fields. Longitudinal stability requirements will lead to a net defocussing effect in the gap and therefore an additional force affecting the transverse beam motion. This effect is particularly significant at low energies and in linacs where many gaps are used to accelerate the beam.

Considering x and y the horizontal and vertical transverse coordinates and assuming an ideal quadrupole, the transverse quadrupole gradient is constant in the good field region and given by:

$$G = \left.\frac{\partial B_x}{\partial y}\right|_{\text{axis}} = \left.\frac{\partial B_y}{\partial x}\right|_{\text{axis}} . \tag{2.28}$$

The Lorentz force components acting on a particle of charge q and velocity v are therefore:

$$F_x = -qvGx \quad \text{and} \quad F_y = qvGy\,. \tag{2.29}$$

and the transverse equations of motion in a quadrupole are given by:

$$\begin{aligned}
\frac{d\gamma\beta_x}{ds} &= \gamma\beta_z\frac{dx^{'}}{ds} = -\frac{qG}{mc}x\,, \\
\frac{dx}{ds} &= x^{'} = \frac{\beta_x}{\beta_z}\,, \\
\frac{d\gamma\beta_y}{ds} &= \gamma\beta_z\frac{dy^{'}}{ds} = \frac{qG}{mc}y\,, \\
\frac{dx}{ds} &= y^{'} = \frac{\beta_y}{\beta_z}\,.
\end{aligned} \tag{2.30}$$

For a positively charged particle, a positive gradient will focus the beam horizontally and defocus it vertically. The equation best describing the particle motion in a quadrupole channel is a second order linear differential equation recognised as Hill's equation:

$$\begin{aligned}
\frac{d^2x}{ds^2} + k(s)x &= 0\,, \\
\frac{d^2y}{ds^2} - k(s)x &= 0\,.
\end{aligned} \tag{2.31}$$

Here $k(s)$ is a periodic focussing function describing the focussing strength along the channel:

$$k(s) = \frac{qG(s)}{mc\gamma\beta}\,. \tag{2.32}$$

Hill's equation above indicates a simple harmonic motion with a restoring force $k(s)$. Consequently, the solution is given by Floquet's theorem and is similar to that of a harmonic oscillator:

$$x(s) = \sqrt{\epsilon\beta(s)}\cos(\phi(s) + \phi_0)\,. \tag{2.33}$$

The above solution has an amplitude which is not constant, but varies with the so called amplitude function, $\beta(s)$. Similarly, the phase along the channel does not necessarily advance linearly with position, but is driven by a phase function $\phi(s)$. Here ϵ and ϕ_0 can be considered arbitrary constants set by the initial conditions. The amplitude and phase functions have the same periodicity as the lattice and are normally scaled to be related by:

$$\phi(s) = \int \frac{ds}{\beta(s)}\,. \tag{2.34}$$

It is also useful to define two other functions of $\beta(s)$:

$$\begin{aligned} \alpha(s) &= -\frac{1}{2}\frac{d\beta(s)}{ds}\,, \\ \gamma(s) &= \frac{1+\alpha(s)^2}{\beta(s)}\,. \end{aligned} \tag{2.35}$$

The $\alpha(s)$, $\beta(s)$ and $\gamma(s)$ functions are known as the **Twiss** or **Courant-Snyder** parameters, used to define the beam along the accelerator. They should not be confused with the relativistic Lorentz factors.

Solutions to linear second order differential equations can also be written using a matrix formalism. Given the initial conditions x_i (the displacement) and $x_i^{'}$ (the divergence angle) and assuming no coupling between planes, the beam displacement at a final point x_f and divergence $x_f^{'}$ can be calculated if a transfer matrix is known. This well known approach is widely used in accelerator optics. A transfer matrix is a useful concept as it contains all the information necessary for tracing particles between any two points given the initial conditions. Returning now to Hill's equation, one can derive an invariant of the form:

$$\gamma x^2 + 2\alpha x x^{'} + \beta x^{'2} = \epsilon\,. \tag{2.36}$$

This is called **the Courant-Snyder invariant** and it is an important result, as it now gives a physical meaning to the Twiss parameters introduced earlier. One can easily notice that the above equation is the equation of an ellipse in the $x-x^{'}$ phase space centred on the origin with an area of $\pi\epsilon$. It represents the history of particle coordinates in phase space after each lattice period. Because of the lattice periodicity, after each cell the new x-$x^{'}$ coordinates will lie on the same ellipse. Of course, a single ellipse does not show what happens to the beam in between the points where the periodic observations were made, but since the Twiss parameters depend on the s position, a different ellipse can be plotted at each step. This representation can be seen in Figure 2.8. The α parameter gives the ellipse tilt so when $\alpha = 0$ the ellipse is upright, while the β function and ϵ are related to the beam size and shape. β is however a property of the machine. The γ parameter is dependent on α and β while the phase advance μ shows how fast the particles are moving in phase-space.

The matrix formalism allows a simple and quick analysis of a focussing structure in

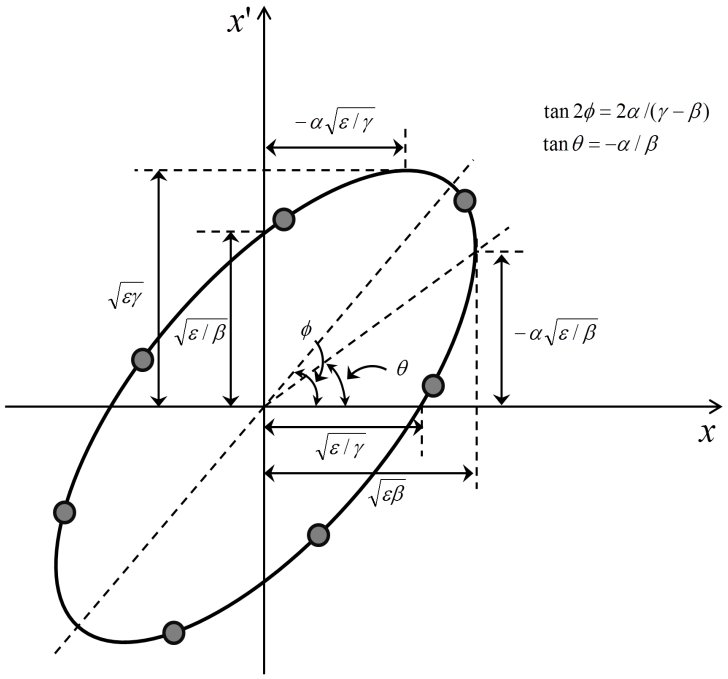

Figure 2.8: Horizontal phase-space Twiss ellipse, showing the main geometric parameters. The area of the ellipse is $\pi\epsilon$.

an accelerator. The general transfer matrix $M_{f,i}$ between two points i and f, can be easily computed by multiplying the transfer matrices of the individual components. By far the most common focussing lattice in linacs is the FODO lattice. As the name suggests, it consists of a focussing lens, a drift space, a defocussing lens of equal strength and an additional drift space. This sequence can then be repeated as many times as needed. This is illustrated in Figure 2.9. A FODO lattice with a phase advance of 90 degrees per cell was chosen, such that after four periods a particle performs a full rotation in phase space. The Twiss ellipse is plotted in the middle of each element, as well as the beta function and the beam envelope ($\sqrt{\epsilon\beta}$) for both the horizontal and vertical planes. One can note that the α parameter is zero in the middle of the lens and that the beta function varies from its maximum in the focussing to the minimum in the defocussing lens.

Throughout this thesis the notion of matched and mismatched beams will be a recurring theme. In general, a beam described by a phase-space ellipse is considered matched if at any particular location along the transport channel, its Twiss parameters match those of the lattice, resulting in a smooth, periodic envelope evolution with a phase advance equal to that of the machine. However, if the beam is not matched, the result is a longer envelope

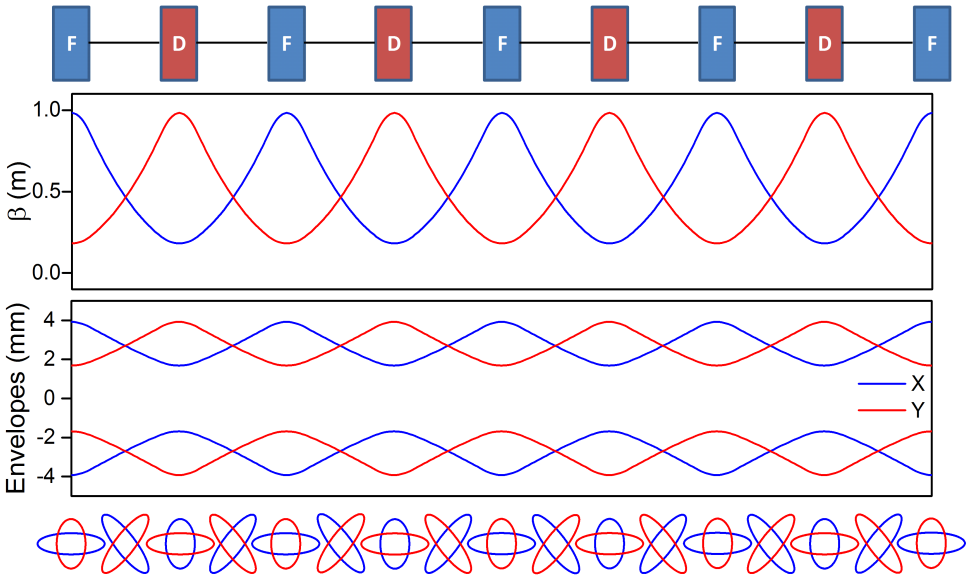

Figure 2.9: Horizontal (X) and vertical (Y) lattice parameters in a four-cell FODO channel. Top: β-functions, Middle: Envelopes ($\sqrt{\epsilon\beta}$) , Bottom: Twiss ellipses at each element. The phase advance is 90 degrees per cell and a typical proton beam was assumed.

oscillation period, with larger and smaller beam sizes than those of the channel. There are different ways to measure the mismatch, but in general a mismatch parameter measures either the increase in the maximum beam size projection, or the increase in the phase-space area resulting from mismatch. The evolution of mismatch is illustrated in Figure 2.10, where in the lattice from the previous example a small initial mismatch was applied in the vertical plane, while the horizontal plane was kept unchanged. The new envelope oscillations as well as the phase space projections can be observed.

Understanding and quantifying mismatch is important, as it is a significant mechanism leading to beam quality degradation. For a mismatched beam and when non-linear forces are prevalent, single particles will start oscillating with different frequencies and therefore turning with different angular speeds in phase-space. This will lead to an increase in the phase-space area swept by the particles. Additionally, parametric resonance effects between single particles oscillating with a different frequency than the core of the beam can lead to energy exchange which eventually translates into halo development [29], [30], [38].

The approach to matching in a linac is fundamentally different than for a ring or a transfer line. In circular machines, the typical procedure is to define a periodic focussing lattice and then require that the beam Twiss parameters are also periodic such that they are the same

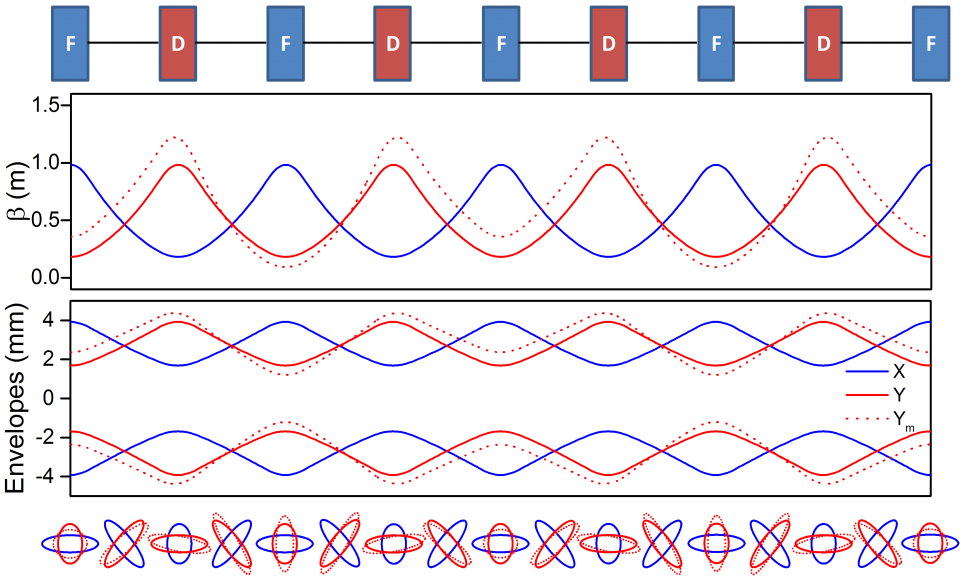

Figure 2.10: Horizontal (X) and vertical (Y) lattice parameters in a four-cell FODO channel with a small vertical mismatch (dotted line).

at the input and output of the lattice. This assumes that each period has the same transfer matrix and works relatively well at high energies. In a linac however, and particularly at low energies, this technique has severe limitations as the assumption of a periodic lattice is no longer valid. Indeed, strong space-charge forces, high relative energy change from cell to cell, strong RF defocussing forces and velocity matched accelerating structures where each cell has a different length, make each lattice period unique. Any periodic matching solution quickly leads to beam mismatch.

An alternative matching method commonly applied for proton linacs is to assume that all lattice parameters change adiabatically from one period to the next as explained in [39]. The matching algorithm then attempts a smooth variation of the transverse and longitudinal phase advance which results in smooth envelopes. Such methods are now used routinely in codes like Trace3D [40] and Tracewin [41] to find an input matched beam at the entrance of a linac. In addition, for transition matching between structures, the periodic matching approach is also used.

For practical reasons, the iterative nature of these methods imposes the use of the RMS envelope equations, which will be detailed later. This approach works well, as long as the beam distribution retains its elliptical shape. In the real world, the particle distribution will develop certain “distortions” and “features” which are normally analysed by means of

multi-particle tracking. Matching with particles is now possible in some codes, although the process is very slow. This is likely to change in the near future due to advancements in computer hardware. Fast particle tracking is valuable not only at the design stage, but also for online modelling. Indeed, very recent developments from LANL suggest that using graphics processing units (GPUs) and dedicated tracking software, can cut multi-particle simulation time with space-charge of the entire 800 m LANSCE linac to ~ 5 s [42].

The overall discussion presented here is a general description of transverse beam dynamics. However, many assumptions have been made, so the theoretical limitations have to be well understood. For simplicity, the quadrupole channel analysed here ignored any RF effects. In reality RF defocussing in a linac plays an important role especially at low energies and is usually taken into account by including an extra force component in Hill's equation in addition to the quadrupole focussing component. The RF defocussing force is proportional to $\pi q E_0 T \lambda \sin\phi / \gamma^3 m c^2 \beta$. Furthermore, one should note that for the perfect quadrupole case analysed here, the transverse forces are linear. In reality however, the fringe fields can be quite significant as the quadrupole poles cannot practically have a perfect hyperbolic shape. This introduces non-linear effects which should be accounted for in high power linacs in which more subtle effects are important to understand and quantify.

2.2.3 Multi-particle Dynamics

In addition to the RF and magnetic external forces affecting the longitudinal and transverse particle dynamics, an important role is played by the internal Coulomb forces induced by the charged particles. These **space-charge** forces are particularly relevant for high intensity machines and in general require multi-particle statistical simulations to calculate the resulting field and its effects on the beam evolution and its dynamics.

Earlier, in Equation 2.36, ϵ, the Courant-Snyder invariant was defined in terms of a particle phase-space coordinates and Twiss parameters and it was highlighted that in phase-space and under linear forces, each particle will describe an elliptical trajectory. As in general phase-space projections of particle beams have elliptical shapes, it is convenient to define a quantity that measures the area of the beam within a certain ellipse. This quantity is called

the **emittance**, usually denoted by ϵ and expressed in units of $\pi.mm.mrad$. In other words, given any particle travelling through an accelerator, the emittance is proportional to the area of the phase-space ellipse projections described by that particle. The projections normally adopted are position and divergence angles in the transverse plane (x-$x^{'}$, y-$y^{'}$) and relative phase and energy ($\Delta\phi$-ΔE) longitudinally. This allows individual horizontal, vertical and longitudinal 2D emittance definition for any 6D beam as:

$$\epsilon = \frac{\text{Area}}{\pi}\,. \tag{2.37}$$

One important property of particle beams is given by **Liouville's theorem** which is simply a phase-space conservation law. Its application for accelerators implies that given a system of particles moving according to Hamilton's equations of motion, the phase space area or volume within a closed contour is conserved over time even though its shape could change. In other words, as long as Hill's equation is valid, the particle density in phase-space remains constant and the system emittance is conserved. However, it should be noted that the theorem is valid provided as the forces acting on the particles are conservative, like those induced by external magnetic and electric fields, and not for space-charge dominated beams or dissipative systems where particles lose part of their energy or interact with other particles or with elements of the machine.

Since one could define the ellipse enclosing the beam at different density levels, a more systematic approach is to introduce the RMS emittance [43]. This allows an emittance to be defined for any particle distribution based on RMS values of position and divergence angles and has the advantage of including information on the beam features inside the distribution in addition to the normal phase-space area. For the horizontal phase space (x-$x^{'}$), the **unnormalised RMS emittance** for a centred beam ($\langle x\rangle$=$\langle x'\rangle = 0$) is therefore given by:

$$\epsilon_{RMS} = \sqrt{\overline{x^2}\;\overline{x'^2} - \overline{xx'}^2}\,, \tag{2.38}$$

while the corresponding ellipse is defined by its respective Twiss parameters (see Figure 2.8).

Earlier, the particle divergence was defined as $x' = p_x/p_z$. With acceleration the longitudinal momentum p_z increases while the transverse momentum p_x remains constant, leading

to a smaller divergence and hence a reduced un-normalised emittance. This required the introduction of a **normalised RMS emittance** which is commonly used in proton linacs as it is independent of acceleration and is defined as $\epsilon_{Norm\_RMS} = \beta\gamma\epsilon_{RMS}$.

One of the challenges of multi-particle simulations is to define realistic beam distributions that reproduce the linac as accurately as possible. When the situation allows, one approach is to use diagnostics to measure the beam parameters at the front end of the accelerator and then re-construct distributions for simulations of the downstream linac. However, this is not always possible, especially at the design stage and several particle distributions are generally used to study the machine. Nevertheless, one should remember that no self-consistent analytic solutions exist for evolving particle distributions in a linac and computer simulations are therefore critical tools .

The emittance phase-space volume can have in general multiple projections in 2D, 4D or 6D for which a distribution function $f(x, x', y, y', \phi, E)$ can be defined (6D here). The evolution of this distribution function is described by Vlasov's equation [44] which can be written generally or for each individual plane in generalised coordinates as [45], [46]:

$$\frac{df}{dt} = \frac{\partial f}{\partial t} + \frac{1}{\gamma m_0} p_x \frac{\partial f}{\partial x} + F(x)\frac{\partial f}{\partial p} = 0\,, \tag{2.39}$$

where $F(x)$ is a function of the external and self fields of the distribution. Additionally, $n(x, y, \phi)$, the real space density of the distribution is:

$$n(x, y, \phi) = \iiint f(x, x', y, y', \phi, E) dx' dy' dE\,, \tag{2.40}$$

and the total number of particles N in the distribution is:

$$N = \iiint n(x, y, \phi) dx dy d\phi\,. \tag{2.41}$$

The KV distribution was proposed by Kapchinsky and Vladimirsky and although not realistic it is a useful theoretical study tool [47]. In the 4D phase-space, particles are distributed uniformly on the surface of the corresponding hyper-ellipsoid, while the 2D distribution pro-

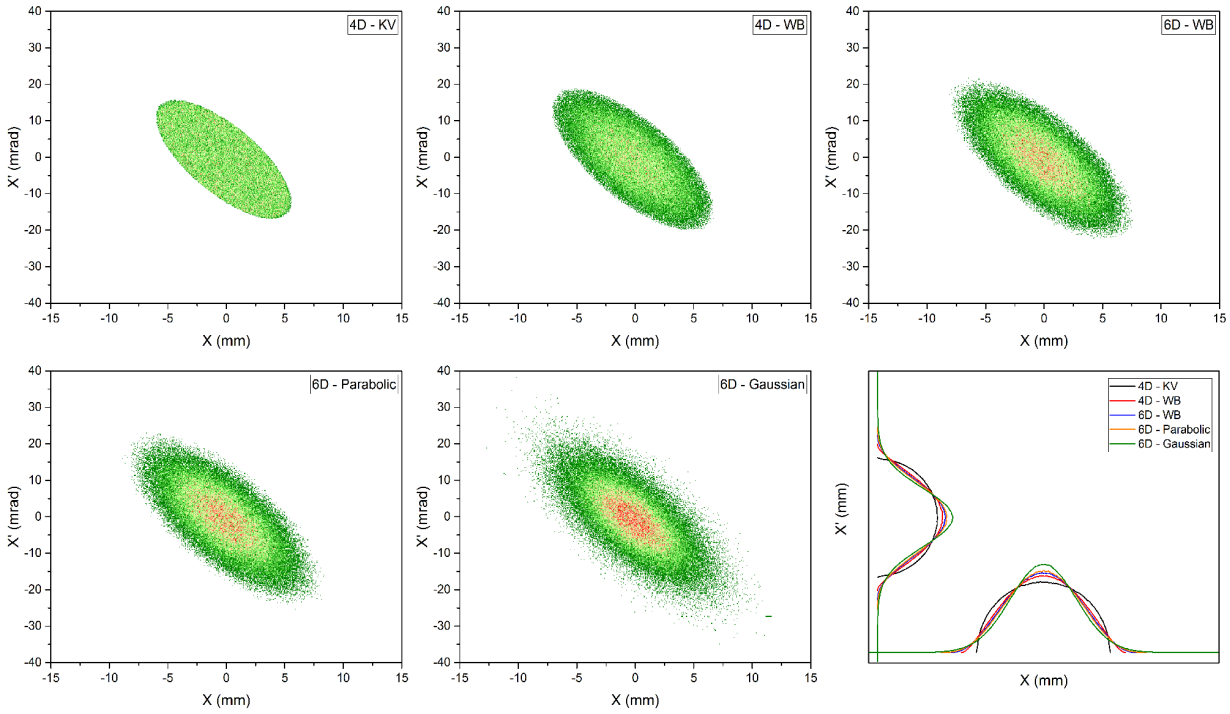

Figure 2.11: 2D projections for several common particle distributions with the same RMS emittance. Top-left: 4D-KV, top-centre: 4D-Waterbag, top-right: 6D-Waterbag, bottom-left: 6D-Parabolic, bottom-centre: 6D-Gaussian, bottom-right: density projection on each axis for the above distributions. The colour scheme assumes red tones for higher density areas and green tones for lower density. This scheme is used throughout the entire thesis.

jections are uniform. The distribution function is defined as:

$$f(x,x',y,y') = \frac{N}{\pi^2 ab\epsilon_x\epsilon_y}\delta\left(\frac{x^2}{a^2}+\frac{y^2}{b^2}+\frac{a^2x'^2}{\epsilon_x^2}+\frac{b^2y'^2}{\epsilon_y^2}-1\right), \tag{2.42}$$

with δ the Dirac function. The particle density in real space is:

$$n(x,y) = \frac{N}{\pi ab} \qquad \frac{x^2}{a^2}+\frac{y^2}{b^2} \leq 1\,. \tag{2.43}$$

However, alternative distributions are often used in simulations. The waterbag distribution represents a uniform filling of the hyper-ellipsoid and is generally a good approximation for low energy, space-charge dominated beams. A more spread out distribution is the parabolic distribution, where as the name suggests, the hyper-ellipsoid is filled with a parabolic density. The Gaussian distribution, has a Gaussian profile with infinite tails. For practical reasons, in simulations a cut is normally made at a few standard deviations ($n\sigma$).

Figure 2.11 shows 2D projections in the horizontal phase-space for several common par-

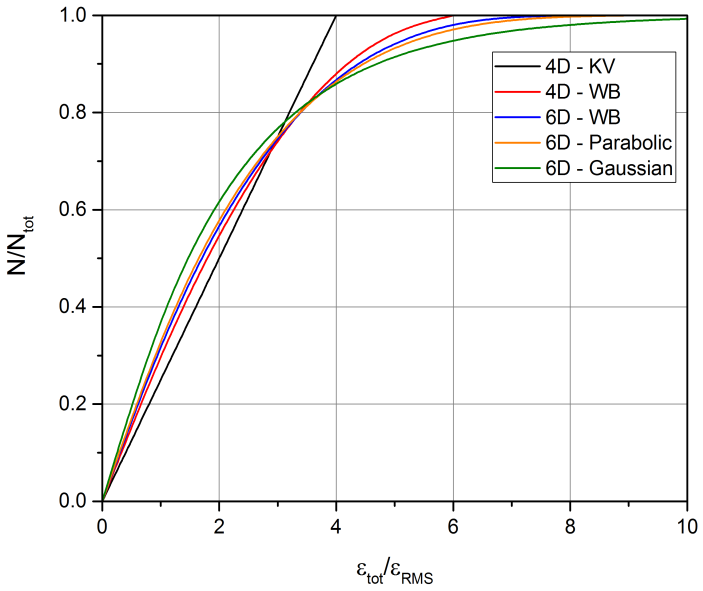

Figure 2.12: Fraction of particles within a specific emittance for different particle distributions.

ticle distributions, as well as the density projections on each axis. A clear distinction can be made between the tail's length for each distribution.

All the distributions plotted here have the same RMS emittance. This raises the question of how large the actual 100% emittance is compared with the RMS. This ratio was calculated for different distributions which have clear boundaries and are uniform in an n-dimensional hyper-ellipsoid [48]:

$$\frac{\epsilon_{100}}{\epsilon_{RMS}} = n + 2\,. \tag{2.44}$$

It follows that for a KV distribution ($n = 2$), the total emittance is 4 times larger than the RMS. For a 4D waterbag ($n = 4$) the ratio is 6 while fo a 6D waterbag ($n = 6$) it is 8. For a 4D parabolic distribution the ratio is also 8 while for the Gaussian distribution it depends at how many standard deviations a cut has been made as otherwise the distribution would extend to infinity. This is illustrated in Figure 2.12 where the fraction of particles (N/N_{tot}) within a certain phase-space ellipse is plotted for distributions discussed above [49].

With these basic concepts defined, we can now return to Hill's equation (Eq. 2.31) and rewrite the equation of motions to take into account the effects of space-charge. In doing so one must consider the repulsive electric forces between charges, as well as the attractive magnetic forces between the moving charge. From Gauss' flux theorem and Ampère's law,

for a moving charge with density $n(r)$, the radial electric field and the azimuthal magnetic field for an axisymmetric beam can be written as [29]:

$$\begin{aligned} E_r &= \frac{q}{\epsilon_0 r}\int^{r} n(r) r dr\,, \\ B_\theta &= \frac{qv\mu_0}{r}\int^{r} n(r) r dr\,, \end{aligned} \tag{2.45}$$

and the resulting Lorentz force as:

$$F_r = q(E_r - vB_\theta) = qE_r(1-\beta^2) = \frac{qE_r}{\gamma^2}\,. \tag{2.46}$$

This simply shows that space-charge effects are important in particular for lower energy beams and therefore for most proton linacs. As the beam is accelerated, the magnetic force becomes stronger and will compensate the electric defocussing force. One can now rewrite Hill's equation to take into account this additional space-charge force:

$$\frac{d^2x}{ds^2} + k(s)x - F_{sc}(x,s) = 0\,. \tag{2.47}$$

An envelope equation can be derived by averaging over the particle distribution ($a_x = \sqrt{\overline{x^2}}$, $a_x' = -\frac{\overline{xx'}}{a_x}$) and differentiating arriving at a new equation describing the RMS beam motion, which for the horizontal plane is [50], [43]:

$$a_x'' + a_x k_x(s) - \frac{\epsilon_{x,rms}^2}{a_x^3} - \frac{\overline{xF_{sc}(s)}}{a_x} = 0\,. \tag{2.48}$$

This equation is also known as the KV envelope equation as it was first derived by Kapchinsky and Vladimirsky for a uniform beam. One significant property of the envelope equation is that although derived for uniform beams, the space-charge dependency with distribution is very weak, making it suitable for all elliptical particle distributions [43].

This equation can be developed further by considering a typical ellipsoidal beam bunch,

with semi-axis r_x, r_y and r_z. The electric field components are given by [51], [29]:

$$\begin{aligned} E_{sc,x}(s) &= \frac{3I\lambda(1-f(s))}{4\pi\epsilon_0 c(r_x+r_y)r_z}\frac{x}{r_x}\,, \\ E_{sc,y}(s) &= \frac{3I\lambda(1-f(s))}{4\pi\epsilon_0 c(r_x+r_y)r_z}\frac{y}{r_y}\,, \\ E_{sc,z}(s) &= \frac{3I\lambda f(s)}{4\pi\epsilon_0 c r_x r_y}\frac{z}{r_z}\,, \end{aligned} \tag{2.49}$$

with the space-charge force components equal to:

$$F_{sc}(s) = \frac{qE_{sc}}{\beta^2\gamma^3 mc^2}\,. \tag{2.50}$$

Here I is the average beam current per RF period, λ is the RF wavelength, ϵ_0 is the vacuum permittivity and $f(s)$ is a form factor describing the bunch aspect ratio. Substituting these results in the envelope equation one can arrive at:

$$\begin{aligned} a_x'' + a_x k_x(s) - \frac{\epsilon_{x,rms}^2}{a_x^3} - \frac{3K_3(1-f(s))}{(a_x+a_y)a_z} &= 0\,, \\ a_y'' + a_y k_y(s) - \frac{\epsilon_{y,rms}^2}{a_y^3} - \frac{3K_3(1-f(s))}{(a_x+a_y)a_z} &= 0\,, \\ a_z'' + a_z k_z(s) - \frac{\epsilon_{z,rms}^2}{a_z^3} - \frac{3K_3 f(s)}{a_x a_y} &= 0\,. \end{aligned} \tag{2.51}$$

Here K_3 is defined as the 3D space-charge parameter:

$$K_3 = \frac{qI\lambda}{20\sqrt{5}\pi\epsilon_0 mc^3\beta^2\gamma^3}\,. \tag{2.52}$$

This set of equations is an important result as it now allows the mapping of RMS beam size motion and the evolution of the distribution in the presence of space-charge. However, one should remember that in arriving at this result some assumptions have been made from the shape of the beam distribution to the characteristics of the transport channel and therefore some limitations will apply.

2.3 Chapter Summary

This chapter presents a summary of key accelerator physics concepts relevant for high power linear accelerators in general and for the purpose of this thesis in particular. The aim was to have a gradual, comprehensive approach in describing the accelerator-beam system. On the subject of RF acceleration in linacs, it was shown that for high efficiency acceleration the aim is to design cavities capable of providing high electric fields on axis for a small input power level, but also that RF choices have a profound effect on the beam dynamics. The sections detailing the longitudinal and transverse linac beam physics emphasised the power of existing theoretical models, but also how interrelated design choices are. The discussion then moved to multi-particle beam dynamics where concepts like emittance or beam distribution could now be presented.

Chapter 3

The Pentagon of Cavity Design

In the context of high power accelerators, one of the main factors analysed in this thesis is beam acceleration in normal conducting proton linacs, in particular the available structures and the cavity design process. While early accelerator designers concentrated mainly on devising new methods of acceleration, in modern machines attention is also paid to accelerating efficiently to limit the machine operational costs as well as carbon emissions. However, although designing accelerating cavities with power efficiency in mind is an important driving factor, other elements must not be ignored. In this chapter, all aspects of cavity design are summarised with an emphasis on their interdependence. These factors and their correlations can be graphically presented in a diagram symbolically called "the pentagon of cavity design". To quantify these cavity design features, this chapter also discusses in detail several essential figures of merit. This creative and unique approach is an essential tool in the methodical examination of normal conducting structures to be presented in Chapter 4.

3.1 Aspects of Cavity Design

The choice of accelerating structures is essential for every linac. In modern linear accelerators, power efficiency has been by far the main consideration when RF cavities are selected for a specific energy range. This is because of a strong demand to build machines which are more cost effective to operate and which have a lower carbon footprint. This concept is taken to another level by the European Spallation Source project in Lund, Sweden, which will be the world's first carbon neutral particle accelerator. This is achieved by powering the machine entirely from renewable sources and by recycling the heat waste into the central heating system for the city of Lund [12]. However, achieving power efficiency should not

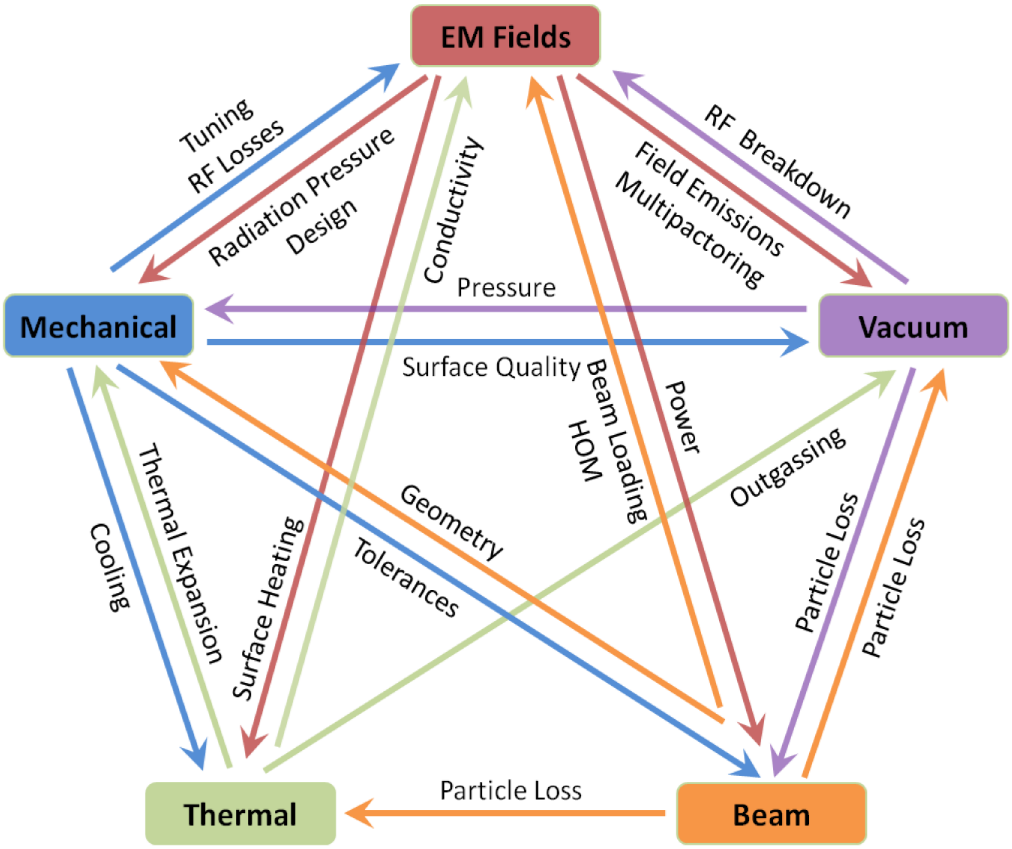

Figure 3.1: The Pentagon of cavity design.

undermine other aspects of cavity design, construction and operation and therefore a solid understanding of all the driving factors is necessary. Furthermore, it is essential to identify how these characteristics influence each other and what are their interdependencies.

The "pentagon of cavity design" is an instrument aimed at listing the main aspects of cavity design and their relationships, constraints and limitations and is intended to demonstrate how intimately interconnected these aspects are. Five such features have been identified as it can be seen in Figure 3.1: beam dynamics, electromagnetic fields, mechanical, thermal and vacuum aspects. Depending on a variety of factors like the intended application, requirements, duty factor, RF frequency, etc., different design aspects can have a different weight. In the following sections, each of the five items will be briefly analysed, with an emphasis on how seemingly unconnected design choice can have significant consequences and on how interdependent technologies can be.

3.1.1 Beam Dynamics

In the holistic approach to cavity design proposed here, beam dynamics plays an important role. Although for many purposes in accelerator design, modelling and operation this subject can be treated separately, there are several aspects to be taken into account.

- **EM Field Aspects.** The main interaction between the beam dynamics and the electromagnetic fields in a cavity is through beam loading. As the particle bunches cross the cavity, they can induce charges in the cavity walls which in turn affect the cavity fields and the subsequent bunches. The outcome can be a reduction of the accelerating field amplitude, a modification of the field profile or a phase shift as well as changes in tuning and a range of transient phenomena. Additionally it can lead to the excitation of higher order modes and power loss, a process particularly relevant for superconducting cavities.

- **Mechanical Aspects.** On the mechanical design of the cavity, beam dynamics choices can limit some design options. To optimise the accelerating structures, a simulation space with fewer constraints is preferable. However, not all parameters are free. The beam size will restrict the beam aperture. This is particularly relevant for normal conducting structures where a small aperture would lead to a higher shunt impedance. On the other hand, to avoid undesirable beam loss, larger apertures are needed. For example, for a DTL, the ratio between the vacuum chamber radius and the RMS beam size is around 10 [52]. This requirement has inevitably led to a variety of proton linac designs with comparable apertures for similar structures.

- **Thermal Aspects.** The most significant potential effect of beam dynamics on the cavity thermal operation is through significant beam loss. Every measure is normally taken in usual machine operation to avoid such catastrophic events. Causes of particle loss in the cavity can vary from component malfunction to systematic losses. Strong radial off-axis forces can also lead to beam deflection and particle loss on the cavity walls. For an Orbit Separated Cyclotron (OSC) which uses multi-cell, linac-type superconducting cavities, it has been found that unless corrected, the beams travelling

off-axis (through design) receive a sufficient transverse deflection to induce beam loss in the subsequent cavities [53], [54].

- **Vacuum Aspects.** The vacuum is mainly influenced by beam dynamics through particle loss. The process involves the beam hitting the vacuum pipe, leading to outgassing through molecular desorption of the cavity walls. This works like a feedback loop, leading to a degradation of the vacuum quality and a further reduction in beam quality and transmission. The mechanism implies an increase in the residual gas levels which can change the charge of the accelerated particles through collisions. This is especially relevant for H^- proton linacs where a degraded vacuum level can lead to electrons being stripped off and the ensuing particles being lost at some point along the linac, as well as an increase in electron-cloud and emittance.

3.1.2 Electromagnetic Fields

The electromagnetic fields section refers mainly to the accelerating field in the cavity, but also to the magnetic fields from transverse focussing elements integrated in the cavity body as in the case of the DTL, where quadrupoles are placed inside the drift tubes.

- **Beam Dynamics Aspects.** The obvious effect of cavity EM fields on beam dynamics is through acceleration. The cavities have to be sufficiently versatile not only to accelerate the beam to the final energy, but also to follow a certain acceleration profile, as required by the beam dynamics. Indeed, linac design philosophies like equipartitioning require a certain longitudinal phase advance through acceleration if space-charge resonances are to be avoided. Errors in EM fields can damage the beam quality and are generally the subject of a meticulous analysis for any linac design at an advanced stage. These errors can vary from variations in field amplitude and phase to an incorrect field flatness and can lead to phase and energy jitter, emittance growth and potentially particle loss, thus limiting operation. For accelerating structures where magnetic focussing elements are incorporated, an additional influence on beam dynamics can be given by the change of magnet position which can affect the focussing channel.

- **Mechanical Aspects.** The mechanical design of a cavity can be influenced at the

design stage by certain EM field requirements, like profile or amplitude. EM fields can also affect mechanical integrity of an RF cavity during operation through radiation pressure. At high accelerating fields this can cause a deformation of the cavity shape through Lorentz force detuning. The process is particularly relevant for superconducting cavities which operate at much higher fields.

- **Thermal Aspects.** The main impact of EM fields on the cavity thermal design is through surface heating. Designs are generally aimed at minimising the heat dissipation and increasing the accelerating field for a given input power. The excess heat needs to be removed by integrating appropriate cooling channels such that the normal cavity operation is not disturbed. The heat levels depend on the intended application, the machine duty cycle, etc. For pulsed linacs typically operating at lower duty cycles (several percent), the power densities are normally below 10 W/cm^2. However, for higher duty cycles or for CW machines, to maintain the thermal cooling difficulty within reasonable limits, power densities are normally limited to less than 20 W/cm^2. This can be achieved by lowering the accelerating field levels, or geometry modifications which usually lead to a reduction in shunt impedance [55].

- **Vacuum Aspects.** EM Fields with the appropriate orientation can cause cavity surfaces to emit electrons which can be further accelerated by the electric fields in the cavity. The process is collectively known as field emission and can lead to RF breakdown and vacuum degradation. Superconducting cavities are even more sensitive to this problem which can cause a range of detrimental effects like the degradation of the quality factor or even quenching [56]. An additional limiting factor which can lead to poor vacuum is given by multipactoring, a process in which the RF can create resonant conditions which can lead to an avalanche of electron emissions. If not controlled, the resulting electron beam can eventually lead to serious cavity damage. For this reason, RF conditioning is an important step in the manufacturing process.

3.1.3 Mechanical Aspects

The mechanical section refers mainly to the design of the cavity geometry, the mechanical structure and the materials used for fabrication and the effects these choices have on cavity operation.

- **Beam Dynamics Aspects.** The mechanical design of the cavity dictates the tolerances which in turn can affect the beam dynamics. Systematic studies to define the acceptable structure errors are part of any machine design. These errors can be positional or rotational machining imperfections as well as alignment faults. Additionally, the ability of the construction process to meet the required manufacturing tolerances can eventually decide the successful operation of any accelerating structure. It is futile to design cavities with extraordinary properties, but with absurd tolerance levels that make any practical implementation unrealistic. For structures which include additional magnetic elements, mechanical deformation or difficult alignment can also lead to a change in the magnet position with further negative consequences on the beam dynamics. Again, such scenarios have to be analysed prior to construction through simulation studies.

- **EM Field Aspects.** Features and constraints of the mechanical design have a big effect on the shape and range of accelerating fields possible in the cavity. During operation, the main effect on EM fields comes from the mechanical deformation which can change the RF resonant frequency and influences the required tuning range and tuner characteristics. It can also affect the position of any magnets integrated in the cavity, leading to a change in the magnetic field and further effects on the beam dynamics. These mechanical errors can appear during manufacturing, assembly, transportation, commissioning, etc. The surface quality of the cavities is another aspect related to the EM fields, as its roughness can lead to additional RF losses with further undesirable consequences. This effect is normally taken into account at the design stage and safety margins are usually imposed such that the power supplies have sufficient overheads to maintain the cavity operating within the desired parameters.

- **Thermal Aspects.** The mechanical design is a major influence on the cavity thermal

design as it can affect and limit the cooling options available. Indeed, certain cavity shapes make the integration of cooling circuits more difficult. This is particularly true for on-axis nose cone regions where high dissipated power levels require reliable cooling channels, but the shape makes their implementation difficult. The problem is exacerbated for high duty cycle applications where an iterative process is needed between the mechanical and the thermal designs to find a suitable solution for both aspects. The result is often a reduction in cavity efficiency.

- **Vacuum Aspects.** The mechanical design has to allow sufficient liberty in implementing appropriate vacuum ports, etc. The surface quality also plays an important role as it can lead to additional outgassing and vacuum degradation with further unintended effects as has already been discussed.

3.1.4 Thermal Aspects

The thermal design section describes the influence of the cavity temperature control and its implementation on the operation of the cavity.

- **EM Field Aspects.** The temperature control is particularly relevant for superconducting cavities, where faults in the cooling system can lead to small temperature increases with potential catastrophic effects. Safety mechanisms that reduce the power levels are of essence if such incidents occur. For normal conducting cavities, high levels of heat can change the material conductivity and therefore the cavity RF performance. However, such scenarios are very unlikely.

- **Mechanical Aspects.** By far, the most notable effect of the thermal design is on the mechanical structure through thermal expansion. This can lead to the mechanical deformation of the cavity structure and all the resulting consequences discussed in the previous section (RF frequency, magnet position, etc.).

- **Vacuum Aspects.** Surface heating can lead to an increase in the outgassing rate from the cavity walls and consequently to vacuum degradation.

3.1.5 Vacuum Aspects

The vacuum design plays an important role and is an entirely separate subject by itself. Depending on the application, different vacuum levels could be required in a machine, varying from 10^{-5} mbar in small medical accelerators to 10^{-12} mbar in antiproton accumulator rings. This obviously leads to variable implementations. From a particle accelerator designer point of view, the vacuum system should ideally deliver zero pressure, with negligible costs and minimum interference in the machine design [57]. This is of course not realistic and a good understanding of the vacuum implementation on accelerator structure design is necessary.

- **Beam Dynamics Aspects.** The main consequence of having an unsuitable vacuum level is a degradation of the beam quality caused by the interaction between the beam and the residual gas in the vacuum pipe (scattering). The scattering process depends on the density of the gas molecules as well as the particles involved and can lead to electron loss or capture, beam ionisation, energy loss or even nuclear reactions. The ultimate outcome of all these effects is beam loss either from particles hitting the beam pipe directly or at a later stage due to an increase in beam emittance, beam size, electron-cloud problems and instabilities. The result is an increase in radiation levels and maintenance difficulties. An additional effect in storage rings can be a reduction in beam lifetime. To control and limit the possible sources of beam loss enumerated above, the acceptable vacuum levels are usually specified at the design stage and the proposed solutions are then analysed such that the other aspects of accelerator design are minimally affected [58].

- **EM Field Aspects.** Low vacuum quality can also lead to RF breakdowns, thus reducing the maximum achievable electric fields and limiting the cavity operation. The J-PARC experience is relevant in this sense. The original 324 MHz, 3 MeV H^- RFQ had been a major source of operational problems and beam trips due mainly to discharge issues. To increase reliability, a new RFQ was commissioned with an identical beam dynamics design, but with an improved engineering and RF design. Improvements in the vane machining, surface treatments and vacuum brazing techniques have led to an improved structure with a much better overall performance and a reduced discharge

risk [59].

- **Mechanical Aspects.** And finally, another aspect to take into account is the influence of the vacuum pressure on the mechanical design. The mechanical structure has to be sufficiently rigid to sustain the pressure and avoid deformation which could lead to additional difficulties as we have seen.

3.1.6 On the Choice of Frequency

The choice of frequency represents a significant decision for any linear accelerator and it is driven by a number of factors. In many machines, the availability of an existing infrastructure (klystrons, waveguides, etc) inherited from decommissioned machines can be the main reason behind the choice. The availability of RF sources at the desired frequency can be another factor to consider, as new developments are expensive and time consuming. If the new machines are part of an accelerator chain, additional constraints will have to be taken into account. However, ultimately the decision is a trade-off between power efficiency, beam dynamics, cost and complexity.

Regarding beam dynamics, the choice of frequency can dictate the beam structure, bunch length, energy spread, beam quality and longitudinal acceptance. Designing machines with appropriate "longitudinal aperture" is critical, since longitudinal halo is notoriously difficult to control and particles lost longitudinally will eventually hit the vacuum pipe with harmful consequences. The common approach in many modern linacs is to make use of a frequency jump, such that at low energies the transverse acceptance benefits from a lower frequency, while at higher energies, a transition to a higher frequency allows the use of higher accelerating gradients and the construction of more compact cavities with an obvious cost saving aspect.

The frequency jump is particularly delicate, as an increase in frequency adds a corresponding decrease in RF wavelength and a reduction in the longitudinal aperture. Consequently, after transition particles can land outside the new longitudinal acceptance. One additional complication comes from the fact that an increase in frequency also leads to an increase in longitudinal phase advance, further affecting the smooth phase advance philos-

ophy normally employed in these machines [60]. There are different procedures to navigate the frequency transition. R. Duperrier et al. in their analysis of the impact of RF frequency change on longitudinal beam dynamics propose several transition methods [61]. One technique is to keep the beam in an equilibrium state by keeping constant the confinement potential shape at transition. An alternative approach is to keep the longitudinal acceptance constant through transition by varying the field and the phase amplitude. A combination of the two can also be adopted, where the phase acceptance is kept constant as well as the phase advance per metre. While these methods applied correctly can lead to smooth transitions without beam loss or emittance growth, they also imply a reduction in the real estate accelerating gradient suggesting that frequency jumps are more beneficial for linacs with a high design output energy.

Regarding the RF efficiency, while the larger aperture and the less stringent tolerances allowed by lower frequency cavities are desirable, lower frequency is also equivalent to a reduced shunt impedance. The shunt impedance scales as the square root of frequency (see Section 3.2). However, this assumes a uniform resizing of all the cavity dimensions, which is unfeasible due to additional constraints (aperture, quadrupoles, etc.).

3.2 Figures of Merit and Definitions

The "pentagon of cavity design" proposes five cornerstones underpinning the successful design, production and operation of RF accelerating cavities: beam dynamics, EM fields, mechanical, thermal and vacuum aspects. However, from a cavity design point of view it is not sufficient to define the requirements (i.e. vacuum pressure, accelerating field, etc.), but methods of meeting them are also needed. This section presents several figures of merit and definitions to be used to analyse the RF cavity performance within the boundaries given by the pentagon and will be brought into play in Chapter 4 where they will be applied to asses several normal conducting cavities. The aim is not only to generate an evaluation based on their theoretical **RF properties**, but also to discuss the effect on the **beam quality**, give a general overview on the **technologies** and the precisions involved, the field stability to be achieved and the **tuning procedure** as well as the structure's sensitivity to RF errors.

Taking all these criteria into account represents a more accurate way of describing the RF properties of normal conducting cavities as well as the complexity and effort involved in the design and the manufacture process.

3.2.1 RF Properties

There are several figures of merit that are used to characterize accelerating cavities and are generally used as guidelines by linac designers [29], [30]. It was shown earlier that the accelerating mode in the cavity has a zero transverse electric field along the axis and a longitudinal field expressed as:

$$E_z(z,t) = E_z(z)\cos(\omega t + \phi)\,. \tag{3.1}$$

The **axial electric voltage** V_0 in the cavity is defined as the integral of the electric field along the axis in a cavity of length L. This is the voltage a particle would experience assuming a DC field equal to the amplitude at the top of the RF wave:

$$V_0 = \int_{-L/2}^{L/2} E_z(z)\mathrm{d}z\,. \tag{3.2}$$

For cavity characterisation it is useful to define an average axial electric field, often referred to as the **accelerating gradient**:

$$E_0 = \frac{V_0}{L}\,. \tag{3.3}$$

This figure of merit allows a direct comparison of different structures in terms of their ability to sustain high accelerating fields. However, as E_0 is defined for each individual cavity, it can also be a misleading number due to the different nature of various structures which can achieve high accelerating gradients but also require additional longitudinal space for transverse focussing elements. Therefore a **real estate accelerating gradient** is also necessary to characterise the RF properties of accelerating structures and it is defined as the

ratio between the energy gain ΔW, over the cavity or accelerator length:

$$E_{RE} = \frac{\Delta W}{qL}\,. \tag{3.4}$$

The quality factor Q is another well-known quantity used to characterise resonators. It is defined as the ratio of the stored energy in the cavity to the energy lost per RF period.

$$Q = 2\pi \frac{\text{Stored Energy}}{\text{Energy Consumed per Period}} = 2\pi \frac{U}{t \cdot P_0} = \omega \frac{U}{P_0} \tag{3.5}$$

U - The energy stored in the cavity.

P_0 - Dissipated power in the cavity walls.

t - RF period.

ω - Angular RF frequency.

The quantity above is often referred to as the unloaded Q, as only Joule heating losses are taken into account. The quality factor is directly related to the surface resistance and to the first order its value will depend on the conductivity of the wall material only. Q is also a dimensionless quantity and gives only the ratio of energies, and not the real amount of power needed to maintain a certain resonant mode. For resonant frequencies in the range 100 to 1000 MHz, typical values are 10000 to 50000 for normal conducting copper cavities and 10^8 to 10^{10} for superconducting cavities. A cavity with high Q has a narrower bandwidth and resonates with a higher amplitude at the resonant frequency than one with a low Q, but it is more difficult to tune, and more sensitive to mechanical errors.

By far, the most quoted figure when comparing the RF efficiency of different cavities is the **shunt impedance**. It is a measure of how effective a structure is at producing an axial accelerating voltage V_0, for a P_0 power dissipated in the cavity walls:

$$r_s = \frac{V_0^2}{P_0}\,. \tag{3.6}$$

It is also useful to define an **effective shunt impedance**, which takes into account the transit time factor T. As the particle crosses the cavity gap, the field also changes and as a result the acceleration is less efficient and the energy gain is only a fraction of the peak

voltage in the gap. This is equivalent to a reduction in the energy gain for a given power dissipation:

$$r = r_s T^2 \,. \tag{3.7}$$

The **effective shunt impedance per unit length** is another convenient "real estate" figure of merit, particularly useful when comparing structures of different lengths, with different field levels:

$$ZT^2 = \frac{r}{L} = \frac{(E_0 T)^2}{P_0/L} \,. \tag{3.8}$$

Certain authors prefer to quote a $ZT^2 \cos^2(\phi)$ as a better measure of energy gain for a given power loss which takes into account the synchronous phase ϕ. As cavities can be operated at different RF phases and considering that lower phases are preferred for lower energy structures for beam dynamics reasons, using this figure of merit when comparing different cavities over larger energy ranges would lead to an unfair comparison and it is therefore avoided here.

Typical values for ZT^2 for normal conducting cavities fall between 20 - 50 MΩ/m. As will be shown in Chapter 4, maximising this figure is an important optimisation drive for cavity designers. For superconducting cavities, which operate at much higher Q values, ZT^2 is less relevant as the beam power is much larger than the dissipated cryogenic power. Instead, attention is paid to increasing the accelerating field while reducing the peak fields to avoid field emissions (minimising the E_{peak}/E_0 ratio) and the breakdown of superconductivity (minimising the B_{peak}/E_0 ratio).

An additional useful figure of merit is the **r over Q ratio**, which depends on the cavity geometry only and not on its surface properties:

$$\frac{r}{Q} = \frac{(V_0 T)^2}{\omega U} \,. \tag{3.9}$$

Another useful parameter introduced in this thesis is the **RF power over energy gain ratio** which gives the power required by a certain structure (in kW) for a 1 MeV increase in beam energy.

The Kilpatrick Limit. In cavity design, RF breakdown is a major source of concern,

as it can limit the maximum electric field achievable and lead to other harmful consequences culminating with irreversible damage. Electron field emission is considered the trigger of RF breakdown in accelerating structures, but a deeper understanding of the chain of events involved at the quantum level is still sought. As such, empirical tests have been performed by many laboratories, to set the practical limits to RF breakdown. One of the pioneers to try to explain the phenomenon empirically was W.D. Kilpatrick in the 1950s, whose experiments led to an expression for the "sparking threshold" [62]. Kilpatrick assumed ions hitting the surface lead to secondary electrons being ejected which enhance the regular field emissions and facilitate breakdowns. Assuming the maximum ion energy is W (in eV), and E_k is the peak electric field (in V/m), Kilpatrick proposed the following relationship [63]:

$$WE_k^2 e^{-1.7\cdot 10^5 \cdot E_k^{-1}} = 1.8 \cdot 10^{14}\,. \tag{3.10}$$

W of an ion of mass M_0 and charge q was calculated from the gap between parallel plates to be:

$$W = \frac{0.153 q E_k^2}{M_0 \pi f^2}\,. \tag{3.11}$$

Making the substitution, one arrives at the following expression:

$$f = 1.64 E_k^2 e^{\frac{-8.5}{E_k}} \tag{3.12}$$

in which the frequency is expressed in MHz and the electric field in MV/m. Equation 3.12 is known as the Kilpatrick criterion and defines empirically the conditions that would result in breakdown-free operation, relating the operating frequency f to the maximum achievable electric field. Assuming a hydrogen ion and expressing the frequency in GHz, the expression above can be rewritten as:

$$E_k e^{\frac{-4.25}{E_k}} = 24.7 f^{\frac{1}{2}} \tag{3.13}$$

The Kilpatrick criterion is plotted in Figure 3.2 left. A Kilpatrick factor of 1, implies a cavity's working point being exactly on this curve for its operating frequency. Although Modern RF cavities have successfully been operated at fields much higher than 1 E_k, the Kilpatrick limit remains a figure of merit. In [63], Wang & Loew have analysed the maximum

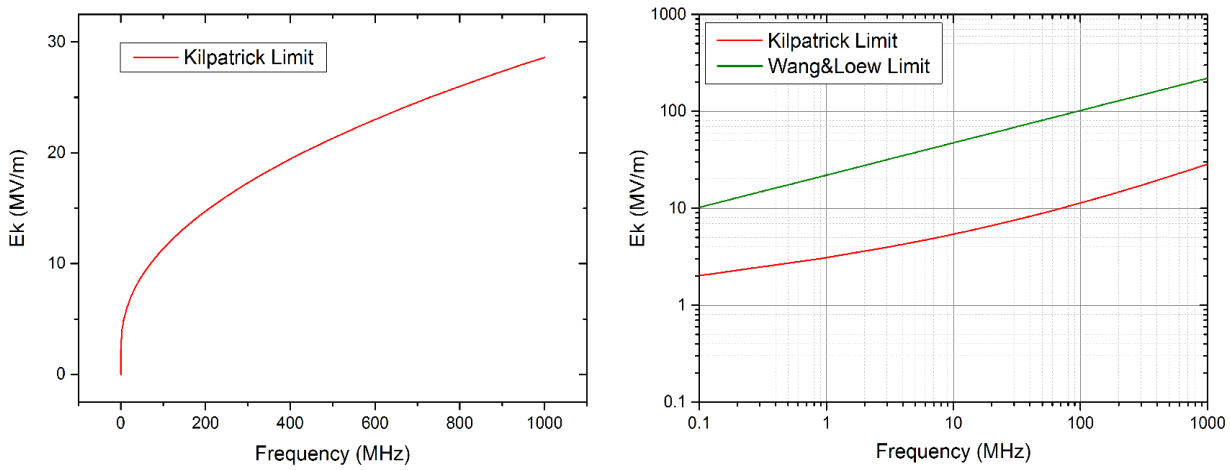

Figure 3.2: The Kilpatrick limit curve (left) and the Wang&Loew fit to modern cavities (right, logarithmic scale).

surface electric field in all modern structures and have produced a fit given by:

$$E_{peak} = 220 \cdot f^{\frac{1}{3}} \tag{3.14}$$

This expression is purely empirical and is plotted in Figure 3.2 right. As can be seen, the fields achieved in modern cavities are several times above the Kilpatrick limit mainly due to higher quality structures and better fabrication techniques. Although the fit above is skewed because of the inclusion of high gradient high frequency structures normally employed for electron application, lower frequency proton accelerators are normally operated above the Kilpatrick limit.

3.2.2 Beam Quality

A second criterion used to determine the cavity performance within the "pentagon" in Section 3.1 is given by beam dynamics. Conventionally treated as a distinct topic, the issue of beam quality and cavity design is particularly relevant for high intensity, high power linacs, where beam acceleration has to take place without compromising the beam characteristics. Multiple scenarios can be imagined by studying the pentagon: unsuitable cavity FIELDS could deteriorate the BEAM characteristics, which could in turn lead to particle loss with further THERMAL problems and VACUUM degradation which could increase RF breakdown and limit the cavity operation.

Beam dynamics considerations have an influence on the choice of the structure parameters from the conception stage of any linac design. As a general rule, the main guidelines followed are the control of losses, the minimisation of emittance growth as well as the control of the halo development. In order to achieve these, several meta-criteria are usually taken into account by most modern linac projects: a zero-current phase advance always below 90 degrees for stability, a longitudinal to transverse phase advance ratio chosen such that space-charge driven resonances and emittance exchange are avoided, good initial matching and a smooth variation of the transverse and longitudinal phase advance per metre.

For the purpose of this study, two aspects are analysed to measure the cavity effect on beam quality: **RMS emittance growth** and **beam loss**. Beam loss is obviously relevant as it can lead to machine activation and further setbacks, as was already shown. Emittance growth is equally important as it can be the underlying cause of beam loss. The beam size growth in phase space could be driven by space-charge effects, but RF defocusing, mismatch and cavity field errors are potential contributing factors. Additionally, lattice limitations imposed by the choice of cavity can also indirectly influence the focussing scheme adopted and hence the beam behaviour.

3.2.3 Technologies

The technologies involved in cavity production and operation represent the third measure of cavity performance. It is key to emphasise that technology has a significant influence an each of the five corners of the "pentagon", and its availability and difficulty can represent a serious manufacturing impediment, ultimately dictating the choice of cavity for a particular application.

The beam dynamics design usually defines the required tolerances for different accelerating structures, but it is the mechanical design that dictates how to achieve these tolerances. Often, sufficiently rigid support structures are needed as well as precise machining and complex adjustment and alignment elements. The surface quality has a direct impact on the vacuum and RF properties of the cavity and therefore the interfaces, assembly and joining techniques, vacuum sealing and RF contacts are all critical.

It is always possible to design a state of the art machine that demands very tight machining and regulation tolerances (over-design), but this approach can lead to very high costs, that is why a fair structure assessment has comparison terms for complexity and effort. In Chapter 4, this aspect is taken into account and for each cavity type a brief description of the steps involved in production is presented. This qualitative approach is aimed at giving a general overview, rather than a difficulty rating. Some of the most common technologies used in manufacturing normal conducting structures include copper plating, welding, brazing, precise machining, RF conditioning, vacuum baking, etc.

3.2.4 Tuning Procedure and Sensitivity to RF Errors

Finally, the fourth measure to be used for characterising the cavities is the tuning procedure and the sensitivity to RF errors. The tuning of normal conducting cavities has three aspects: frequency tuning, field profile tuning and stability tuning against perturbation. For each individual structure the overall tuning procedure will be described, as well as the field and frequency stability to be achieved.

RF errors at the klystron level translate directly into accelerating voltage errors which in turn will have an impact on the beam quality; that is why in high-current proton linacs, precise tuning of RF amplitude and phase is indispensable to reduce uncontrolled beam loss and beam quality deterioration. In general, tuning goals are set to ± 1 degree in RF phase and $\pm 1\%$ in amplitude at the klystron level. However, the effects of these RF errors can be different for different structure types and will be reviewed for each accelerating cavity examined.

3.3 Chapter Summary

This chapter is a necessary introduction to the requirements of cavity design. The "pentagon of cavity design" proposed here is intended to be the starting point of any linac structure choice and a generic cavity design tool. The pentagon summarises five key aspects of cavity design: Beam Dynamics, EM Fields, Mechanical Structure, Thermal Design and Vacuum Issues. The high degree of interdependency is highlighted and a list of figures of merit are

further proposed as a minimum requirement for a fair cavity comparison. These figures of merit include the RF properties of the cavity, the beam quality, the technologies involved and the tuning precision and the sensitivity to RF errors required. This forms the basis of the comprehensive comparative cavity analysis to follow in Chapter 4.

Chapter 4

Comparative Assessment of Normal Conducting Accelerating Structures for High Power Proton Linacs

In this chapter, an in-depth analysis of several normal conducting accelerating structures for high-power linear accelerators is presented using the comprehensive approach described in Chapter 3. These designs are traditionally developed by leading proton accelerator laboratories (CERN, RAL, SNS, J-PARC, etc) and the design choices often reflect previous experience with existing machines. The approach adopted here is to extract from the study of several designs a key set of technical drivers that govern the choice of accelerating structure, and then explore the impact of the compromises that any given choice implies. The structures examined are the Drift Tube Linac (DTL), the Separated Drift Tube Linac (SDTL), the Crossbar H-Mode DTL (CH-DTL), the Cell-Coupled DTL (CCDTL), the Pi-Mode Structure (PIMS), the Cell Coupled Linac (CCL) and the Annular-Ring Coupled Structure (ACS). A comparative assessment will be presented, which will be the first time such an effort is made for the entire family of normal conducting structures spanning the full energy spectrum where these cavities are normally employed. The concluding graphs and tables are intended as reference design tools to support future accelerator design efforts and offer a more strongly justified choice of technological solutions for any potential high intensity proton linacs.

This analysis was started as part of the High Intensity Pulsed Proton Injectors (HIPPI) Joint Research Activity, a European R&D collaboration aimed at developing a common European technology base for the construction of high intensity linacs. HIPPI coordinated the work on several topics including normal conducting structures with the aim of investigating

RF properties and technological alternatives. Three main projects were involved in HIPPI: the 160 MeV Linac4 accelerator at CERN, the 70 MeV proton injector for the FAIR project at GSI and the ∼200 MeV linac at RAL, proposed at the time as a possible replacement for the ISIS proton injector [64].

In addition to these, for the purpose of this thesis, three other projects have been studied: the 400 MeV J-PARC linac, the 1 GeV SNS linac and the 2 GeV ESS proton linac. As a result, the full range of normal conducting cavities currently available for proton linacs is included in this systematic analysis. The aim of this chapter is to investigate each structure type not only on its RF properties but also on additional aspects like beam dynamics, technologies necessary, tuning mechanisms and errors.

Normal conducting RF structures are good candidates for beam acceleration in a pulsed proton linac, up to an energy exceeding 100 MeV [55]. This is especially true if this is the final linac energy, as in the case of Linac4, RAL and FAIR linacs, because investment in cryogenic infrastructure can be avoided. For higher energy projects where superconducting cavities are also used, the transition between normal and superconducting is often a matter of technological limits, local constraints and cost optimisation [23]. From a beam dynamics point of view, depending on the subsequent accelerator chain, the requirements can be quite different. For example, in the case of CERN, Linac4 has to be able, with a high duty factor, to deliver a beam quality that is adequate both for injection in the PS Booster as well as for a high energy superconducting linac (i.e. a beam without halo, low emittance, etc).

Different requirements for the proposed linac projects led to different choices of RF structures and beam dynamics. In the case of CERN, a classical beam dynamics design was adopted, and the type of structures used are the DTL from 3 to 50 MeV, the CCDTL from 50 to 102 MeV and the PIMS up to 160 MeV. A cell coupled structure (CCL) was also analysed as a possible alternative to the PIMS. For the GSI linac with a final energy of ∼70 MeV, the "KONUS" beam dynamics was adopted, with the use of CH-DTL structures over the entire energy range. For the RAL linac several schemes have been under study with the most advanced design consisting of a DTL up to 75 MeV followed by a CCL up to the final energy [18]. At J-PARC, a DTL is used up to 50 MeV, followed by an SDTL up to 181 MeV and the ACS structure up to the final energy. The SNS linac uses a DTL up to 87 MeV

and a CCL up 186 MeV. Above this energy superconducting elliptical cavities are used up to the final energy. A similar approach is adopted for ESS where a DTL is used up to 90 MeV followed by superconducting spoke and elliptical cavities. It should be mentioned that all these projects have adopted a similar front end with the RFQ the accelerating structure of choice for energies up to several MeV. In the following sections, each cavity type will be analysed [65].

4.1 Simulation Tools

RF simulations are carried out using 2D and 3D electromagnetic codes. One established option is Poisson Superfish, a 2D code developed at LANL and benchmarked against most RF linacs operational today [66]. Unless otherwise specified, most RF calculation results presented in this chapter will have been performed with Superfish. For 3D simulations several solutions are available, mostly commercial. CST Microwave Studio offers advanced options for modelling accelerator structures and has been the tool of choice for many linac designs, including this study [33]. However, simulation codes have inherent limits and often scaling factors need to be added to take into account additional effects and power losses as well as include safety margins. Furthermore, discrepancies can also arise from using different codes.

To understand better the limitations of the 2D and 3D EM codes to be used in this thesis, as well as benchmarking the codes against real data, a study has been carried out in the ISIS linac. A shunt impedance comparison has been made using power consumption data collected from ISIS and the results obtained when simulating each of the four DTL tanks with Superfish and CST Microwave Studio. The aim is to check the accuracy of simulation codes and models and to assess their relative performance [67].

The ISIS linac consists of four DTL tanks operating at 202.5 MHz that accelerate a 50 Hz, 20 mA H^- beam up to 70 MeV before injecting it into an 800 MeV synchrotron. Parts of the linac are nearly 60 years old and a more detailed machine description will be presented in Chapters 5 and 6. At the time the linac was designed, the limited computing power available and the absence of advanced electromagnetic simulation codes, made the

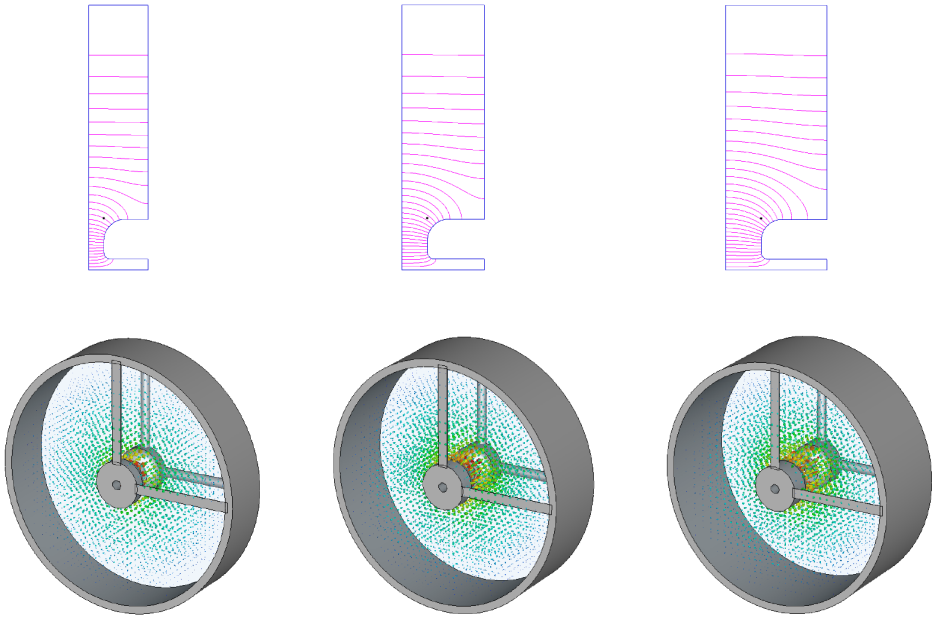

Figure 4.1: 2D (Superfish) and 3D (CST MWS) models of a single DTL cell at 10 (left), 20 (centre) and 30 MeV (right).

creation of a design optimized for power efficiency almost impossible, so from this point of view, the DTL is quite simple by today's standards.

Using the exact cell dimensions as in the ISIS linac, an accurate 2D model of the four DTL tanks has been prepared using Superfish. The code evaluates RF cavities with cylindrical symmetry, but it can make corrections to take into account the effect of the stems, or the end plates on frequency and shunt impedance. The 148 cells have also been modelled in CST Microwave Studio, which can additionally handle problems that lack cylindrical symmetry, like the effect of tuners, post-couplers, stems, vacuum pumping ports, etc. The geometry of a single cell at 10, 20 and 30 MeV can be seen in Figure 4.1 as well the electric field lines and vectors as calculated by Superfish and Microwave Studio.

In Figure 4.2, the evolution of the effective shunt impedance per unit length along the linac is presented as predicted by the two models. The agreement between the two codes is reasonably good, although the 3D results seem to be more sensitive to the choice of mesh. As can be seen, Microwave Studio predicts a constantly higher shunt impedance than Superfish in each of the four DTL tanks by up to 6%, although the two curves follow a very similar path. A big jump in shunt impedance can be seen at the transition between the tanks, due to the effects of the end plates, but also a lower average value in tanks 2 and 3. This is due

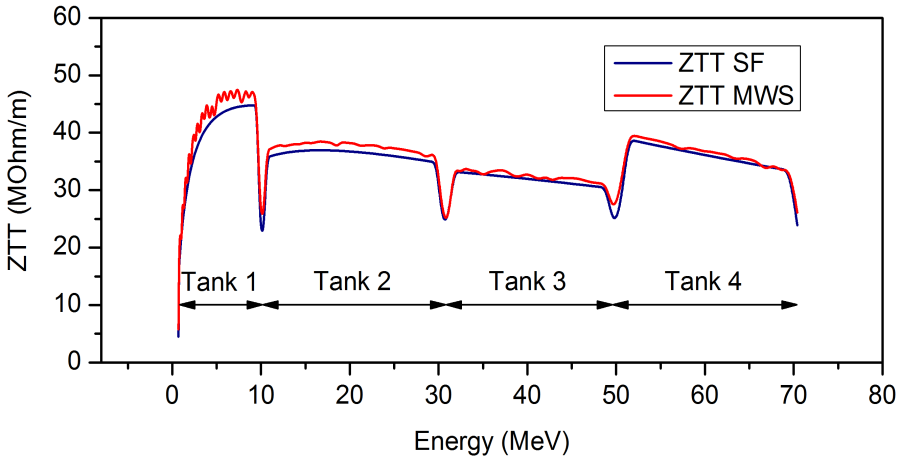

Figure 4.2: Effective shunt impedance variation in the ISIS linac as calculated by Superfish (blue curve) and CST Microwave Studio (red curve).

to the fact that these tanks being quite old have been designed and built with an emphasis on reliability rather than power efficiency. Tanks 1 and 4 being of a later generation have a slightly different cell geometry and a higher shunt impedance indicating a different design approach.

However, a comparison between the shunt impedance calculated by the two models and the actual power levels measured in each of the four DTL tanks shows a mixed picture. As can be seen in Figure 4.3, for tank 1, the measured power level is 0.49 MW, while Superfish and Microwave Studio predict 0.43 and 0.4 respectively, thus requiring a ∼13% adjustment for Superfish and ∼20% for Microwave Studio. The best agreement seems to be for tank 3 where the predicted shunt impedance has to be reduced by only ∼10% for Superfish and

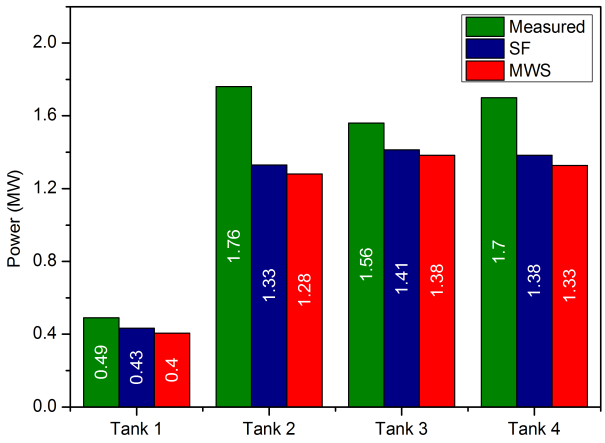

Figure 4.3: Measured and calculated power levels in the ISIS DTL tanks.

∼12.5% for Microwave Studio. On the other hand, for tanks 2 and 4, the models overestimate the shunt impedance by a much higher fraction: 32%/37% for tank 2 and 23%/28% for tank 4. The significant disagreement between simulations and measurements for tanks 2 and 4 can be explained if we assume that these tanks are being operated at a higher electric field gradient than the design value. However, this assumption is very difficult to verify as in the current DTL setup, the electric field gradient cannot be accurately measured.

Nevertheless, it is encouraging to note the good agreement between Superfish and Microwave Studio throughout the linac, although the actual power dissipation is constantly underestimated by an average of ∼20% by Superfish and ∼25% by Microwave Studio. This difference is normal, and it is due to the effects of surface imperfections, coupling holes, post-couplers, tuners and other auxiliary equipment and as we shall see, it is the power scaling factor used in most normal conducting linac designs.

4.2 The Drift Tube Linac - DTL

The classic Drift Tube Linac is a typical accelerating structure for the lower to medium energy part of normal conducting proton linacs. It operates in 0-Mode and to maintain synchronicity with the RF field the length of each accelerating cell increases with particle velocity. This leads to a decrease in RF efficiency at energies approaching 100 MeV, where alternative structures are normally employed. A schematic 3D view of a generic DTL section is shown in Figure 4.4. Many DTLs have been in continuous operation for decades in machines around

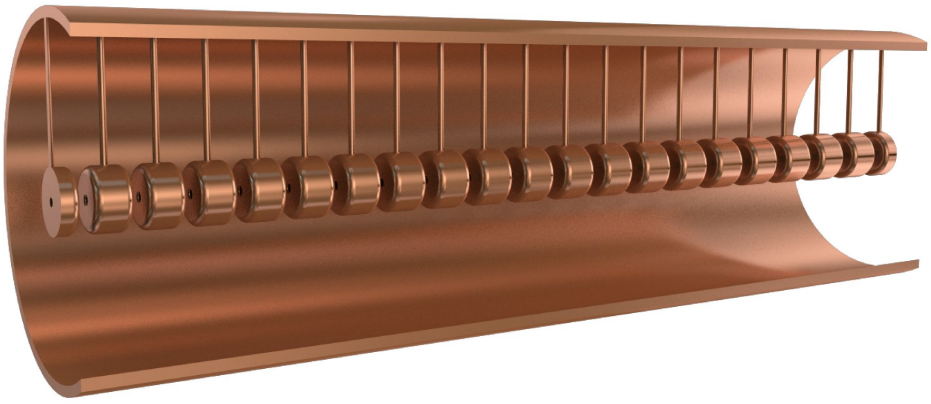

Figure 4.4: Schematic 3D layout of a DTL section.

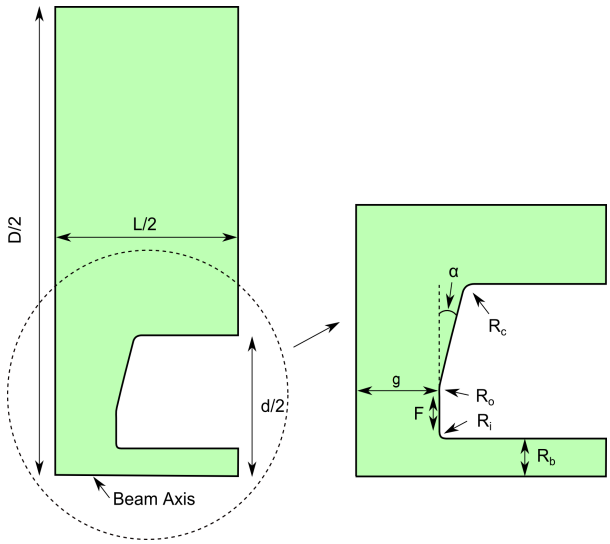

Figure 4.5: DTL cross-section as modelled by Superfish. Main parameters: D - Tank Diameter, d - Drift Tube Diameter, L - Cell Length, R_b - Aperture Radius, g - Gap Length, R_i - Inner Nose Radius, R_o - Outer Nose Radius, R_c - Corner Radius, F - Flat Segment, α - Face Angle (Adapted from [66]).

the world, like the 50 MeV Linac2 injector at CERN or the ISIS 70 MeV linac at RAL both operating at 202.5 MHz. For this study the five DTLs analysed are the Linac4 (50 MeV), RAL (75 MeV), J-PARC (50 MeV), SNS (87 MeV) and ESS (90 MeV) designs.

4.2.1 DTL Optimisation Procedure Example

The starting point in the electromagnetic design of DTLs is a basic geometry which is usually optimised for high shunt impedance while taking into account several boundary conditions. These boundary conditions include the reduction of the Kilpatrick factor, providing sufficient space for quadrupoles inside the drift tubes and a sufficiently large aperture to avoid beam loss, accomplishing designs with reasonable tolerances that can be easily manufactured, cooled, etc. The geometry optimisation initially implies a parameter scan of a multidimensional space for a single DTL cell. A typical cell geometry is shown in Figure 4.5, where a 2D cross-section of a quarter of a cavity can be seen with no fewer than nine free parameters, the variation of which has to be well understood. Furthermore, after the initial single cell has been calculated, this process is repeated and an entire succession of cells forming a tank will be optimised, thus creating an even more complex design space.

It is important to understand that the choice of geometrical parameters is not entirely

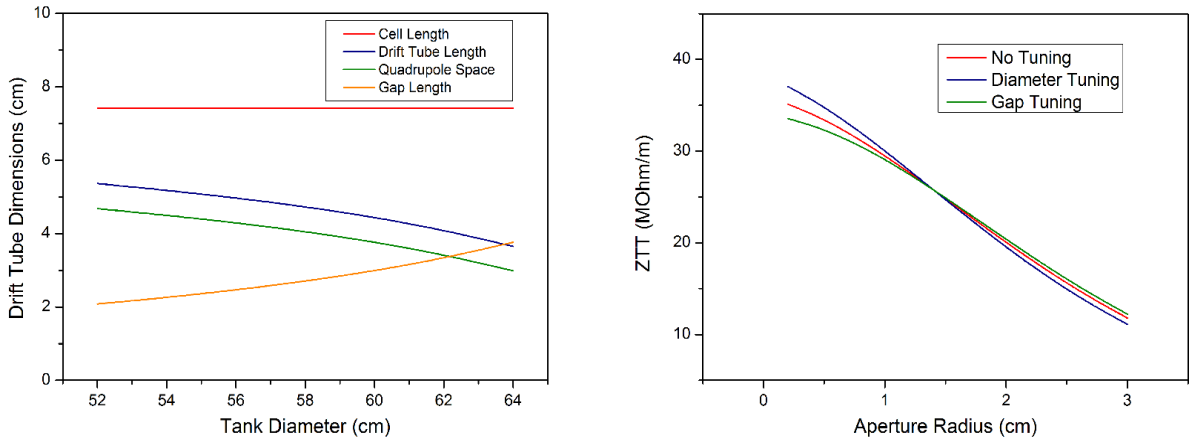

Figure 4.6: Evolution of the drift tube dimensions as a function of the tank diameter for a single 324 MHz DTL cell at 3 MeV (left), and of the effective shunt impedance per unit length as a function of the aperture radius for a single cell at 10 MeV (right).

free, as most are interdependent. Every parameter change that will improve the shunt impedance will invariably also modify the resonant frequency and an additional adjustment of a geometrical parameter will be needed to arrive again at the resonant frequency. Typically the gap length or the face angle are used to retune the cavity, although for single cells the tank diameter can also be changed. This additional change can however lead to an increase of the Kilpatrick factor, or a reduction in the space available for quadrupoles. This is better illustrated in the following study (Figure 4.6 left), in which the diameter of a single cell at 324 MHz and 3 MeV is gradually increased. The cell length remains obviously constant, but the gap length increases as it is being used to retune the cavity. The result is that the length of the drift tube decreases and so does the available space for quadrupoles.

Figure 4.6 right shows the evolution of the effective shunt impedance with beam aperture radius for a single cell at 10 MeV and 324 MHz. The three curves show the cases where the cavity is not retuned or retuned by varying the diameter or the gap length. It is immediately clear that the bore aperture has a very strong influence on cavity efficiency. However, the aperture radius is not a free parameter as such, as its choice is usually dictated by beam dynamics considerations. As a general rule, the ratio between pipe size and RMS beam size is kept between 5 and 10 in most linacs.

The drift tube face angle influence on the shunt impedance is shown in Figure 4.7 left and it indicates that a larger face angle will help concentrate the axial electric field on axis and

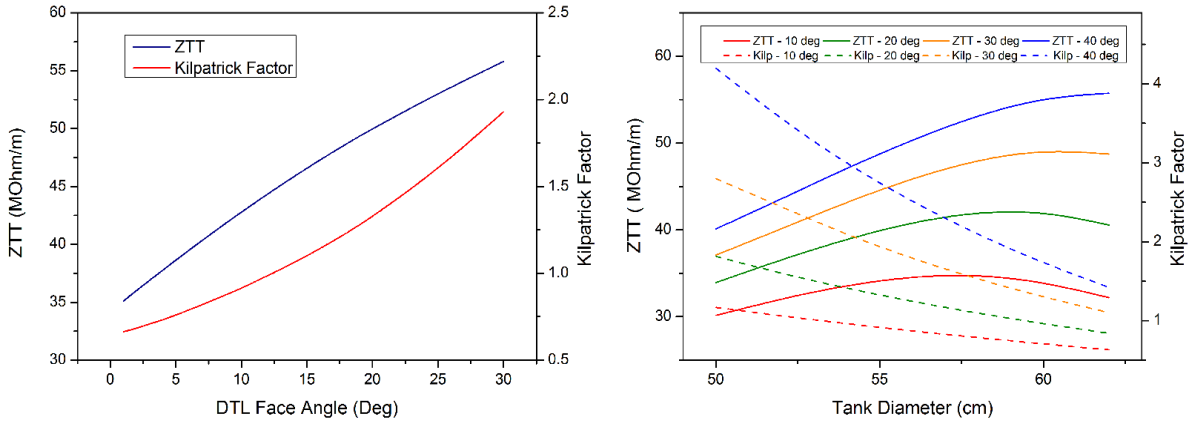

Figure 4.7: Effective shunt impedance per unit length and Kilpatrick factor evolution as a function of cell face angle (left) and of the tank diameter for different face angle values (right) for a 324 MHz DTL cell at 10 MeV.

increase the structure's efficiency, but also leads to an increase in the Kilpatrick factor. Also, reducing the gap will increase the transit time factor, thus the effective shunt impedance. However, the face angle defines the geometry of the drift tube, whose shape is not a free parameter, as it has to hold a quadrupole magnet inside. At the same time, the gap length cannot be made too small as it will limit the voltage gain for a given peak surface electric field, increasing the Kilpatrick factor.

The shunt impedance and Kilpatrick factor variation with tank diameter have an opposite trend (Figure 4.7 right), with larger diameters leading to more efficient structures, less prone

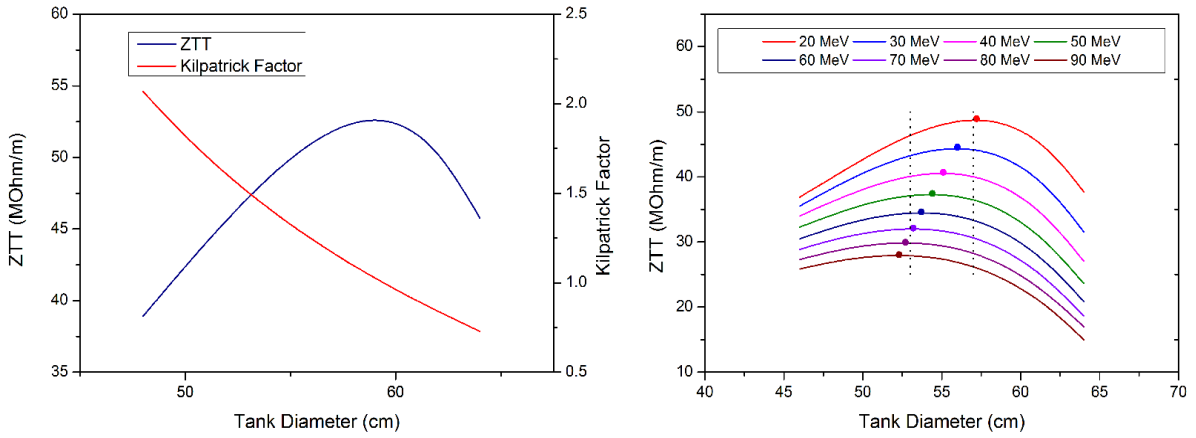

Figure 4.8: Study of optimum tank diameter at 10 MeV (left) and throughout acceleration (right), showing the effective shunt impedance and Kilpatrick factor variation with the DTL diameter (left), as well as the effective shunt impedance change with energy for different DTL diameters (right).

to breakdown. Nevertheless, an optimum tank diameter cannot be chosen for every single cell, as it would lead to an unpractical and unstable overall structure. In modern designs, an attempt to find the best possible diameter is made and then used for the entire DTL section. Figure 4.8 shows how such a choice can be made. The optimum diameter varies with energy and is larger for higher energies. However, two limits have to be added. The lower limit is given by the Kilpatrick factor and efficiency, while the upper limit is given by quadrupole length.

As can be seen, the optimisation process has to take many factors into consideration, and for a single DTL cavity this can be done in several steps. First the drift tube geometry is chosen so that it can accommodate quadrupole magnets, has the required bore radius and a tank diameter optimised for the entire energy range; then the gap length and the drift tube shape are optimised in order to maximise the r/Q and keep the Kilpatrick factor within reasonable limits; and finally the overall geometry is adjusted in order to maximise the quality factor Q, while retuning the cavity to the nominal resonant frequency [68].

4.2.2 DTL RF Properties

The RF properties of the five DTLs under consideration will be discussed below. Three resonant frequencies have been studied: 324 MHz for RAL and J-PARC, 352.21 MHz for Linac4 and ESS and 402.5 MHz for SNS. Linac4 accelerates the beam to 50 MeV using 3 tanks with a total peak dissipated power of 2.8 MW. This number includes a 20% margin as discussed in Section 4.1 and does not include the power delivered to the beam. This is because each design uses different beam currents and a comparison including beam loading values would be misleading. The average axial electric field E_0 is kept constant at 3.2 MV/m, while the Kilpatrick factor is 1.6. The synchronous phase varies from -30 to -20 degrees [69], [70], [71]. The ESS DTL accelerates the beam to 90 MeV using five tanks and broadly follows the Linac4 design. The peak dissipated power is 5.5 MW, and is as expected higher than Linac4 as the DTL is longer and accelerates the beam to a higher energy. Both the synchronous phase (-35 to -25 degrees) and the accelerating field (E_0 = 2.9 - 3.2 MV/m) are ramped in the first tank and then kept constant as dictated by the beam dynamics design. This technique is used to improve longitudinal beam capture in the first tank and reduce

longitudinal emittance growth by having constant focussing forces with energy, as well as reduce the Kilpatrick factor in the first few cells where sparking is more likely [72], [73], [12].

The J-PARC DTL accelerates the beam to 50 MeV using 3 tanks and total of 3.3 MW dissipated power. E_0 varies from 2.5 to 2.9 MV/m while the synchronous phase from -30 to -26 degrees. The peak Kilpatrick factor is 1.3 [74]. Operating at the same frequency, the RAL DTL accelerates the beam to 75 MeV using four tanks and 5.5 MW of dissipated RF power. The accelerating field varies from 2.7 to 2.9 MV/m with a maximum Kilpatrick factor of 1.44 [75], [76].

And finally, the SNS DTL which has been the first of the new generation of linacs to be commissioned, accelerates the beam to 87 MeV and operates at the highest RF frequency. The peak dissipated power is 6.5 MW and the accelerating field increases from 1.13 to 3.77 MV/m with a Kilpatrick factor of 1.3. As with the previous examples, a synchronous phase ramp law is also adopted here: -45 to -30 degrees [77].

The RF properties of the five DTLs are summarised in Table 4.1. As can be seen, the performance of the structures can be quite different as it reflects local requirements and different design choices not just on the RF but also on the beam dynamics or mechanical construction. The total dissipated peak power is as expected, higher for linacs accelerating to higher energies, but the increase is not linear. The power split in each tank and consequently the energy gain is dictated by the available klystron power, the safety margins considered and the beam power.

For a more realistic structure comparison two additional figures of merit were added: the real estate gradient and the RF power over energy gain. All the structures have similar real estate gradient values with Linac4 the highest at 2.4 MV/m and J-PARC the lowest at 1.75 MV/m. This number has the advantage of compressing information that would otherwise be difficult to compare like the effect of ramping the field and the different ramping laws, the additional space for transverse focussing elements, matching or diagnostics as well as how radical or conservative the design is in terms of acceptable peak electric fields.

The RF power over energy gain parameter is a useful indication of how much power is dissipated in the structure for an energy gain of 1 MeV and it includes the consequences of

	Linac4	RAL	ESS	J-PARC	SNS
Input Energy (MeV)	3	3	3.6	3	2.5
Output Energy (MeV)	50	75	90	50	87
Peak Dissipated Power (MW)*	2.8	5.5	5.5	3.3	6.5
E_0 (MV/m)	3.2	2.7-2.9	2.9-3.2	2.5-2.9	1.13-3.77
ϕ_s (deg)	-30 - -20	-42 - -21	-35 - -25	-30 - -26	-45 - -30
Kilpatrick Factor	1.6	1.44	1.55	1.3	1.3
Frequency (MHz)	352.21	324	352.21	324	402.5
Real Estate Gradient (MV/m)	2.4	1.95	2.2	1.75	2.28
RF Power/Energy Gain (kW/MeV)	60	76.8	63.5	70	76.9
ZTT (MOhm/m)*	30 - 56	25 - 46	35 - 60	27 - 38	20 - 50
Total Length (m)	20	36.6	39	27	37

Table 4.1: RF Properties of Linac4, RAL, ESS, J-PARC and SNS Drift Tube Linacs.
* - these values include a 20% reduction in shunt impedance and a corresponding increase in power dissipation.

having different phase ramp laws. Linac4 offers the best performance at 60 kW/MeV while the worst is the SNS DTL at 76.9 kW/MeV. However, as this number is an average for the entire energy range of each DTL, it is a disadvantageous measure for linacs which accelerate the beam to higher energies where the DTL is normally less efficient.

The evolution of the effective shunt impedance per unit length for the five DTLs is

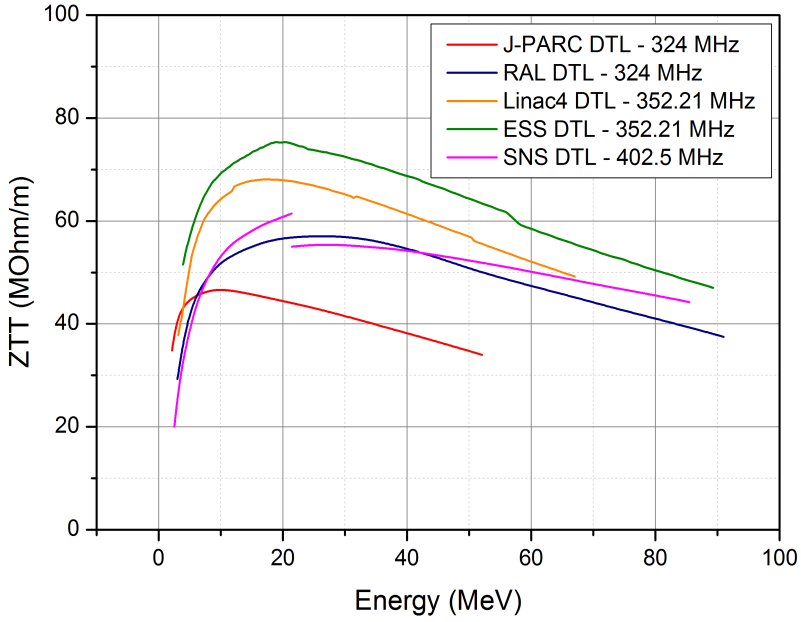

Figure 4.9: Effective shunt impedance per unit length vs. energy in the J-PARC, RAL, Linac4, ESS and SNS DTLs. The discontinuities reflect their respective structure or lattice choices.

shown in Figure 4.9. Although a shunt impedance variation with frequency is expected (the shunt impedance scales with the square root of frequency), several other factors exist and the scaling law is not respected. As already explained, the bore radius is approximately constant for all five DTLs as required to reduce beam losses and therefore does not scale with frequency. In addition, the DTLs can also differ in the approach taken to optimising geometrical parameters like the face angle or the diameter of the stems. A variable face angle for each cell can lead to a better shunt impedance, but at the same time a much more complicated mechanical design with many unique parts to be machined.

All aspects considered, the plot indicates that the Linac4 and ESS DTLs have the highest shunt impedance and J-PARC the lowest. The SNS curve shows a decrease after the second tank at 21 MeV of $\sim$10%. This is caused by an increase in the stem diameter to support heavier drift tubes. The shunt impedance of the J-PARC DTL is the result of several factors. It is at the lower frequency end and also the only DTL examined here using EM quadrupoles which are bulkier and offer fewer geometry optimisation options. It also has the most conservative approach, sometimes described rather euphemistically as a "luxury design".

This review confirms how seemingly unrelated design choices like focussing elements and lattice, frequency or adoption of novel technologies are reflected in the overall structure performance leading to various instances of the same cavity type.

4.2.3 DTL Beam Dynamics

The overall beam dynamics design philosophy for the DTLs under study is to provide a good transmission, minimise emittance growth and generally preserve the beam quality. For "hands-on" machine maintenance, a general rule is to keep losses below 1 W per metre of tunnel to avoid machine activation. As it was shown in the previous sections, the DTLs under study here employ different lattices, longitudinal and transverse phase advances, accelerating field and synchronous phase laws, etc. It is therefore important to assess their relative performance in terms of beam dynamics.

The approach used here was adapted from the work done on the Linac4 end-to-end

simulations, which were aimed at identifying possible limitations and improving the linac layout [52], [78], [79], [80]. Three input distributions have been used and tracking was performed using Tracewin [41]:

- A Gaussian distribution (3σ) with 50k macro-particles generated at the input of the DTL intended to test the structures without space-charge (Distribution 1).
- The same Gaussian distribution (3σ) generated at the input of the DTL but with space-charge (50k macro-particles) (Distribution 2).
- The output distribution from the simulation of the previous structure (MEBT), tracked with space-charge (50k macro-particles) (Distribution 3).

Matching for all DTLs is achieved transversely by varying quadrupoles at transition between tanks and longitudinally by offsetting the synchronous phase and accelerating field in selected cells. With the exception of J-PARC, all DTLs analysed here use permanent magnet quadrupoles which are not adjustable, so EM quadrupoles are normally added at transitions. Initial matching is reached by varying quadrupoles in the MEBT.

For Linac4, several different focussing schemes have been studied. The baseline design uses an FFDD lattice in the first tank and a FODO lattice for the rest of the DTL. This change of lattice was implemented in order to reduce the required integrated gradient that

Structure	Distribution	Input Emittance (Norm. RMS) $\epsilon_{x,y}$ - π.mm.mrad ϵ_z - π.deg.MeV	Emittance Growth(%)	Transmission (%)
Linac4 DTL	Distribution 1 (0 mA)	ϵ_x=0.28	0	100
		ϵ_y=0.28	0	
		ϵ_z=0.17	0	
	Distribution 2 (65 mA)	ϵ_x=0.28	10.7	100
		ϵ_y=0.28	7.1	
		ϵ_z=0.17	5.8	
	Distribution 3 (62 mA)	ϵ_x=0.33	2.5	100
		ϵ_y=0.28	12.8	
		ϵ_z=0.16	12.6	

Table 4.2: Emittance growth and beam transmission in the Linac4 DTL (compiled from [78]).

Structure	Distribution	Input Emittance (Norm. RMS) $\epsilon_{x,y}$ - π.mm.mrad ϵ_z - π.deg.MeV	Emittance Growth(%)	Transmission (%)
RAL DTL	Distribution 1 (0 mA)	ϵ_x=0.27	0	100
		ϵ_y=0.27	0	
		ϵ_z=0.14	0	
	Distribution 2 (43 mA)	ϵ_x=0.27	3.9	100
		ϵ_y=0.27	2.5	
		ϵ_z=0.14	2.7	
	Distribution 3 (43 mA MEBT)	ϵ_x=0.30	1	100
		ϵ_y=0.30	1	
		ϵ_z=0.15	2.7	

Table 4.3: Emittance growth and beam transmission in the RAL DTL.

would have been needed in the lower energy section of Tank 1. The transition between the two lattices is smooth and with correct matching no emittance growth has been observed. The result of tracking the three different test cases is shown in Table 4.2.

The RAL DTL uses a FODO lattice throughout the entire linac, with equipartitioning between the transverse and longitudinal energies obtained in the first tank and then maintained by varying the quadrupole settings. The tracking results are shown in Table 4.3.

Equipartitioning is also used in the J-PARC linac where a FODO lattice is adopted. The DTL uses novel, relatively compact EM quadrupoles, which is normally a desirable feature

Structure	Distribution	Input Emittance (Norm. RMS) $\epsilon_{x,y}$ - π.mm.mrad ϵ_z - π.deg.MeV	Emittance Growth(%)	Transmission (%)
J-PARC DTL	Distribution 1 (0 mA)	ϵ_x=0.21	0	100
		ϵ_y=0.21	0	
		ϵ_z=0.09	0	
	Distribution 2 (30 mA)	ϵ_x=0.21	2.8	100
		ϵ_y=0.21	4.6	
		ϵ_z=0.09	5.9	
	Distribution 3 (30 mA MEBT)	ϵ_x=0.23	1.0	100
		ϵ_y=0.23	4.2	
		ϵ_z=0.10	7.2	

Table 4.4: Emittance growth and beam transmission in the J-PARC DTL.

Structure	Distribution	Input Emittance (Norm. RMS) $\epsilon_{x,y}$ - π.mm.mrad ϵ_z - π.deg.MeV	Emittance Growth(%)	Transmission (%)
ESS DTL	Distribution 1 (0 mA)	ϵ_x=0.23	0	100
		ϵ_y=0.23	0	
		ϵ_z=0.13	0	
	Distribution 2 (62.5 mA)	ϵ_x=0.23	13.0	100
		ϵ_y=0.23	3.1	
		ϵ_z=0.13	8.3	
	Distribution 3 (62.5 mA MEBT)	ϵ_x=0.28	6.6	100
		ϵ_y=0.26	10.3	
		ϵ_z=0.14	9.3	

Table 4.5: Emittance growth and beam transmission in the ESS DTL.

as it allows various operational regimes and machine flexibility. On the other hand, this design choice also means a penalty on RF efficiency as we have seen in the previous section. The tracking results with the three test cases are shown in Table 4.4.

The ESS DTL also uses a FODO lattice, but does not adopt the equipartitioning rule. Instead, the tune depression is kept at 0.4 and constant in all planes with a smooth phase advance and careful transition between structures. The emittance growth and transmission for the three test cases are shown in Table 4.5.

Finally, the SNS DTL has adopted an FFODDO lattice with every third drift tube

Structure	Distribution	Input Emittance (Norm. RMS) $\epsilon_{x,y}$ - π.mm.mrad ϵ_z - π.deg.MeV	Emittance Growth(%)	Transmission (%)
SNS DTL	Distribution 1 (0 mA)	ϵ_x=0.25	0	100
		ϵ_y=0.25	0	
		ϵ_z=0.12	0	
	Distribution 2 (38 mA)	ϵ_x=0.25	2.7	100
		ϵ_y=0.25	1.4	
		ϵ_z=0.12	11.1	
	Distribution 3 (38 mA MEBT)	ϵ_x=0.31	2.1	100
		ϵ_y=0.28	8.5	
		ϵ_z=0.13	13.5	

Table 4.6: Emittance growth and beam transmission in the SNS DTL.

available for diagnostics. The design is also equipartitioned and makes use of PMQs. The tracking results of the three test cases are shown in Table 4.6.

Comparing the results for the five DTLs studied it is obvious that the various structure designs are adequate for their relative input beams. Although the optics layout can be quite different, no significant deterioration in beam quality has been observed and no individual solution can be singled out. This is because for all DTLs, efforts were made to avoid beam mismatch at input as well as at the transition between tanks, to provide sufficient acceptance both transversely and longitudinally and to avoid space-charge resonances.

4.2.4 DTL Technologies

There are several viable solutions successfully used for building Drift Tube Linacs and usually the method of choice depends on the technological requirements, the available budget, as well as on the existing local expertise. As an example, a brief description of the Linac4 strategy will be outlined below, aimed at illustrating the scale of the technological challenges. This is a succinct review based on several sources [69], [81], [82], [83] and from extensive discussions with the Linac4 design team. For the other DTLs, similar approaches have been followed.

The primary goal of the mechanical design has been to reduce the complexity of the structure as well as of the adjustment procedure while maximising stability and minimising maintenance. One early decision made was to machine drift tubes and holders to high precision. As a result, adjustment and positioning mechanisms are no longer needed, thus simplifying the entire process. This method had to be tested before the DTL production began and several preliminary models were built, including a scaled cold model and a full-scale prototype tank section.

The final cavity consists of several components: steel tank and girder, drift tubes assembled from pre-machined copper pieces, accessories for mounting drift tubes in girders, tuning, stabilisation, support, vacuum pumping, alignment and other ancillary equipment. The tolerances are stringent but following advances in machining quality, they are considered feasible without any further adjustment mechanism and assuming all parts undergo metrology before assembly [84].

4.2.5 DTL Tuning and Sensitivity to RF Errors

As with the previous section, the Linac4 approach will be described below. From an RF point of view the DTL is split into three tanks. The first tank is ∼3.5 m long while tanks 2 and 3 are ∼7 m long, each made of two sections of about the same length as tank 1, but connected to minimise the number of transitions.

The following tuning strategy is envisaged. For field adjustment, a total of 25 fixed tuners are used (5 for the first tank and 10 for each of the following tanks). To keep the tanks on frequency during operation, one movable tuner is used for each tank section. Field stabilisation is achieved using post-couplers (9 in tank 1, 16 in tank 2 and 23 in tank 3). For effective stabilisation, the post-couplers have to follow the "post-coupler criterion", a rule that sets certain length limits proportional to the DTL dimensions as shown in Equation 4.1:

$$0.95 \geq \frac{[(D-d)/2]}{\lambda/4} \geq 0.90\,, \tag{4.1}$$

where λ is the RF wavelength, while the D and d are shown in Figure 4.5 [85], [55]. In the case of Linac4, to increase the RF efficiency of the structure, the drift tube diameter has been reduced, leaving the post-coupler length at the limit for achieving effective stabilisation. However, a 3D analysis of post-coupler modes indicates that even for a configuration with fewer post-couplers, stabilisation can be achieved with a field flatness of ± 1%. Beam dynamics simulations show that even less stringent requirements are acceptable [81], [70].

The sensitivity to RF errors in the Linac4 DTL has been studied at CERN by tracking a Gaussian distribution over hundreds of runs, with random errors uniformly distributed. Two different types of dynamic errors ("Klystron errors") have been applied: an error in RF phase and an error in amplitude. These errors appear at the RF power source level (3 for the DTL), are applied coherently to all RF gaps powered by the same source and cannot be fixed.

The impact of the klystron errors on the beam has been quantified by checking the beam phase, energy jitter and RMS emittance at the end of the DTL. Values between ±0.5% and ±2% for the amplitude and values between ±0.5 and ±2 degrees for the phase have been considered. From the results one can deduce that the amplitude errors have more impact

than the phase errors and that a variation of ±2% in amplitude causes an emittance growth and an energy jitter above what is tolerable. A control of the amplitude and phase within ±0.5% and ±0.5 degrees would be ideal, but ±1% and ±1 degree is also acceptable [86].

4.3 The Separated Drift Tube Linac - SDTL

The Separated Drift Tube Linac (SDTL) is an alternative option to the classic DTL structure and is in many ways operationally similar with the DTL. The SDTL also operates in the 0-Mode and has been first proposed at J-PARC where it has also been implemented for the medium energy section of the J-PARC H^- linac [87].

Accelerating the beam from 50 to 181 MeV, the J-PARC SDTL presents several advantages. With the notable decrease in shunt impedance with energy, geometry optimisation is vital to maintain structure efficiency. However, in the case of a classic DTL, the presence of focussing and steering elements inside the drift tubes makes the optimisation process very difficult, as strict conditions have to be met concurrently. In an SDTL this difficulty is solved by moving the quadrupoles outside the tanks leaving the drift tubes empty, in much the same way transverse focussing is achieved in superconducting linacs. The result is a design with much shorter tanks made of only several cells and much easier to build and cool than a classic DTL. In Figure 4.10 an artist's impression of an SDTL tank is presented.

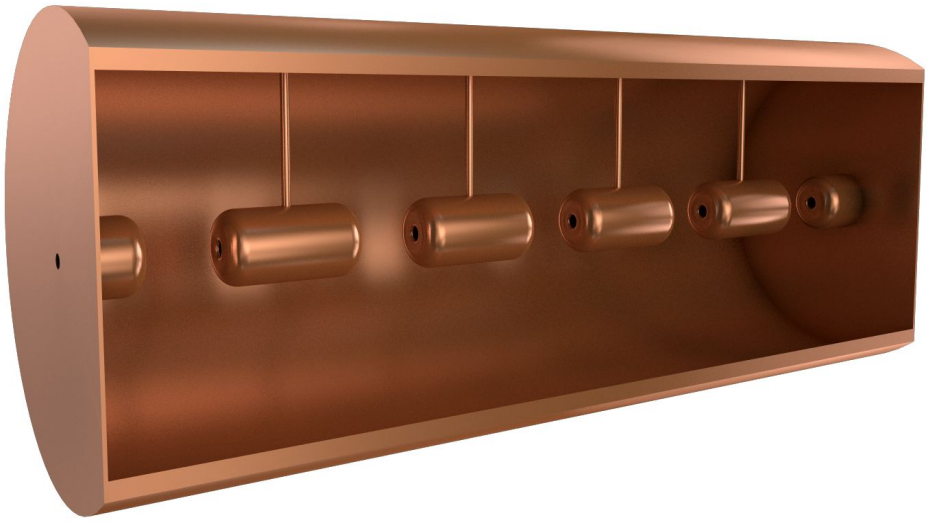

Figure 4.10: Schematic 3D layout of an SDTL tank.

4.3.1 SDTL RF Properties

A five cell configuration for each J-PARC SDTL tank has been adopted. A total number of 30 tanks is needed to reach 181 MeV with a 2 $\beta\lambda$ space between tanks. Two additional end tanks are used for beam bunching. The tank lengths increase from 1.5 to 2.5 m. Groups of two tanks are powered by a single klystron (16 in total). The resonant frequency is 324 MHz, the same as the preceding DTL. The average axial electric field is ramped from 2.5 to 3.7 MV/m with a Kilpatrick factor of 1.3 chosen with the view of limiting the discharge and allowing long term stable operation. The synchronous phase is -27 degrees [74], [88].

A summary of the main SDTL RF properties is presented in Table 4.7. It is interesting to see that the figure for the real estate gradient is lower than any of the DTLs analysed in the previous section. This is normal and reflects the fact that having the quadrupoles outside the cavity structure inserts additional beam line space where no acceleration takes place. Similarly, the RF Power/Energy gain figure is higher than for the DTL. It should be noted that these figures average the entire energy range spanned by the SDTL. Therefore a DTL employed up to 180 MeV would have similar or poorer properties

The effective shunt impedance per unit length is shown in Figure 4.11. The downward trend indicates that the structure becomes less efficient at higher energies as is also the case with the DTL. For this reason, at 181 MeV, the J-PARC linac switches to yet another

	J-PARC SDTL
Input Energy (MeV)	50
Output Energy (MeV)	181
Peak Dissipated Power (MW)*	14.7
E_0 (MV/m)	2.5 - 3.7
ϕ_s (deg)	-27
Kilpatrick Factor	1.3
Frequency (MHz)	324
Real Estate Gradient (MV/m)	1.56
RF Power/Energy Gain (kW/MeV)	112
ZTT (MOhm/m)*	18 - 40
Total Length (m)	84

Table 4.7: RF Properties of the J-PARC Separated Drift Tube Linac.
* - these values include a 20% reduction in shunt impedance and a corresponding increase in power dissipation.

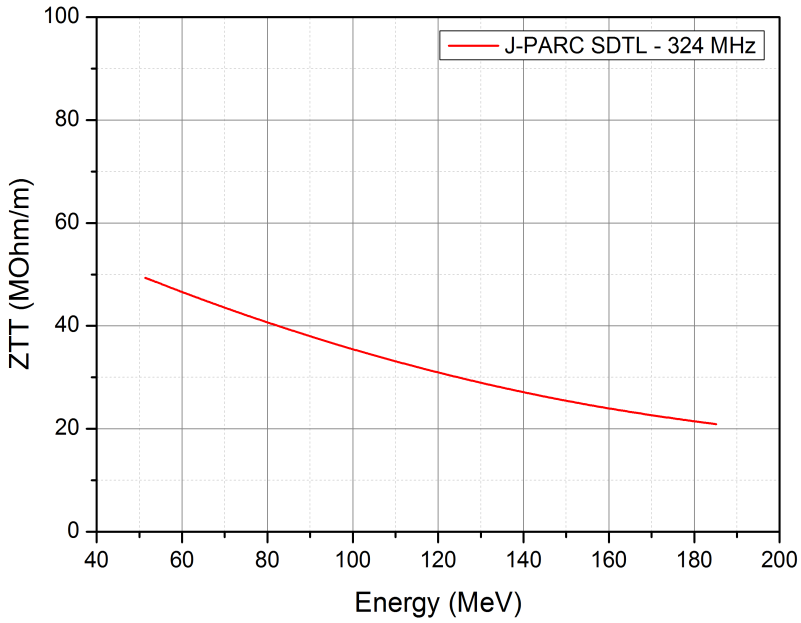

Figure 4.11: Effective shunt impedance per unit length vs. energy in the J-PARC SDTL.

structure, the Annular-ring Coupled Structure (ACS). However, the slope of the SDTL shunt impedance decrease is not as steep as for a DTL.

4.3.2 SDTL Beam Dynamics

The SDTL beam dynamics design follows a similar low loss philosophy as the DTL. Equipartitioning established in the first DTL tank is also kept in the SDTL. A doublet focussing scheme has been adopted and since the transverse focussing period is now longer, the larger beam size requires a larger cavity aperture if beam loss is to be avoided. This can have serious effects on the shunt impedance. Consequently, an iterative process is normally carried out where the number of cells per tank, the available power from the klystron, the structure efficiency and the beam size are carefully optimised. In the case of J-PARC an aperture radius of 18 mm was chosen.

The choice of frequency is also expected to have a positive influence on the beam dynamics: by operating at the same frequency as the DTL, the transition between structures can be made smoother and less disruptive longitudinally. Adopting the SDTL shifts the frequency jump to a higher energy where space-charge effects are weaker and the bunch length is sufficiently short to reduce the nonlinear effects.

Structure	Distribution	Input Emittance (Norm. RMS) $\epsilon_{x,y}$ - π.mm.mrad ϵ_z - π.deg.MeV	Emittance Growth(%)	Transmission (%)
J-PARC SDTL	Distribution 1 (0 mA)	ϵ_x=0.23	0	100
		ϵ_y=0.23	0	
		ϵ_z=0.1	0	
	Distribution 2 (30 mA)	ϵ_x=0.23	4.5	100
		ϵ_y=0.23	6.9	
		ϵ_z=0.1	1.7	
	Distribution 3 (30 mA DTL)	ϵ_x=0.24	4.1	100
		ϵ_y=0.24	8.2	
		ϵ_z=0.11	1.2	

Table 4.8: Emittance growth and beam transmission in the J-PARC SDTL.

Matching between DTL and SDTL is achieved transversely by tuning quadrupoles at transition. Several sets of DTL and SDTL quadrupoles are used. In operation four wire scanners and four quadrupoles are normally sufficient. Longitudinal matching is reached by varying the accelerating fields in the first few tanks of the SDTL.

To test the robustness of the SDTL linac design for J-PARC, a similar approach was adopted as in the DTL case, with three test cases simulated. The results are presented in Table 4.8. No unusually large emittance growth and halo development has been observed and no significant drop in the beam quality, provided a good initial match can be attained. This is somehow expected as the design is equipartitioned. However, the general question of whether this is the most suitable approach will be examined more carefully in Chapter 6.

4.3.3 SDTL Technologies

In many respects, the technology required for the successful commissioning of an SDTL is similar to that of a classic DTL, but several aspects make the construction much simpler. By placing the quadrupoles, steering elements and diagnostics in the inter-tank space, the alignment of the drift tubes is much less difficult. Consequently, the tolerances can be eased, the fabrication cost reduced and cooling simplified. The transverse tolerance is set at $\pm$ 0.3 mm, which is a factor of three larger than for the DTL.

Regarding actual technologies employed, it is worth mentioning the use of the advanced

copper electroforming electrolysis on all inner surfaces of the SDTL tanks as well as for the DTL. This was aimed at suppressing any potential electrical discharge in view of increasing reliability and optimising high power operation.

4.3.4 SDTL Tuning and Sensitivity to RF Errors

One of the other advantages of using the SDTL is its intrinsic field stability against any perturbation. Consequently, stabilising devices like post-couplers or multi-stems which are normally employed in classic DTLs are generally not needed here. This makes both the RF design and the mechanical construction much easier, as it has been mentioned. To tune the frequency and the field, the SDTL uses two fixed and one movable tuners for each tank. This configuration is sufficient to arrive at the resonant frequency and to obtain a field uniformity on axis of ±1% [89], [90].

Concerning the RF errors, the acceptable dynamics errors are similar to the DTL: ±1% in amplitude and ±1 degree in phase. The klystron employed is the pulsed Toshiba 3 MW model at 324 MHz (E3740A).

4.4 The Crossbar H-Mode DTL - CH-DTL

Over the last decades, several H-Mode type cavities have been proposed for different applications. The Crossbar H-Mode DTL is a new multi-cell drift tube cavity recently developed at IAP Frankfurt, operating in the TE_{210} mode (H_{210}). As the name suggests, the electric field is in the transverse direction and therefore it needs to be "bent" longitudinally to be useful for beam acceleration. As a result, strictly speaking these are no longer pure H-Mode cavities. For a CH-DTL axial electric field is obtained using small drift tubes and by carefully arranging the stem position. In general, H-Mode structures have good properties, with high shunt impedance, high accelerating fields and compact designs. They have been used for pulsed high intensity proton and ion linacs covering the low and medium energy range like the Linac3 lead injector at CERN. More recently, the CH-DTL has been chosen as the basis for the new 70 MeV proton linac for the GSI FAIR project [91]. A schematic layout of a CH-DTL tank is shown in Figure 4.12. Although there is little operational experience with

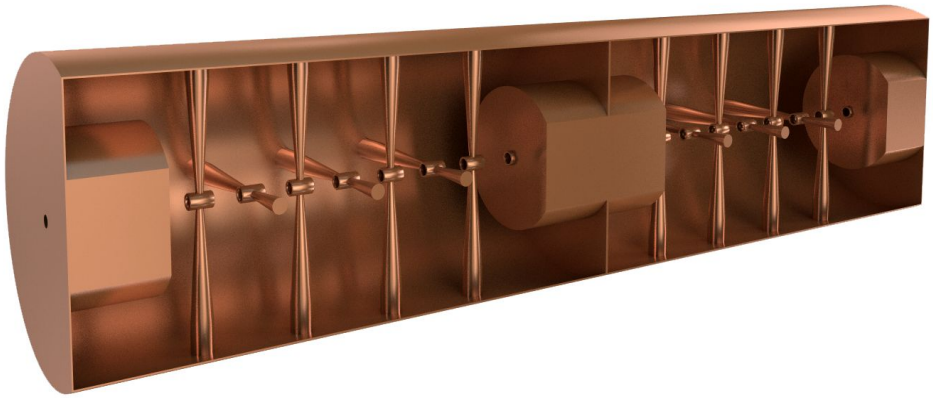

Figure 4.12: Schematic 3D layout of a CH-DTL accelerating module.

this structure, its RF properties make it quite attractive as an alternative to classic DTLs especially at low energies and at the moment it is being analysed as an option for future accelerators, like the IFMIF and EUROTRANS facilities.

4.4.1 CH-DTL RF Properties

The CH-DTL is essentially an extension of the well established Interdigital H-Mode cavities to a higher frequency. The CH-DTL operates in Pi-Mode and is characterised by the lack of internal focussing elements, which allows the construction of extremely compact cavities with a positive impact on shunt impedance. In addition, such cavities can stand high RF fields in routine operation due to the small surface of the drift tubes.

The FAIR proton injector at GSI will employ 12 CH-DTL type cavities with a variable number of gaps operating at 325 MHz, to accelerate a 35 mA proton beam from 3 to 70 MeV. A beam current upgrade up to 70 mA is envisaged at a later stage. In order to match the klystron power level, the cavities are grouped in 6 pairs of coupled structures. Each resonator consists of 2 cavities connected by an inter-tank section which hosts a magnetic lens for transverse focussing and which distributes the input power between the accelerating structures. Three coupled resonators accelerate the beam up to 35 MeV where a dedicated diagnostics section will be positioned, while the final acceleration up to 70 MeV will be done by the last three coupled resonators. The total length of the CH-DTL section of the linac is 23 m and the average accelerating gradient per cavity varies from 3 to 8 MV/m [92]. A summary of the RF properties of the CH-DTL can be seen in Table 4.9.

	FAIR CH-DTL
Input Energy (MeV)	3
Output Energy (MeV)	70
Peak Dissipated Power (MW)*	5.3
E_0 (MV/m)	3 - 8
ϕ_s (deg)	-45, -35, -30, 0
Kilpatrick Factor	2.0
Frequency (MHz)	325
Real Estate Gradient (MV/m)	2.91
RF Power/Energy Gain (kW/MeV)	80.0
ZTT (MOhm/m)*	40 - 95
Total Length (m)	23

Table 4.9: RF Properties of the FAIR CH-DTL Linac.
* - these values include a 5% reduction in shunt impedance and a corresponding increase in power dissipation.

The geometry of the structure was optimised at IAP Frankfurt and GSI for high shunt impedance by means of 3D EM modelling using CST Microwave Studio. It was observed that the stems are not only responsible for the mechanical stability of the structure, but they also carry the highest current density and provide the accelerating axial electric field, so for this reason their design needs special attention. Initially based on the existing IH structure but modified for the crossbar geometry, the shape of stems has eventually evolved into a conical profile with two cylinders. In order to preserve the efficiency of the structure the size of the stems was carefully reduced so that the capacitive load between each pair of stems would be also decreased. The axial accelerating electric field is produced by orientating two neighbouring stems at 90 degrees one against the other [93].

The effective shunt impedance variation along the FAIR linac can be seen in Figure 4.13. The theoretical results predicted by simulation codes have been verified by RF measurements on a test model build at Frankfurt University and a reduction in shunt impedance of $\sim$5% has been observed. In terms of efficiency, it is clear that at low energies, the CH-DTL is highly efficient. This is due to the small drift tubes as mentioned above, but it is the actual field configuration that has the biggest impact. By having the electric field direction transversal, the cavity surfaces will have less magnetic field and therefore fewer losses. The downside to this is that in order to maintain the TE_{210} mode in the cavity, the end cell

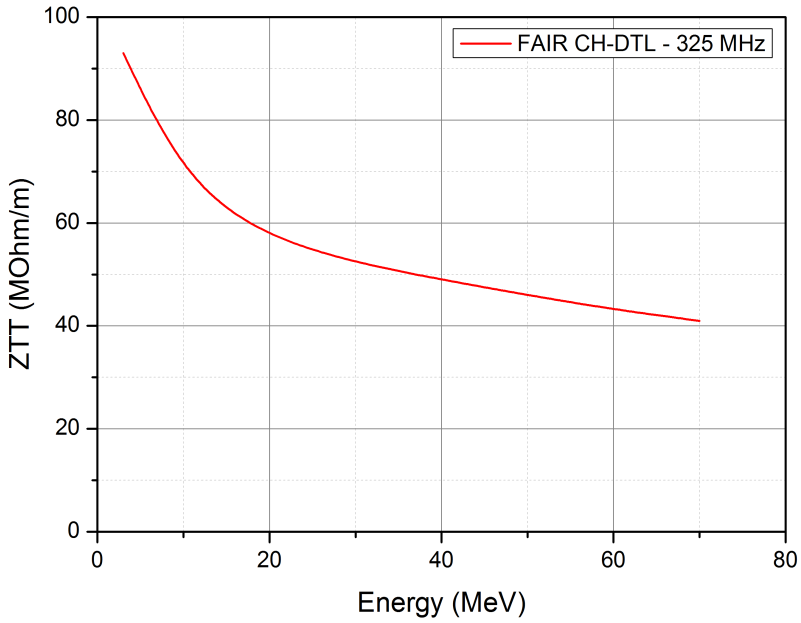

Figure 4.13: Effective shunt impedance per unit length vs. energy in the FAIR CH-DTL.

design becomes relatively complicated as the electric field lines have to be perpendicular to conducting surfaces. Therefore, to benefit from their low loss operation, a cavity design with more cells is desirable [22].

4.4.2 CH-DTL Beam Dynamics

The main disadvantage of having more cells and hence longer cavities is the longer transverse focussing periods. To compensate the high space-charge forces at low energies, short transverse lattice periods are normally adopted as in the case of the DTL. For CH-DTLs however, this is not possible and the KONUS beam dynamics scheme was invented instead. KONUS stands for "**Ko**mbinierte **Nu**ll Grad **S**truktur" (Combined Zero-Degree Structure). It is an alternative focussing system devised at Frankfurt University, in which the transverse RF defocussing forces are reduced compare with traditional structures, thus allowing longer transverse focussing periods without dramatically compromising the beam quality [94].

A typical KONUS lattice has the following main elements:

- For transverse focussing, a quadrupole triplet is adopted, placed in the inter-tank space.
- The first few gaps of the resonator have a small negative synchronous phase used for longitudinal focussing and matching.

- Main acceleration occurs in the long 0 degree phase section of the structure.

The first CH-DTL tank of the FAIR proton injector consists of 10 gaps to limit the cavity length in order to avoid transverse emittance growth and potential beam loss. Following the KONUS scheme, the first 3 gaps operate at -30 degree synchronous phase to bunch the beam, while the following 7 gaps operate at 0 degree and provide the main acceleration up to ∼6 MeV. At this point a magnetic quadrupole triplet is used to focus the beam transversely. The second section of the coupled CH-DTL resonator consists of 3 bunching gaps (-35 degree) followed by the 9 gaps operating at 0 degree. The following modules follow a similar pattern up to the final energy.

Table 4.10 presents the RMS emittance growth along the linac when tracking a beam generated with PARMTEQ [95] and transported through the FAIR RFQ (35 mA, 325 MHz, 4000 particles). Although the transmission is 100%, a high emittance growth is observed in both transverse and longitudinal planes. This beam behaviour is the result of having longer focussing periods and high space-charge forces. In addition, due to the large input emittance in the longitudinal plane, the design aim was to minimize the growth in this plane, while simply avoiding beam loss transversely. However, for the requirements of the FAIR proton injector, it is believed that the linac output beam properties are satisfactory [92].

Nevertheless, although the structure is tested in existing machines, the beam performance remains a key question mark in deciding whether such linac designs are suitable for high power applications, as beam loss can potentially lead to severe operational limitations.

Structure	Distribution	Input Emittance (Norm. RMS) $\epsilon_{x,y}$ - π.mm.mrad ϵ_z - π.deg.MeV	Emittance Growth(%)	Transmission (%)
FAIR CH-DTL	Distribution 3 (35 mA RFQ)	ϵ_x=0.39	56	100
		ϵ_y=0.38	60	
		ϵ_z=0.18	63	

Table 4.10: Emittance growth and beam transmission in the FAIR CH-DTL (compiled from [92]).

4.4.3 CH-DTL Technologies

The fabrication steps involved can be summarised as follows [92], [96]. The outer tank is double walled to facilitate the cooling design and is built from stainless steel and copper plated. This leads to substantial cost savings. Unlike the DTL, a girder was not adopted to reduce the risk of structure deformation, although a mechanical design with girders exists.

The stems, like the tank, are also made from stainless steel. They are directly welded onto the tank from inside and then the whole structure is copper plated. The design of the stems aims for RF efficiency as well as mechanical stability in order to reduce the potential misalignment of the drift tubes. This leads to a conical geometry towards the centre, ending with a cylindrical shape that will be joined to the outer tank, as can be seen in Figure 4.12.

The drift tubes are made from bulk copper and will be welded onto the stems. Special attention has to be paid to the welding quality. One proposed alternative is to add a central stainless steel ring to the stem in which a drift tube, previously cooled in liquid nitrogen would be inserted, resulting in a strong bond after the thermal expansion.

4.4.4 CH-DTL Tuning and Sensitivity to RF Errors

The CH-structure can be locally tuned by varying the gap/period length ratio at the design stage, leading to relative freedom in achieving a certain field profile. This is done using drift tubes with different lengths and precise positioning. Local gap voltage changes in the range $\pm 20\%$ can be achieved.

In order to approximate the zero-mode, the end cells need to be modified. Their resonant frequency is decreased by lengthening the last half drift tube and therefore increasing the volume of the cell. In addition it is also possible to increase the radius of the last half drift tube inducing a strong capacitance with the closest stem. Using this method a 25% increase in the electric field in the last cell has been achieved.

For normal operation mobile tuners will be used. Two or three tuners per cavity depending on the number of cells will provide the required degree of field and frequency tuning. Simulations and RF tests indicate that a field flatness of $\pm$1-2% is achievable [92].

Phase and voltage errors from amplifiers have also been investigated in the FAIR linac

to determine the tolerances for mechanical construction and the required RF control during operation. A similar approach was adopted as already described for the previous structures, where errors in phase and amplitude were randomly applied at the klystron level and the emittance degradation analysed. The study indicates that a ±1 degree error in phase is tolerable, but due to the distinctive characteristics of the KONUS focussing scheme, a reduction in voltage is not desirable; that is why the design aims for a more stringent ±0.2% error in voltage at the klystron level [97].

4.5 The Cell-Coupled Drift Tube Linac - CCDTL

At intermediate linac energies, alternative structures to the conventional drift tube linac can be used, providing comparable energy efficiency and a simplified construction and alignment. Different designs have been considered, all based on short DTL-like tanks containing only a few empty drift tubes, with quadrupoles placed externally between tanks. One such design is the SDTL currently employed at J-PARC and already discussed in Section 4.3. An alternative option is the Cell-Coupled Drift Tube Linac (CCDTL). One of the main advantages of these structures is their lower price per metre compared to a DTL, whose cost is dominated by the complex construction and alignment of the drift tube-quadrupole assembly and by the machining, handling and plating costs of the long DTL tanks. For

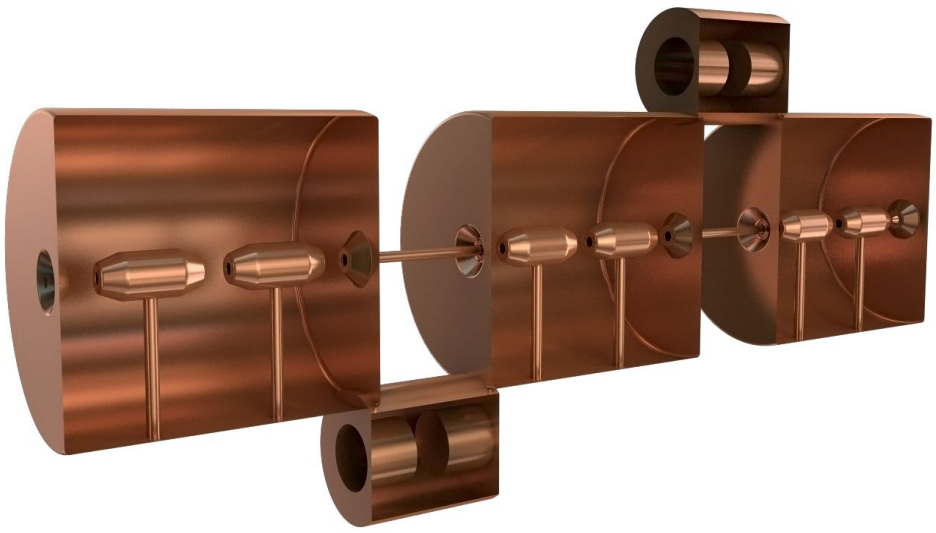

Figure 4.14: Schematic 3D layout of a CCDTL accelerating module.

structures with external quadrupoles, the drift tube alignment tolerances are much less demanding than for a DTL and a good shunt impedance can be maintained while having the additional benefit of adjustable electromagnetic quadrupoles. On the other hand, placing quadrupoles outside of the accelerating structure increases the length of the focussing periods leading to a larger beam size and therefore a CCDTL is not a suitable candidate for lower energies and is usually adapted at a later stage of the acceleration. The actual switch to a CCDTL involves weighing the optimal RF efficiency against beam dynamics considerations (e.g. acceptable transverse phase advance) [98]. A 3D layout of a CCDTL module is shown in Figure 4.14.

4.5.1 CCDTL RF Properties

For the new Linac4 injector at CERN, a CCDTL operating at 352.21 MHz has been adopted for the 50 to 102 MeV energy range. The CCDTL structure was first proposed at Los Alamos National Laboratory, and is essentially a sequence of several accelerating cavities coupled together by small off-axis coupling cells. The accelerating cavities are of the Alvarez type and consist of only several gaps making the structure in some respect similar to an SDTL. A CCDTL operates in the 0-Mode between the gaps in the tank and in the $\pi/2$-Mode between the tanks [99]. In the case of Linac4, the accelerating tanks have three gaps, and a set of three accelerating tanks and 2 coupling cells form a "module" which will be fed by a single klystron.

The Linac4 CCDTL section consists of 21 accelerating cavities grouped in 7 modules. Each accelerating cavity houses two drift-tubes and three gaps. A 2D model as simulated by Superfish can be seen in Figure 4.15, showing the geometry outline and the longitudinal electric field lines. The optimisation method is similar with the procedure described for a DTL. In order to simplify the geometry, a constant cavity diameter is desirable for the entire energy range. Initial simulations were performed, aimed at finding the optimum for the maximum shunt impedance. A constant diameter does not compromise the efficiency of the design, as a solution can be found in the optimum range for all particle velocities. Similarly, all other geometric parameters were analysed in order to maximize the shunt impedance within certain boundaries. The RF properties of the CCDTL are given in Table 4.11. The

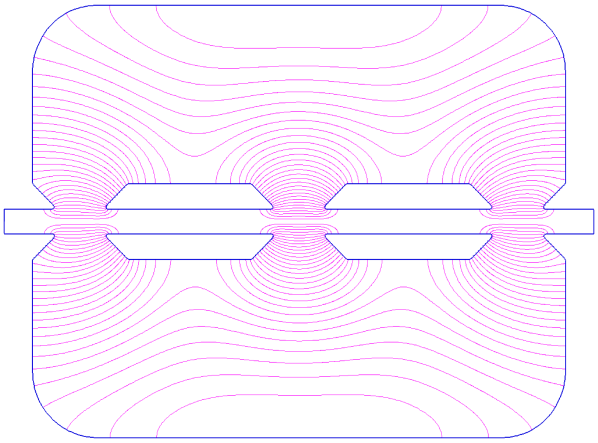

Figure 4.15: 2D Superfish model of a CCDTL accelerating module at 352.21 MHz and 50 MeV showing the cavity outline and the longitudinal electric field lines.

peak dissipated power is 4.83 MW for the entire section, with an axial electric field between 4 and 4.4 MV/m and a Kilpatrick factor of 1.7. The real estate gradient is 2.1 MV/m and the RF power over energy gain is 93 kW/MeV [100], [101], [102].

The effective shunt impedance per unit length over the considered energy range can be seen in Figure 4.16. As in the case of the SDTL, having the focussing elements in the space between the tanks allows more design freedom in optimising the drift tube geometry for higher efficiency. The sudden increase in ZTT at around 75 MeV is due to the fact that the first three modules have been designed for a lower Kilpatrick field, thus compromising the

	Linac4 CCDTL
Input Energy (MeV)	50
Output Energy (MeV)	102
Peak Dissipated Power (MW)*	4.83
E_0 (MV/m)	4 - 4.4
ϕ_s (deg)	-20
Kilpatrick Factor	1.7
Frequency (MHz)	352.21
Real Estate Gradient (MV/m)	2.1
RF Power/Energy Gain (kW/MeV)	93
ZTT (MOhm/m)*	32 - 41
Total Length (m)	25

Table 4.11: RF Properties of the Linac4 CCDTL Linac.
* - these values include a 17% reduction in shunt impedance and a corresponding increase in power dissipation.

efficiency of the structure. The shunt impedance decreases rapidly with velocity and for this reason at around 100 MeV, a different accelerating structure was adopted for Linac4.

4.5.2 CCDTL Beam Dynamics

Since the CCDTL does not follow the velocity profile cell by cell, it can only be employed at higher energies. With the quadrupoles placed outside the tanks, the transverse focussing period also becomes longer, which is likely to lead to larger beam sizes limiting further the stage at which the CCDTL can be adopted. For Linac4 the optimum transition is at 50 MeV. The FODO lattice adopted in the second DTL tank is continued. The average synchronous phase in each tank is -20 degrees and the focussing period is $3\beta\lambda$ long. At the transition between tanks, when one or more gaps are missing, the phase of the neighbouring cavities is adjusted to cope with the transition and to ensure a smooth variation of the longitudinal phase advance.

To test the beam behaviour in the CCDTL, the same approach already described in the DTL section has been adopted with three input distributions tested. The simulation results are presented in Table 4.12. The CCDTL is characterised by a very small emittance growth and 100% transmission, indicating a good choice of parameters [78], [80].

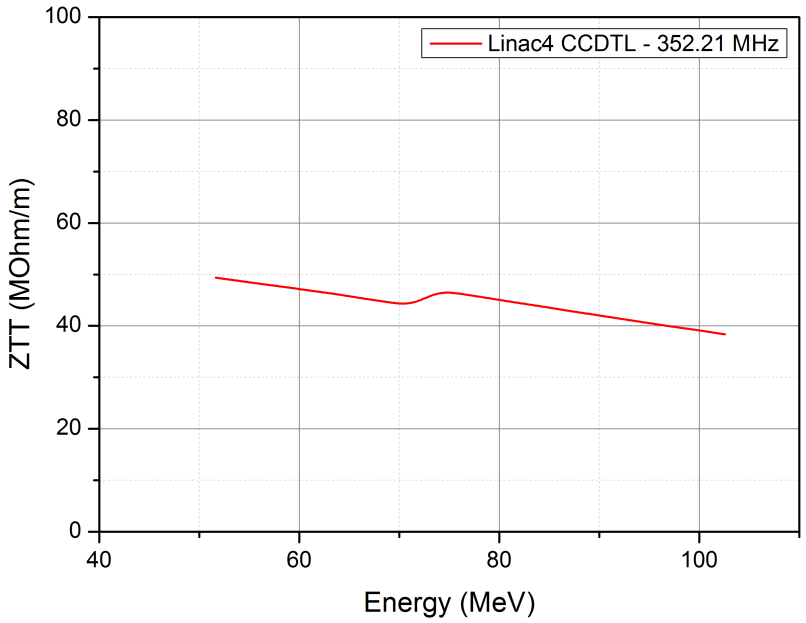

Figure 4.16: Effective shunt impedance per unit length vs. energy in the Linac4 CCDTL.

Structure	Distribution	Input Emittance (Norm. RMS) $\epsilon_{x,y}$ - π.mm.mrad ϵ_z - π.deg.MeV	Emittance Growth(%)	Transmission (%)
Linac4 CCDTL	Distribution 1 (0 mA)	ϵ_x=0.33	0	100
		ϵ_y=0.32	0	
		ϵ_z=0.17	0	
	Distribution 2 (65 mA)	ϵ_x=0.33	-3	100
		ϵ_y=0.32	3	
		ϵ_z=0.17	0	
	Distribution 3 (65 mA DTL)	ϵ_x=0.34	-1	100
		ϵ_y=0.32	1.7	
		ϵ_z=0.18	0.8	

Table 4.12: Emittance growth and beam transmission in the Linac4 CCDTL (compiled from [78]).

4.5.3 CCDTL Technologies

The manufacturing of the CCDTL accelerating module consists primarily of the production of the tank, the drift tubes and of the ancillary equipment. Each CCDTL tank is assembled out of two copper-plated stainless steel half-tanks. The half-tanks are machined out of pre-shaped "bucket-like" pieces. One fabrication alternative is to construct the tanks from discs and cylinders and weld them together using an electron-beam or a Gas Tungsten Arc welding technique. This different method has indeed been used in the prototyping phase. However, for production, although more expensive, the pre-shaped raw material is preferred owing to improved material and surface properties and savings in machining and welding time. A smooth surface on the inside of the tank instead of a machined welding, reduces the risk of porosities under the copper plating in the welding area and improves vacuum characteristics. Cooling channels are machined into the external part of the tanks.

Each half-tank contains one drift tube machined out of solid copper which is cooled via the supporting copper stem. The drift tubes are electron-beam welded to the stem and then fixed on a girder, which is fixed on top of the tanks. The alignment and fixing mechanism of the stem will be adapted from the CERN DTL design and it relies on the machining precision of the stem holder. This means that there is no possibility to change the alignment of the stems, other than re-machining the stem holder. Since there are no quadrupoles inside

the drift tubes, the required alignment precision for the stem is much less critical than for a DTL. The welding between the stem and the drift tube is a critical item because it defines the perpendicularity of the ensemble and thus the alignment precision of the drift tube in the tank [82], [83].

4.5.4 CCDTL Tuning and Sensitivity to RF Errors

As described in the SDTL section, the shorter tanks ease the tuning procedure and remove the necessity of having post-couplers for field stability. The definition of the tuning requirements involved cavity modelling and the construction of a module prototype. The modelling was performed by means of circuit analysis in which the change in field amplitude was quantified. Static errors of up to ±20 kHz in each cell are likely (i.e. residual tuning errors). In addition, dynamic frequency errors of up to ± 50 kHz can be expected (i.e. due to temperature change). Simulations indicate that these frequency changes will lead to maximum voltage errors of ±0.4% in the accelerating cavities with respect to the nominal case. This is acceptable from the beam dynamics point of view and consequently only one motorized tuner is necessary for each CCDTL cavity. The tuner frequency variation necessary to match the correct resonant frequency of the $\pi/2$-Mode is 150 kHz [83], [103].

Regarding the RF errors, beam tracking studies indicate that the klystron's amplitude and phase should be controlled ideally to 0.5% and 0.5 degree to limit the energy and phase jitter at the CCDTL output, but values of 1% and 1 degree are still acceptable [84], [86].

4.6 The Coupled Cavity Linac - CCL

At energies approaching 100 MeV, the shunt impedance of drift tube based structures like the DTL, SDTL or CCDTL starts to decrease rapidly, and the only option to maintain a high acceleration efficiency is to switch from structures operating in the "0-Mode" to structures operating in "π-Mode", which present a shunt impedance increasing with energy. At the same time, the reduced bunch length at high energy due to phase damping allows the increase of the RF frequency, with a further gain in shunt impedance and the possibility to operate at higher gradients. However, the smaller cell dimensions impose a drastic change in

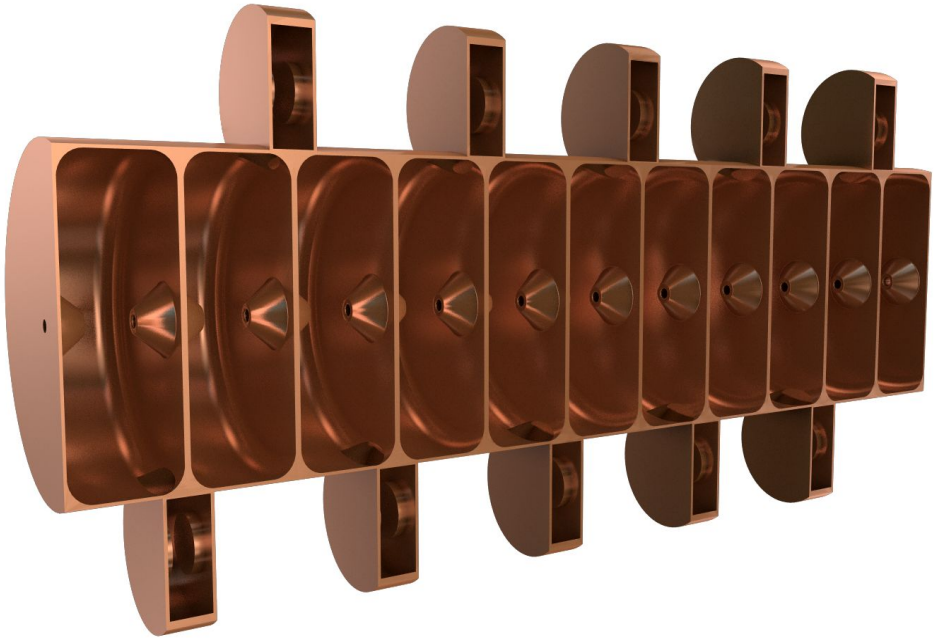

Figure 4.17: Schematic 3D layout of a CCL cavity.

the mechanical construction technique, swapping from the bolted units made out of copper-plated stainless steel to modules made of smaller, brazed, full copper cells.

The Coupled Cavity Linac sometimes known as the Side Coupled Linac or the Cell Coupled Linac, was developed in the 1960s at the Los Alamos National Laboratory and used reliably in several machines (LANL, FNAL, ORNL, etc.). Its peculiarity is that in addition to accelerating cells it also contains coupling cells, placed sidewise as can be seen in Figure 4.17. From the beam point of view, this is a sequence of accelerating gaps operating in the π-Mode, spaced by a distance of $\beta\lambda/2$ in order to keep the synchronism between particles and accelerating field. From the RF point of view, it is a bi-periodic chain of resonators (accelerating and coupling cells) operating in $\pi/2$-Mode. In this Mode, fields in adjacent cells have a 90 degrees phase difference, all coupling cells have zero fields, while the accelerating cells are excited with the correct polarity.

Three CCLs have been considered for this study. At CERN, the Linac4 CCL design was originally the structure chosen for the 92 to 163 MeV energy range before being replaced by a different structure for reasons discussed at a later stage. However, important developments have been made at the design and prototyping stage. At RAL, a CCL is considered as a possible upgrade to the existing ISIS linac as the intermediate stage to either 180 (75 to

180 MeV) or 800 MeV (75 to 196 MeV). And finally, the SNS 1 GeV linac uses a CCL structure to accelerate the beam from 87 to 186 MeV and has been operational for several years.

4.6.1 CCL RF Properties

The original Linac4 CCL was devised to accelerate the particles from 90 to 160 MeV and important contributions have been made to the development by CERN, LPSC and INFN-Napoli. The operating frequency is 704.42 MHz, twice that of the DTL and the CCDTL. Each tank contains 11 accelerating cells and 10 coupling cells placed on alternating sides of the accelerating cells. The cells are magnetically coupled by slots at the intersection between accelerating and coupling cells. Electromagnetic quadrupoles are placed between tanks, and in order to form a continuous RF structure the tanks are bridged by off-axis 3-cell coupler units. This allows several tanks to be fed by a single klystron. Considering a maximum klystron output power of 4MW, 5 tanks can be connected to form a module of 117 coupled cells [104], [105].

The design accelerating gradient for the CERN CCL was chosen at 4 MV/m as a cost analysis indicated that it minimises the structure and the RF cost. At this gradient, the peak

	Linac4	RAL	SNS
Input Energy (MeV)	92	75	87
Output Energy (MeV)	163	196	186
Peak Dissipated Power (MW)*	9.7	17.5	12.1
E_0 (MV/m)	4.0	2.4	3.7
ϕ_s (deg)	-20	-22	-28 - -30
Kilpatrick Factor	1.2	0.6	1.3
Frequency (MHz)	704.42	648	805
Real Estate Gradient (MV/m)	2.5	1.3	1.8
RF Power/Energy Gain (kW/MeV)	136	145	121
ZTT (MOhm/m)*	29 - 36	23 - 32	39 - 50
Total Length (m)	28	92	55

Table 4.13: RF Properties of Linac4, RAL and SNS Coupled Cavity Linacs. Of these, only the SNS CCL is operational.
* - these values include a 20% reduction in shunt impedance and a corresponding increase in power dissipation.

surface field is not a critical parameter, and simulations show that the maximum electric field level is always kept below 1.2 Kilpatrick [70]. The real estate gradient is lower at 2.5 MV/m, while the RF power over energy gain parameter is as expected, higher than the previously analysed structures at over 130 kW/MeV [70], [106].

The CCL cavity under consideration at RAL operates at 648 MHz. As in Linac4, this is twice the DTL frequency. The design is however much more conservative with a constant field gradient of 2.5 MV/m and a maximum Kilpatrick of 0.6. The total length of the CCL section is nearly 92 m. Groups of 10 accelerating cells and 9 coupling cells form a single cavity. Depending on the available klystron power, several cavities are grouped together to form a module to be fed by a single klystron. A klystron peak power of 3 MW is sufficient to feed six cavities grouped together. To accelerate to 196 MeV, a total of 56 cavities are needed.

A double frequency jump is also used in the SNS CCL from 402.5 to 805 MHz. Eight accelerating cells and seven coupling cells form a single cavity. Multiple cavities are coupled via a bridge coupler. The klystron peak power rating is 5 MW and can feed a single module made of 12 coupled cavities. To accelerate to the final energy of 186 MeV, four full modules are needed. The accelerating field gradient is constant at 3.7 MV/m and the Kilpatrick factor is always below 1.3. The real estate gradient is 1.8 MV/m [77]. A full summary with

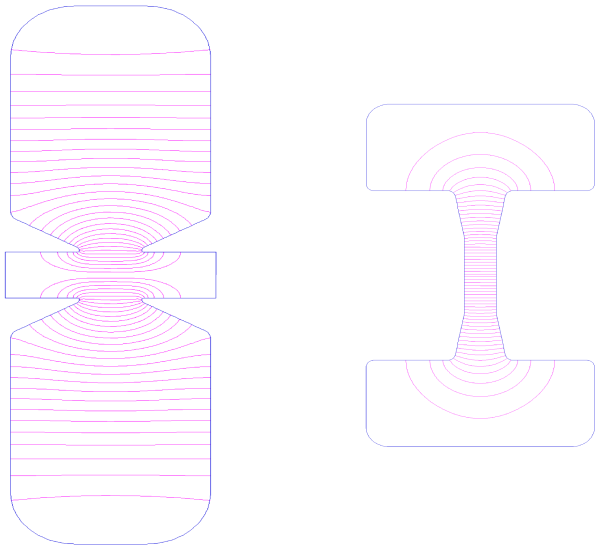

Figure 4.18: 2D Superfish model of a CCL accelerating cell (left) and of a coupling cell (right) operating at 648 MHz and 100 MeV, showing the cavity outline and the longitudinal electric field lines.

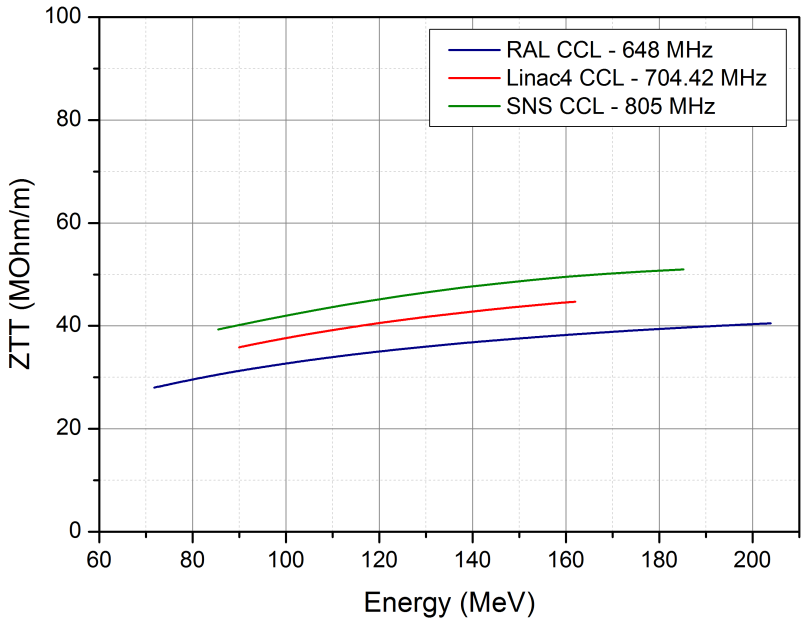

Figure 4.19: Effective shunt impedance per unit length vs energy in the Linac4 CCL.

the RF properties of the three CCLs discussed is presented in Table 4.13.

The basic cell design for CCLs follows the same optimisation procedure already described for the previous structures in which the structure geometry is optimised for efficiency within certain boundary conditions. For each individual cavity the cell length is kept constant to ease the construction and increases from cavity to cavity in proportion to the particle velocity. As described in the DTL section, the aperture radius affects significantly the shunt impedance and would ideally be made smaller. However, a relatively large aperture is required to provide a sufficient margin against halo particles loss when operating at high average beam currents. Consequently, the shunt impedance does not scale as expected with frequency, although a higher frequency is desirable. An additional optimisation has to be carried out to find out the coupling slot dimensions to arrive at the correct coupling coefficient. Figure 4.18 illustrates 2D accelerating and a coupling cells as modelled by Superfish at 648 MHz and 100 MeV.

The effective shunt impedance per unit length for the three CCL designs is presented in Figure 4.19. As expected, the efficiency increases with energy for this structure type, there is a frequency dependence due to the designs being relatively similar and the values fall within a relatively close bandwidth.

Structure	Distribution	Input Emittance (Norm. RMS) $\epsilon_{x,y}$ - π.mm.mrad ϵ_z - π.deg.MeV	Emittance Growth(%)	Transmission (%)
Linac4 CCL	Distribution 1 (0 mA)	ϵ_x=0.30	0	100
		ϵ_y=0.30	0	
		ϵ_z=0.18	2.7	
	Distribution 2 (65 mA)	ϵ_x=0.30	-3.3	100
		ϵ_y=0.30	6.6	
		ϵ_z=0.18	2.7	
	Distribution 3 (65 mA CCDTL)	ϵ_x=0.34	0	100
		ϵ_y=0.32	4.3	
		ϵ_z=0.18	2.7	

Table 4.14: Emittance growth and beam transmission in the Linac4 CCL (compiled from [52]).

4.6.2 CCL Beam Dynamics

A similar approach to beam dynamics simulations as explained in the DTL section was also adopted here, with three beam distributions used: a zero current and a full current distribution generated at the input of the CCL section and a distribution resulting from matched tracking through the previous structures. This simple but effective test is used to check whether the beam dynamics philosophy adopted and allowed by the particular structure configuration is suitable from an emittance growth and beam loss point of view.

In Linac4, the CCL continues the conventional FODO lattice used in two DTL tanks and in the CCDTL, with quadrupoles placed between tanks. A phase advance ratio $\sigma_l/\sigma_t \simeq 0.7$ was retained in order to obtain a strong transverse focussing and a smaller transverse beam size while operating in a stable region close to equipartitioning, thus compensating for the longer period lengths. Transversely, matching is achieved by varying several quadrupoles at the end of the DTL and the beginning of the CCL. The variation of the longitudinal phase advance due to the frequency jump is controlled by adjusting the phase in the modules at the transition. The resulting phase advances vary smoothly and do not lead to emittance growth. The result of beam tracking can be seen in Table 4.14 [70], [52].

A FODO lattice is also used in the RAL CCL, with the cavity placed in the drift space between the quadrupoles. Each focussing period is $12.5\beta\lambda$ long which includes two cavities

Structure	Distribution	Input Emittance (Norm. RMS) $\epsilon_{x,y}$ - π.mm.mrad ϵ_z - π.deg.MeV	Emittance Growth(%)	Transmission (%)
RAL CCL	Distribution 1 (0 mA)	ϵ_x=0.30	0	
		ϵ_y=0.30	0	100
		ϵ_z=0.15	0	
	Distribution 2 (43 mA)	ϵ_x=0.30	4.2	
		ϵ_y=0.30	5.1	100
		ϵ_z=0.15	3.5	
	Distribution 3 (43 mA DTL)	ϵ_x=0.31	3.8	
		ϵ_y=0.31	4.4	100
		ϵ_z=0.15	4.1	

Table 4.15: Emittance growth and beam transmission in the RAL CCL.

with 20 accelerating cells each $0.5\beta\lambda$ and a $2.5\beta\lambda$ space for magnets. The synchronous phase is kept constant at -22 degrees throughout acceleration except at transitions where matching is required. The entire CCL section is equipartitioned. Beam tracking results are shown in Table 4.15.

At SNS, the period length is $13\beta\lambda$ long with a total of 48 identical quadrupoles placed in the spaces between cavities. The lattice adopted is also a FODO. The period length at the beginning of the CCL is comparable with the period length at the end of the DTL where a FFODDO lattice is used instead. This helps achieve a smooth transition between structures

Structure	Distribution	Input Emittance (Norm. RMS) $\epsilon_{x,y}$ - π.mm.mrad ϵ_z - π.deg.MeV	Emittance Growth(%)	Transmission (%)
SNS CCL	Distribution 1 (0 mA)	ϵ_x=0.30	0	
		ϵ_y=0.30	0	100
		ϵ_z=0.12	0	
	Distribution 2 (38 mA)	ϵ_x=0.30	4.5	
		ϵ_y=0.30	5.3	100
		ϵ_z=0.12	3.6	
	Distribution 3 (38 mA DTL)	ϵ_x=0.32	5.1	
		ϵ_y=0.30	3.9	100
		ϵ_z=0.13	2.5	

Table 4.16: Emittance growth and beam transmission in the SNS CCL.

and very good matching. Tune ratios are chosen such that resonance induced emittance growth is avoided. Beam tracking results are presented in Table 4.16.

4.6.3 CCL Technologies

The CCL manufacturing process requires almost crucially the construction of cold and hot models. The cavity construction involves several distinct components: the accelerating cells, the coupling cells and the bridge couplers. The techniques used for a CCL differ from those of the structures already discussed (DTL, CCDTL, etc.) because of the higher frequency and smaller size. The CCL accelerating and coupling cells are machined out of solid copper blocks, and then all cells are joined together to form a single tank using furnace brazing and machining. RF tuning of the individual cells is normally required before brazing. Cooling channels are pre-machined in the walls separating the cells.

Ideally, one important aim of the physical and mechanical engineering design is to provide a structure that is simple to machine and has reasonable tooling requirements. This can sometimes mean a small reduction in cavity efficiency, but this disadvantage is surpassed by manufacturing benefits. At SNS several choices were made in this regard. The CCL diameter is kept constant and the coupling cells have the same shape throughout the entire acceleration chain. The cell length within a single cavity is also the same irrespective of the particle velocity. Certain corners within the cell have the same radii and the shapes of the coupling slot and cell nose are constant. These simplifications reduce greatly the machining complexity [107], [108].

4.6.4 CCL Tuning and Sensitivity to RF Errors

The $\pi/2$-Mode is intrinsically stable against perturbations coming from mechanical errors, beam loading etc., meaning that the longitudinal field distribution remains flat even in the presence of asymmetries between cells. Stabilisation is obtained because modes around the $\pi/2$-Mode give equal and opposite contributions from perturbations, finally cancelling out [29].

Tuning of a Side-Coupled Structure corresponds to setting the frequency of the accelerat-

ing cells equal to that of the coupling cells, which in turn consists of closing the stop-band in the dispersion curve of the bi-periodic structure. When the structure is correctly tuned, the accelerating and coupling cell pass-bands in the dispersion diagram will meet and as a result, all modes contributing to perturbations (i.e. all the modes on the dispersion curve around the operating $\pi/2$-Mode), will appear in pairs equally spaced around the $\pi/2$-Mode. In the presence of a "perturbation" (small asymmetry in the chain of resonators), the new ("perturbed") field will be a linear combination of all modes in the dispersion curve, but modes from the upper and lower branches of the dispersion curve will give equal contributions with opposite sign, thus cancelling out in accelerating cells [104].

In practice, the tuning is done by iteratively machining a tuning ring inside each accelerating cell until a value slightly lower than the accelerating mode frequency has been achieved. The next step is to create a full cavity assembly from stacked accelerating and coupling cells and a second fine tuning is performed first on the coupling cells (by squeezing or expanding the cell across the noses) and then on the accelerating cavities (by deforming the wall of each cell at special pre-designed thinned areas on the side of the cell). Additional mechanical tuners are also used and during operation, temperature controlled tuning can also be employed. At SNS, a field flatness of $\pm 0.4\%$ inside a single cavity can be achieved, well within the beam dynamics requirement of $\pm 1\%$ [109].

Regarding the RF errors, as with the previous structures, a 1 degree error in phase and a 1% amplitude error at the klystron level is considered to be acceptable for both the Linac4 and SNS CCLs.

4.7 The Annular-ring Coupled Structure - ACS

One alternative to the CCL cavity is the annular-ring coupled structure. Like the CCL, the ACS also operates in the $\pi/2$-Mode with a 90 degrees phase difference between neighbouring cells, so from an RF point of view the two structure types have many similarities. Comparable technologies can be employed for manufacture as well as operation. The main difference consists in the way the coupling cell is implemented. In a CCL, off-axis coupling cells are used (see Figure 4.17) with a single coupling slot between each accelerating and coupling cell.

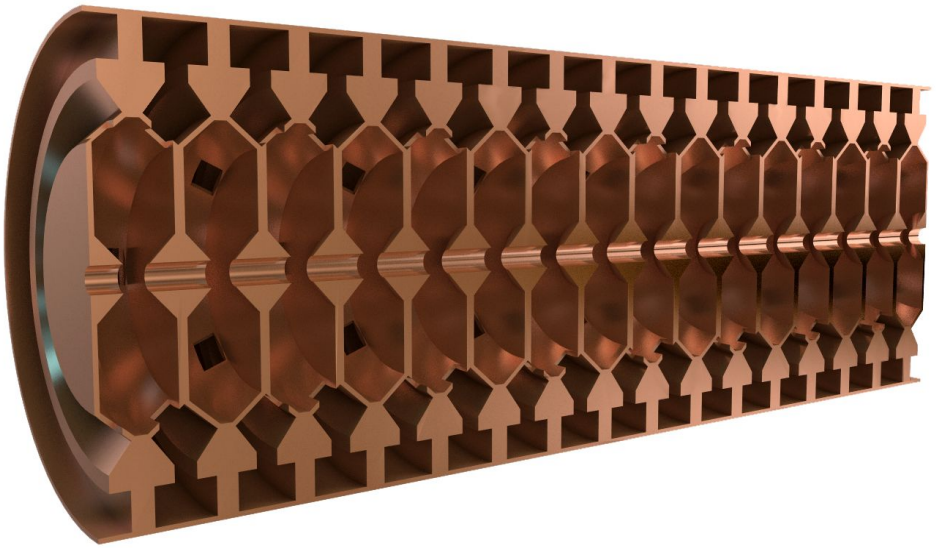

Figure 4.20: Schematic 3D layout of an ACS cavity.

In an ACS, the coupling cell geometry is annular with a rotational symmetry around the beam axis. This is illustrated in Figure 4.20. The cell length is maintained at $\beta\lambda/2$ as in a CCL and the coupling cells do not take any additional beamline space. The main advantage of an ACS comes from the coupling cell design. Although more elaborate, the ACL coupling cell is connected to the accelerating cell via four symmetrically located coupling slots. As a result, the weak dipole mode that is normally present in a CCL due to the asymmetrical positioning of the coupling cells, is absent here. Differences in the coupling cell design have led to alternative $\pi/2$-Mode cavities like the on-axis coupled structure or the disk-and-washer structure. The ACS was first developed in Japan and its performance in the J-PARC linac will be briefly analysed in this section [110].

4.7.1 ACS RF Properties

An ACS linac has been recently commissioned at J-PARC as part of a staged power upgrade. It accelerates the beam from 190.8 to 400 MeV with the design beam energy achieved in early 2014. The operating frequency is 972 MHz, a three-fold increase from the upstream structures (DTL and SDTL). The optimisation process is in many ways similar with the procedure described for other structures and it aims at arriving at an efficient geometry that can be built and cooled with relative ease.

	J-PARC ACS
Input Energy (MeV)	190.8
Output Energy (MeV)	400
Peak Dissipated Power (MW)*	33.4
E_0 (MV/m)	4.26
ϕ_s (deg)	-30
Kilpatrick Factor	0.85
Frequency (MHz)	972
Real Estate Gradient (MV/m)	1.9
RF Power/Energy Gain (kW/MeV)	160
ZTT (MOhm/m)*	29 - 36
Total Length (m)	110

Table 4.17: RF Properties of the J-PARC ACS.
* - these values include a 20% reduction in shunt impedance and a corresponding increase in power dissipation.

The design is relatively conservative with a Kilpatrick factor of 0.85, an accelerating field gradient of 4.26 MV/m and a synchronous phase of -30 degrees. The ACS cells are grouped together to form a single tank. Each tank contains 15 accelerating cells, 14 coupling cells and two additional end-coupling cells. Two tanks are coupled via a bridge coupler to form a single module. The bridge coupler also operates in the $\pi/2$-Mode and is a disk-loaded structure with nine cells (five exciting cells and four coupling cells). Every module is powered by a single 2.5 MW klystron through an RF window located on the bridge coupler [111].

The separation between the accelerating tanks is $4.5\beta\lambda$, which means the real estate gradient is reduced to 1.9 MV/m. To reach the final energy a total of 21 modules are being used. Two additional ACS modules have been built to be used as debunchers. Two ACS buncher modules have also been added at the transition between the SDTL and ACS. The bunchers have a similar geometry but fewer cells. Table 4.17 presents a summary with the RF properties of the J-PARC ACS.

The effective shunt impedance per unit length is shown in Figure 4.21. The ascending trend specific for $\pi/2$ cavities is also seen here. As with the previous structures, no additional heat loss corrections were included at this stage.

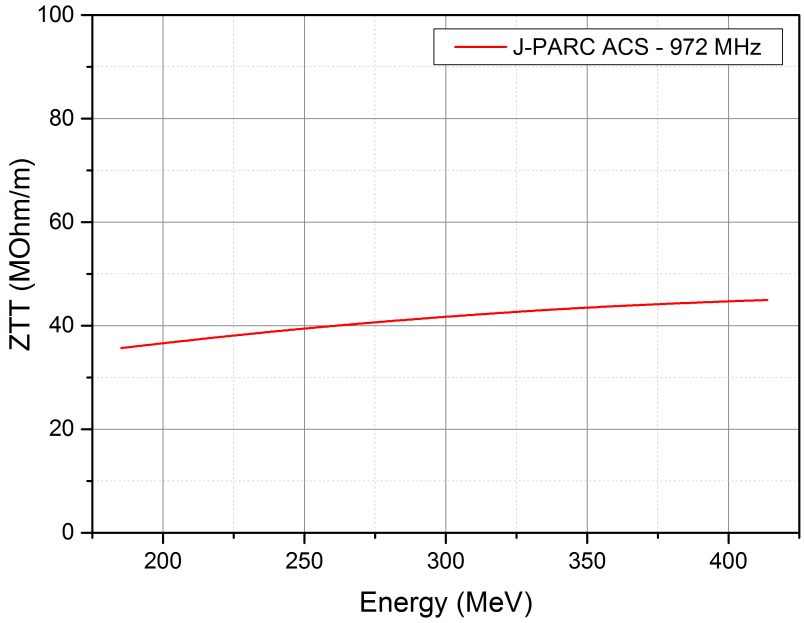

Figure 4.21: Effective shunt impedance per unit length vs. energy in the J-PARC ACS.

4.7.2 ACS Beam Dynamics

The beam dynamics in the ACS section follows the same philosophy as the rest of the J-PARC linac adopting an equipartitioned design and a FODO lattice. For transverse focussing a quadrupole doublet is placed in the space between tanks. To facilitate matching into the ACS over a triple frequency jump, the J-PARC linac includes a 15 m long transport line. Longitudinal matching is achieved using two ACS type buncher modules while transverse matching is done using 12 quadrupoles. As the focussing period is different in the SDTL and ACS, the matching sections ensure a smooth transition without any abrupt changes in phase advance. The adopting of a matching section between structures, although more costly, has the advantage of allowing a variety of operating conditions in terms of emittance and beam current [112].

To test the lattice, the same approach described previously was also used here, with three beam distributions tracked. The results can be seen in Table 4.18 with no unusually large increases in RMS emittance or beam loss.

Structure	Distribution	Input Emittance (Norm. RMS) $\epsilon_{x,y}$ - π.mm.mrad ϵ_z - π.deg.MeV	Emittance Growth(%)	Transmission (%)
J-PARC ACS	Distribution 1 (0 mA)	ϵ_x=0.25	0	100
		ϵ_y=0.25	0	
		ϵ_z=0.1	0	
	Distribution 2 (30 mA)	ϵ_x=0.25	5.7	100
		ϵ_y=0.25	7.2	
		ϵ_z=0.10	1.5	
	Distribution 3 (30 mA SDTL)	ϵ_x=0.26	6.9	100
		ϵ_y=0.25	8.3	
		ϵ_z=0.11	4.5	

Table 4.18: Emittance growth and beam transmission in the J-PARC ACS.

4.7.3 ACS Technologies

As in the CCL case, tighter manufacturing tolerances given by the higher frequency have to be attained. The geometry has been optimised to facilitate this without compromising the efficiency and complicating the cooling design. The cell length is kept constant within a single tank, as are other cavity parameters. A small increase in shunt impedance can be obtained by individually optimising every single cell and by tolerating a higher Kilpatrick factor, but the gain does not justify the complexity increase. To test the required technologies and construction choices, cold models and hot prototypes are an essential part of the fabrication process.

The manufacturing process itself implies the construction of modules made of half the accelerating cell, half the coupling cell, vacuum and coupling ports, cooling channels, etc. These modules are then stacked together to form a single tank, so maintaining a constant geometry is advantageous. Oxygen-Free Copper (OFC) is forged into blocks with approximately the right profile and rough machined to the required shape. All blocks are then heat treated to remove internal stress before precise machining is applied. This is an important step to obtain an accurate finish. Further, the coupling slots, the cooling channels and the additional ports are machined with a milling machine and finally each cell is finished with a super-precision machine tool. Silver-alloy brazing is then used to form a single tank from the half-cell pieces. For the bridge coupler, brazing with a gold-alloy is used [113].

4.7.4 ACS Tuning and Sensitivity to RF Errors

Compared with the CCL structure, the tuning procedure of an ACS is more difficult. This is because in an ACS, the accelerating cell is completely surrounded by the coupling cell and therefore applying a CCL specific tuning method like structure deformation from the outside is not possible and a different approach is taken.

The target frequency is 972 MHz ±100 kHz and a field flatness of 1%, although tracking studies indicate that a 5% flatness is still acceptable. For reference, a ±100 kHz frequency target corresponds to a machine accuracy of ±7 μm. As the brazing process alters the frequency considerably, substantial effort was put into quantifying this frequency change and ensuring the results are reproducible. For the accelerating cell, it will increase the frequency by 0.1 MHz, while for the coupling cell by 0.7 MHz and therefore during machining and before brazing a lower resonant frequency is sought.

To arrive within 100 kHz of the target frequency before brazing, an iterative process is employed in which the frequency of each cell is measured and if it is outside the acceptable range, tuning bumps present in each cell will be cut with a high precision machine tool. For the accelerating mode, this is the only frequency tuning needed. During operation, a total of five movable plungers in the multi-cell bridge cavity are available with a tuning range of ±0.5 MHz to provide a fast frequency tuning while avoiding mode mixing problems.

The structure sensitivity to RF errors is similar with other structures, with a 1% error in phase and a 1 degree error in amplitude acceptable from a beam dynamics point of view [114], [74].

4.8 The CERN Pi-Mode Structure - PIMS

As already mentioned, for the Linac4 project at CERN the CCL cavity type was initially foreseen to be used for the high energy section. This idea however has been abandoned and the Pi-Mode Structure (PIMS) was adopted instead. The PIMS is an axisymmetric structure and as the name suggests, it operates in the π-Mode. Each cavity is made of multiple identical cells with off-axis coupling holes. Although a structure of this type is in

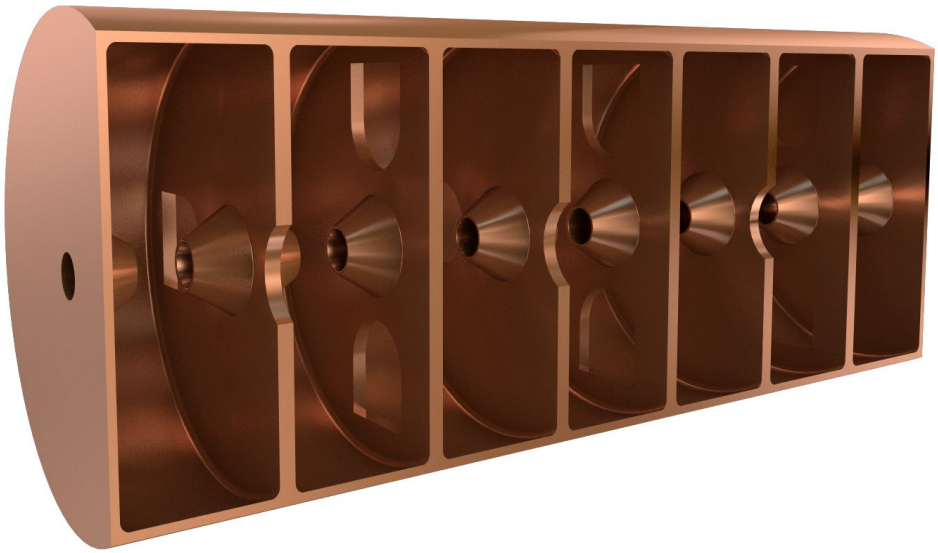

Figure 4.22: Schematic 3D layout of a PIMS cavity.

general less efficient than a $\pi/2$-Mode structure over the same energy range, for Linac4 it has the advantage that it allows the operation of the linac at only one frequency (no frequency jump necessary). Its simple design and ease of manufacturing is expected to reduce the overall cost of the linac. The PIMS is based on CERN expertise from the Large Electron-Position Collider (LEP) and makes use of all mechanical solutions developed for the LEP cavities [115]. A 3D drawing illustrating the geometry of a PIMS cavity can be seen in Figure 4.22.

4.8.1 PIMS RF Properties

Twelve PIMS cavities are needed in Linac4 to accelerate from 102 to 160 MeV. Each cavity has seven cells (84 in total) operating at 352.2 MHz. This is an advantage compared to the previous design employing the CCL structure, which was projected to use a total of 220 accelerating cells grouped in 20 tanks and operating at 704.4 MHz to accelerate beam from 90 to 160 MeV. The basic PIMS design is a scaled version of the normal conducting LEP accelerating structure modified for medium β operation and higher cell to cell coupling.

The accelerating gradient in the first 10 cavities has been adjusted to a relatively high value of 4 MV/m, resulting in a maximum power of $\sim$1 MW per cavity. The Kilpatrick factor is also higher at 1.8. Using a high gradient limits the number of cells per cavity to

	Linac4 PIMS
Input Energy (MeV)	102
Output Energy (MeV)	160
Peak Dissipated Power (MW)*	9
E_0 (MV/m)	4.0
ϕ_s (deg)	-20
Kilpatrick Factor	1.8
Frequency (MHz)	352.21
Real Estate Gradient (MV/m)	2.6
RF Power/Energy Gain (kW/MeV)	155
ZTT (MOhm/m)*	27 - 30
Total Length (m)	22

Table 4.19: RF Properties of the Linac4 PIMS.
* - these values include a 30% reduction in shunt impedance and a corresponding increase in power dissipation.

7 and makes it easier to obtain a flat field distribution. The last 2 cavities are used not only for acceleration but also for energy painting for injection into the subsequent Proton Synchrotron Booster (PSB). In order to achieve a high ramping speed in these cavities, the nominal accelerating gradient was lowered to 3.1 MV/m [116]. The basic design was made with Superfish and the 3D calculations to determine the coupling coefficients, shunt impedance degradation (due to coupling, tuners, etc), and end-cell tuning were made with GdfidL [117]. An overview of the main PIMS parameters is given in Table 4.19.

In addition to these standard calculations, the Linac4 team also investigated the effect on shunt impedance of operating at a much higher duty cycle (SPL injection). Since thicker walls are needed to accommodate suitable cooling channels, the efficiency of the structure is reduced. The decrease in shunt impedance is of the order of 10-15% depending on energy.

After the geometry of the basic PIMS cell had been optimised, an extensive set of shunt impedance simulations was performed, investigating the effects that generate additional heat losses. These effects, including the surface roughness, wave-guide coupler, e-beam welding groove, tuning rings and tuners, coupling slots and safety margins, account for a $\sim$30% reduction in shunt impedance. This is significantly higher than the scaling used for the other structures, which take into account only 20% additional losses [116]. The effective shunt impedance per unit length can be seen in Figure 4.23.

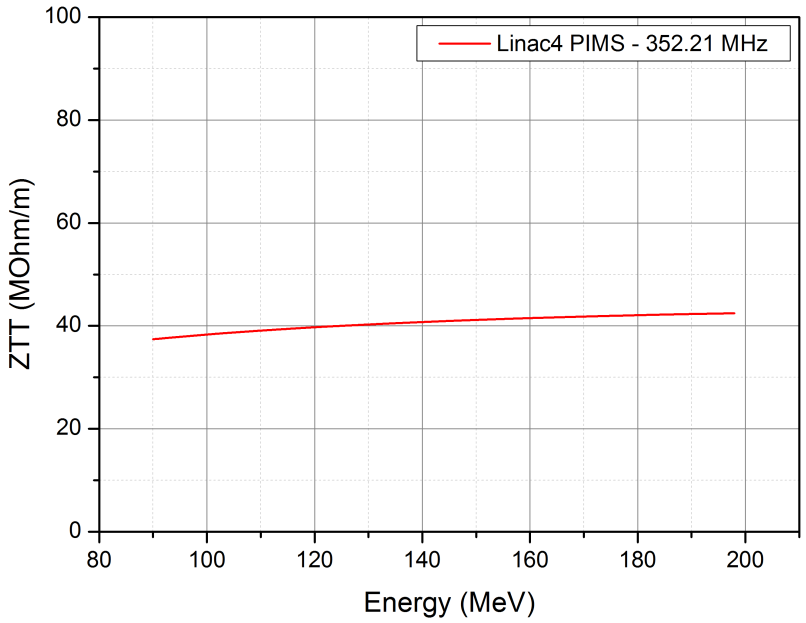

Figure 4.23: Effective shunt impedance per unit length vs. energy in the Linac4 PIMS.

4.8.2 PIMS Beam Dynamics

The equipartitioning condition established in the DTL is also maintained in the PIMS section. A FODO lattice is used and the synchronous phase is kept at -20 degrees. A total of 12 EM quadrupoles placed between the tanks are used for transverse focussing. The distance between quadrupoles is $5\beta\lambda$. The particular cell arrangement make the PIMS focussing period ∼30% longer than the CCL alternative initially proposed at CERN for the same en-

Structure	Distribution	Input Emittance (Norm. RMS) $\epsilon_{x,y}$ - π.mm.mrad ϵ_z - π.deg.MeV	Emittance Growth(%)	Transmission (%)
Linac4 PIMS	Distribution 1 (0 mA)	ϵ_x=0.30	0	100
		ϵ_y=0.30	0	
		ϵ_z=0.18	0	
	Distribution 2 (65 mA)	ϵ_x=0.30	9.3	100
		ϵ_y=0.30	8.6	
		ϵ_z=0.18	7.0	
	Distribution 3 (65 mA CCDTL)	ϵ_x=0.35	4.9	100
		ϵ_y=0.33	2.2	
		ϵ_z=0.18	2.7	

Table 4.20: Emittance growth and beam transmission in the Linac4 PIMS section.

ergy range, resulting in a larger beam size. This is however compensated by increasing the aperture of the PIMS modules.

Transverse matching between the CCDTL and the PIMS is achieved using several quadrupoles at transition, while maintaining a smooth phase advance. Owing to the elimination of the frequency jump, longitudinal matching becomes much easier. This was tested using the same criteria applied for the previous structures with tracking using three beam distributions. The results can be seen in Table 4.20 [118].

4.8.3 PIMS Technologies

The PIMS structure consists of discs and cylinders that are machined out of pre-shaped solid OFE copper blocks. About 40% less copper is needed for the PIMS with respect to the CCL for approximately the same energy range. The following procedure is used. Cooling channels are drilled from the outside into the discs so that any brazing or welding between vacuum and water can be avoided, thus preventing any risk of water leaking into the vacuum of the cavity. All copper ports including the RF, tuner and vacuum ports are electron-beam welded onto the cylinders. Seven cells were clamped together to form a cavity on which low level RF tests are being performed. The cavity is then reopened and the tuning rings are being machined. The procedure is repeated several times until the desired resonant frequency is reached and then the complete cavity is electron-beam welded.

The cells were coupled by two coupling slots, which are turned by 90 degrees from cell to cell to minimise the second neighbour coupling. The geometry of the coupling slots was analysed by means of 2D and 3D EM modelling so that the optimum coupling coefficient is achieved, the efficiency is maximised and losses are reduced. Three 3-cell and one 7-cell cold models have been built and measured at CERN in order to understand the simulation results and to verify the construction steps. This has confirmed that the overall design and the manufacture procedure is much simpler than for the CCL and has validated the structure choice. The following stage involved the commissioning of a high power prototype of a complete 7-cell PIMS module. Its successful delivery and tests allowed the complete module production to proceed and at the time of writing this is in an advanced construction

phase awaiting installation in the Linac4 tunnel [116], [119], [120].

4.8.4 PIMS Tuning and Sensitivity to RF Errors

The frequency tuning of the structure is done in two stages. Before the joining of the discs and cylinders, the machined cells are clamped together and the cell frequencies are measured. Deviations are then corrected in one or several steps by re-machining the tuning rings, taking into account the expected frequency shifts due to vacuum, welding, heating, etc. The tuning rings are divided in two sections of 90 degrees to avoid field disturbances in the coupling region and are expected to provide a rough tuning range between -1.5 and +1.0 MHz. A second, more accurate tuning is done using piston tuners placed in each cell. A fully penetrated tuner will increase the cell's frequency by 1 MHz. Tuners in cells 2 and 6 in the 7-cell PIMS module will be motorized to allow an active control of the resonant frequency and the field tilt, while all the other cells have fixed tuners, which are cut to length after the assembly of the complete cavities.

The aim is to achieve a range of ±25 kHz for the RF tuning, but even with a ±50 kHz range, a ±2.5% field flatness can be achieved. Beam dynamics simulations indicate that a ±5% field stability is acceptable [116].

The sensitivity to klystron errors has been analysed as already described for the previous structures. The simulations confirm that klystron phase and amplitude should ideally be controlled to 0.5% and 0.5 degree to limit energy and phase jitter, but values of 1% and 1 degree are still acceptable. However, this is a hard limit as for successful energy painting at injection into the PSB, the energy jitter must be well controlled [86].

4.9 Comparative Assessment

This chapter individually described seven different linac RF structures currently employed or proposed for proton linac projects worldwide. The original idea of this work was to investigate not simply the RF properties of these structures, or their RF efficiency, but other design and construction aspects like the effect on beam dynamics, the technologies needed for production and assembly, the tuning approach necessary and the sensitivity to RF errors. For

a better understanding of their relative performance, a comparative assessment is necessary and valuable.

4.9.1 RF Properties

Throughout this chapter, RF properties were presented and examined for each individual cavity. They echo different design philosophies and construction choices. The mixture of all these cavity features is eventually reflected in the energy gain profile of the machines where the structures are employed. This is shown in Figure 4.24 where six separate plots with the same scale can be seen for the ESS Linac (Normal Conducting Section), FAIR Proton Linac, J-PARC Linac, Linac4, RAL Linac (Normal Conducting Section) and SNS Linac (Normal Conducting Section). The curves have been obtained from beam tracking simulations of each individual linac. These profiles show not only the structure choice at each acceleration stage, but allow the estimation of an overall machine accelerating gradient. It is also interesting to note that every design choice can eventually influence how quickly the acceleration takes place, but also how similar the acceleration curves appear for machines using the same structures (i.e. DTLs). For instance, the relatively conservative design adopted for the RAL linac (low Kilpatrick Factor, low accelerating gradient) leads to a machine that needs more length to reach the same energy, which eventually equates with a safer but more costly design.

One of the most representative outcomes of this study is the production of a comparative assessment of the effective shunt impedance per unit length for each individual structure. This is shown in Figure 4.25. There are five DTLs (ESS, J-PARC, Linac4, RAL, SNS - tones of red), one SDTL (J-PARC), one CCDTL (Linac4), one CH-DTL (FAIR), one PIMS (Linac4), one ACS (J-PARC) and three CCLs (Linac4, RAL, SNS - tones of blue). The CH-DTL has the highest effective shunt impedance at energies up to $\sim$30 MeV when it becomes comparable with the DTL. Of the five DTLs analysed, the ESS design has the highest shunt impedance, while J-PARC the lowest. The difference can be explained by several factors. J-PARC uses EMQs, which are bulkier and leave very little room to optimise the geometry for efficiency, while for ESS, the introduction of PMQs allow an individual optimisation of every single cell. Frequency also plays a role. ZTT is expected to scale with the square

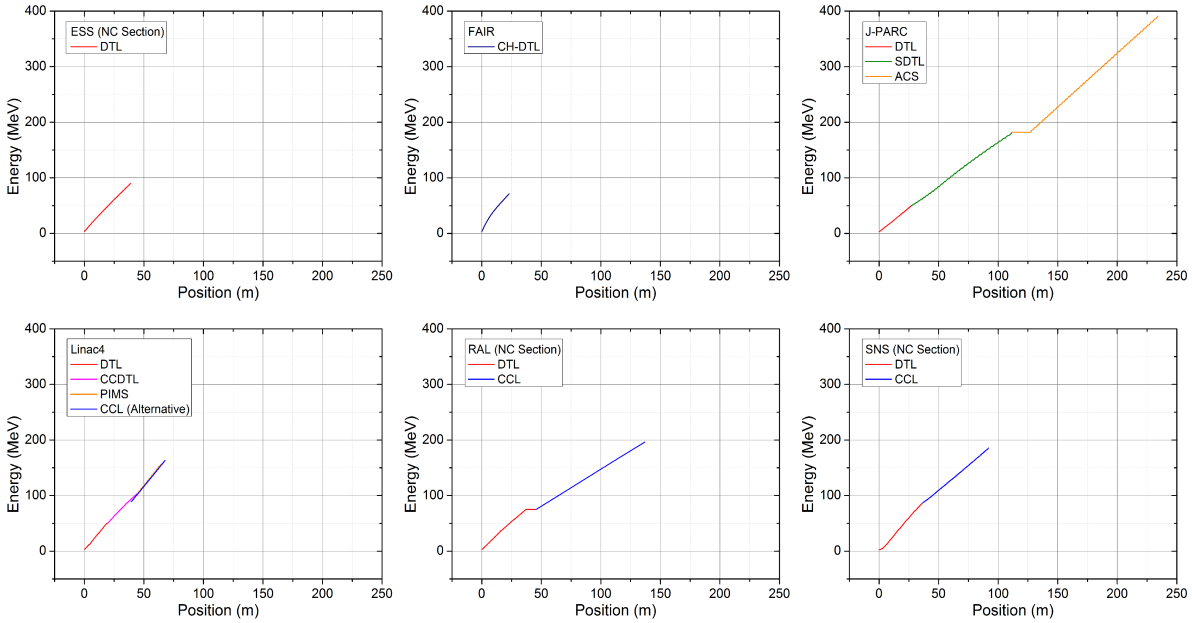

Figure 4.24: Energy gain profile in the RF structures examined above: ESS Linac (Normal Conducting Section), FAIR Proton Linac, J-PARC Linac, Linac4, RAL Linac (Normal Conducting Section) and SNS Linac (Normal Conducting Section).

root of the frequency, so a doubling in frequency should lead to a ∼40% increase in shunt impedance when the entire geometry is scaled proportionally. However, as already discussed in the DTL section, the scaling law is not entirely preserved, as several parameters remain relatively constant independent of frequency (i.e. the bore radius is kept approximately the same for most structures under study to avoid beam loss). Therefore any apparent frequency dependence should be taken cautiously as there are usually a number of other factors at play. For intermediate energies, alternative structures like the CCDTL or the SDTL are good options, but with efficiencies comparable to the DTL. The advantage of adopting these structures consists however in a much simplified construction compared to the DTL. And finally, for higher energies, the switch to cavities that have an effective shunt impedance that increases with energy is imperative (CCL, ACS, PIMS), as the efficiency of 0-Mode structures decreases dramatically. However, the increase of ZTT with energy is relatively slow and for high energy linac projects, this plot is a good reference point in deciding if and at what stage superconducting technology should be adopted.

The curves in Figure 4.25 have been obtained directly from 2D and 3D EM simulations. In reality however, the shunt impedance values have to be scaled to take into account addi-

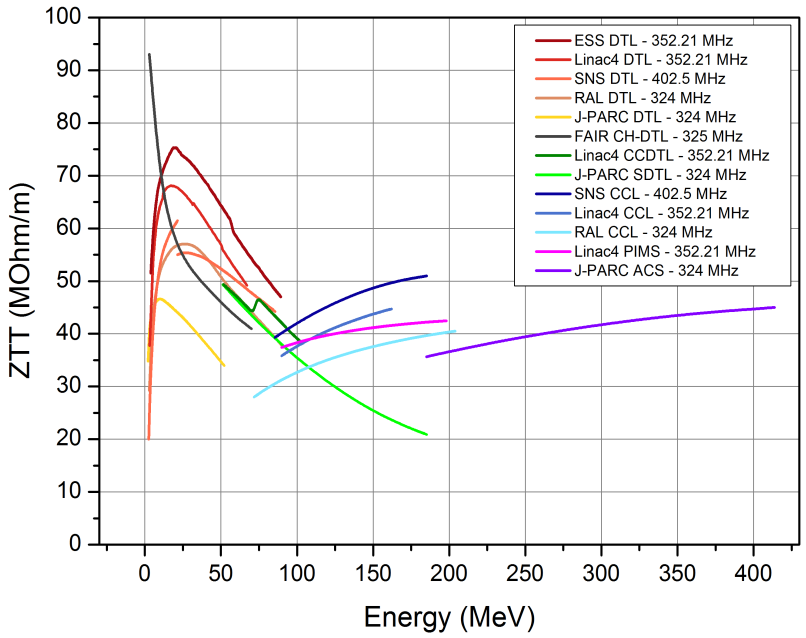

Figure 4.25: Effective shunt impedance per unit length vs. energy for the DTL, SDTL, CCDTL CH-DTL, CCL, PIMS and ACS linac RF structures as employed in the ESS, FAIR, J-PARC, Linac4, RAL and SNS linacs.

tional losses that are normally not captured by simulations. These losses include the surface roughness, imperfections, tuners, coupling slots, ancillary equipment, etc. Scaling factors are normally obtained for each structure from experience operating the machines (i.e. DTL, CCL), or from direct measurements on hot models. Figure 4.26 shows the effective shunt impedance per unit length for each structure analysed where each value has been scaled accordingly.

In Figure 4.27, a comparison between the maximum accelerating gradient and the real estate gradient is presented for all the structures investigated. For the DTL, the real estate gradients of the five examples are comparable, with an average of about ∼2.1 MV/m. In the same way, the ratios of maximum gradient to real estate gradient are also comparable. This is explained by the similarity of the designs. Due to their nature (long structures, integrated quadrupoles), the DTLs have the smallest drop in accelerating gradient (from maximum to real estate). For the other structures, as the transverse focussing elements have to be placed outside the cavities, the drop is more significant, as beam line space has to be made available between the RF structures. Also notable in this plot is the CH-DTL structure which has the highest real estate gradient, made possible as already explained by the innovative drift tube

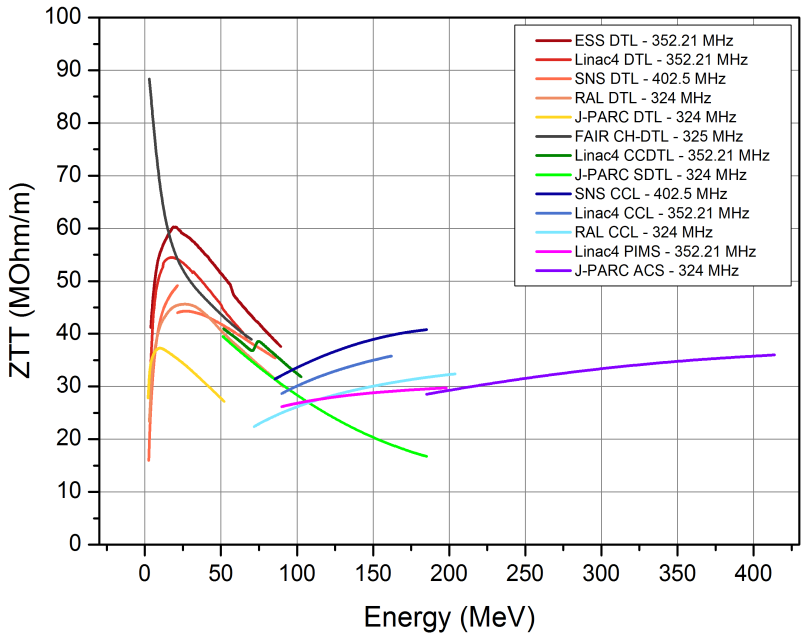

Figure 4.26: Effective shunt impedance per unit length vs. energy for the DTL, SDTL, CCDTL CH-DTL, CCL, PIMS and ACS linac RF structures as employed in the ESS, FAIR, J-PARC, Linac4, RAL and SNS linacs. Calculated ZTT values have been scaled down to take into account additional losses. The following factors have been used:
DTL - a 20% reduction which does not include the contribution of the post-couplers.
SDTL - a 20% reduction.
CH-DTL - simulations in good agreement with measurements. A 5% reduction has been used.
CCDTL - a 17% reduction.
CCL - a 20% reduction.
PIMS - a 30% reduction.
ACS - a 20% reduction.

design. At 2.91 MV/m, this value however is only ∼25% higher than the average of the five DTLs. This illustrates the limit in accelerating gradients achievable in normal conducting structures. The average real estate gradient for all the structures under study is 2.1 MV/m.

Figure 4.28 presents a summary of the Kilpatrick factors for each structure. With the exception of the RAL CCL and J-PARC ACS, where a more conservative design approach was adopted throughout, all the other structures break the Kilpatrick criterion. This is expected and is mostly due to technological progress that has made possible the delivery of surface finishes that can push the breakdown limits. For the cases investigated here, the CH-DTL has the highest Kilpatrick at 2 and is normally considered an upper limit. The average for all the structures is ∼1.4.

Finally, the RF power over energy gain factor is presented in Figure 4.29 and is essentially

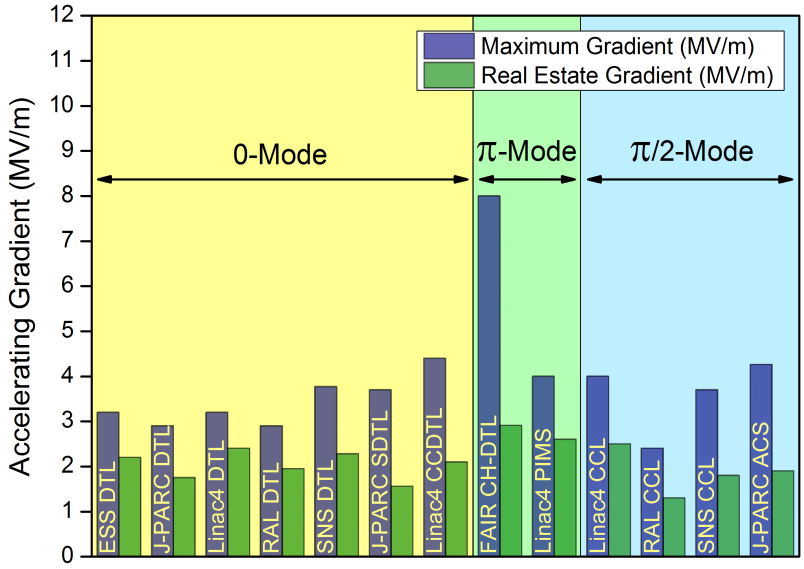

Figure 4.27: Maximum and Real Estate Accelerating Gradient in the DTL, SDTL, CCDTL, CH-DTL, PIMS, CCL and ACS cavities adopted for the ESS, FAIR, Linac4, J-PARC, RAL and SNS linacs.

a measure of the cost of acceleration assuming all structures have already been built and the machines commissioned. This is an important result and reveals several features of normal conducting acceleration. First, the "cost" of employing normal conducting cavities increases with energy, which leads back to the question of finding the correct transition to superconducting structures. Secondly, at low to intermediate energies the DTL remains the

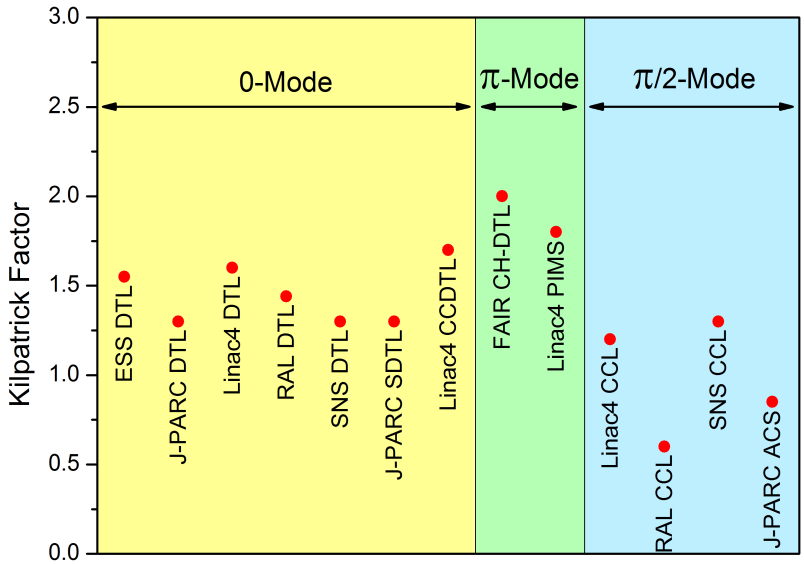

Figure 4.28: The Kilpatrick Factor in the DTL, SDTL, CCDTL, CH-DTL, PIMS, CCL and ACS cavities adopted for the ESS, FAIR, Linac4, J-PARC, RAL and SNS linacs.

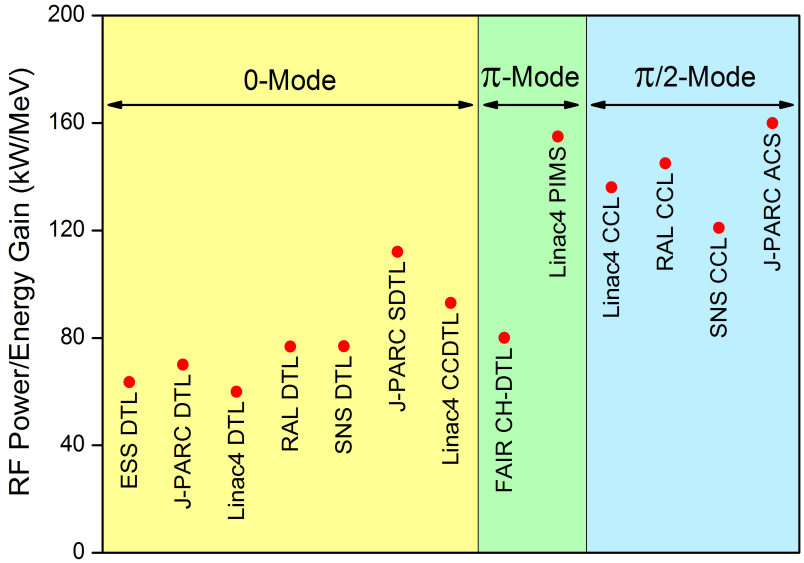

Figure 4.29: The RF Power over Energy Gain in the DTL, SDTL, CCDTL, CH-DTL, PIMS, CCL and ACS cavities adopted for the ESS, FAIR, Linac4, J-PARC, RAL and SNS linacs.

most suitable structure, with an RF power over energy gain factor somehow comparable to that of the more efficient CH-DTL. This might seem surprising, but can be explained when considering that these values are averages over the entire accelerating range of each structure. Lastly, the benefits of intermediate energy structures like the SDTL and the CCDTL do not include higher efficiencies but easier development and manufacturing.

4.9.2 Beam Dynamics

On the beam dynamics side, the six linacs investigated have adopted different philosophies and this part of the study was important in order to understand the behaviour of these RF cavities when employed in different lattices, with different phase advances and in machines that choose to implement or avoid equipartitioning. The study has followed the CERN approach of modelling Linac4 in which each accelerating section was tested with three input beam distributions: Gaussian distribution generated at the beginning (with and without space-charge) and a distribution tracked through the previous section. With the exception of the FAIR linac where a machine model was not available, this test was applied on all the other machines as part of this study and was also repeated on Linac4 to have a consistent simulation framework.

For each structure, these tests reveal solid beam dynamics designs with RMS emittance growths below 10% for most sections in each machine, both transversely and longitudinally and a 100% transmission. To gain some perspective on these values, it is interesting to mention that a measurement looking for a 10% emittance increase is already relatively difficult. For the CH-DTL however, although no beam losses are recorded, simulations performed at Frankfurt University, indicate an RMS emittance growth of ∼60% both transversely and longitudinally. This can be explained if we consider the configuration of the FAIR Proton Linac. CH-DTL modules are used for acceleration with focussing elements placed between them. At low energies, strong and uniform focussing is normally required to counter the high space-charge forces, but due to the very nature of the CH-DTL, the focussing period is much longer leading to a larger beam size. This might be acceptable if a CH-DTL linac is used as a single injector, but careful consideration must be undertaken if this is the first stage of a higher energy linac employing different cavity types as beam degradation at low energies can lead to emittance growth and halo development further downstream.

Another outcome of the beam dynamics analysis is a series of design rules that have generally been applied in the machines studied:

- Every effort should be put into achieving a good matching both at the beginning and at transition between structures. This is normally done transversely by varying the currents in several dedicated quadrupoles and longitudinally by varying the phase and amplitude in transition cavities.
- A smooth and continuous phase advance and a regular lattice are also highly desirable.
- The zero current phase advance should be below 90 degrees both transversely and longitudinally to avoid instabilities.
- To limit the halo development the tune depression should be kept at reasonable values, usually above 0.5.
- Space-charge resonances should be avoided by choosing the correct phase advances.
- Beam loss has to be avoided to limit the machine activation. This should be achieved by having sufficient beam aperture without compromising the machine efficiency and

by placing lower limits on the transverse phase advance and period lengths such that the beam size is contained.

4.9.3 Technologies, Tuning and Sensitivity to RF Errors

For each individual cavity, a succinct description of the manufacturing process and the technologies involved was presented in the relevant sections. These are important consideration often overlooked by cavity designers and sometimes unwisely labelled as "engineering de-

Technologies	DTL	SDTL	CCDTL	CH-DTL	PIMS	CCL	ACS
Assembly	E-Beam Welding	E-Beam Welding	Brazing, E-Beam Welding	E-beam Welding	E-beam Welding	Brazing	Brazing
Focussing Elements	PMQ/EMQ Inside DT	EMQ External	EMQ External	EMQ External	EMQ External	EMQ External	EMQ External
Raw Cavities	Cold drawn Stainless Steel	Forged Stainless Steel	Forged Stainless Steel	Stainless Steel	Forged OFE Copper	Forged OFE Copper	Forged OFE Copper
RF Contacts	Helicoflex Seals	Helicoflex Seals	Helicoflex Seals	Helicoflex Seals	Helicoflex Seals	Brazing	Brazing
Stabilization	Post Couplers	No	Coupling Cells	No	No	Coupling Cells	Coupling Cells
Surfaces	Copper Plating, OFE Copper	Copper Plating, OFE Copper	Copper Plating, OFE Copper	Copper Plating	OFE Copper	OFE Copper	OFE Copper
Tolerances	Precise Machining, Laser Tracking	Precise Machining	Precise Machining	Precise Machining	Precise Machining	Precise Machining	Precise Machining
Tuning	Tuners	Tuners	Tuners, Drift Tube Machining	Tuners	Tuners, Tuning Ring Machining	Dinging, Tuning Ring Machining	Tuners, Tuning Bumps Machining
Vacuum Sealing	Helicoflex Gaskets	Helicoflex Gaskets	Helicoflex Gaskets	Helicoflex Gaskets	E-Beam Welding	Brazing	Brazing

Table 4.21: Summary of technologies involved in manufacturing the DTL, SDTL, CCDTL, CH-DTL, PIMS, CCL and ACS cavities.

tails". Manufacturing simplicity and available technological "know-how", are critical aspects to take into account when choosing linac cavity types. It is ultimately useless to design the perfect accelerating structure, which is incredibly difficult and absurdly expensive to build.

A summary of the technologies and tuning mechanisms needed for each cavity type is presented in Table 4.21. It allows the reader to gain an overall understanding of the processes and complexities involved. The general consensus is that the DTL production is the most complicated, mostly due to its length, the number of cells and individual parts, placement of transverse focussing elements and alignment procedures. Frequency also plays a role as higher frequency, smaller size structures demand tighter tolerances. Likewise, the duty cycle can also increase the production complexity mainly due to additional cooling constraints.

Regarding the sensitivity to RF errors, the general conclusion is that all structures can safely tolerate a $\pm 1\%$ error in amplitude and a ± 1 degree error in phase at klystron level. However, for a better control of the energy and phase jitter, the beam dynamics would benefit from a better error control, ideally ± 0.5 degrees in phase and $\pm 0.5\%$ in amplitude.

4.10 Chapter Summary

In this chapter, a comparative assessment of seven normal conducting accelerating structures was presented. The cavities are proposed or in use in six pulsed proton linacs: the ESS linac, the FAIR Proton Injector, the J-PARC Linac, Linac4 at CERN, the RAL Upgrade Linac and the SNS linac. The cavity types analysed are the DTL, SDTL, CCDTL, CH-DTL, CCL, PIMS and ACS. The operating energy range is 3 to 400 MeV and the frequencies are 324, 352.21, 402.5, 648, 704.42 and 805 MHz. The performance of each individual structure has been evaluated based on several criteria: RF properties and power efficiency, beam quality, technologies, tuning procedure and sensitivity to RF errors.

It is the first time that such a comprehensive study has been carried out. While information on each individual cavity was available from their respective home laboratories (i.e. CERN, J-PARC, etc.), the merit of this work lie in the creation of a common framework where the performance of the cavities can be analysed. This is especially true for the RF and beam dynamics analysis where electromagnetic and beam tracking models were prepared in

order to have an analogous simulation environment.

The final comparative assessment suggests that for the lower energy range (3 - 50 MeV) the DTL and CH-DTL structures are more suitable offering a high shunt impedance. However, the CH-DTL beam dynamics should be carefully analysed for each intended application. At linac energies above ∼50 MeV, alternative structures to the conventional DTL, like the SDTL and the CCDTL, can also be used, providing comparable energy efficiency, but simpler construction and alignment. Above ∼100 MeV the shunt impedance of drift tube based structures starts to decrease rapidly and the only option to maintain a good acceleration efficiency is to pass from structures operating in the 0-Mode to structures operating in the π-Mode or $\pi/2$-Mode which present a shunt impedance increasing with energy like the PIMS, the CCL and the ACS. For high energy projects the suitability of superconducting technology should be assessed.

It is interesting to note that while some cavities appear to have superior characteristics, the final choice of a linac structure requires a complex analysis and depends on the particularities of each individual project. The operating frequency, the required duty cycle and beam current, the existing accelerators and infrastructure as well as the available local expertise all play an important role in the final decision. The objective of this chapter was to present an unbiased description of the work on normal conducting cavities done at different research laboratories and at RAL and to produce results that can be useful tools for future linac designers.

Chapter 5

Front End Medium Energy Beam Transport Line (MEBT) Design

This chapter tackles the problem of initial mismatch, a mjor limitation to high intensity operation. More specifically, we try to answer a simple question: "What is the optimal way of designing a MEBT line with choppers for high intensity, high power linac operation?" We start by presenting the ISIS experience which emphasises the need to avoid initial mismatch if lossless operation is a priority. Several existing modern MEBT designs are then analysed with an emphasis on the ISIS Front End Test Stand (FETS) chopper line. A novel MEBT chopper concept is then presented with a proposed implementation, as well as a beam dynamics performance review and comparison with alternative designs.

5.1 Introduction

The demand for high power beams was discussed extensively in Chapter 1 with a number of applications identified [121]. For all these high power applications lossless operation is critical and therefore high quality beams are essential. As a result, significant technical development is necessary especially at the low energy (∼3 MeV) front end.

One of the critical sections of the linac is the MEBT chopper line that matches the beam from the RFQ to the DTL. Beam dynamics in the low energy part of the linac will impact heavily on the beam evolution as it defines the initial beam characteristics and dictates the operation and reliability of downstream accelerators. In addition to this, beam chopping at high duty cycle (1 - 10%) is required to minimise beam loss and the induced radioactivity at injection into downstream circular accelerators.

The MEBT design is a particularly challenging problem and the existing or proposed MEBT lines are often a compromise between beam quality and chopping efficiency. To avoid the deterioration in beam quality, direct RFQ to DTL injection is often suggested for proton linacs that do not need chopping. This has the obvious disadvantage of limited linac tuning options and reduced beam information at low energy due to the lack of diagnostics.

The purpose of this systematic study is to offer definitive design guidelines for a high efficiency MEBT with choppers that avoid initial mismatch, emittance growth, halo development and subsequent beam loss.

5.2 The ISIS Experience

Over the past 25 years, the ISIS spallation source has been delivering neutrons to generations of scientists from all over the world, creating a key centre for physical and life sciences research at Rutherford Appleton Laboratory in the UK. The accelerator consists of a 70 MeV H^- injector, an 800 MeV synchrotron and two target stations [7]. The injector starts with an H^- ion source, followed by a three-solenoid low energy beam transport line (LEBT) and a 665 keV, four-rod RFQ operating at 202.5 MHz. A Drift Tube Linac (DTL) accelerates the beam to 70 MeV. The DTL consists of four tanks which have been recycled from previous high energy physics projects. Tanks 2 and 3 were commissioned in the 1950s for the RAL

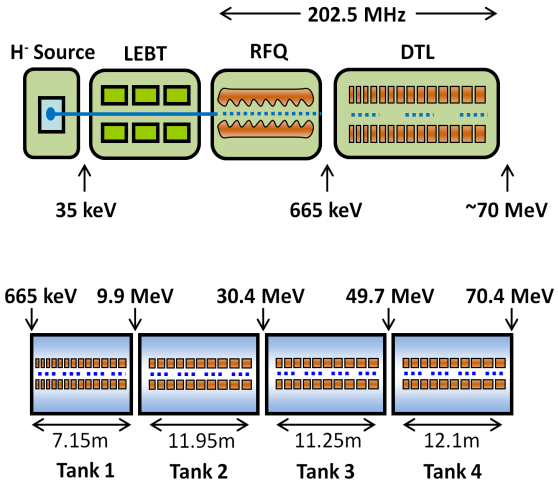

Figure 5.1: Schematic layout of the ISIS linac (top), with details of the DTL section (bottom).

Energy	70.4	MeV
Frequency	202.5	MHz
Pulse Length	200 - 250	μs
Peak Current	25	mA
Repetition Rate	50	Hz
Total Length	55	m
Duty Cycle	1 - 1.25	%

Table 5.1: ISIS linac parameters.

Proton Linear Accelerator, while tanks 1 and 4 were copies of part of the Fermilab DTL built in the 1970s, originally intended for the Nimrod accelerator, but first used in ISIS [122]. A schematic layout of the linac can be seen in Figure 5.1 and a list of parameters is given in Table 5.1.

Over the last decades, the linac has proved to be a stable and reliable injector for ISIS, which is a significant achievement considering that two of the tanks are nearly 60 years old. However, ISIS is an aging machine. Whilst the need for an upgrade to the linac has been clear for some time [28], potential improvements to the present DTL which may be achieved with little more than extended maintenance are being investigated.

At the time the machine was designed, the limited computing power available and the absence of modern modelling codes, made the creation of a complex simulation model almost impossible. Over the last few years however, computer tools have became an integral part of any accelerator design. As a result the first elaborate beam dynamics model of the ISIS linac was built. It allows comparisons to be made between the simulation results and machine operation data as well as possible linac tuning scenarios and recommended upgrades. The information gained from these models is invaluable as lessons learned can be applied at the design stage of future machines.

5.2.1 ISIS Simulation Model

There are multiple challenges in developing accurate simulation models for such an old machine like ISIS and every effort has been put into reconciling the original design data with changes implemented over the years as well as operational parameters. The baseline DTL

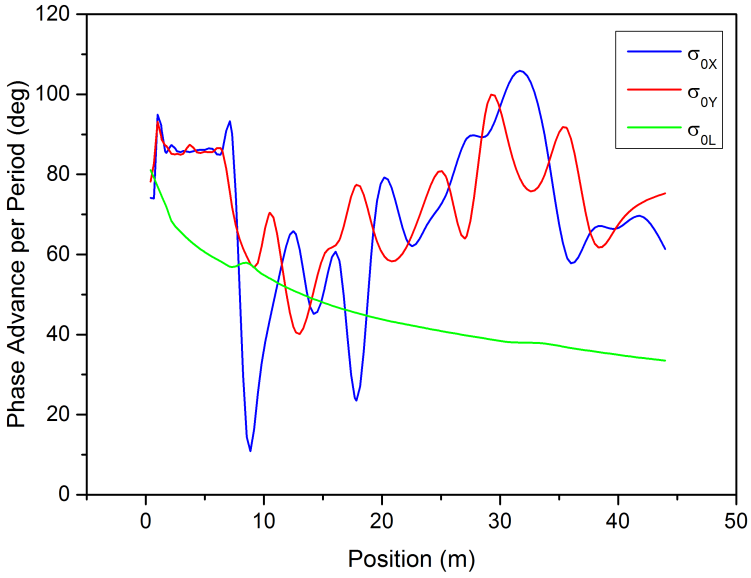

Figure 5.2: Zero current phase advance per period in the ISIS linac.

design uses an FFDD focussing scheme that is only broken at transition between tanks 1 and 2. The synchronous phase is kept constant at -30 degrees and the transverse zero current phase advance per period is generally kept below 90 degrees although it varies significantly (see Figure 5.2). The accelerating gradient is slowly ramped in tank 1 from 1.6 - 2.2 MV/m, while in tanks 2, 3 and 4 it is kept approximately constant in the region of 2.5 MV/m. A detailed DTL parameter list can be seen in Table 5.2.

To understand the linac behaviour, 2D and 3D electromagnetic models have been devel-

		Tank 1	Tank 2	Tank 3	Tank 4
Input Energy	MeV	0.665	9.90	30.4	49.7
Output Energy	MeV	9.90	30.4	49.7	70.4
Accelerating Gradient E_0	MV/m	1.6 - 2.2	2.45 - 2.55	2.3 - 2.4	2.6
Synchronous Phase	Deg	-30	-30	-30	-30
Max. Surface Electric Field	Kilp	0.67	0.81	0.84	0.87
Focussing Scheme			FFDD		
Number of Cells		56	41	27	24
Tank Diameter	cm	93.4	92.71	81.28	88
Drift Tube Diameter	cm	18	17.78	17.78	16
Aperture Diameter	cm	2.5	3.81	3.81	3
Stems/Cell		1	2	2	1
Total Length	m	7.15	11.95	11.25	12.1

Table 5.2: Main DTL parameters.

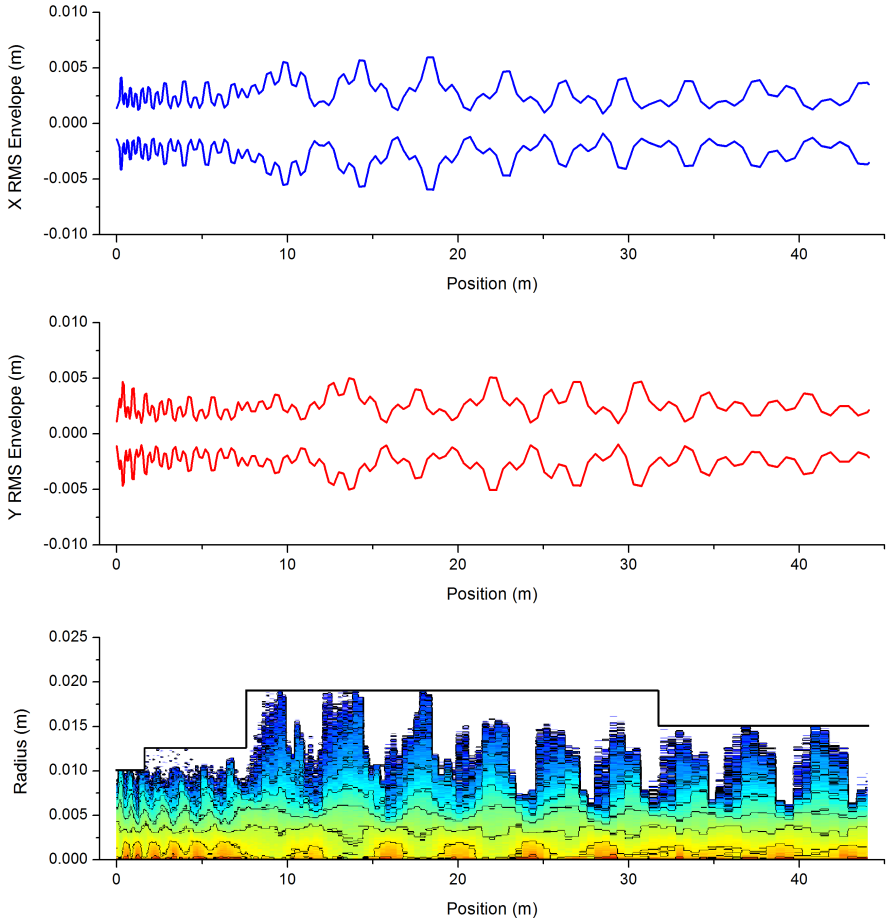

Figure 5.3: DTL transverse RMS beam envelopes and radial beam density (from TraceWin). The beam density colour scheme assumes red tones for higher density areas and blue tones for lower density.

oped for each individual accelerating cell based on the original DTL manufacturing notes [67]. This allowed the correct calculation of the transit time factors and formed the basis of a complex beam dynamics model. Several optics codes have been used for this study including GPT, Impact, Parmila, TraceWin and Trace3D [123], [124].

Figure 5.3 shows the transverse RMS beam envelopes from the RFQ output to the end of the DTL, when using the baseline lattice with a typical machine setup employed during normal operation. A waterbag distribution has been used (ϵ_x=0.5 mm.mrad (RMS normalised), α_x=0.338, β_x=0.147 mm/mrad, ϵ_y=0.55 mm.mrad, α_y=-0.295, β_y=0.0818 mm/mrad, ϵ_z=0.12 deg.MeV, α_z=0.0294, β_z=1076 deg/MeV), based on the Twiss parameters predicted by RFQSim, the simulation code used to design the ISIS RFQ [125]. A clear mismatch between the RFQ and the DTL can be seen, leading to a beam loss in excess of 15% in the first

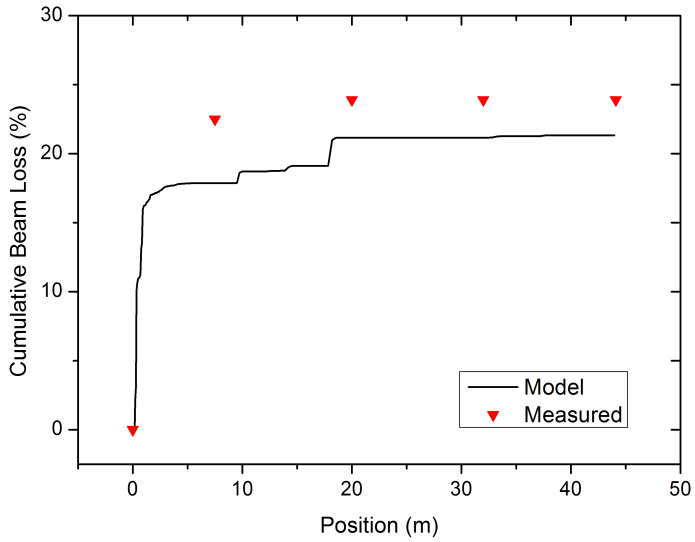

Figure 5.4: Cumulative beam loss at different positions along the ISIS linac.

metre of Tank 1. The mismatch has been expected after a new RFQ was installed to replace the old Cockroft-Walton injector. The RFQ improved dramatically the machine reliability, but it required direct injection into the existing DTL, without the possibility of adding a matching section, due to space and layout restrictions.

The losses predicted by simulation are confirmed by measurements performed at the end of each tank with current monitors, as can be seen in Figure 5.4. The small discrepancy is of course expected when considering several factors: an idealised input beam distribution has been used; there are small dimensional discrepancies in the lattice especially in the inter-tank regions that can only be resolved with a systematic dimensional metrology campaign; the measured losses can vary by as much as several percent with every new ion source or different operational settings [126].

5.2.2 Proposed RFQ to DTL matching section

While efforts have been put into re-tuning the linac by readjusting the quadrupoles, tracking studies indicate that losses cannot be lowered below 10%. To overcome this, a matching section is required between the RFQ and the DTL. A potential upgrade MEBT is useful in understanding the DTL behaviour. It differs from higher energy designs like J-PARC, Linac4 and SNS, where choppers were required and the transverse normalised emittances

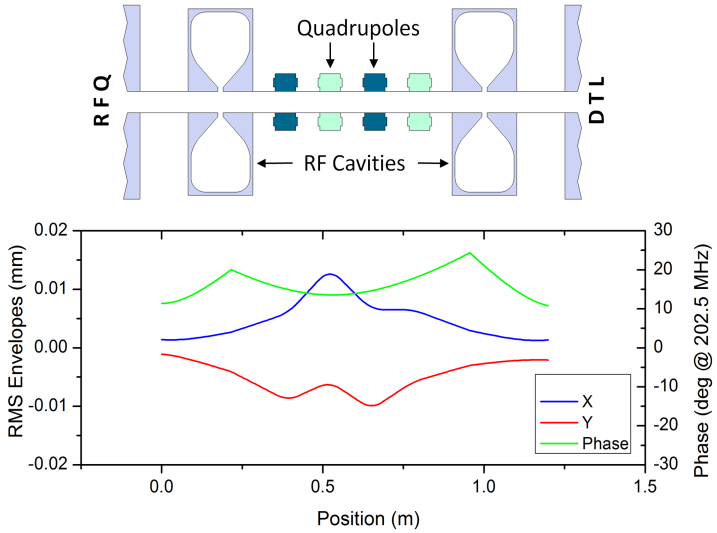

Figure 5.5: Layout of the proposed RFQ to DTL matching section (top) and the resulting transverse and longitudinal RMS envelopes along the new MEBT (bottom).

were less than half. The proposed design is ∼1.2 m long and consists of two re-bunching cavities and four quadrupoles, allowing 6D matching into the DTL. Buncher effective voltages are ∼60 kV and the quadrupole lengths are 70 mm. To avoid any MEBT beam loss, the respective quadrupole and buncher bore radii are 30 and 15 mm respectively.

The MEBT allows matching into a modified tank 1, and a match may also be made from tank 1 to tank 2, using four quadrupoles at transition. The beam does not stay matched, however, as quadrupole strengths increase and decrease along tanks 2, 3 and 4, unlike in most linac designs where the quadrupole strengths decrease smoothly with increasing energy (see phase advance plot in Figure 5.2). To mitigate this problem, a new matched lattice was found by modifying quadrupole gradients throughout the linac, to obtain a smooth phase advance variation. This has been made difficult by the fact that some quadrupoles are connected to the same power supply. Figure 5.6 shows the new transverse beam envelopes when using the same RFQ output beam, with beam amplitudes clearly smaller. Total beam loss is dramatically reduced to less than 0.5%.

It has been suggested that linacs that do not require fast beam chopping could benefit from direct RFQ to DTL injection as the MEBT can severely break the lattice periodicity with possible emittance growth effects. While this is true, the ISIS experience indicates that care has to be taken to avoid mismatch at transition between the RFQ and the DTL. With

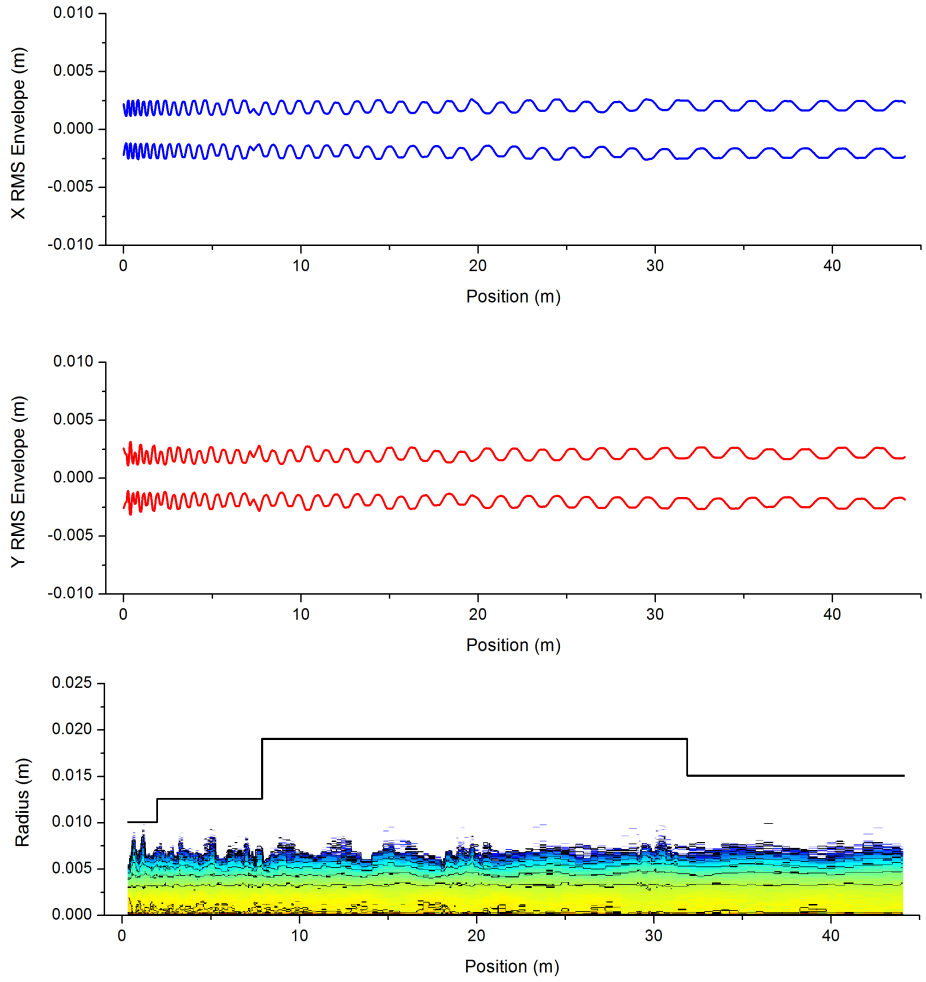

Figure 5.6: DTL transverse RMS beam envelopes (horizontal (top) and vertical (middle)) and radial beam density (bottom) with a new RFQ to DTL matching section. Density scale as in Figure 5.3.

most modern linac designs using permanent magnet quadrupoles and in the absence of a MEBT, a potential RFQ to DTL mismatch would be very difficult to correct [127].

The latest ISIS tracking studies correctly predict and explain beam losses along the linac, indicating that an increase in beam current of 25 - 30 % is achievable with the new MEBT. They also highlight the necessity to match the beam to the RFQ correctly. However, the question of finding a good and versatile MEBT design remains unanswered.

5.3 MEBT Design Challenges

The main reason the MEBT is a particularly problematic segment of the low energy linac is that it has to take into account rather different and usually conflicting requirements. These requirements are dictated mainly by two factors: beam optics and beam chopping.

5.3.1 Optics Requirements

From a beam optics point of view the MEBT is a transport line, matching the beam between the RFQ and the following accelerating structure, usually a DTL. At several MeV, the beam energy is sufficiently low for the space-charge forces to have a considerable impact on the beam dynamics. This is especially true for several forthcoming linacs in which the requirement for higher beam power has also increased the beam current, driving the operating point towards a space-charge dominated regime. This is illustrated in Equation 5.1 and Figure 5.7

$$K = \frac{Iq}{4\pi\epsilon_0 m_0 c^3} \frac{2}{\beta^3\gamma^3}\,, \tag{5.1}$$

where K is the beam perveance, a dimensionless parameter defined by Lawson [128] indicating the scale of the space-charge effect on the beam [36].

To control emittance growth, linac design guidelines recommend regular lattice optics and strong focussing. Transversely, the requirement is for regular betatron oscillations amplitudes

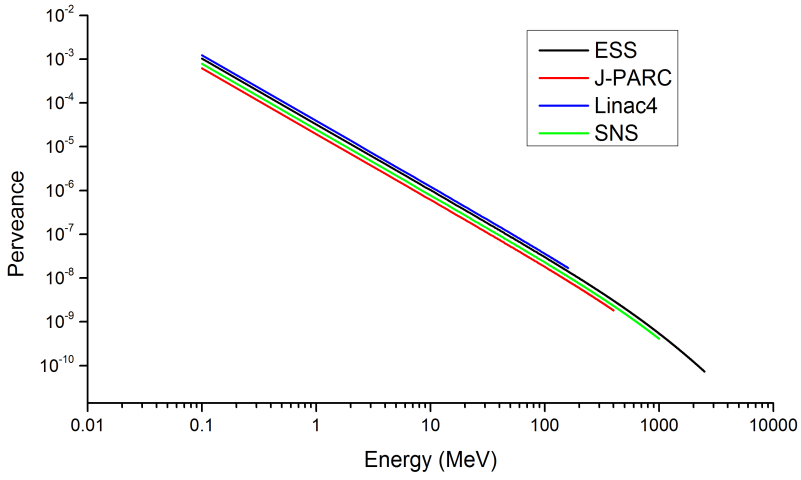

Figure 5.7: Variation of the generalised perveance K with energy for different linac projects (no space-charge neutralisation included).

as equal as possible in both planes. For a typical FODO cell this is equivalent to having a zero current phase advance below 90 degrees and it is achieved by choosing the right quadrupole gradients. A strong and uniform longitudinal focussing is also imposed, this being accomplished by adjusting the voltages in the re-bunching cavities [129], [130].

A typical beam has a non-linear transverse distribution, so a change in aspect ratio of the beam cross-section leads to a new ratio of non-linear to linear space-charge forces. Rapid, ratio changes need to be minimised, as the non-linear forces lead to emittance growth. All quadrupole focussing channels have changing beam aspect ratios and, in this respect, they are inferior to solenoid systems [131], [132]. However, if the downstream section is a DTL, a quadrupole matching section is needed in addition to the solenoid.

In addition, the MEBT has to negotiate the transition between different sections successfully, which is especially challenging. Care has to be taken to ensure a smooth transition and avoid sudden changes in the focussing strength. In a metaphoric way the beam should not notice the transition between the RFQ, MEBT and the DTL. In theory, this can be achieved by employing the same "adiabatic optics" described above in which the variation of the beta functions and thus the envelope excursion is minimised. In practice this task is made much more difficult by the fundamental nature of these different sections [133].

To illustrate this challenge, the transverse RMS beam envelopes as well as the phase advance per period in the RFQ and the first DTL tank of the ESS linac [12] are shown in Figure 5.8. The phase advance is ∼30 - 50 degrees in the RFQ and ∼80 - 60 degrees in the DTL. In the RFQ the focussing period is $\beta\lambda$ ($2\beta\lambda$ in the DTL). At 3 MeV and 352.21 MHz (ESS frequency) this is ∼68 mm. To ensure a smooth adiabatic transition, the MEBT section should ideally employ a lattice with characteristics that are not widely different from those mentioned above. However, additional MEBT constraints make this design guideline difficult to attain. As we shall see, in most modern MEBT designs much longer focussing periods have to be used, with beta functions even 10 times larger than those in the RFQ or the DTL.

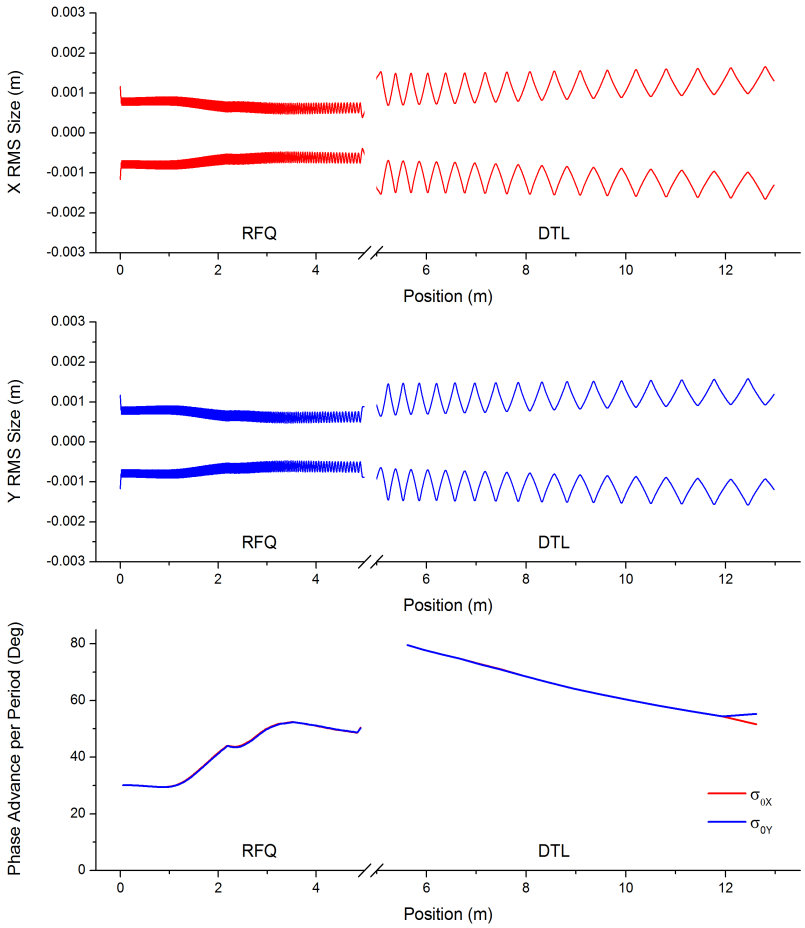

Figure 5.8: RFQ and DTL transverse RMS beam envelopes (horizontal (top) and vertical (middle)) and the phase advance per period (bottom) along the ESS Linac.

5.3.2 Chopping Requirements

With the increasing demand for high power, high intensity beams, modern accelerators have severe restrictions on beam loss. In machines where linac beams are injected into accumulator rings, a major source of particle loss is because of the linac bunches falling outside the stable area of the ring RF buckets (Figure 5.9). This is a serious problem particularly for high energy, high current machines as it leads to machine activation, maintenance and operational difficulties.

One way to mitigate this problem is to use beam choppers to create well defined gaps in the linac pulse train by removing bunches that would otherwise fall at the edges of the ring bucket [70]. Several technical solutions for the choppers have been employed and consist mainly of travelling wave electrostatic deflectors or RF cavity deflectors operating in the TE mode. In ISIS for instance, where the linac frequency is 202.5 MHz and the ring frequency

is 1.3 MHz, the injection losses amount to 5 - 10 % which could be drastically reduced by installing a chopper.

Even for machines where rings are not involved, like the long pulse ESS accelerator to be built at Lund, having a chopping system is still practical for several reasons [134]:

- The beam pulse from the ion source will have a natural rise/fall time of tens of μs. It is likely that this segment of the beam (which will have very different space-charge conditions) will be lost either in the RFQ or further downstream. A chopper might then be needed to control these possible losses.
- During beam commissioning, different beam modes will be required. A beam chopper could be useful in forming pulses as short as a few μs (a pilot pulse), tens of μs (diagnostics pulse) or hundred of μs (tuning pulse).
- For setting up the linac, beam line and target and for operational flexibility, various beam time structures will probably be necessary.
- It provides an in-built redundancy system for an emergency beam stop.

There are two main requirements in designing a chopping system: speed and amplitude.

Chopping speed

The obvious location for a beam chopper is at the low energy end thus minimising the induced radioactivity as well as easing the technical specifications of the deflectors. Choppers have

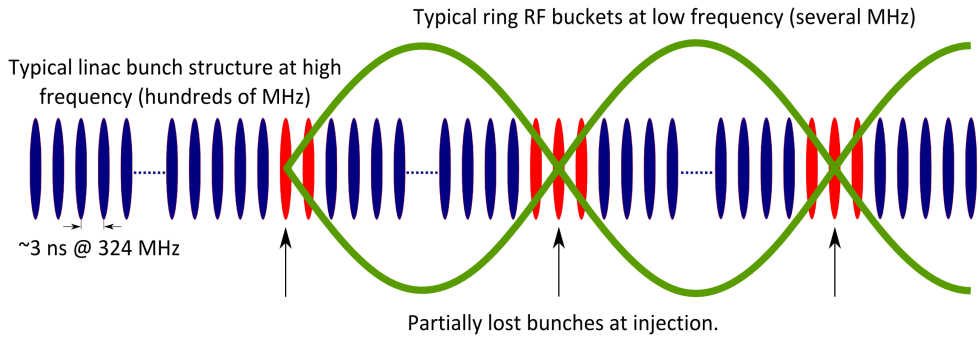

Figure 5.9: Typical linac bunch structure and ring injection losses - graphics idea courtesy of F. Gerigk.

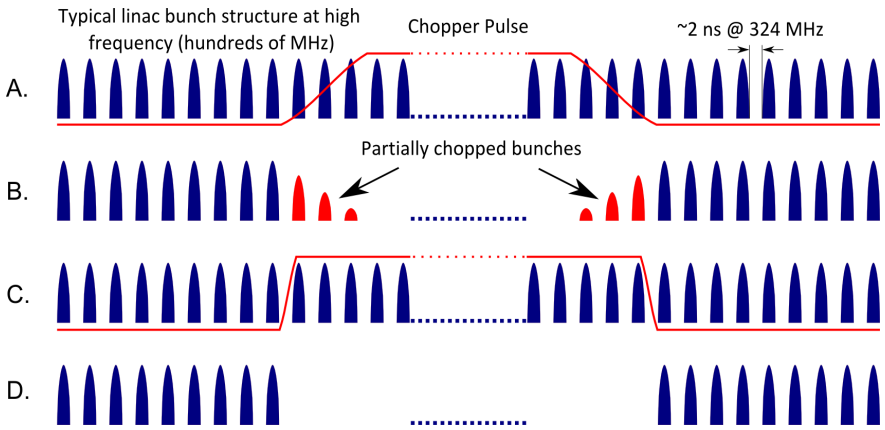

Figure 5.10: Illustration of slow and fast chopper pulse transition. A slow chopper pulse transition (A.) will lead to partially chopped bunches (B.). With a fast chopper transition time (C.), clean chopping can be achieved (D.) - graphics idea courtesy of A. Letchford.

been proposed both before the RFQ in the Low Energy Beam Transport (LEBT) section (tens of keV), as well as after the RFQ in the MEBT (a few MeV). The main benefit of placing the chopper in the LEBT is the reduced actual deflecting voltage. However, the limitation comes from the change in the degree of space-charge neutralisation. Since up to 50 μs will be required for the space-charge compensation to recover, this leads to relatively long transition times, making the LEBT chopper usually too "slow" for the linac requirements. This creates the potential problem of having the partially chopped beam being captured and lost in the RFQ or further downstream.

On the other hand, chopping in the MEBT benefits from the fact that the beam is bunched. This opens the possibility of achieving perfect chopping, by removing individual bunches. At the typical linac frequency of hundreds of MHz, the separation between bunches is of the order of several ns (~3 ns at 324 MHz). The requirement is for the deflecting field to have a transition time sufficiently fast to be able to rise and fall between adjacent bunches, as it is illustrated in Figure 5.10. If this requirement cannot be met, partially chopped bunches can survive and be accelerated to higher energies where if lost, they will have damaging consequences [135], [136].

Chopping amplitude

In addition to the speed requirement, a high deflection force is also necessary in order to provide enough separation between the chopped and unchopped beams at the beam dump

location. Equation 5.2 shows the deflection angle θ in the case of an electrostatic chopper:

$$\theta = \frac{qLV}{m_0 c^2 \beta^2 \gamma D} \qquad x^{"} = \frac{qV}{m_0 c^2 \beta^2 \gamma D} \tag{5.2}$$

where V is the plate voltage, L is the chopper length and D is the half plate separation. It follows clearly that in order to increase the deflection angle, one can increase the voltage and the chopper length and reduce the plate separation. The plate separation however is more or less set by the beam dynamics as the minimum distance that allows beam passage without creating a beam loss bottleneck. Achieving a high voltage, although desirable, is usually limited by the driver capabilities, as high voltage and fast transition times are requirements technically difficult to meet at the same time. Consequently, the chopper length remains the relatively free variable to be optimised in order to achieve sufficient deflection.

Considering a typical deflection angle of 10 mrad, with a 20 mm plate separation and a $\pm$1 kV deflection voltage, the chopper length required at 3 MeV would be $\sim$640 mm. The MEBT therefore needs long spaces to house both the chopper plates and the diagnostic systems. Future linacs will require improved diagnostic systems, so space provision will become increasingly important.

The dilemma surrounding the MEBT design now becomes clear. On one hand, for optimal beam dynamics, smooth transitions with regular focussing are required. On the other hand, beam choppers are also needed. However, choppers are large devices and long drift spaces have to be reserved in the line as well as for the beam dumps and ancillary equipment. Suddenly the focussing period is an order of magnitude or more higher than in the RFQ or the DTL. This breaks the optics periodicity and the symmetry. As a result all modern MEBT designs are a compromise between these two conflicting requirements, often with negative repercussions on beam quality.

5.4 Review of Modern MEBT Designs with Choppers

For most modern linacs, a typical MEBT layout is divided in three sections [130]:

- The Front Section matches the beam from the RFQ into the first chopper section.

This is done by using a combination of focussing elements (quadrupoles, solenoids and re-bunching cavities). Usually two focussing periods are needed as well as re-bunching cavities.

- The Central Section comprises the beam choppers with their respective beam dumps as well as additional beam focussing elements.

- The End Section matches the beam to the downstream accelerator. To achieve a good 6D matching, a similar layout is needed as for the Front Section.

In this section four existing or proposed MEBT designs will be analysed: SNS, J-PARC, Linac4 and ESS. Each layout will be briefly described and its performance will be analysed from a beam dynamics point of view. We will look in particular at the emittance and envelope evolution throughout the MEBT as well as the resulting output distribution.

5.4.1 Simulation Details

Input Distribution

The envelope and tracking studies for each lattice have been done using TraceWin. An input 6D Waterbag distribution with 10^5 macroparticles has been used. For each design it has the same transverse emittance: 0.25 π.mm.mrad (RMS normalised). The Twiss parameters and the longitudinal are slightly different for each case as they are dictated by the design and frequency of the RFQ upstream. A typical input distribution can be seen in Figure 5.11.

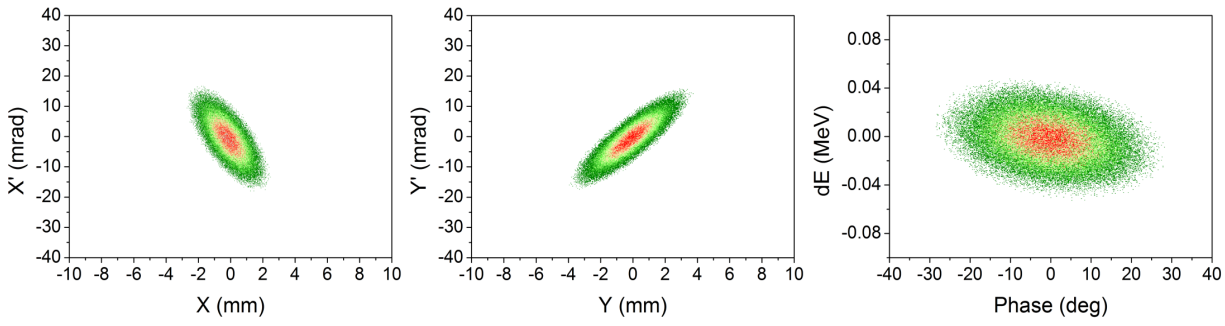

Figure 5.11: Typical MEBT input distribution (horizontal, vertical and longitudinal phase-space). Scale as in Figure 2.11.

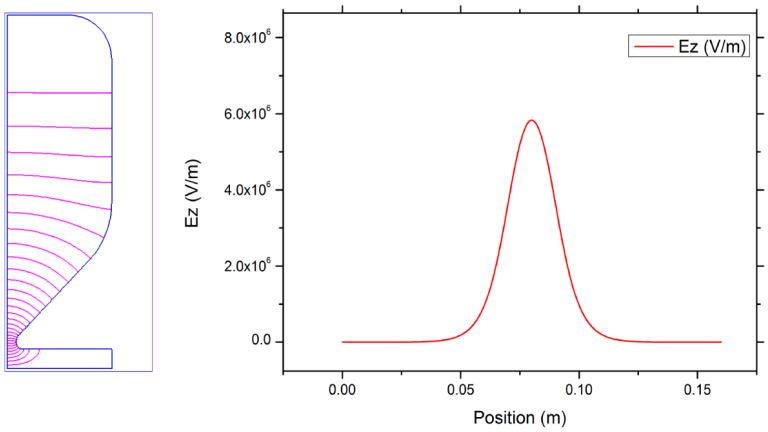

Figure 5.12: Cavity cross-section as modelled by Superfish (left) and the resulting electric field on axis (right).

Cavities

The most direct way to model the cavities is to use the drift-gap-drift model in which the cavity is a zero-length element. In this approximation the particle travels to the centre of the cavity where it receives a kick, after which it continues with the new velocity. This method is implemented in most linac codes. However, the drift-gap-drift technique has its limitations. Previous studies have indicated that the slight differences in beam divergence produced in the accelerating gap can grow progressively down the linac until the disagreement is quite marked when compared with a simulation using field maps [137]. As a result, equivalent field maps have been produced using EM simulation codes. Figure 5.12 shows the 2D cross-section of a cavity modelled in Superfish and the resulting 1D field map. The field can be scaled to achieve the desired effective voltage on-axis [26].

Choppers

The effect of the choppers has been modelled using the inbuilt chopper element in TraceWin that applies a transverse electrostatic deflection according to Equation 5.2. To take into account the fringe field effect, as well as the reduced coverage factor created by the strip line structure, a 2D Superfish model has also been created, as it can be seen in Figure 5.13. It consists of parallel plates at fixed potential with the correct length and separation [138].

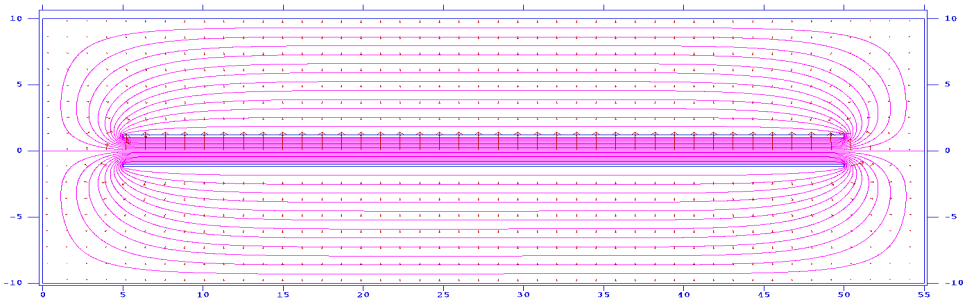

Figure 5.13: Superfish beam chopper model showing a 2D longitudinal section through the chopper (blue) and the equipotential lines (red).

Quadrupoles

Quadrupoles have initially been modelled as hard-edge elements defined by their length and magnetic field gradient. To take into account the effect of the fringe fields, field maps are normally needed. However, EM quadrupole modelling can be inconsistent if the precise quadrupole geometry is not known. In consequence, an analytical model has been implemented to generate 1D gradient field maps. The model is adapted from a similar approach proposed by K. Halbach [139] for permanent magnet quadrupoles (PMQs) and used in Trace3D [40].

Given the maximum magnetic field gradient G_0 and a certain fringe field function $F(z)$, the gradient along the length of the quadrupole is given by:

$$G(z) = G_0 F(z)\,. \tag{5.3}$$

The fringe field function is given by:

$$F(z) = \frac{1}{2}\left\{1 - \frac{z}{8}\left(\frac{1}{r_1} + \frac{1}{r_2}\right)\left[\frac{a_1^2 a_2^2\left(a_1^2 + a_1 a_2 + a_2^2 + 4 + \frac{8}{a_1 a_2}\right)}{a_1 + a_2}\right]\right\} \tag{5.4}$$

where z is the longitudinal position, r_1 and r_2 are control parameters and a_i is defined as

$$a_i = \left[1 + \left(\frac{z}{r_i}\right)^2\right]^{-1/2}, \qquad = 1, 2\,. \tag{5.5}$$

To generate the full quadrupole gradient, two fringe field functions of opposite sign are

generated. The resulting gradient map is obtained by offsetting one function by the length of the quadrupole and superimposing them. This can be seen in Figure 5.14 as well as the resulting gradient field map for a 30 T/m magnet.

This fast method of generating fringe fields for quadrupoles also has the advantage of being very flexible. By adjusting the r_1 and r_2 parameters, a number of field shapes can be created such that more realistic conditions are included in simulations (Figure 5.15).

3D Field Development

While TraceWin can handle magnetic field maps, it cannot deal with gradient maps. As a result, a new feature had to be developed and integrated in TraceWin that allows 3D field development based on an input gradient map.

The 3D magnetic field components and their derivatives for a multipole magnet in the region close to the axis can be expressed as given by the gradient of a scalar magnetic potential function, $V_n(x, y, z)$. The proposed solution in the literature for the scalar potential has the following form [140], [141], [142]:

$$V_n(x,y,z) = (n!)^2 \left[\sum_{q=0}^{\infty} (-1)^q \frac{G^{(2q)}(z)\,(x^2+y^2)^q}{4^q q!\,(n+q)!} \right] \left[\sum_{m=0}^{n} \frac{\sin\left(m\frac{\pi}{2}\right) x^{n-m} y^m}{m!\,(n-m)!} \right] . \tag{5.6}$$

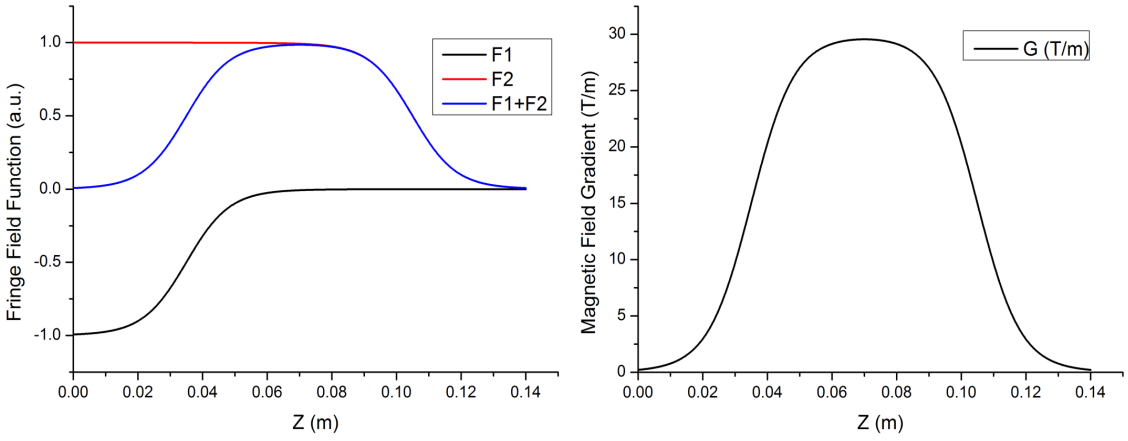

Figure 5.14: Details of fringe field function construction (F1, F2 and F1+F2 - left) and the resulting field gradient map for a 30 T/m quadrupole (right).

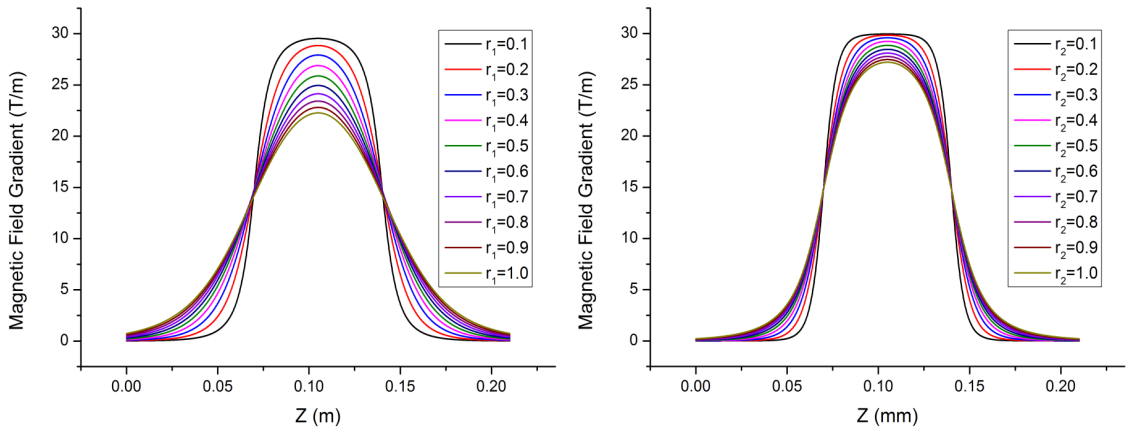

Figure 5.15: Examples of fringe field shapes for a 30 T/m quadrupole obtained by adjusting the r_1 (left) and r_2 parameters (right). r_1 and r_2 have values between 0.1 and 1.

More explicitly, for a quadrupole (n=2), it can be shown that the scalar potential is:

$$V(x,y,z) = \left[G(z) - \frac{G''(z)\,(x^2+y^2)}{12} + \frac{G''''(z)\,(x^2+y^2)^2}{384} - \frac{G''''''(z)\,(x^2+y^2)^3}{23040} + \ldots \right] (xy)\ . \tag{5.7}$$

The resulting magnetic field components in Cartesian coordinates are simply given by $B = \nabla V$. Starting from the input gradient data $G(z)$, to estimate the scalar potential the required derivatives G', G'', etc., can be evaluated numerically. The magnetic field components are then calculated by differentiating the potential function, as seen above.

One alternative is to fit an Enge-type function to the data that can be differentiated

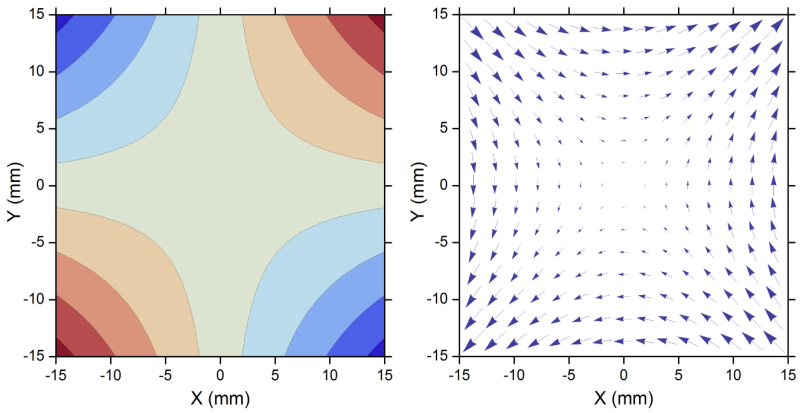

Figure 5.16: Left: Scalar potential developed using the gradient map in Figure 5.14. Right: The corresponding magnetic field obtained by differentiating the potential function. The potential colour scale varies from red (maximum) to blue (minimum).

analytically [143], [144]:

$$G(z) = \frac{G_0}{1 + \exp[C_0 + C_1 \frac{z}{2R_0} + C_2 \left(\frac{z}{2R_0}\right)^2 + C_3 \left(\frac{z}{2R_0}\right)^3 + C_4 \left(\frac{z}{2R_0}\right)^4 + C_5 \left(\frac{z}{2R_0}\right)^5]} . \quad (5.8)$$

R_0 is the pole tip radius and C_n are free coefficients that are adjusted by the fitting routine. Both the Enge function and the numerical approach give consistent results. An example is given in Figure 5.16 where the scalar potential is shown as well as a 2D slice of the resulting magnetic field map, when starting with the gradient map from Figure 5.14.

5.4.2 The SNS MEBT Line

The SNS MEBT matches and transports the beam from a 402.5 MHz RFQ to a DTL downstream. It uses an electrostatic fast chopper designed to remove the 2.5 MeV H^- beam partially and it operates in tandem with the LEBT pre-chopper. The device itself consists of two ∼35 cm long symmetric plates carrying the voltage pulse and separated by a 1.8 cm gap. To meet the rise time requirements, it is necessary to match the speed of the wave of the deflecting electric field along the beam axis to the particle velocity. To achieve this, the wave is sent along a meander-folded line. By travelling over a longer path, the wave phase velocity along the beam axis is reduced to that of the beam (β=0.073). The rise/fall time of the structure is ∼1 ns. However, the limitation in reaching short chopper rise/fall times does not come from the transmission line structure, but from the 2.5 kV pulse generator which has a rise time of ∼10 ns. As a result, three bunches will be partially deflected, but an anti-chopper is in place to return the beam on axis [145], [146].

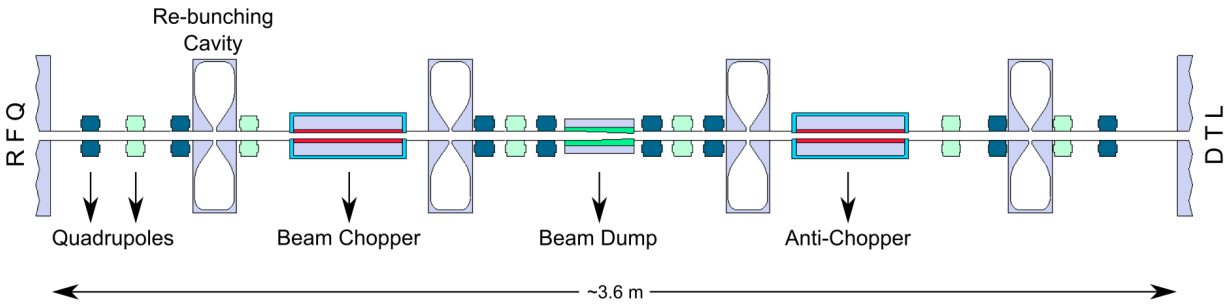

Figure 5.17: Schematic layout of the SNS MEBT line.

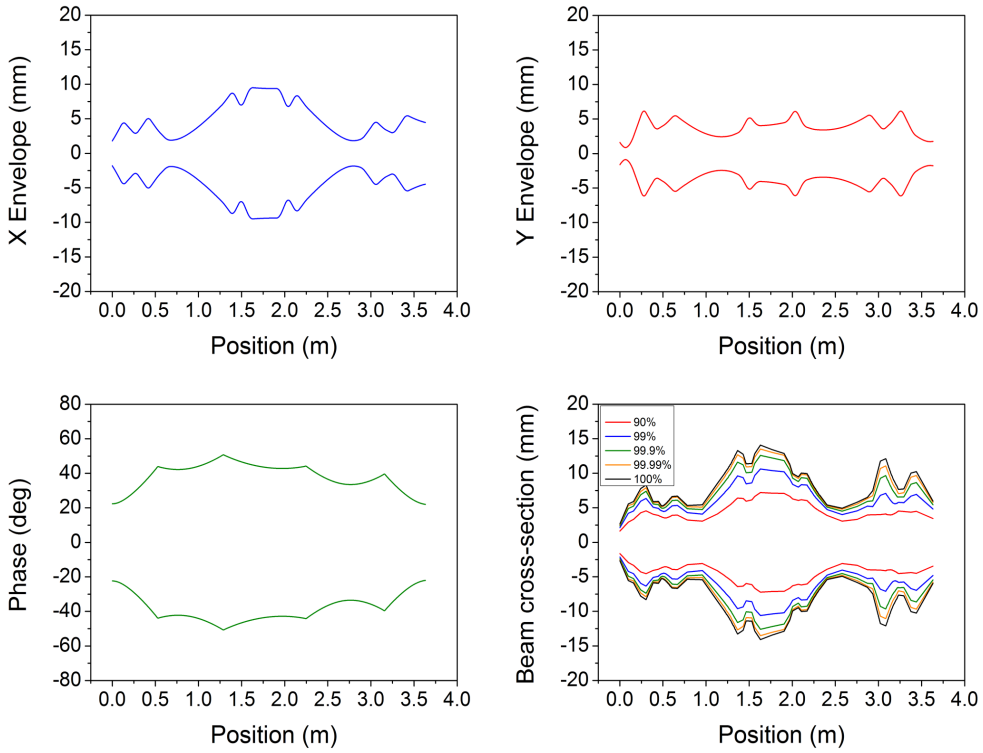

Figure 5.18: SNS MEBT envelopes: horizontal (top-left), vertical (top-right) and longitudinal (bottom-left). Bottom-right: beam cross section at 90%, 99%, 99.9%, 99.99% and 100% density levels.

A schematic layout of the SNS MEBT can be seen in Figure 5.17 [147], [148]. It consists of 14 quadrupoles, 4 re-bunching cavities, the choppers, beam dump and diagnostics. A FODO lattice has been adopted, although its periodicity is broken by the choppers. The beam current is 38 mA, the kinetic energy 2.5 MeV and the bunch frequency is 402.5 MHz. The beam envelopes can be seen in Figure 5.18 as well as the beam cross section (90%, 99%, 99.9%, 99.99% and 100% density level). The long drifts reserved for choppers can

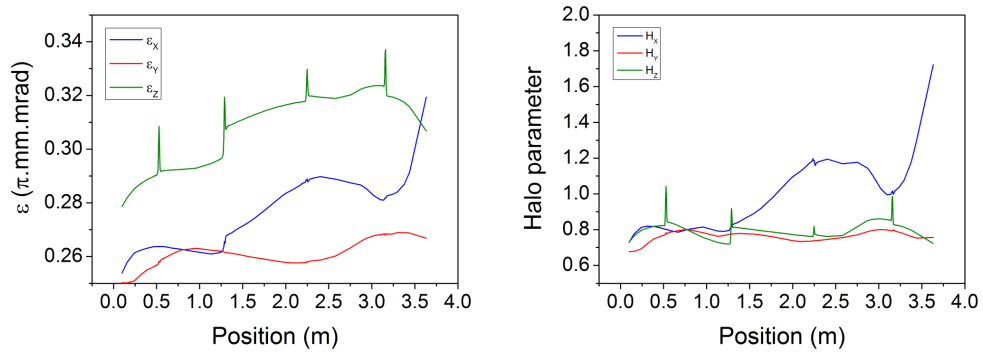

Figure 5.19: Evolution of the horizontal, vertical and longitudinal RMS emittance (left) as well as the corresponding halo parameters (right) in the SNS MEBT.

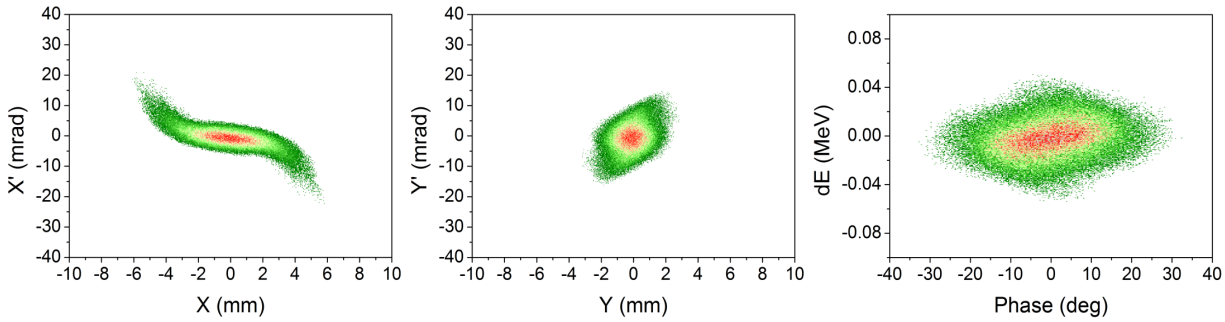

Figure 5.20: SNS MEBT output distribution (horizontal, vertical and longitudinal phase-space). Scale as in Figure 2.11.

be easily identified. The beam density lines illustrate how quickly halo can develop. The emittance and halo evolution are shown in Figure 5.19. An emittance growth of at least 10% is observed both transversely and horizontally. In reality, a higher growth is expected when using a more realistic distribution of the RFQ output beam. Higher emittance growth can lead to beam loss. This aspect has not been studied here, as it required detailed knowledge of MEBT aperture. Also, some designs intentionally allow the beam to be scraped at certain locations in order to reduce transverse halo in the downstream accelerator.

The beam distribution at the MEBT output can be seen in Figure 5.20. Although the MEBT is only ∼3.6 m long, the beam has quickly developed tails transversely and longitudinally, consistent with non-linear space-charge forces and fields. This results in an approximate matching into the linac with further negative repercussions in terms of emittance growth, halo development and eventually beam loss.

The MEBT has been built and commissioned at SNS and although it met all the design specifications, the chopper failed during high power operation. Uncontrolled beam loss and poor cooling capabilities caused the copper to overheat leading to severe structure damage. As a result, a more robust design has been adopted and the deflector has been modified with short strip lines connected by delay lines. The anti-chopper idea has also been abandoned and a new lattice is being investigated to improve the output beam quality [149], [135].

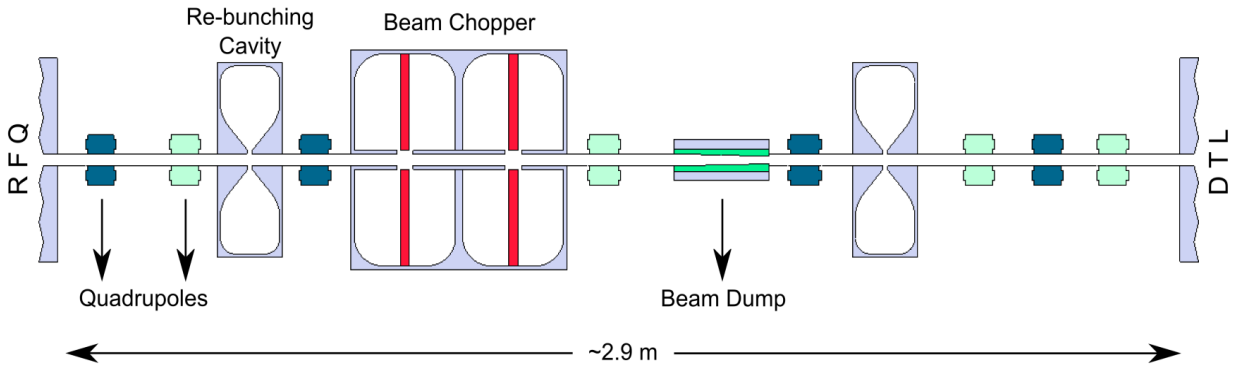

Figure 5.21: Schematic layout of the J-PARC MEBT line.

5.4.3 The J-PARC MEBT Line

At J-PARC an RF chopper has been developed. The deflector consists of two RF cavities operated in a TE11 mode at 324 MHz. To save space in the MEBT, the two cavities have been constructed as a whole. Two electrodes are mounted in each cavity to concentrate the electric field and two beam pipes are added to shield the beam from the reverse deflecting effect of the magnetic field generated between the electrodes and the cavity walls. The

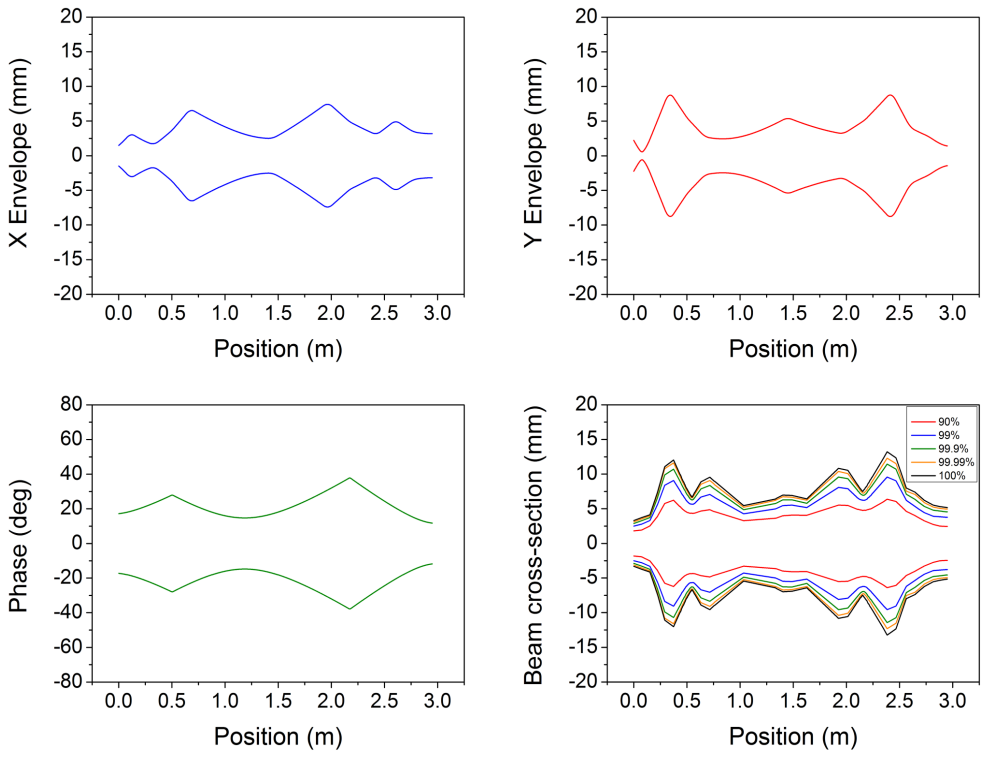

Figure 5.22: J-PARC MEBT envelopes: horizontal (top-left), vertical (top-right) and longitudinal (bottom-left). Bottom-right: beam cross section at 90%, 99%, 99.9%, 99.99% and 100% density levels.

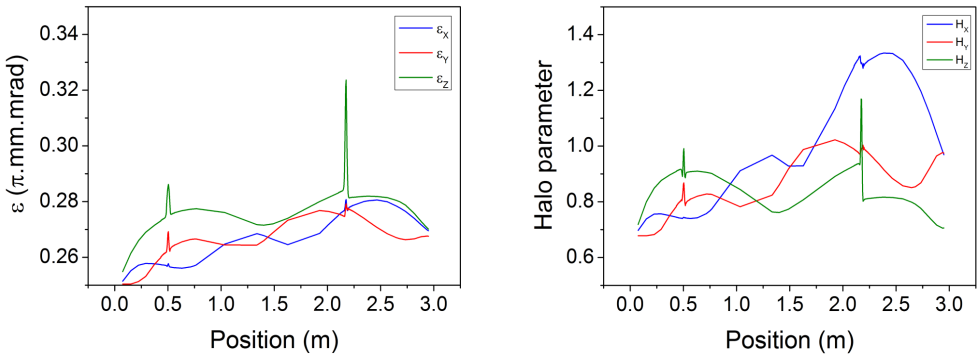

Figure 5.23: Evolution of the horizontal, vertical and longitudinal RMS emittance (left) as well as the corresponding halo parameters (right) in the J-PARC MEBT.

transverse electric field oscillating between the electrodes deflects the beam away from the beam axis to a dedicated beam dump [150].

By lowering the loaded Q value of the cavity a fast rise time can be achieved. For a Q of 10, the measured rise time of the deflector system is about 27 ns, including a 15 ns contribution from the amplifier. However, by operating the RF cavities with a high driving power (36 kW), a chopped beam rise time of ∼10 ns has been achieved. This is due to the fact that the deflecting field amplitude is sufficiently large before the RF pulse reaches the top plateau. By reducing the driving power by ∼40%, a good deflection was still observed, but the rise time has increased to ∼15 ns [151].

The J-PARC RF deflector has the advantage of having a high deflecting field and a short rise time, which are the basic requirements for clean chopping. The experience at J-PARC suggests that the cavities are compact and easy to manufacture and the overall chopping system has so far proved reliable and flexible. However, bunch by bunch chopping is not

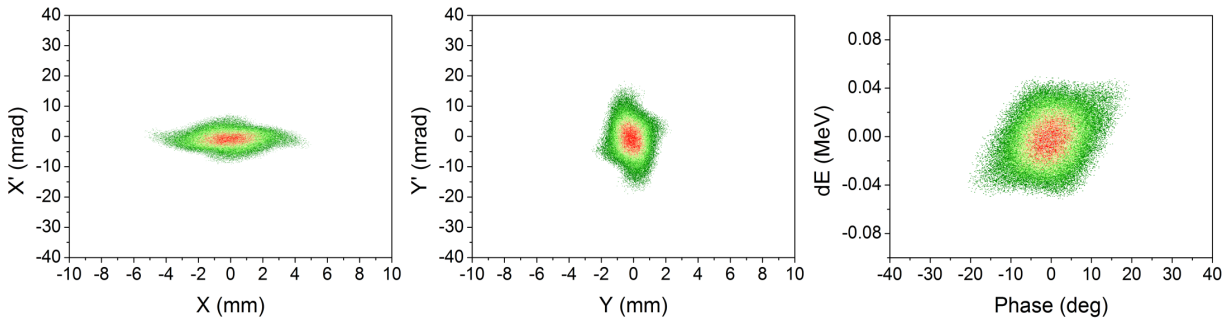

Figure 5.24: J-PARC MEBT output distribution (horizontal, vertical and longitudinal phase-space). Scale as in Figure 2.11.

possible and three adjacent bunches are partially deflected during the chopper rise time.

From a beam optics point of view, a triplet lattice has been adopted, with 8 quadrupoles, 2 re-bunching cavities, the RF chopper cavity, the beam dump as well as diagnostics. The MEBT layout is only 2.9 m long and can be seen in Figure 5.21. The beam current is 30 mA, the kinetic energy is 3 MeV and the bunch frequency is 324 MHz. Like in the SNS case, the lattice periodicity is also broken by the chopping elements, although to a smaller degree as the deflecting elements are shorter. The beam envelopes and the evolution of the beam cross-section is shown in Figure 5.22. Figure 5.23 shows the emittance growth with levels similar with SNS. And like in the SNS case, the output beam distribution (Figure 5.24) is affected by the rapid change in the beam aspect ratio, the resulting change in the non-linear to linear space-charge forces ratio as well as the RF fields.

5.4.4 The Linac4 MEBT Line

A MEBT fast chopper is currently being commissioned for the CERN Linac4 project to be used in parallel with the LEBT chopper. It operates at 3 MeV and it consists of two units. Each unit is 50 cm long and houses the deflecting plates (40 cm). To reduce the total length of the line, the chopper units are designed to fit inside the bore of two MEBT quadrupoles which keep the beam focussed in the chopping plane and to provide a 90 degree phase advance between the centre of the chopper and the beam dump. By placing the deflectors inside the quadrupoles, their length can be increased without compromising the beam dynamics. This in return minimises the required voltage between the chopper plates.

The design of the chopper structure is similar to the SNS chopper described above and it

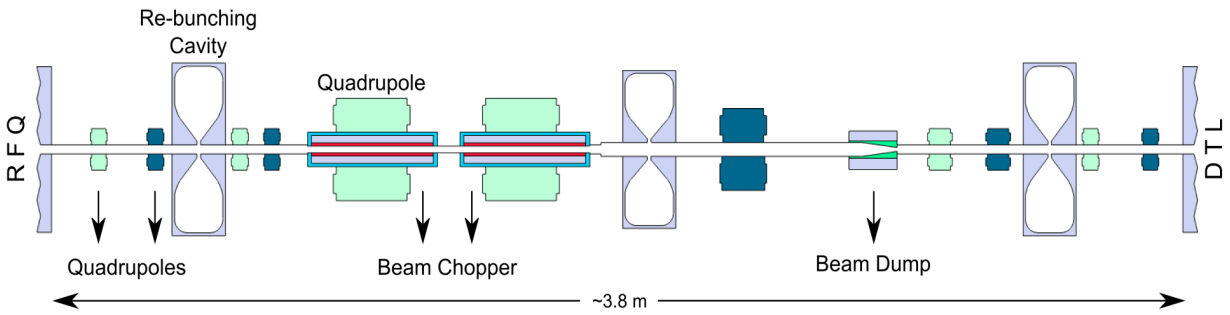

Figure 5.25: Schematic layout of the Linac4 MEBT line.

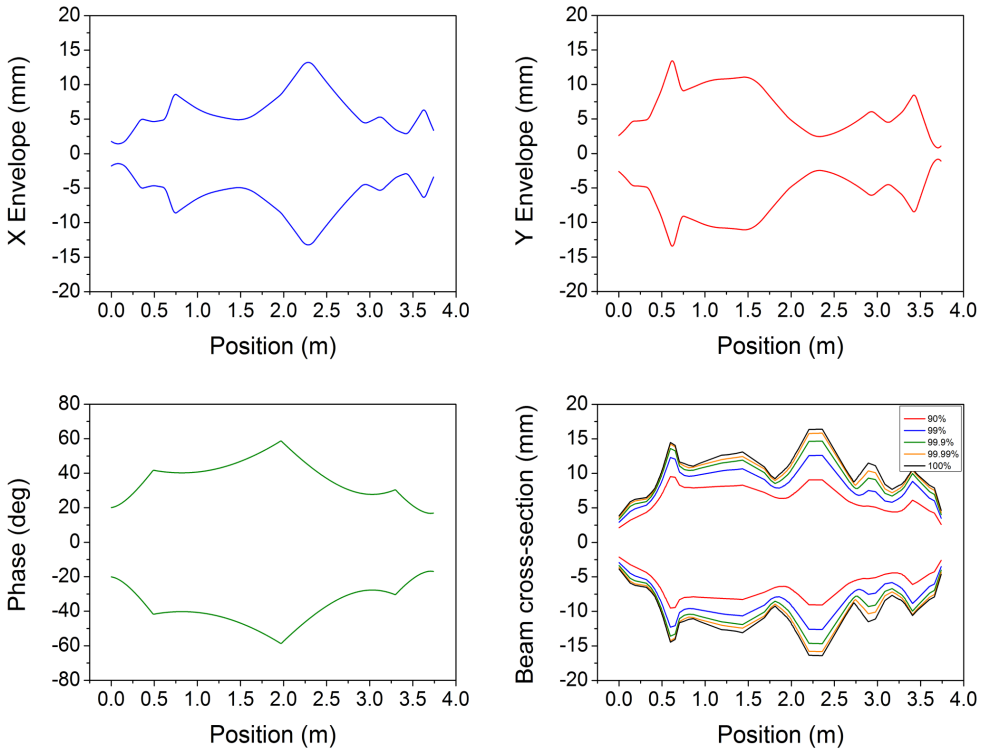

Figure 5.26: Linac4 MEBT envelopes: horizontal (top-left), vertical (top-right) and longitudinal (bottom-left). Bottom-right: beam cross section at 90%, 99%, 99.9%, 99.99% and 100% density levels.

consists of a double-meander stripline matched to the beam velocity (β=0.08) and printed on an alumina substrate (better radiation hardness, heat transfer). The chopper driver is capable of delivering a maximum voltage of ±600 V and a rise time of ∼2 ns. At a frequency of 352.21 MHz, the bunch separation is ∼2.8 ns, meaning that bunch by bunch chopping will be possible [152], [153].

The Linac4 MEBT layout can be seen in Figure 5.25. 11 quadrupoles are being used,

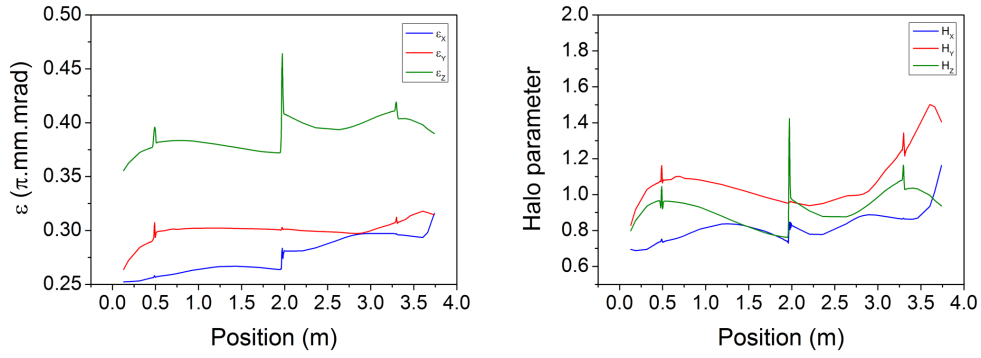

Figure 5.27: Evolution of the horizontal, vertical and longitudinal RMS emittance (left) as well as the corresponding halo parameters (right) in the Linac4 MEBT.

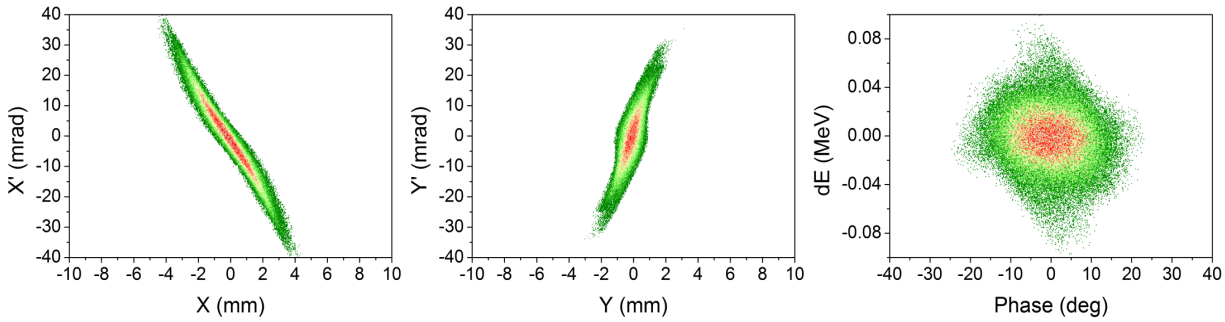

Figure 5.28: Linac4 MEBT output distribution (horizontal, vertical and longitudinal phase-space). Scale as in Figure 2.11.

together with 3 re-bunching cavities, the choppers and the beam dump. A FODO-type lattice was adopted. The beam current is 70 mA, and the kinetic energy is 3 MeV. The envelopes can be seen in Figure 5.26. Like in the SNS and J-PARC designs, the beam size is kept transversely under ±10 mm to avoid scraping on the choppers and optics elements. Longitudinally, the maximum phase length is kept as much as possible under ±50 degrees at 352.21 MHz [154].

The rather high beam current is required as margin for potential MEBT beam loss that would lead to a reduction in the linac design beam power. Consequently, a larger emittance and halo increase is observed than in other designs as seen in Figure 5.27 (∼20% transverse and ∼10% longitudinal emittance growth). The MEBT output distribution is also affected by the same non-linear effects described above and can be seen in Figure 5.28, with clear wings developing in all three phase-space planes.

5.4.5 The ESS MEBT Line

The MEBT design currently under consideration at ESS, takes as a starting point the Linac4 MEBT and adopts the CERN chopper solution, with deflection plates incorporated in long quadrupoles. The chopping system is 1 m long, with two sets of plates each 40 cm long. The MEBT layout can be see in Figure 5.29. It consists of 10 quadrupoles, 3 re-bunching cavities, choppers and the beam dump. The proton beam current is 50 mA, the kinetic energy 3 MeV and the bunch frequency 352.21 MHz. The beam envelopes can be seen in Figure 5.30.

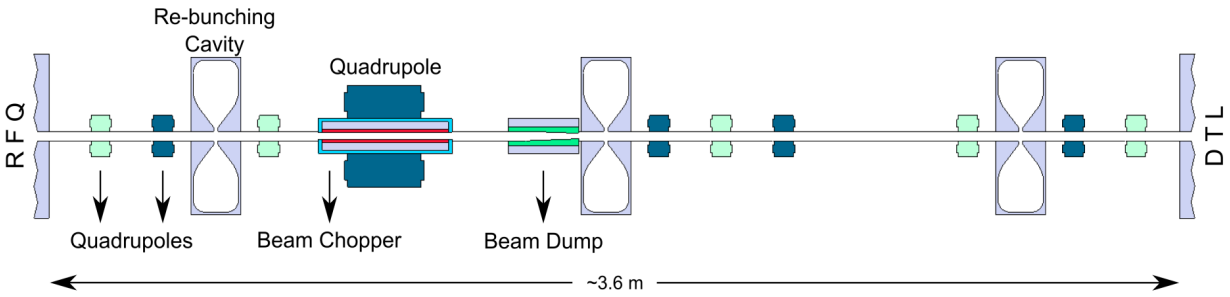

Figure 5.29: Schematic layout of the ESS MEBT line.

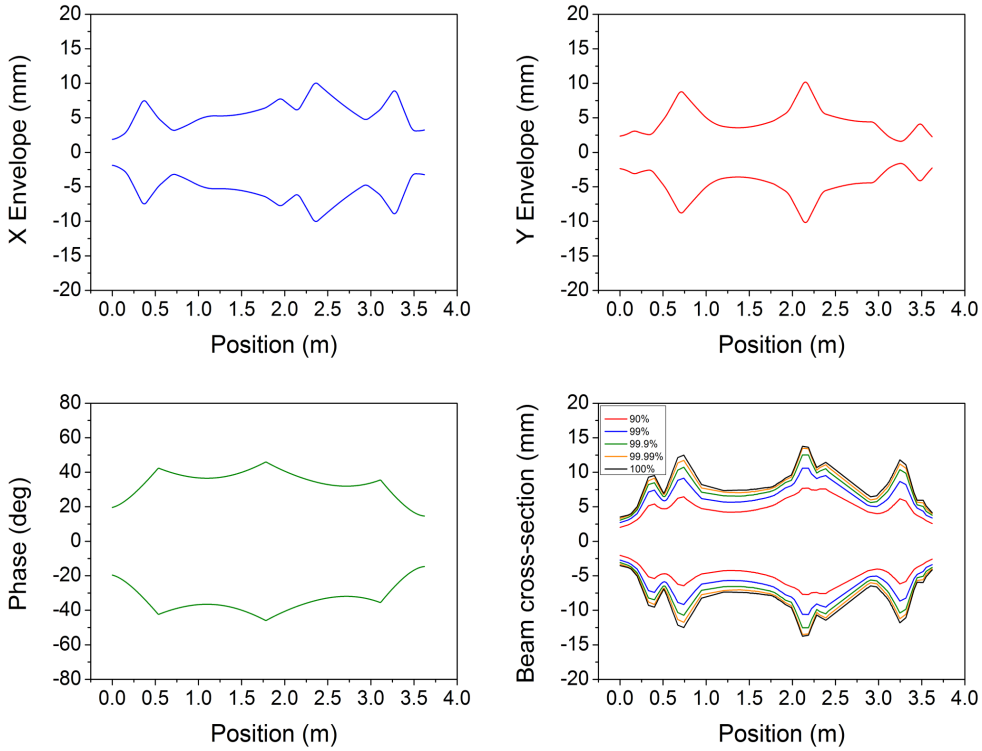

Figure 5.30: ESS MEBT envelopes: horizontal (top-left), vertical (top-right) and longitudinal (bottom-left). Bottom-right: beam cross section at 90%, 99%, 99.9%, 99.99% and 100% density levels.

ESS has adopted a triplet focussing lattice. This offers longer uninterrupted drift spaces for choppers. Having a lower beam current and fewer constraints at the design stage, allows for a better design optimisation. To increase the chopper efficiency, the beam is made flat at the beam dump location. To avoid losses, the beam is kept as small as possible, although this enhances the space-charge effects. A typical 10% emittance growth is still observed transversely (Figure 5.31), and the output beam distribution also develops the characteristic wing-like features seen in other designs (Figure 5.32). Furthermore, when using a more realistic RFQ output distribution, the beam quality deteriorates further. This calls for a

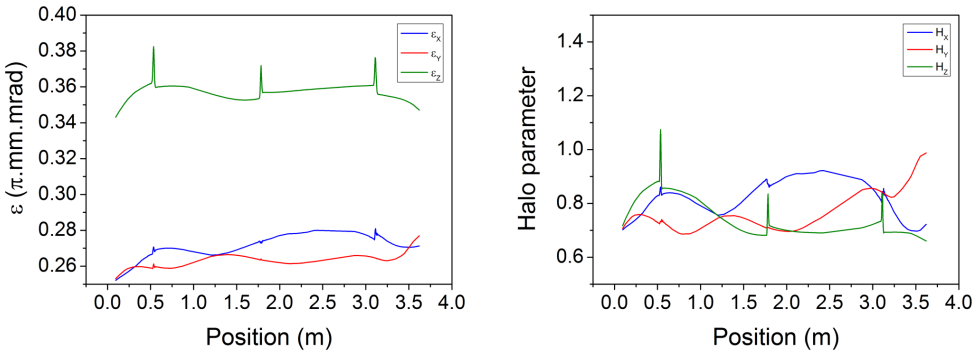

Figure 5.31: Evolution of the horizontal, vertical and longitudinal RMS emittance (left) as well as the corresponding halo parameters (right) in the ESS MEBT.

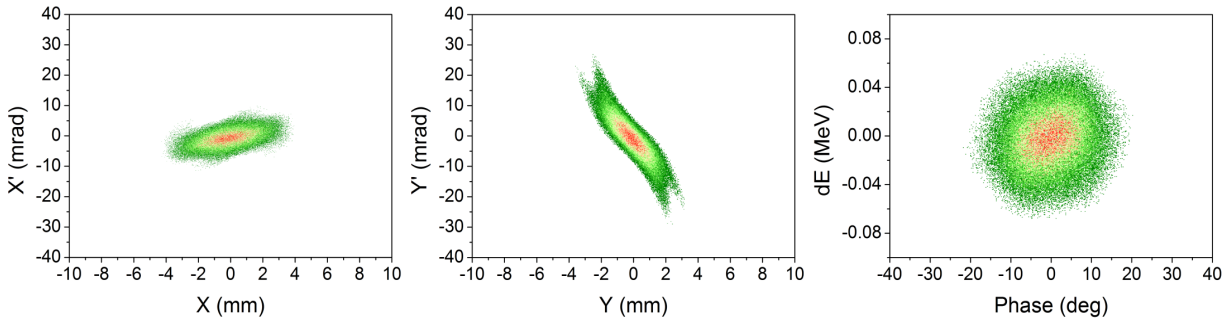

Figure 5.32: ESS MEBT output distribution (horizontal, vertical and longitudinal phase-space). Scale as in Figure 2.11.

collimation system to be included in the MEBT, a feature present in most designs [155].

5.5 The Front End Test Stand (FETS) Project

The Front End Test Stand was first proposed over a decade ago [156], as a demonstrator for fast, high quality beam chopping. Since then, FETS has become the main proton R&D project in the UK, being a collaborative effort between Rutherford Appleton Laboratory where it is being built, and several universities as well as international partners [157]. FETS has been identified as an essential first ingredient for the next generation of high power proton accelerators that are aiming to deliver beam powers in the megawatt range, in particular, the ISIS upgrade plans and the UK neutrino factory design efforts [28].

A schematic FETS layout can be seen in Figure 5.33. Through its component parts, FETS has triggered the development of a high brightness, 60 mA H^- ion source, a three-solenoid Low Energy Beam Transport line (LEBT), a 3 MeV, 324 MHz four-vane Radio-

Frequency Quadrupole (RFQ) and a Medium Energy Beam Transport line (MEBT) with a high speed chopper. The project is well advanced and when operational should be sufficiently versatile to explore a range of operating conditions. When completed it will deliver a 60 mA (unchopped), 2 ms, 50 Hz cleanly chopped H^- beam at 3 MeV. [158].

5.5.1 The Fast-Slow Chopping Concept

The FETS chopping system uses an innovative tandem deflection scheme. Its successful delivery and proof of principle is the main motivation behind the FETS project. The scheme has evolved from an early idea developed by M. Clarke-Gayther for ESS and has been adapted for the FETS requirements [159].

As explained in Section 5.3.2, in order to avoid losses and produce a precisely defined timing structure in the bunch train, the chopping field has to rise and fall in the interval between two adjacent bunches. At 324 MHz a typical bunch length is 120 degrees resulting in a bunch separation of ∼2 ns. At the same time, depending on the timing requirements, a field duration of up to hundreds of μs may be required. However, fast transition time and long duration are conflicting requirements, very difficult to meet at the same time.

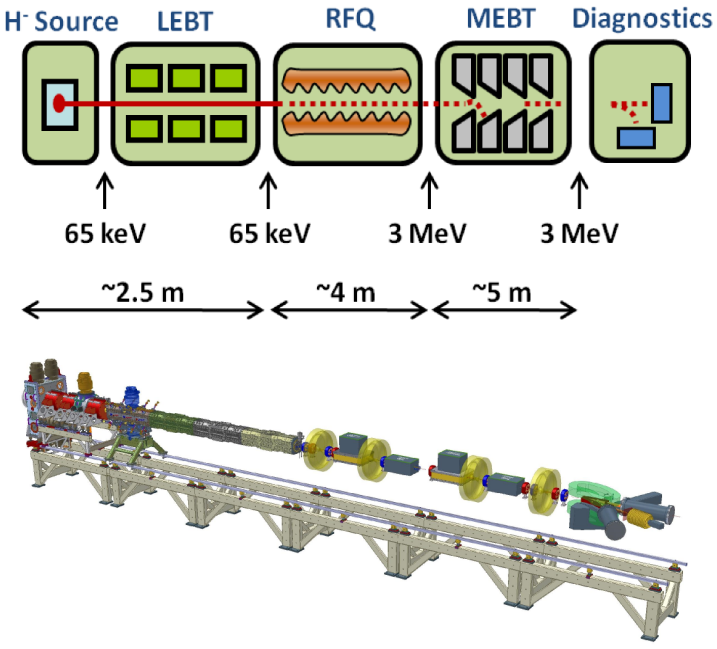

Figure 5.33: Schematic FETS layout - bottom photo courtesy of P. Savage.

	Fast Chopper	Slow Chopper	
Chopper Potential	±1.4	3	kV
Pulse Transition	2	12	ns
Pulse Duration	0.012	0.17 - 100	μs
Pulse Repetition Frequency	2.6	1.3	MHz
Coverage Factor	82	85	%
Duty Cycle	0.27	1.7	%
Burst Duration	0.3 - 2	0.3 - 2	ms
Burst Repetition Frequency	50	50	Hz
Electrode Gap	20	20	mm

Table 5.3: Key chopper parameters.

The FETS scheme resolves this problem by separating the chopper field requirements into two components: a fast transition, short duration field working in tandem with a slow transition, long duration field, hence the "fast-slow" name. Each field is produced by separate electrodes. The basic working principle is explained in Figure 5.34. At the beginning and the end of the chopping interval, the fast chopper creates a gap in the bunch train of 10 - 15 ns, by removing several adjacent bunches. These gaps will then be used by the second chopper field as a transition interval, thus preventing bunches being partially chopped [160], [161], [136].

Each device consists of two long symmetric plates carrying the voltage pulse, separated by a 20 mm gap. A folded transmission line approach similar to SNS has also been adopted here to reduce the wave phase velocity along the beam axis to that of the beam (β=0.079). The main deflector parameters are presented in Table 5.3.

The development of the electrode structures has been based on the existing SNS and

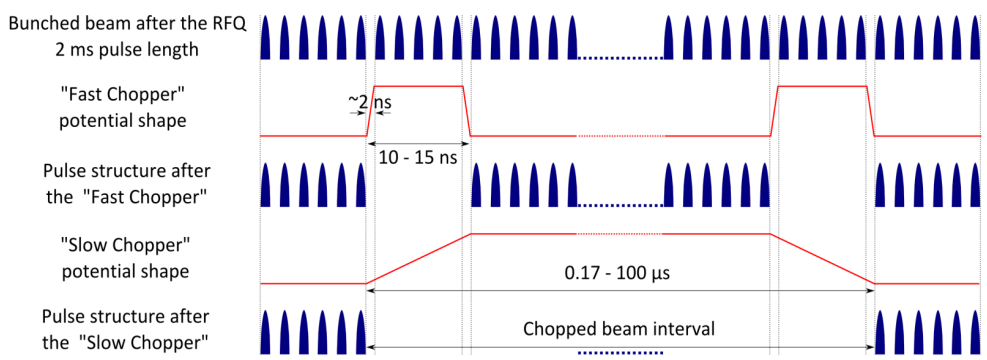

Figure 5.34: The "fast-slow" chopping scheme - graphics idea courtesy of M. Clarke-Gayther.

		CERN	J-PARC	SNS	RAL
Beam Current	mA	70	30	38	60
Beam Energy	MeV	3	3	2.5	3
Bunch Frequency	MHz	352.21	324	402.5	324
Beam Pulse Length	ms	0.4	0.5	1	2
Repetition Rate	Hz	50	25	60	50
Deflector Type		E-static	RF Cavity	E-static	E-static
Deflector Details		Stripline	TE11 Mode	Stripline	Stripline/Coaxial
Deflector Length	cm	$2 * 40$	17.2	$2 * 35$	$2 * 60$
Rise Time	ns	2	10	10	2
Deflector Voltage/ Field	kV	± 0.6	1.6 MV/m	± 2.5	± 1.5
Bunch by Bunch Chopping		Yes	No	No	Yes

Table 5.4: Main MEBT chopper parameters at CERN, J-PARC, SNS and RAL.

CERN solutions, with the aim of achieving better mechanical and thermal stability as well as an improved coverage factor. A helical and a planar solution have been proposed. The helical transmission line consists of strip lines connected by coaxial cable delay lines. For the planar solution, the delay line is part of the strip line structure. Figure 5.35 shows sections of the two electrode structures [162].

Table 5.4 shows a summary of the capabilities of the "fast-slow" chopping scheme as well as those of the other main chopping solutions currently operational or under construction: CERN, J-PARC and SNS. Beam dynamics aspects of these alternative schemes have been extensively discussed in Section 5.4.

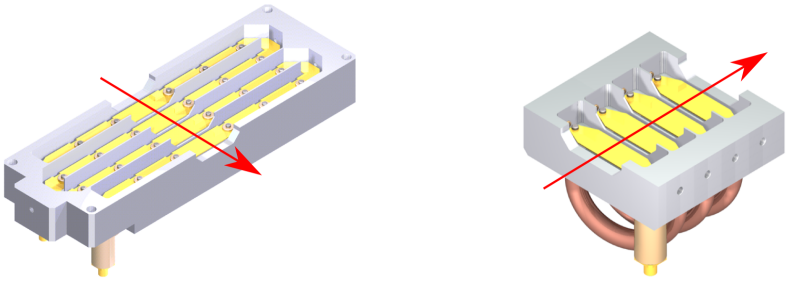

Figure 5.35: Illustrations of the planar (left) and helical (right) slow-wave electrode structures. The red arrow indicates the beam direction (Adapted from [162] - courtesy of M. Clarke-Gayther).

5.5.2 The MEBT Line

The current FETS MEBT has evolved from an original lattice first intended for a short-pulse ESS facility. With the proof of principle of the proposed "fast-slow" chopping scheme becoming one of the main FETS objectives, the MEBT had to be adapted to accommodate the new requirements. The baseline design takes into account both optics and chopping requirements and assumes injection into a DTL downstream [159], [163], [164].

For the FETS project requirements, given that the facility will be an advanced accelerator physics test bench, it has been decided that more beam line space is required for additional diagnostics and ancillary equipment to allow precise characterisation of the full FETS machine. This has inevitably led to design modifications and the overall performance being affected. Nevertheless, the FETS MEBT still remains a benchmark for injection lines with beam choppers. This section will analyse the MEBT on mainly two criteria:

- Beam Optics: beam size, emittance evolution, halo development, beam loss.
- Chopping efficiency: extinction rate, bunch separation at beam dump location, bunch length in the fast chopper, power density on the beam dump plates.

The MEBT performance has been evaluated assuming a 6D waterbag distribution.

MEBT Layout

Table 5.5 lists the main MEBT parameters, while the overall MEBT layout can be seen in Figure 5.36. It consists of 11 quadrupoles, 4 cavities, 2 beam choppers with dedicated beam dumps and a range of diagnostics. Just like the designs analysed in Section 5.4, the FETS MEBT is divided in three main sections: two matching sections and a main chopping

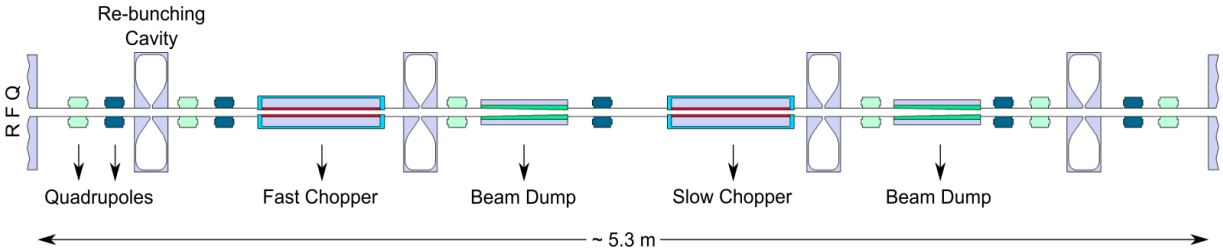

Figure 5.36: Schematic layout of the FETS MEBT line.

Number of quadrupoles	11	-
Maximum quadrupole gradient	20	T/m
Number of cavities	4	-
Maximum effective cavity voltage	100	kV
Chopper electrode length	600	mm
Maximum fast chopper effective voltage	±1.15	kV
Maximum slow chopper effective voltage	2.55	kV
Beam dump length	410	mm
Total Length	∼5.3	m

Table 5.5: Main FETS MEBT parameters.

section. The input section matches the beam from the RFQ, while the final section matches the beam to accelerators downstream.

Particle species	H^-	MeV
Beam energy	3	MeV
Peak current	60	mA
Bunch frequency	324	MHz
Number of macroparticles	∼100000	-
	ϵ_x=0.29	π.mm.mrad
Emittance (RMS Normalised)	ϵ_y=0.30	π.mm.mrad
	ϵ_z=0.45	π.mm.mrad

Table 5.6: FETS MEBT input distribution properties.

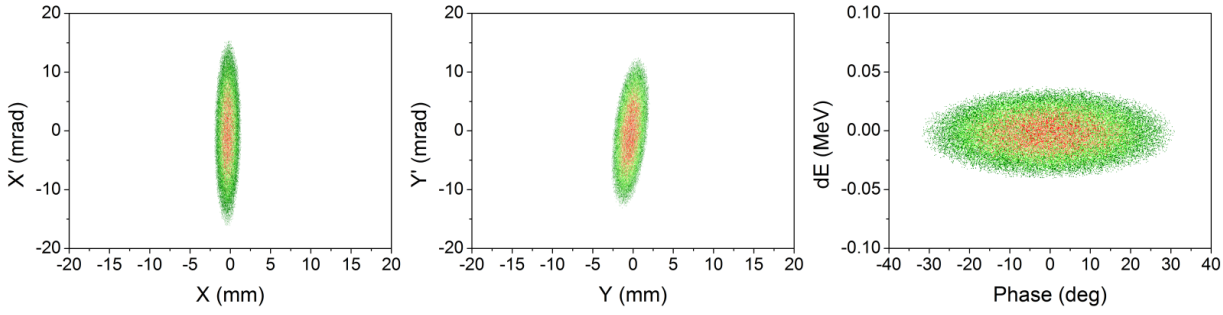

Figure 5.37: FETS MEBT input waterbag distribution (horizontal, vertical and longitudinal phase-space). Scale as in Figure 2.11.

Beam dynamics

The input MEBT beam distribution can be seen in Figure 5.37 and the relevant distribution parameters are presented in Table 5.6. The beam has an emittance of ∼0.3 π.mm.mrad transversely and ∼0.45 π.mm.mrad longitudinally (∼0.17 π.deg.MeV). The emittance values are estimates obtained from RFQ tracking. It should be noted that the expected values for the transverse emittance from similar projects under development are 20-30% lower (0.2-0.25 π.mm.mrad) and work is under way in FETS to limit the beam emittance output from the ion source and control its growth in the LEBT and RFQ.

In refining the MEBT design, assuming an input waterbag beam is an important step. Although this scenario is not realistic, it allows the identification and characterisation of effects on the beam generated by the MEBT itself by eliminating any halo and beam irregularities that might have been "inherited" from upstream accelerators (RFQ, LEBT). The beam dynamics model follows the design philosophy described in Section 5.4 and attempts to meet both optics and chopping requirements. The result is a compromise between these two main drivers.

Transversely, the MEBT employs a FODO lattice with relatively high quadrupole gradients (up to 20 T/m). Re-bunching cavities are added such that the longitudinal focussing of the beam is also maintained. Regrettably, the FODO symmetry is broken by the long drift spaces required for the chopper structures. The 5∗RMS emittance beam envelopes in the transverse plane as well as the beam spread in the longitudinal plane can be seen in Figure 5.38. It is immediately clear that the beam size is larger in the horizontal plane. This is a design feature which leads to an increase in the overall transmission by squeezing the beam in the chopping plane where the aperture is smaller. The beam cross-section can also be seen in the same figure and it gives an indication of the maximum beam radius throughout the MEBT for different density levels: 90%, 99%, 99.9%, 99.99% and 100%. The maximum beam extent is $\sim \pm 17$ mm transversely and $\sim \pm 65$ degrees longitudinally. For the purpose of FETS the beam is intentionally allowed to debunch more than one would do in an operational machine. This is to reduce voltage requirements on the re-bunching cavities and hence manufacturing and running costs.

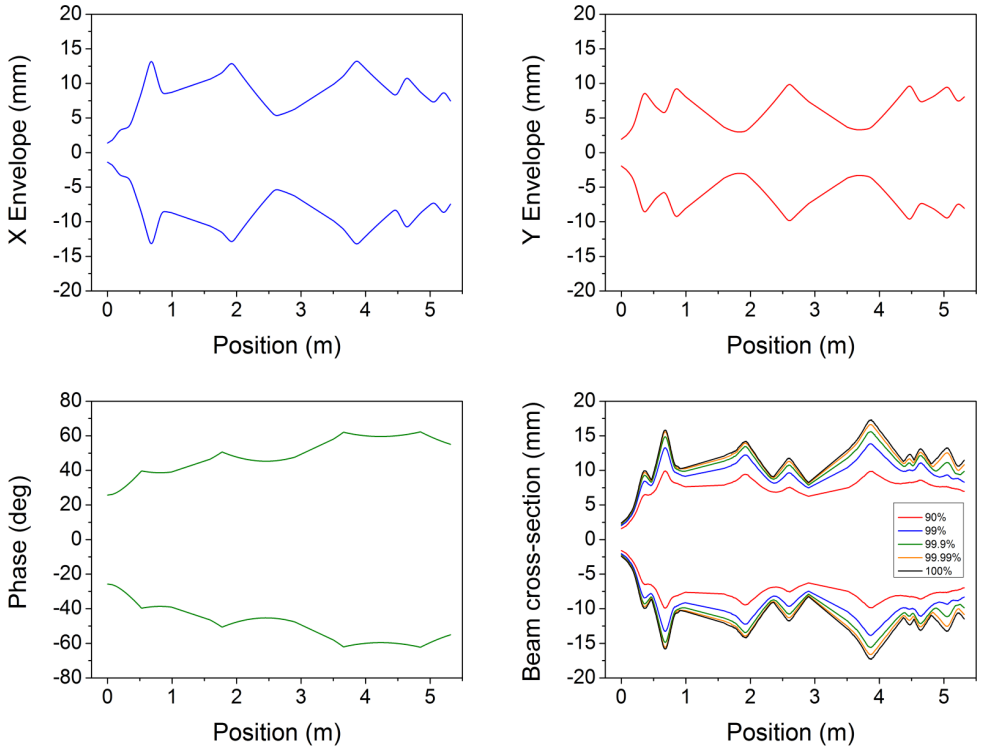

Figure 5.38: FETS MEBT 5∗RMS emittance beam envelopes and beam radius at different density levels when using an input waterbag distribution. Horizontal (top left), Vertical (top right), Longitudinal (bottom left), Beam Radius (bottom right)

A more detailed cross-section plot is shown in Figure 5.39 where the transverse planes are plotted independently, as well as the beam pipe aperture. It now becomes evident that the deflector plates and the beam dumps are the main vertical bottlenecks for beam transmission. By carefully adjusting the MEBT optics, several solutions with no losses have been found. However, although simulations indicate total transmission, at several locations the beam outside the 99% core arrives dangerously close to the vacuum chamber, especially in the

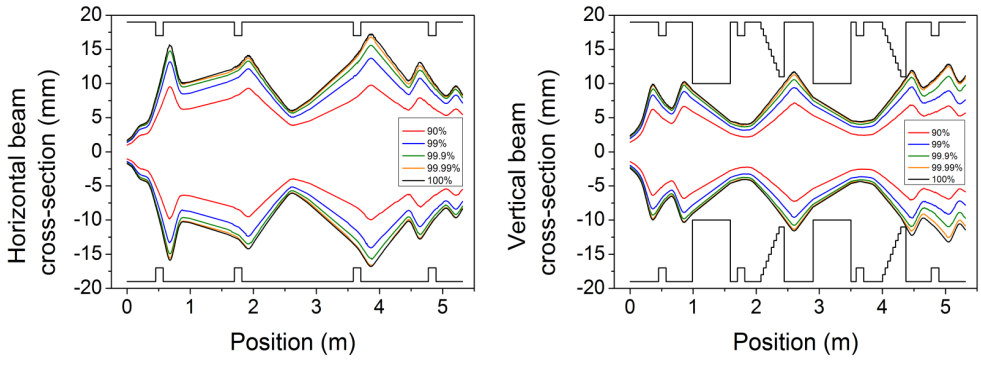

Figure 5.39: Beam cross-section in the FETS MEBT when using a waterbag input distribution.

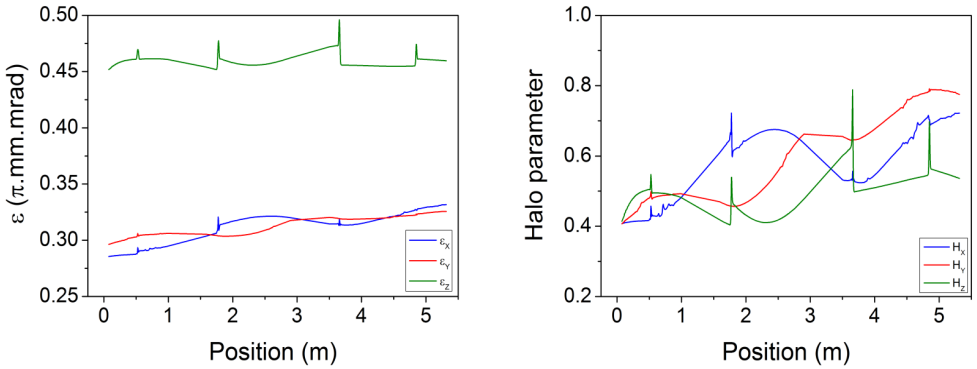

Figure 5.40: Evolution of the normalised RMS beam emittance (left) and halo parameters (right)in the FETS MEBT when using a waterbag input distribution.

vertical plane. This is comparable or better than similar designs and is the result of the compromise between optics and chopping requirements. For comparison, in a typical DTL the ratio between the vacuum chamber radius and the RMS beam size is kept between 8 and 10. In the FETS MEBT as expected this ratio varies widely due to the unusual aperture profile, but can be as low as 3.5 at the beam dump tip [52].

Another important factor in reviewing the design strength is the evolution of the beam emittance and halo through the MEBT which can be seen in Figure 5.40. Strong space-charge forces have the overriding influence on the beam behaviour at this high beam current and low energy. Due to additional chopping requirements the lattice periodicity is severely broken and a smooth phase advance can no longer be maintained. The transition from the RFQ to the MEBT sees a sudden jump to a much slower phase advance as the basic FODO-type cell is now at least $7\beta\lambda$ long. All these mechanisms combined have a detrimental effect on the beam quality and as it can be seen, some degradation is unavoidable. The emittance growth is 16.2% horizontally, 0.9% vertically, while longitudinally the growth is much smaller: 1.7%.

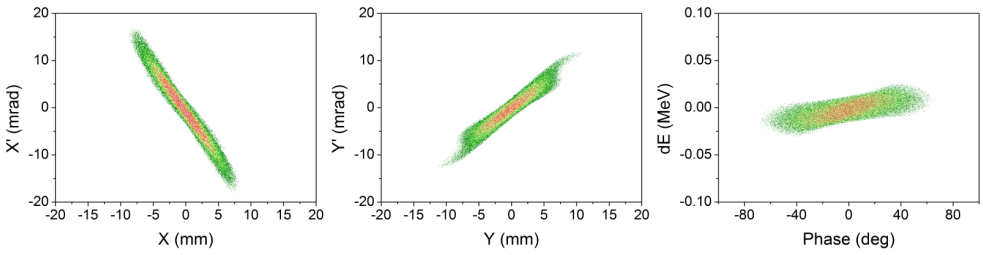

Figure 5.41: FETS MEBT output distribution when using a waterbag input distribution (horizontal, vertical and longitudinal phase-space). Scale as in Figure 2.11.

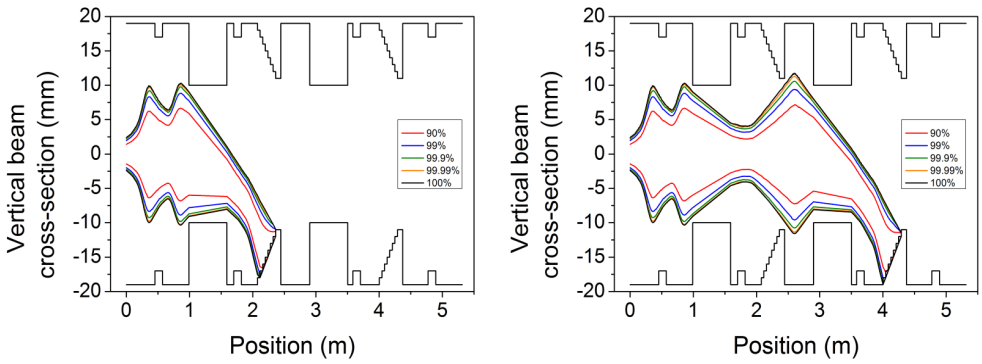

Figure 5.42: Deflected beam cross-section in the FETS MEBT when using a waterbag input distribution. Left: Fast Chopper ON, Slow Chopper OFF, Right: Slow Chopper ON, Fast Chopper OFF.

The evolution of the halo parameters reflect the input distribution type and although some growth is observed, the values remain relatively low.

The MEBT output beam distribution can be seen in Figure 5.41. As currently no matching to a downstream accelerator is required for FETS, the projections illustrate just one possible phase space configuration. Four quadrupoles and one re-bunching cavity are used for matching and a wide range of output states can in theory be attained. It is interesting to observe that just like in every other MEBT design investigated in Section 5.4, the output beam displays a certain degree of space-charge driven filamentation and tail formation.

The chopping efficiency analysis requires special consideration, as one of the main FETS drivers is the demonstration of high speed clean chopping using the "fast-slow" deflection scheme. The electrode structures described in Section 5.5.1 are being used. For the fast chopper, a maximum effective voltage of ±1.15 kV is assumed which includes the coverage

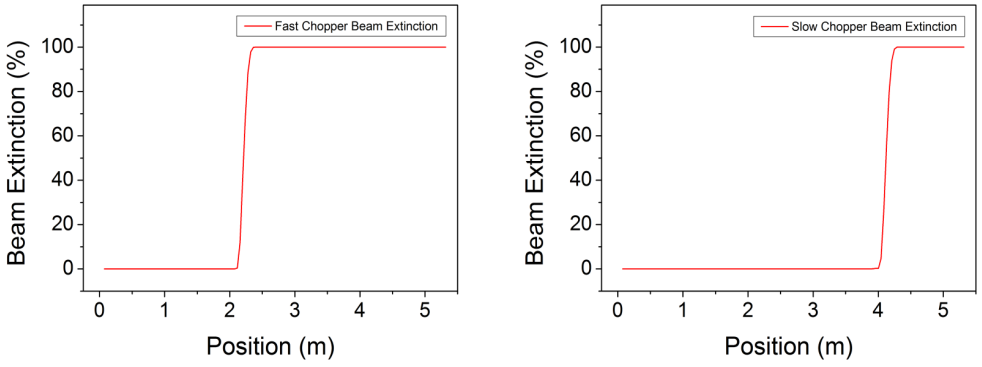

Figure 5.43: Beam extinction in the FETS MEBT when using a waterbag input distribution. Left: Fast Chopper (100%), Right: Slow Chopper (100%).

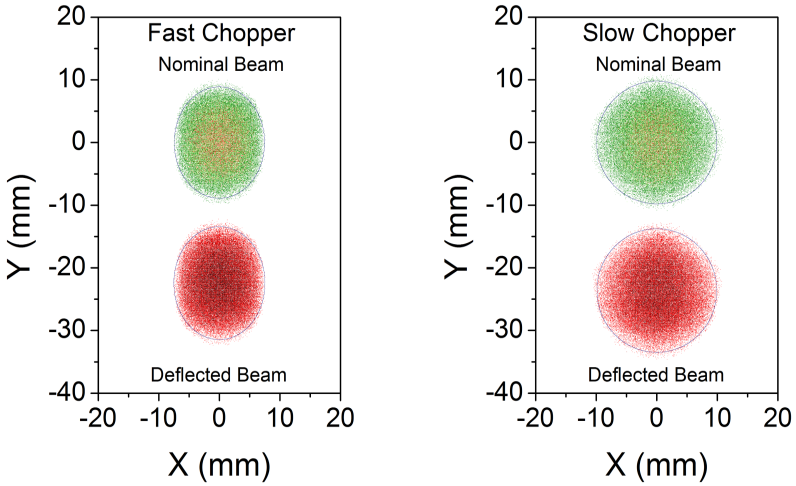

Figure 5.44: Beam separation at the end of the chopper beam dump when using a waterbag input distribution. The 99% emittance ellipse is also shown. Left: Fast Chopper, Right: Slow Chopper.

factor reduction. For the slow chopper the maximum effective voltage is slightly higher: 2.55 kV (equivalent to ±1.275 kV). To compensate for the limited available voltage, a change in beam optics has been implemented that leads to an increase in chopping efficiency. This is done by placing a defocussing quadrupole after the chopper such that the beam can be made flat at the beam dump location.

Figure 5.42 shows the beam envelopes when the choppers are on. The extinction rate when using this distribution is 100% for both choppers, with the entire chopped beam hitting the beam dump. In addition, the voltage can be slightly lowered while maintaining the deflection efficiency. The chopping efficiency is further illustrated in Figure 5.43.

An important measure of chopping efficiency is the separation between the centres of the chopped and nominal beams as well as the distance between the 99% emittance ellipses at the end of the chopper beam dumps. This is illustrated in Figure 5.44. The results further confirm the robustness of the design. For the fast chopper, the distance between the beam centres is 22.3 mm with a 4.4 mm ellipse separation. For the slow chopper, the centre separation is 23.1 mm while the ellipses are 3.5 mm apart.

Another aspect relevant for beam loss control is the bunch length inside the fast chopper plates. As illustrated in Figure 5.34, the fast chopper field has a transition time of ∼2 ns. At 324 MHz the period duration is ∼3 ns, therefore the maximum tolerable bunch length is ∼1

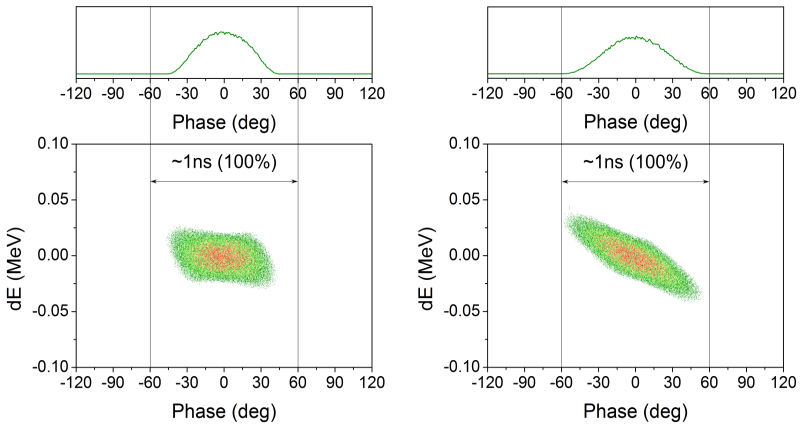

Figure 5.45: Bunch length in the FETS fast chopper when using a waterbag input distribution. Left: chopper start. Right: chopper end.

ns (120 deg). This is to prevent the beam seeing the deflecting field at transition. A lower deflecting field could lead to a reduction in the chopping efficiency and undesirable negative consequences in accelerators downstream. A partially deflected beam could theoretically be trapped and accelerated at higher energies where losses have more serious consequences like machine activation and even equipment damage.

In normal operation, the bunch length is kept sufficiently short such that the beam does not experience the nonlinear part of the RF. For FETS however, the beam is allowed to debunch slightly more in order to reduce requirements on the re-bunching cavities as well as to ease the transverse optics design, by having lower RF defocussing forces. This poses an additional potential beam loss risk and care has to be taken to maintain the bunch length at reasonable values. Figure 5.45 shows the bunch length inside the chopper when using a waterbag input beam. The beam is plotted in the longitudinal phase space at the entrance and the exit of the fast chopper. It can be clearly seen that the beam slowly debunches, but is still well within the safety limits of 120 deg.

At 3 MeV and 60 mA current, the peak beam power is 180 kW. Although in reality FETS will run at a maximum 10% duty cycle, the peak power is extremely relevant in designing the beam dumps and estimating heat dissipation, required cooling and suitable materials. Figure 5.46 shows the peak beam power dissipation on the chopper beam dump. It has been obtained by tracking the deflected bunch through the MEBT and calculating the intersection with the plane of the beam dump. For both fast and slow choppers, the peak beam power

density is ∼100 W/mm^2. The "hot" spots can be clearly identified at several locations and although this figure is relatively high, initial 3D modelling indicates that standard cooling methods will provide adequate heat control.

Component design and implementation

The MEBT technical design described so far is currently being implemented at RAL. A brief description of each accelerator component will further be given. **Electromagnetic quadrupoles (EMQs)** have been designed with a relatively large bore diameter (43 mm pole-tip diameter, 38 mm beam pipe radius) and a total length restricted to a maximum of 80 mm. The length restriction is dictated by the overall optics design in which an attempt is made to keep the MEBT as short as possible in order to minimise emittance growth, halo formation and subsequent beam loss in the downstream linac. The larger bore radius allows additional freedom in manipulating the beam size while avoiding beam loss. The quadrupole can produce a maximum field gradient of ∼20 T/m [165].

Permanent magnet quadrupoles (PMQs) have also been considered. With a very small size and high field gradients, PMQs represent an attractive option with several modern linac projects adopting this solution. However, the inability to adjust the field level is a major inconvenience for a test stand like FETS and the idea has been abandoned.

Similarly, a hybrid quadrupole solution has been investigated. The main aim was to

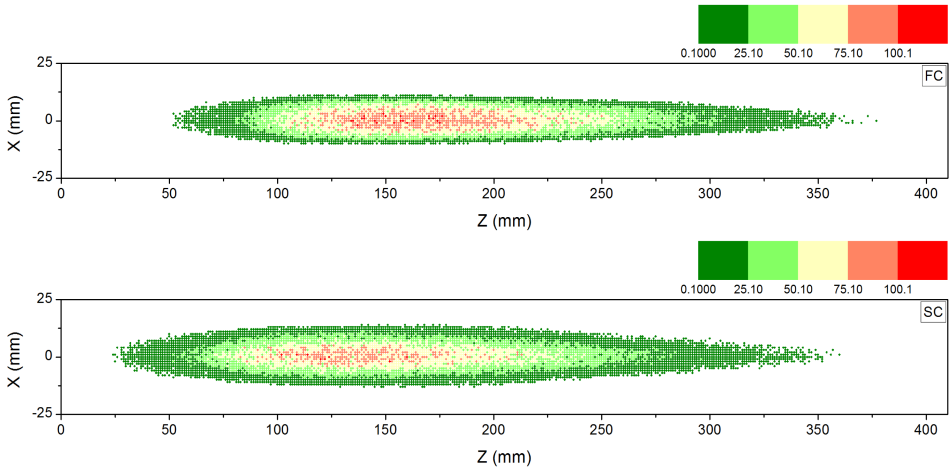

Figure 5.46: FETS MEBT beam power dissipation on the chopper beam dumps when using an input waterbag distribution. Top: Fast Chopper. Bottom: Slow Chopper. Scale as in Figure 2.11.

Effective length	80	mm
Magnetic length	83	mm
Aperture diameter	43	mm
Vacuum pipe diameter	38	mm
Maximum field gradient	20	T/m
Minimum field gradient	4	T/m
Maximum integrated field	1.7	T
Field quality	±0.5	%

Table 5.7: Main FETS MEBT EM quadrupole parameters (compiled from [165]).

address the requirement for a compact design, combined with a (limited) ability to adjust the field gradient. The hybrid quadrupole is a concentric combination of PMQ and laminar conductor EMQ types (Lambertson quadrupole). Relatively small magnetic fields can be obtained by etching the coils turns on a flexible printed-circuit board. The circuit board is rolled to form a cylinder that will provide a quadrupole field. By placing this structure inside the aperture of a PMQ, one can adjust the magnetic field by varying the current in the laminar conductors. The resulting structure is a very compact adjustable PMQ. Given the design complexity and the limited adjustability level, this rather exotic design has been replaced by the more traditional EMQ solution. However, it still remains a promising solution for modern linac projects where variable quadrupole fields are paramount [166],[26],[167]. The three proposed quadrupole designs can be seen in Figure 5.47 with a summary of the main EM quadrupole given in Table 5.7.

A total of four **rebunching cavities** are envisaged for the MEBT line. The main

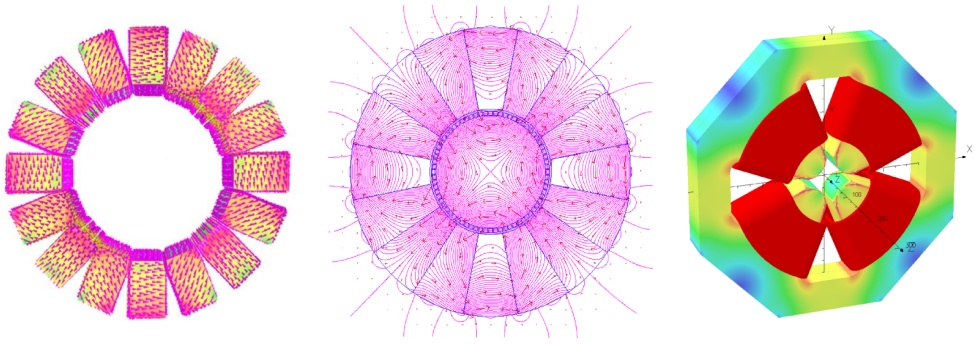

Figure 5.47: FETS MEBT quadrupole designs. Left: PMQ. Centre: Hybrid quadrupole. Right: EMQ. (EMQ picture adapted from [165] - courtesy of S. Lawrie)

requirements have been specified by the beam dynamics design: a 324 MHz frequency, a 17 mm aperture radius and a maximum effective voltage of 160 kV. In designing the cavities several aspects and guidelines have been generally followed:

- High shunt impedance and thus a reduced power consumption and simplified cooling.
- Peak electric field limited to a Kilpatrick factor of 1.6 in order to avoid electrical discharge problems.
- Mechanical design: the cavities have to fit inside the physical limits imposed by the optics design.
- Manufacturing: cooling options, tolerances and generally ease of manufacture.

Different candidate cavity types have been analysed and evaluated by means of electromagnetic modelling and a decision has been made to adopt a single gap pillbox-type cavity with nose cones. 2D (Superfish) and 3D (CST MicroWave Studio) codes have been then extensively used to optimise the cavity geometry by scanning a multidimensional parameter space. Figure 5.48 shows a cavity simulation model as well as an example of a step in the optimisation routine in which a combination of cavity and gap lengths is chosen such that the effective shunt impedance per cavity is maximised while minimising the peak electric field. A summary with the main cavity parameters is given in Table 5.8. It should be noted that a ∼20% increase in shunt impedance can be achieved by reducing the aperture radius

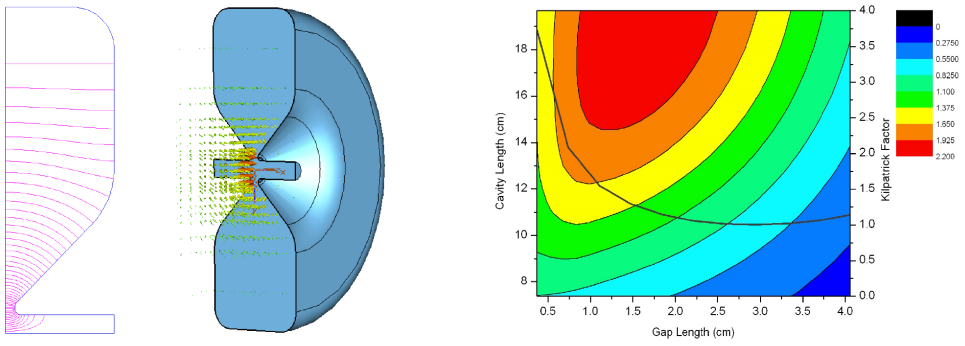

Figure 5.48: FETS MEBT re-bunching cavity. Left: 2D and 3D simulation models. Right: Effective Shunt Impedance per cavity as a function of cavity length and gap as well as the Kilpatrick factor with gap length.

to 15 mm. For FETS this would likely equate with a slight increase in beam loss and is therefore avoided [26],[167],[168].

The development of the **beam choppers** has been explained in detail in Section 5.5.1. The helical and planar electrode designs have been prototyped and are currently being further analysed for potential improvements. The modular nature of these electrodes makes it possible to develop beam choppers of a variable length. For FETS, to reduce the voltage requirements, a 600 mm chopper length has been chosen. The fast and slow pulse generators have been manufactured and are generally compliant with the FETS requirements [160].

Dedicated **chopper beam dumps** are under development. The slow chopper beam dump is particularly challenging as current specifications envisage up to one third of the beam being deflected. For a 10% duty cycle this amounts to ∼6 kW average beam power and because of the beam dump geometry cooling control will be especially hard. The design of the fast chopper beam dump is made easier by the much lower average beam power. For both dumps, pure aluminium is the preferred material due to its excellent radiation performance, although its poor mechanical properties make the design more difficult from an engineering point of view. It should be noted that in reality, when chopping for injection into an ISIS-like synchrotron, a shorter pulse length must be used and a much smaller fraction of the beam will be removed (∼20%). This reduction in machine and chopping duty cycles

Frequency	324	MHz
Effective voltage	160	kV
Q	27444	-
ZTT	12.2	MOhm/m
ZTT per cavity	1.83	MOhm
Kilpatrick/Peak electric field	1.63/29.13	- / MV/m
Power dissipation	13.98	kW
r/Q	33.33	Ohm
Cavity diameter	59.36	cm
Cavity length	15.0	cm
Bore radius	1.7	cm
Gap length	1.6	cm

Table 5.8: Main FETS MEBT re-bunching cavity parameters. For power requirements, an additional 20% factor has to be taken into account to include the effects of tuners, additional ports and ancillary equipment.

will greatly ease the beam dump requirements.

A permanent comprehensive set of **diagnostics** is envisaged for the entire MEBT line to characterise the beam fully, as well as the chopping efficiency. Transversely, the aim is to measure beam profile, beam position, emittance and halo. In the longitudinal plane, transmission, average beam energy, energy spread, bunch shape profile and chopping extinction rate will be analysed. The relevant instruments (current transformers, position monitors, slit-slit and pepperpot emittance scanners, etc) are being developed in-house or acquired commercially. In addition, a laser based, non-destructive emittance measurement instrument will be located at the end of the MEBT line [164], [169].

5.6 Improved MEBT Design with Choppers

The detailed examination of the FETS MEBT design in Section 5.5.2 has revealed that although a satisfactory solution has been found, it is not optimal. Indeed, studies performed with a more realistic beam distribution indicate further beam quality degradation. The observed emittance growth, halo development and small beam loss, although contained, are effects that are not desirable in a high intensity linac. Furthermore, the difficulty of front end beam transportation and chopping has also been made clear in Section 5.4, by analysing the SNS, Linac4, J-PARC and ESS designs, all of which use the same design philosophy as FETS, in which long drifts are reserved for choppers. Although, one might argue that this limitation must be accepted, it is clear that the question of finding an optimised MEBT design with choppers is still relevant and other avenues must be investigated.

5.6.1 The Distributed Chopper Concept

As we have seen, the main difficulty in meeting the beam optics requirements of the chopper line comes from the relatively long electrostatic deflectors and their dedicated beam dumps. These elements break the MEBT symmetry and make it impossible to achieve strong focussing and a smooth phase advance.

The notion that one could instead use several shorter length deflectors placed along the MEBT working synchronously was first suggested as part of the German spallation source

project (SNQ), an early precursor of ESS proposed in the 1980s. Operating at 200 MHz, SNQ required 2.4 m long deflectors for complete beam separation. As reserving such a long space was impractical, a proposal was made to separate the deflectors in six, 40 cm long elements. By choosing a periodic FODO lattice configuration, each cell would hold a deflector at a location such that their kicks would add up for eventual complete beam separation [170]. More recently, a similar idea has been suggested at SNS, as a possible replacement for the current MEBT [129].

The concept itself is in fact an extrapolation of a widely used beam extraction method in circular accelerators in which orbit bumps are created transversely by employing a lattice configuration with several thin dipole kicks [37]. Assuming a single kicker is placed at a certain position in the beam line, the beam coordinate at the beam dump location is given by:

$$\begin{pmatrix} X_D \\ X'_D \end{pmatrix} = M_{(D|K)} \begin{pmatrix} X_K \\ X'_K \end{pmatrix} \tag{5.9}$$

$$M_{(D|K)} = \begin{pmatrix} \sqrt{\frac{\beta_D}{\beta_K}}(\cos\sigma + \alpha_K \sin\sigma) & \sqrt{\beta_K \beta_D}\sin\sigma \\ -\frac{1+\alpha_K\alpha_D}{\sqrt{\beta_K\beta_D}}\sin\sigma + \frac{\alpha_K-\alpha_D}{\sqrt{\beta_K\beta_D}}\cos\sigma & \sqrt{\frac{\beta_K}{\beta_D}}(\cos\sigma - \alpha_D \sin\sigma) \end{pmatrix} \tag{5.10}$$

where $M_{(D|K)}$ is the transfer matrix between the kicker and dump location, α and β are the respective Twiss parameters and σ is the phase advance.

For a kicker deflection angle θ (see Equation 5.2) and assuming an instant deflection kick, from Equation 5.10 it is straightforward to calculate the beam displacement ΔX_{DK} at the beam dump location:

$$\Delta X_{DK} = \theta\sqrt{\beta_K \beta_D}\sin\sigma \tag{5.11}$$

Equation 5.11 shows the two main requirements to maximise the beam displacement and minimise the deflection angle:

- Large beta functions at the kicker and beam dump location.
- A 90 degrees phase advance between the kicker and beam dump.

Of course, in conventional designs like the FETS MEBT, implementation of these guide-

lines has been attempted, but the very nature of the lattice limits the beam optics control. However, a lattice with shorter choppers would overcome these problems, as the much shorter drifts allow improved lattice control.

In consequence, a MEBT line with distributed choppers can be designed following these basic rules. By starting with a simple beam optics lattice, the MEBT can be a sequence of identical cells. If the deflector plates are to be placed in the first cell, for maximum beam displacement, the beam dump would have to be located at 90 degrees phase advance further downstream. For simplification, by choosing a 90 degrees phase advance per cell, the beam dump would be placed in the second cell of the lattice. If the deflection is insufficient, a second deflector can placed in the following cell and the process repeated. It is immediately clear that for optimal chopping, each two adjacent deflector plates would have to be placed 180 degrees in phase advance apart. This is also true for the beam dumps.

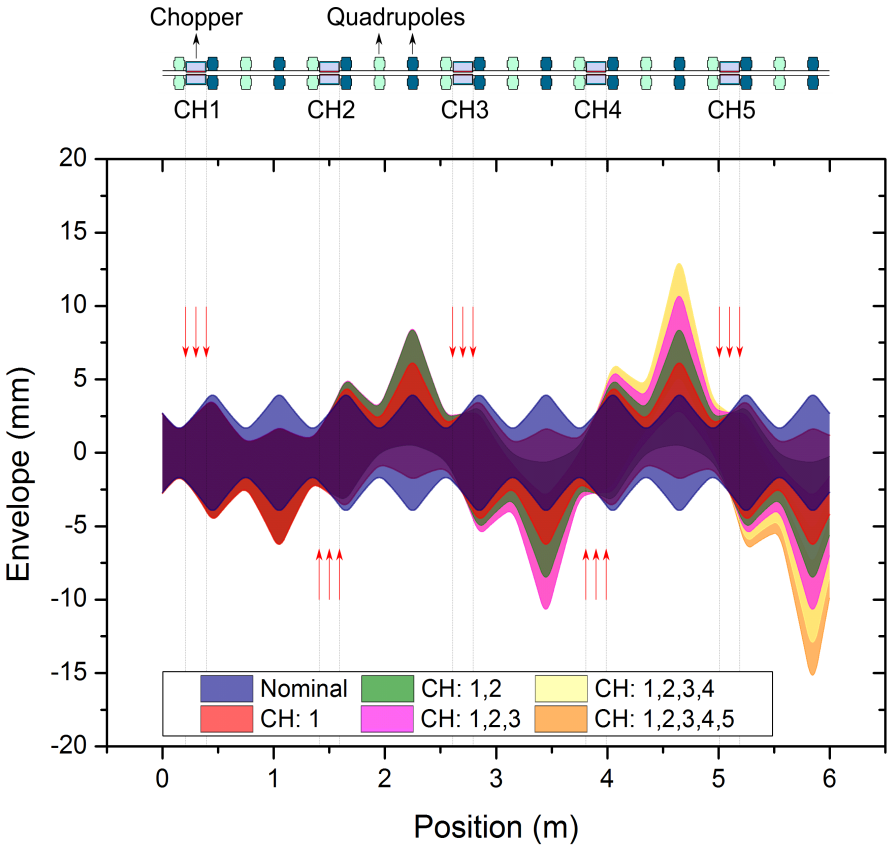

Figure 5.49: 5∗RMS emittance beam envelopes in a 10-cell FODO channel, illustrating the distributed chopping concept. Larger beam amplitudes can be observed, as more deflectors are switched on in succession. The red arrows indicate the position and the direction of the chopping field.

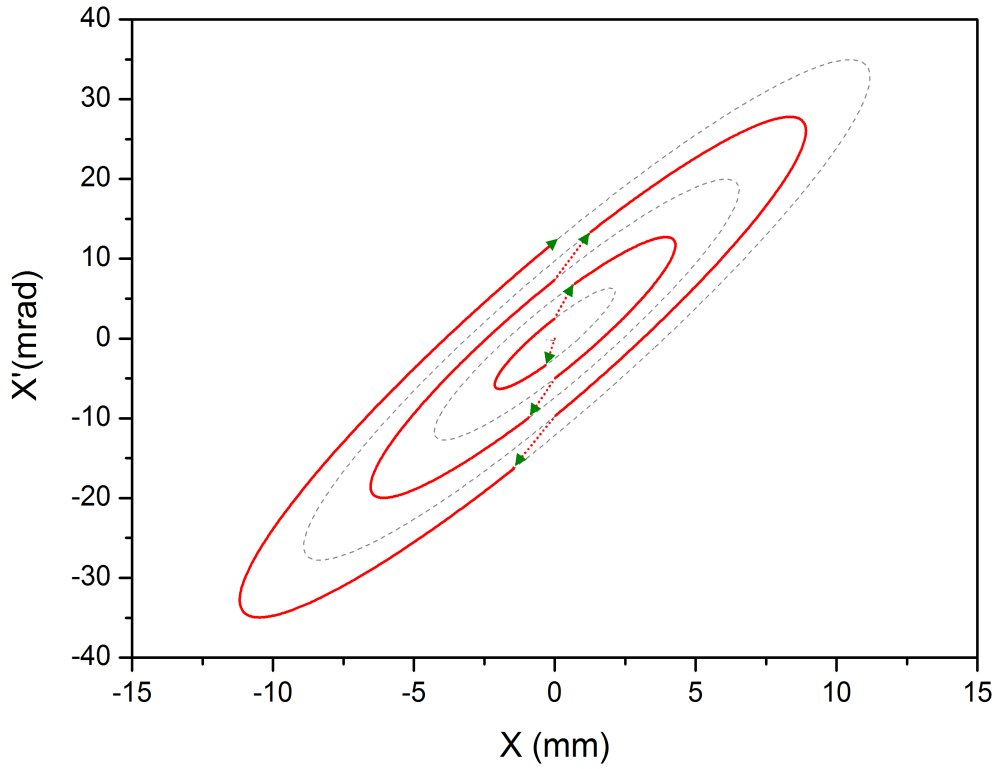

Figure 5.50: Beam centroid trajectory in the horizontal phase space (X-X'). The arrows indicate each of the five deflectors seen in Figure 5.49.

This is illustrated in Figure 5.49 where a transfer line has been designed using 10 FODO cells. Each FODO cell is 60 cm long with 10 cm long quadrupoles separated by 20 cm drift lengths. A total of 5 identical choppers are used, each providing an effective voltage of 1 kV. The nominal beam envelopes are small and uniform, a product of having a regular lattice with strong focussing. As the first chopper is switched on, the beam reaches larger amplitudes, arriving at a maximum at regular intervals. This is where the beam dumps would have to be placed. A second chopper placed in the third cell is then turned on, operating in tandem with the first chopper. Given that the phase advance between them is 180 degrees, for the two deflections to add up, the second chopper kicks the beam in the opposite direction. With additional choppers, the beam amplitudes grow linearly, until the required deflection is attained. The concept is further demonstrated in Figure 5.50 which shows the beam centroid trajectory in the $X - X'$ phase space. It is interesting to see the beam "jump" from one ellipse to another with each kick, as well as the ideal location for the choppers and kickers.

5.6.2 The Novel "Fast-Slow" Distributed Chopping Scheme (FSDC)

The idea of having improved beam dynamics in the MEBT chopper line by employing a distributed chopping scheme, opens the possibility of having an integrated solution that also provides extremely fast chopping. As a result, an innovative design is proposed that combines the "fast-slow" chopping principle to be used in FETS and presented in Section 5.5.1 with the distributed chopping idea.

As the "fast-slow" scheme requires two separate choppers, with the necessary condition that the fast chopper precedes the slow chopper, it appears that the obvious solution in developing a "fast-slow" distributed design is to double the MEBT length such that space is made available for all the deflectors. Consequently, for the benefit of having a fast chopper, the example lattice shown in Figure 5.49 would be 12 m long. This is both uneconomical and impractical.

Nevertheless, a simple solution is proposed in which the fast and the slow choppers are separated in the two transverse planes. The fast chopper deflects the beam horizontally, while the slow chopper deflects it vertically. By adopting this idea, the overall lattice length does not increase. The deflector plates are placed in adjacent drift spaces and the phase advance is kept constant at 90 degrees per cell in both planes, such that the separation between the deflectors is maintained at 180 degrees, as required for maximum deflection.

A lattice illustrating the principle is presented in Figure 5.51. It consists of 11 identical FODO cells as described in the previous section with the location of the choppers easily identifiable. The horizontal and transverse beam envelopes for the nominal (choppers OFF) and chopped (choppers ON) cases can be clearly seen, with complete extinction amplitudes reached in each plane after 5 deflectors with the same configuration as in Section 5.6.1.

The requirement of placing the fast before the slow chopper such that the gap in the bunch train is fully created by the time the slow chopper is turned on is no longer followed. Instead, the short length fast and slow deflectors are interleaved. Consequently, some bunches will be partially deflected vertically by the rising field of the slow chopper.

Assuming a slow chopper pulse transition time of $\sim$12 ns (FETS slow chopper), at 324 MHz, four bunches will experience the rising field of the slow chopper. For a linear

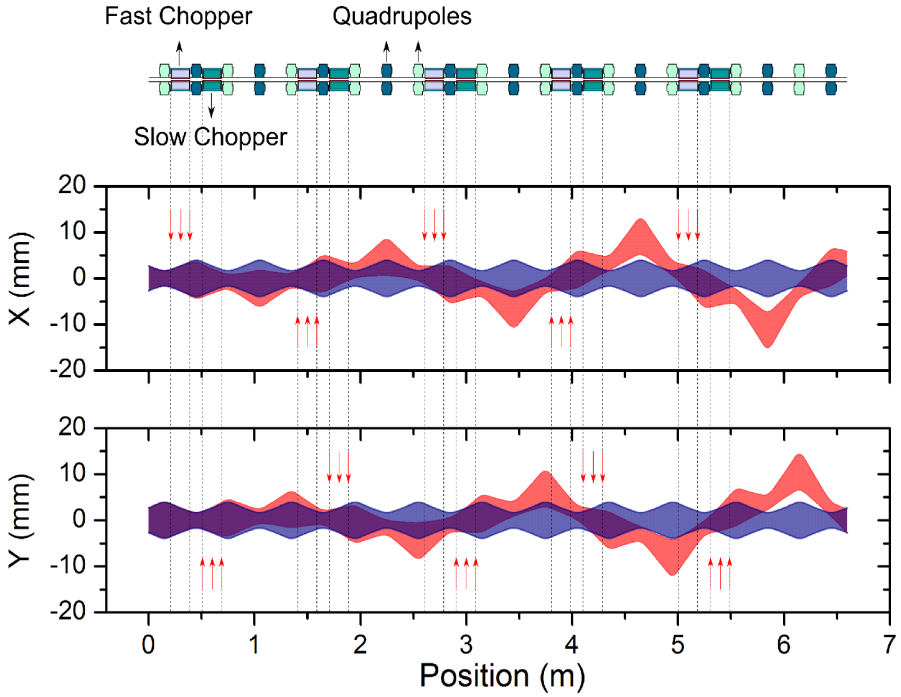

Figure 5.51: Horizontal and transverse 5∗RMS emittance beam envelopes in an 11 cell FODO channel, illustrating the FSDC concept. The nominal beam is shown in blue, while the deflected in red. The red arrows indicate the position and the direction of the chopping field.

field rise, the corresponding fields for each bunch in respect to the peak are approximately 20, 45, 70 and 95%. However, this does not affect the overall beam extinction efficiency, as the same bunches will see the full fast chopper deflection but in the horizontal plane. One consequence of having the additional slow chopper field is a small displacement of the nominal beam position inside the deflectors, but the very nature of the meander line structure means that the structure field amplitude and quality is not affected. On the other hand, the rising slow chopper field can have the additional benefit of partially chopping the beam deflected by the fast choppers, thus reducing the load on their respective beam dumps.

The beam centroid trajectory in the transverse plane when both choppers are fully operating is illustrated in Figure 5.52. It describes an approximate spiral path driven by the successive deflector kicks, with additional twists given by the MEBT lattice. For both the fast and slow choppers, the beam movement in the $X - X'$ and $Y - Y'$ phase space is as already described in Figure 5.50.

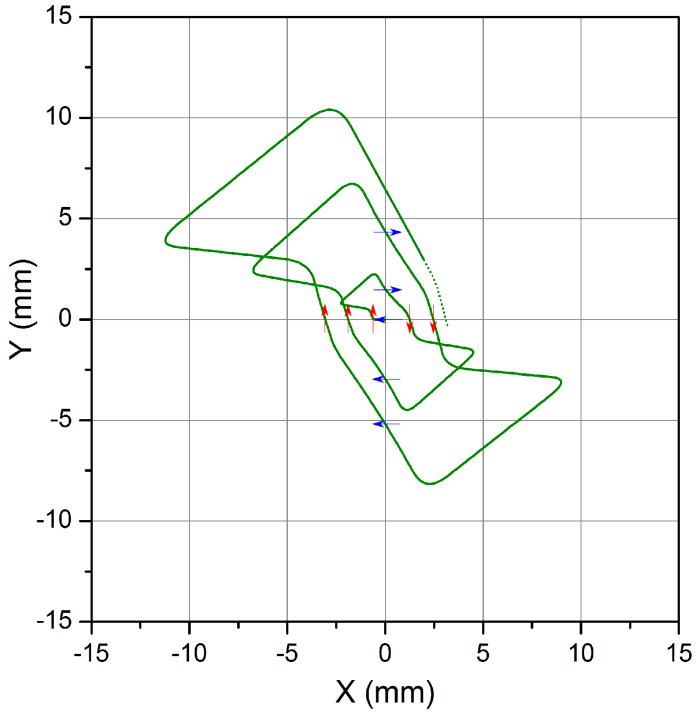

Figure 5.52: Transverse beam centroid trajectory (XY plane) with both fast and slow choppers operating. The blue arrows indicate the fast chopper deflection (horizontal), while the red arrows indicate the slow chopper (vertical).

5.6.3 A "Fast-Slow" Distributed Chopper MEBT Line

The novel "fast-slow" distributed chopper proposed here is theoretically promising, but further effort is required to translate the concept into a realistic design. This is because in a normal MEBT additional space is required to accommodate re-bunching cavities for longitudinal beam control, chopper beam dumps, diagnostics and ancillary equipment. A complete implementation is proposed and analysed here. A FODO type lattice is adopted as the basic optics cell and makes use of the same components assumed for the FETS project: quadrupoles, re-bunching cavities and deflector electrodes. The layout is similar with the

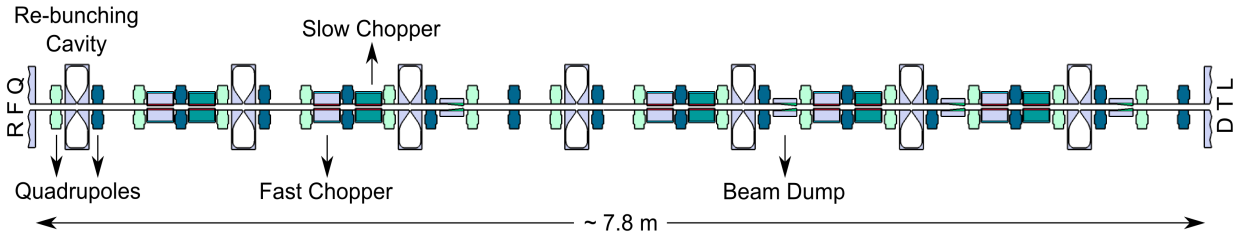

Figure 5.53: Schematic layout of an FSDC MEBT line using a FODO-type lattice.

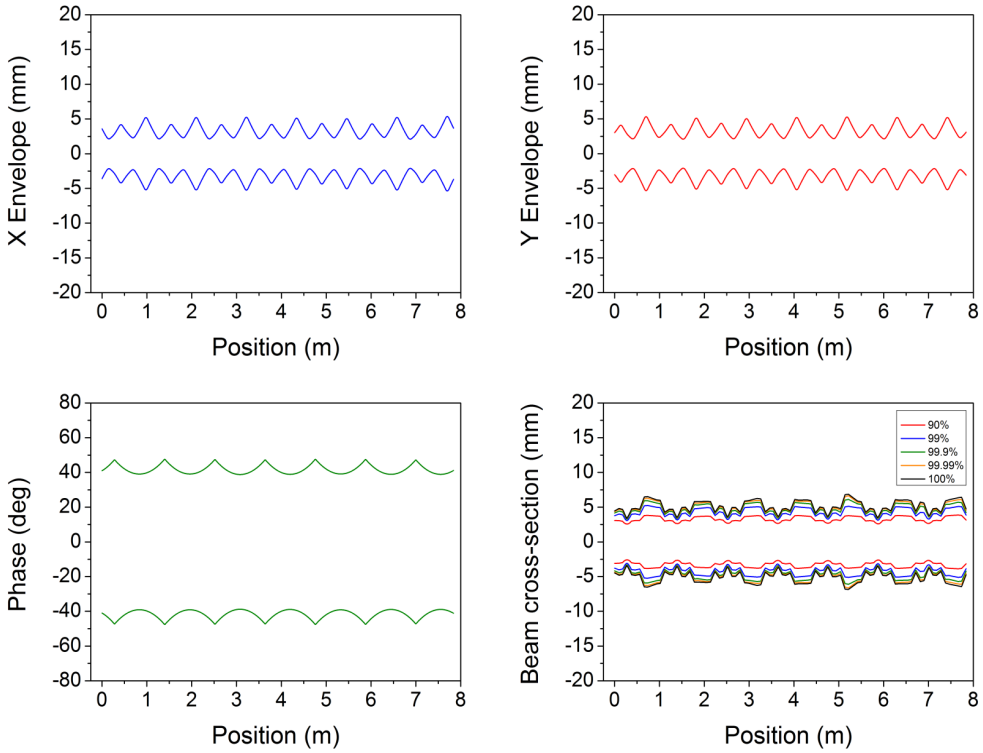

Figure 5.54: 5∗RMS emittance beam envelopes and beam radius at different density levels in the FSDC MEBT line. Horizontal (top left), Vertical (top right), Longitudinal (bottom left), Beam Radius (bottom right)

conceptual lattice presented above and can be seen in Figure 5.53. The distance between quadrupoles is kept constant at 20 cm. This leaves sufficient room for a single chopper deflector module to fit in the appropriate drift space. Should the drift need to be made shorter, a new electrode design would be needed. The overall MEBT length is ∼7.8 m and consists of 14 cells. This is dictated by the requirement to achieve complete beam extinction by the end of the line with both the fast and the slow choppers. A small input section consisting of two quadrupoles is added at the beginning of the line to match the beam from the RFQ. A similar matching section is added at the end of the line for DTL matching. Furthermore, two cells in the middle of the MEBT are intentionally left without deflectors and reserved for diagnostics, thus providing ∼60 cm of supplementary space. The overall MEBT dedicated diagnostics space is ∼120 cm. This is in addition to the space available inside quadrupoles and in small gaps for BPMs, steerers and toroids.

From a beam optics point of view, a zero current transverse phase advance of 90 degrees per cell is chosen, so as to maximise the chopping efficiency and avoid envelope instabil-

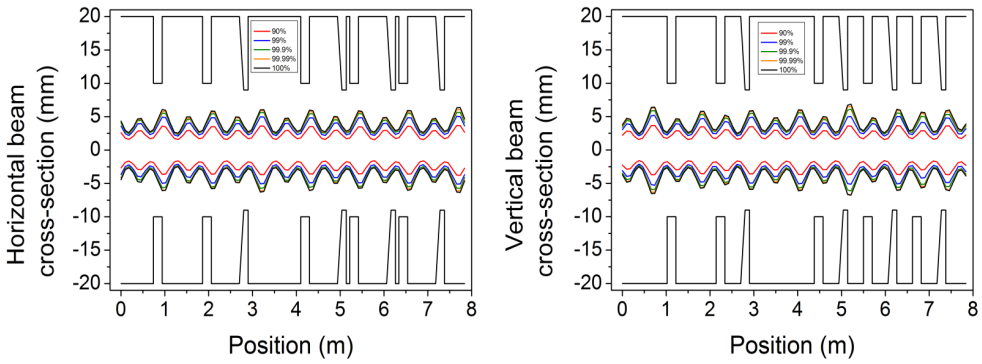

Figure 5.55: Beam cross-section in the FSDC MEBT line.

ity. Figure 5.54 shows the 5∗RMS emittance beam envelopes horizontally, vertically and longitudinally as well as the radial cross-section when tracking a FETS-like beam: 60 mA, 324 MHz bunching, waterbag distribution with 100000 macroparticles (see Figure 5.37). As emphasised previously, the advantage of using a periodic lattice is immediately reflected in the regular, smooth beam envelopes. The result is a much smaller beam size than in conventional MEBT designs, with a maximum extent of ±11 mm transversely and ±47 degrees longitudinally, which effectively eliminates the possibility of the beam experiencing the fast chopper field at transition, which is a concern for the FETS MEBT. Figure 5.55 shows the transverse beam cross-section at different density levels, as well as the beam pipe aperture. The beam is well within the aperture limits and extensive particle tracking indicates a loss free operation.

A better illustration of the improved beam dynamics in this scheme is given in Figure 5.56, which shows the RMS beam emittance evolution as the well as the halo parameters when

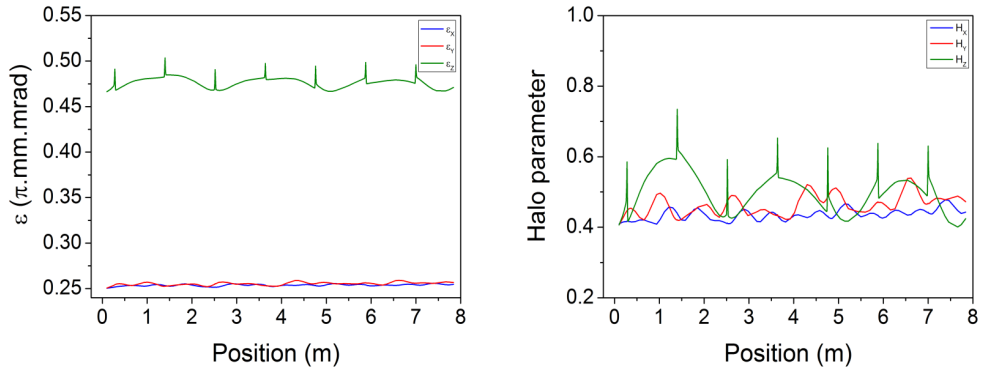

Figure 5.56: Evolution of the normalised RMS beam emittance (left) and halo parameters (right) in the FSDC MEBT line.

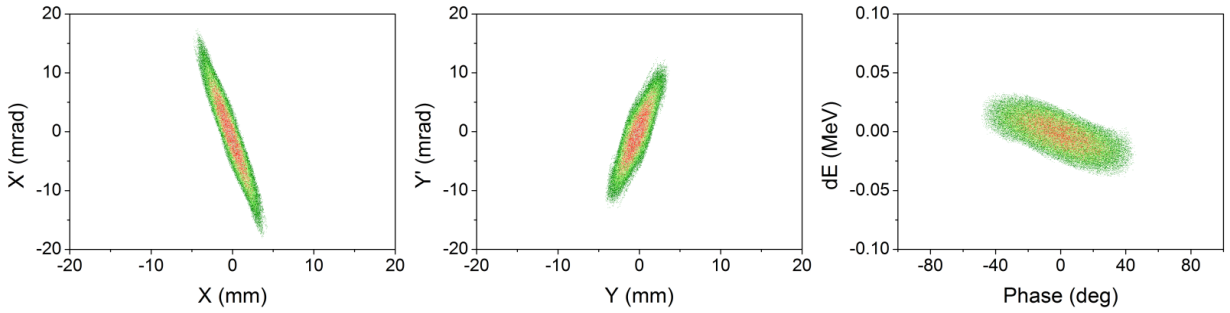

Figure 5.57: Output beam distribution in the FSDC MEBT line (horizontal, vertical and longitudinal phase-space). Scale as in Figure 2.11.

tracking the same particle distribution. The overall emittance growth is less than 5% in all the planes, while the halo parameters, although on an ascendant trend, remain more or less constant. The importance of low beam emittance is a well recognised essential requirement for high intensity high power operation, and the very low growth observed here illustrates the design robustness. A 5% emittance growth is almost outside the capabilities and resolution of existing beam diagnostics devices. The output beam distribution without any additional matching constraints can be seen in Figure 5.57. However, this MEBT arrangement allows a range of beam configurations in terms of Twiss parameters.

Overall, this particular MEBT layout needs 28 quadrupoles and 7 buncher cavities. This rather large number of elements is the price to pay for improved beam dynamics. If necessary, the number of quadrupoles and cavities could be reduced by removing the matching and the dedicated diagnostics sections, as the scheme could potentially be modified to allow matching using only the chopping cells. One advantage of this scheme is the possibility of designing an RFQ to DTL transport channel that allows a smooth phase advance transition. The entire MEBT would become a matching section following a certain phase advance curve, with additional choppers that would have to be placed at locations such that their deflections would be synergistic.

For a very high chopping efficiency, five fast and five slow quadrupoles are needed when assuming the FETS deflector operational characteristics. The radial cross section in both planes, when choppers are on, can be seen in Figure 5.58. One dedicated beam dump is envisaged for each pair of fast and slow choppers, with the exception of the first set, where the deflected beam amplitudes are not sufficiently large to reach the beam dump aperture,

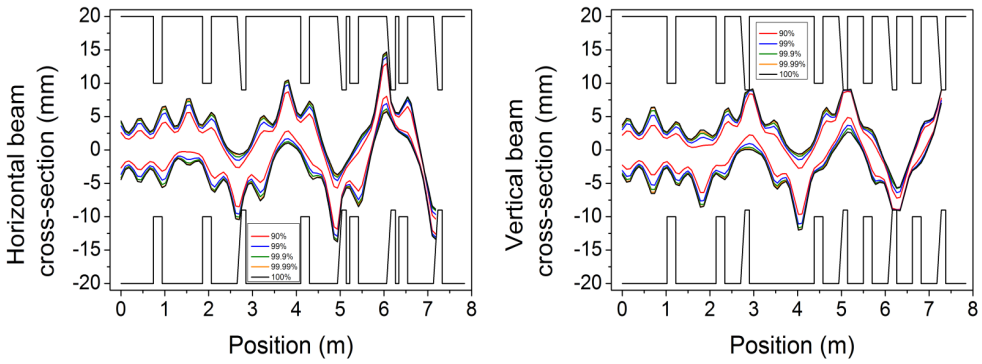

Figure 5.58: Deflected beam cross-section in the FSDC MEBT line.

thus the beam dump becomes obsolete and is therefore removed. The beam extinction evolution for both the slow and the fast choppers can be seen in Figure 5.59. In both planes a 100% efficiency is reached, with the last deflectors needing only a reduced voltage, thus allowing additional safety margins, or potentially operating the entire MEBT with reduced deflector voltages. The separation between the chopped and nominal beam at the last beam dump is much higher than any of the established designs analysed so far.

For different initial conditions and requirements, such a chopping scheme can be easily modified. Should the total deflecting voltage not be sufficient, additional cells with choppers can be added without any degradation in beam quality. Similarly, the MEBT can also be made shorter. The requirement of having four separated beam dumps, although it increases the project complexity, has the indisputable benefit of reducing the average beam power per dump, thus easing the cooling requirements. For the beam dump design, adjustable apertures are foreseen, which is a major advantage in limiting operational losses, decreasing

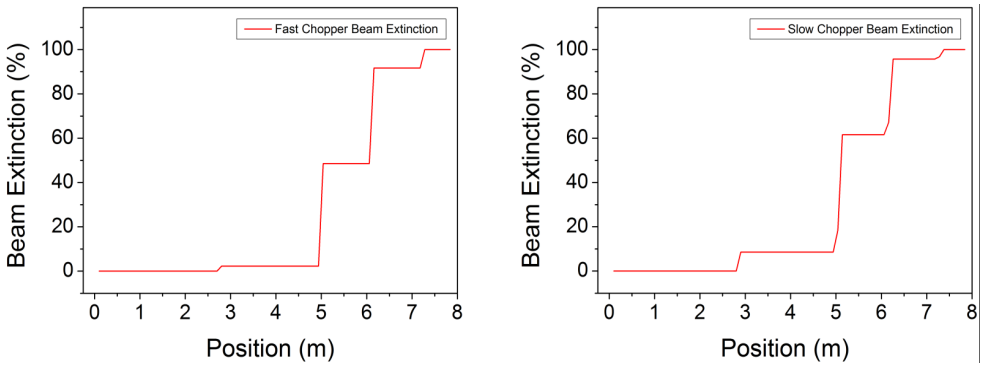

Figure 5.59: Beam extinction in the FSDC MEBT line. Left: Fast Chopper (100%), Right: Slow Chopper (100%).

the deflector voltages and increasing operational flexibility.

Alternative focussing lattices

The MEBT scheme described above shows clear advantages when compared with the baseline FETS MEBT. Different focussing lattices can be employed as an alternative to the FODO cell. One such option is an FFDD lattice.

Considering a FODO cell of length $2L$, with quadrupoles of focal length f and a phase advance per cell μ, from the cell transfer matrix, the phase advance per unit length is:

$$\sigma = \frac{\mu}{2L} = \frac{1}{2f} \tag{5.12}$$

For an FFDD cell:

$$\sigma = \frac{\mu}{4L} = \frac{\sqrt{2}}{2f} \simeq 1.4\frac{1}{2f} \tag{5.13}$$

It follows that with an FFDD lattice, the same phase advance per unit length can be achieved as with a FODO cell, but with reduced quadrupole gradients, thus easing the quadrupole requirements. A certain FFDD MEBT can be imagined. For such an arrangement, the maximum beta functions would be in the drift sections. By placing the deflectors in these drifts, the chopping efficiency would be highest (see Equation 5.11). On the other hand, longer focussing periods lead to a growth in beam size and since aperture is limited, the viability of such a scheme would have to be analysed.

5.6.4 End-to-end linac simulations with MEBT

To characterise the capabilities of the "fast-slow" distributed chopper MEBT scheme (FSDC) further, an end-to-end simulation study of high intensity beam dynamics and beam transport was undertaken. A comparative assessment of two different MEBT design approaches has been performed, when the FETS and the FSDC MEBT designs were each fed into the same linac structure. This approach allows a better understanding of the matching capabilities of the two schemes, as well as observing any effects that are triggered in the MEBT, but take much longer to develop [154].

The linac structure used is the DTL section of one of the early linacs proposed for ISIS upgrades. The complete linac is ∼245 m long, not including the high energy beam transport and ring injection line. It consists of a FETS-like front end (H^- ion source, LEBT, 3 MeV, 324 MHz RFQ and MEBT), followed by a DTL that will accelerate the beam up to ∼75 MeV. A superconducting linac at 648 MHz will further accelerate the beam up to 800 MeV using three families of elliptical cavities with transition energies at ∼196 and ∼412 MeV [171], [172].

The DTL itself is ∼37 m long and accelerates the beam in four tanks. The average axial electric field is ramped from 2.9 to 3.1 MV/m in the first tank and then kept constant. A FODO focussing lattice is used throughout the linac. From a beam dynamics point of view, equipartitioning between the transverse and the longitudinal energies is obtained in the first tank and maintained up to the final energy. Longitudinally, a large acceptance is needed at the beginning of the DTL and consequently, the synchronous phase is set to -42 degrees in the first few cells. As the beam becomes more bunched, the phase is slowly increased. Inter-tank matching is done transversely with six transition quadrupoles, while longitudinally it is achieved by offsetting the synchronous phase in selected tank end cells.

The reason that only the DTL section has been used for this study is to do with a certain feature of the 800 MeV linac. To limit the losses downstream, a collimation section is added at the end of the DTL, before injection into the superconducting linac. This intermediate beam transport section is intended to intercept halo and far off-momentum particles with stripping foils and loss collectors, and therefore, any higher order effects originating from the front section are in theory either partially mitigated in this section, or masked further downstream.

For this study, the FETS MEBT presented in Section 5.5.2 and the FSDC MEBT presented in Section 5.6.3 have been employed with minor modifications: the addition of a supplementary quadrupole at the end of the FETS MEBT matching section to match the focussing sequence of the DTL. A total of five quadrupoles and two rebunching cavities are needed for matching. For the same reasons, one quadrupole is removed from the FSDC MEBT where matching is done without an additional matching section, but using the elements of the chopper cells. This alters the ideal phase advance for chopping in the last

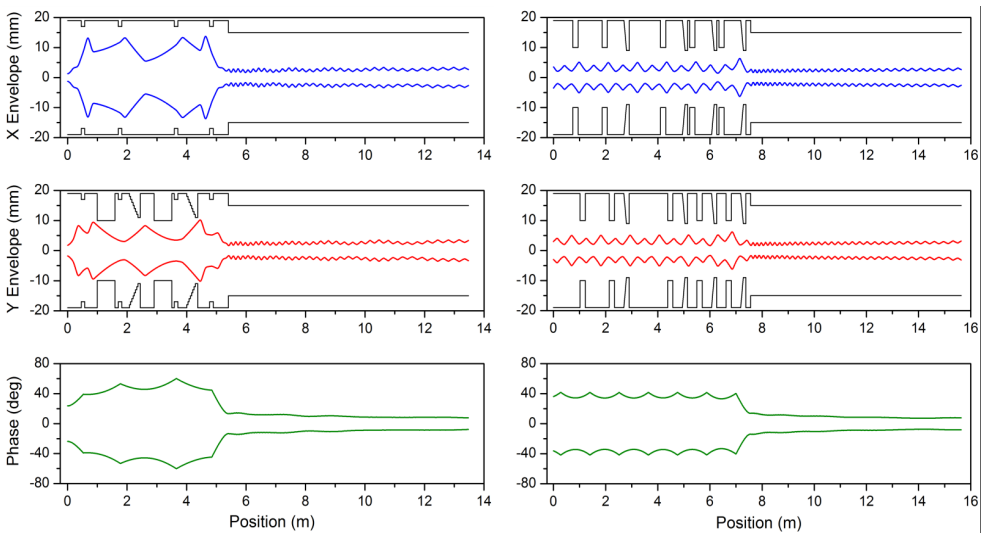

Figure 5.60: 5∗RMS emittance beam envelopes in a ∼20 MeV single DTL tank when using a FETS-type (left) and an FSDC-type MEBT (right).

cells, but has no effect on the chopping efficiency, as the voltage budget is sufficient for compensation.

The 5∗RMS emittance beam envelopes in the MEBT and the first DTL tank are presented in Figure 5.60 for the two cases when using a waterbag input distribution. The beam current is 43 mA, as per linac specifications. For both cases, the envelope evolution (from the envelope equation) is smooth indicating a good envelope match. However, when estimating the envelope from beam tracking, for the FETS case, small envelope oscillations can be observed along the DTL. These oscillations appear despite an apparently good envelope matching at the MEBT to DTL transition and are caused by the beam features at the end of the FETS MEBT that lead to a small distribution mismatch into the DTL.

The normalised RMS emittance evolution (longitudinal and transverse) is shown for both cases in Figure 5.61. A smaller emittance growth can be observed at the end of the FSDC MEBT than in the FETS MEBT, attributed to a variety of factors already discussed. This difference is subsequently preserved throughout the DTL, an indication of a solid linac design. For the FETS case, the total growth is ∼12.2% transversely and 5.1% longitudinally, while in the FSDC case, it is 4.5% transversely and 3.5% longitudinally. For comparison, the RMS emittance growth in the same DTL without a MEBT is ∼4.4% transversely and 2.1% longitudinally. Regarding the halo, the halo parameters (using Wangler's definition [29])

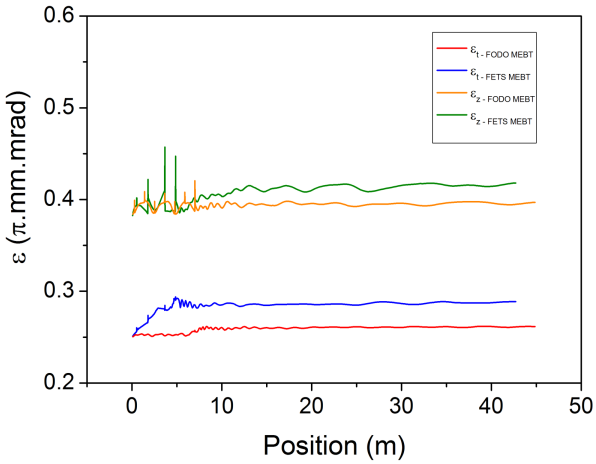

Figure 5.61: Evolution of the normalised RMS beam emittance in a DTL linac when using a FETS-type and an FSDC-type MEBT.

starting from the same initial conditions increase by 20% transversely and 35% longitudinally over the length of the linac for the case using the FSDC MEBT. For the FETS MEBT, the increase is 50% transversely and 60% longitudinally.

5.7 Chapter Summary

In this chapter a generic analysis of a linac front end was performed, with the aim of understanding the limitations in designing an RFQ to DTL matching section where both high quality beams and high efficiency chopping are sought. These are key ingredients for future high power, high intensity machines in which initial mismatch is to be avoided if low loss operation is paramount. The first comprehensive beam dynamics model created for the ISIS linac emphasised the necessity of designing suitable MEBT lines. While the simple MEBT proposed for ISIS would reduce the 20% linac beam loss observed at the moment to less that 1%, the question of optimal MEBT design with choppers remained. Four proposed or operational MEBTs were further analysed: ESS, Linac4, SNS and J-PARC. A comprehensive summary of the chopping capabilities was presented. With this analysis, a broad list of requirements was produced emphasising the fundamentally conflicting demands for MEBT design in terms of beam dynamics and beam chopping.

Attention was then shifted to the Front End Test Stand project, now under construction at RAL. Like many similar projects, FETS consists of an H^- ion source, a solenoid LEBT,

an RFQ and a MEBT line. It has the declared aim of producing high quality chopped beams and will employ a novel "fast-slow" chopping scheme. The ample FETS MEBT analysis illustrated further the difficulty in meeting both the beam chopping and beam quality demands.

A distributed chopper concept was then discussed as a potential alternative to conventional chopper lines. This idea was then adapted to produce a novel MEBT design with a "fast-slow" distributed chopper. The proposed MEBT, although economically more expensive due to its length and the larger number of components, has the unrivalled benefit of preserving the beam quality while achieving extremely fast, perfect chopping. The small emittance growth, the absence of beam loss or partially chopped bunches, the lower deflection voltages, the multiple beam dumps, the much easier upstream matching as well as the design flexibility and modularity make the proposed scheme a strong alternative to existing MEBT lines with choppers.

Chapter 6

Options for the Next Generation ISIS Linac

This chapter applies the concepts discussed in this thesis regarding overcoming energy and intensity limiting factors in proton linacs, to the design of the next generation ISIS linac. The general design rules and choices are outlined both in terms of RF structures and linac configuration as well as beam dynamics. Emphasis is placed on equipartitioning, a rather contentious subject on which diverging opinions are often shared among linac designers. As an addition to this subject and a justification for some of the design choices, preliminary results are presented from recent work performed on the J-PARC linac. In this experiment, for the first time, space-charge induced emittance exchange driven by the $k_z/k_t = 2$ resonance was measured in a linac with emittance ratios close to 1. In the second part of the chapter, details are given on the design of three linacs, which are proposed as potential ISIS upgrades under different scenarios.

At the time of writing, several ISIS linac upgrade options are being considered. As already explained, the linac being the oldest part of the machine is in continuous need of maintenance just to keep the current level of performance and therefore small updates are taking place regularly and a solid work programme is ongoing. However, a more major upgrade is inevitable. While plans for a new machine are welcome, any proposal has to take into account several factors, of which two are more essential.

The first requirement is that any upgrade work should take into account the high likelihood of a phased upgrade. This simply means that any design choice should be made in the wider context such that later upgrade efforts are not hampered by early choices.

The second requirement takes into account the wider context of neutron science in Eu-

rope. With several experimental reactors due to be retired and with ESS not being fully operational for another decade, ISIS remains the main source of neutrons. Indeed, demand for beam time is at an all time high. This makes machine availability the dominant user requirement and as a result, potential upgrades with minimum user disruption should be proposed. Three linac upgrades[173] will be outlined in this chapter:

- **A new 100 MeV linac** to replace the old 70 MeV injector. This potential upgrade, uses the existing linac tunnel, so it has the benefit of a reduced overall budget as little civil engineering work will be needed. By operating at a higher frequency and optimising the design, energies in excess of 100 MeV can be achieved with a machine having the same length as the current 70 MeV linac.

- **A new 180 MeV linac** would require a new tunnel and therefore will be a bigger financial effort. This solution however, would not only solve the current reliability issues, but would also lead to a increase in the total beam power by injecting at a higher energy thus allowing an increased ring intensity.

- **A new 800 MeV linac** is part of a wider long term upgrade scenario that would require the use of superconducting technology and the construction of additional rings that would offer MW level beam powers.

6.1 General Design Choices

This section will describe and defend the general design choices adopted for the upgrade linacs proposed here. The frequency choice is strongly linked with the choice of frequency for the FETS project. The current RF frequency of the ISIS linac is 202.5 MHz and a proposal was made to keep the existing frequency as a cost saving measure as existing klystrons, amplifiers and RF equipment could be reused. Additionally, a lower frequency provides more space for quadrupoles and reduces the requirement on manufacturing and alignment tolerances. However, this option was quickly ruled out as it would have led to a long and inefficient linac using a frequency mostly abandoned, for which no possible R&D collaboration exists. Instead the choice was reduced to the 324 and 352 MHz frequencies, both used in a number

of international projects. 324 MHz is the frequency adopted by the J-PARC linac for which Toshiba has a highly successful klystron development and it is the lowest frequency where klystrons maintain their efficiency. 352 MHz is the frequency inherited from the LEP accelerator, which has also been adopted by a number of modern projects and for which Thales has developed a klystron. While 352 MHz opened the possibility of collaboration with two main projects in Europe (i.e. Linac4 and ESS), at the time the frequency choice decision was made (early 2000s), the immediate availability of the 324 MHz Toshiba klystron for the FETS project and the simplified chopper design made possible by the lower frequency led to the 324 MHz choice as the fundamental frequency for FETS and subsequently for the upgrade linacs for which FETS is adopted as the front-end [174].

6.1.1 Structures

The choice of accelerating structures for the three linacs described here is derived from the broad comparison of RF cavities presented in Chapters 3 and 4 and will be outlined below.

- For **the low energy part** (up to 100 MeV), the choice is between the DTL and the CH-DTL. The DTL offers the advantage of being a stable, well-understood and "safe" structure, while the CH-DTL has the advantage of high power efficiency. However, this stage of the linac is planned to be only the initial acceleration phase, to be followed by additional structures in subsequent upgrades and therefore further constraints had to be taken into account. One of the main disadvantages of the CH-DTL structure is a much higher emittance growth than the DTL, caused by the nature of its transverse optics. This would not be particularly problematic if the linac injected directly into a ring, but since matching to the downstream accelerating structures is needed, more limiting factors had to be considered. Medium and higher energy structures have strict aperture budgets and if high power operation is sought, lossless operation becomes paramount. This makes the higher output emittance of a CH-DTL linac difficult to overcome and consequently a DTL operating at 324 MHz was adopted instead, as a good compromise between RF efficiency and beam dynamics.

- For **the medium energy range** ($\sim$100 - 200 MeV) several choices were analysed:

SDTL, CCDTL, CCL, ACS and PIMS. Amongst many aspects considered, the overall linac design simplicity was one of the driving factors. This led to the decision to minimise the number of cavity types, thus making construction easier and removing additional transitions where matching schemes would have been necessary. As a result, it was decided to keep the DTL structure up to ∼100 MeV and avoid switching to a different structure at around 50 MeV where more options become available. Consequently, structures like the SDTL, and the CCDTL were ruled out and so the choice was reduced to a $\pi/2$ or π-Mode structure. The π-Mode as described in Chapter 4, offers comparable shunt impedance to a $\pi/2$ structure, but the advantage of avoiding a frequency jump. However, for the ISIS upgrade linac, it was considered necessary to have a frequency jump after the DTL. This takes into account the requirements for the future 800 MeV linac for which a higher frequency structure will be necessary. By having a frequency jump after the DTL, necessary klystron development can begin early and therefore be available for the next, higher energy upgrade stage where the same frequency would be kept. Additionally, recent experience gained at CERN with the construction of the PIMS cavities suggests that the level of difficulty greatly exceeded expectations and raised the project complexity, cost and delivery times. Consequently, the CCL $\pi/2$-Mode structure was chosen operating at 648 MHz, twice the DTL frequency. The ACS alternative, while it has good characteristics, represents a much higher manufacturing effort as was shown in Chapter 4 and was therefore not adopted.

- For **the high energy range** (above ∼200 MeV) it became obvious that the most economic solution was to adopt superconducting cavities. Operating at the same frequency as the upstream CCL cavities, 648 MHz elliptical cavities are proposed to accelerate the beam to 800 MeV.

6.1.2 Beam Dynamics

The beam dynamics design follows several general rules already discussed in Chapters 2 and 4. Every effort is put into achieving a good matching both at the beginning and at transition

between structures. Initial matching is particularly important as it can limit the performance of the entire machine. A good MEBT design therefore becomes essential and the novel "fast-slow" distributed chopper solution proposed in Chapter 5 will be adopted. In addition to this, a smooth and continuous phase advance and a regular lattice will be implemented, with the zero current phase advance always below 90 degrees both transversely and longitudinally to avoid quadrupole-type envelope instabilities [36]. To limit the halo development the tune depression is kept at reasonable values, usually above 0.5. Space-charge resonances are avoided by choosing the correct phase advances. Beam loss also has to be minimised to limit the machine activation. This is achieved by having sufficient beam aperture without compromising the machine efficiency and by placing lower limits on the transverse phase advance and period lengths such that the beam size is contained.

6.1.3 The J-PARC Space Charge Resonance Experiment

These general rules have been the broad design guidelines used for the three linacs to be presented here. One rather contentious subject is the rule regarding choosing the correct phase advances such that space-charge resonances are avoided. As shown in Chapter 4, modern linacs like J-PARC, ESS (2012 design), FAIR Linac and Linac4/SPL have been designed to follow the "equipartitioning rule", while others like ESS (2014 design) and SNS have a different approach. It is not surprising that diverging opinions regarding this subject are shared among linac designers. The limits of equipartitioning will be further discussed in the context of an experiment recently performed at J-PARC.

Background Physics

Space-charge coupling resonances have long been recognised as possible sources of emittance growth or exchange with potentially severe consequences for beam quality and transmission rates. Historically, in high intensity linacs resonances have been avoided by designing "equipartitioned" (EQP) machines in which the beam "temperatures" or "energies" are kept equal in the transverse and longitudinal planes:

$$\frac{T_t}{T_z} \sim \frac{k_t \epsilon_t}{k_z \epsilon_z} \sim 1\,. \tag{6.1}$$

In equation 6.1, t and z represent the transverse and longitudinal planes, while k is the tune and ϵ the RMS emittance. The mechanism behind this philosophy implies that non-equipartitioned states can become equipartitioned by exchanging energy, thus leading to a corresponding increase and decrease in emittance in the relevant planes. The effect was identified as a coherent space-charge instability and analytical work by I. Hofmann, R. Jameson and others based on the integration of Vlasov's equation for 2D, KV beams, leads to the identification of several eigenmodes. Particle density redistribution can excite these modes, which can grow exponentially producing non-linear fields that can lead to an emittance redistribution. Multiparticle computer simulations were then used to simulate the effect of these eigenmodes on the beam quality with the recommendation that such instabilities are to be avoided. Indeed, an EQP design avoids these instabilities, as there is no free energy available to drive the emittance exchange. However, EQP also implies a strict phase advance law throughout the linac. Consequently, this imposes limits on the selection of working points leading to a potentially less optimised design. This is especially true for superconducting linacs where the availability of high electric fields leads to a higher longitudinal phase advance. However, to follow the EQP rule the phase advance needs to be kept within certain limits, usually by lowering the electric fields. The result is a longer, more expensive linac design which does not use the entire voltage available from the cavities [175], [176], [177], [38].

A further development of the analytical work on coherent space-charge instabilities was the realisation that high current non-equipartioned beams do not necessarily evolve towards equilibrium and the resulting emittance redistribution. Provided the tunes are chosen such that coupling resonances are avoided, linacs that break the EQP rule can be safely designed and operated [178].

Stability diagrams have been developed that chart the unstable areas where coupling resonances can be excited and where coherent space-charge instabilities affect the beam. These charts, often called "Hofmann diagrams", show analytically calculated growth rates for different emittance ratios as a function of tune depression and longitudinal to transverse focussing ratio and are now a practical design tool for linac beam dynamics [179]. An example of a stability diagram is seen in Figure 6.1 for two emittance ratios: $\epsilon_z/\epsilon_t = 1.2$ and

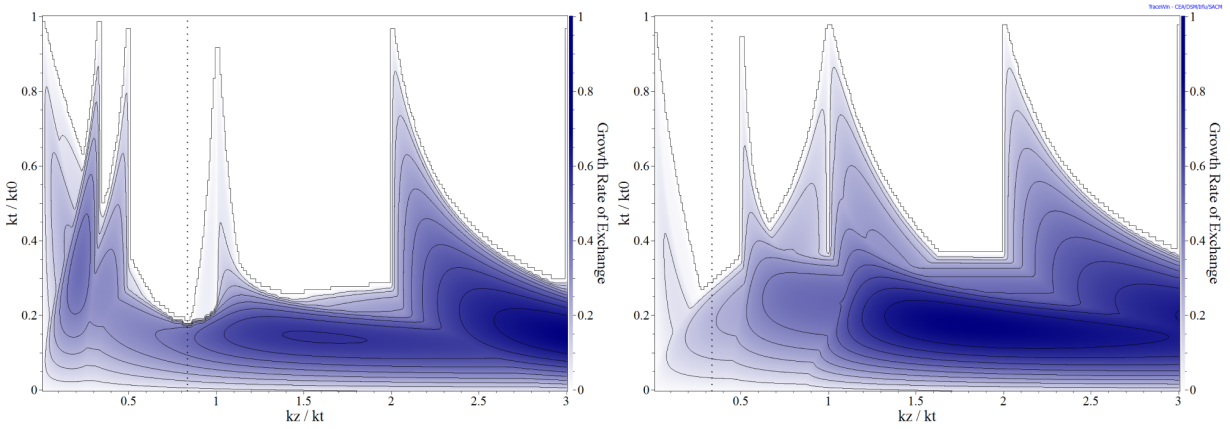

Figure 6.1: Hofmann stability charts for emittance ratios ϵ_z/ϵ_t=1.2 (left) and 3 (right). The dashed line represents the EQP region.

$\epsilon_z/\epsilon_t = 3$. The dashed line indicates the limit of the equipartitioning zone, while the coloured contours indicate regions in the tune diagram where coherent space-charge instabilities affect the beam due to the excitation and growth of particular resonant eigenmodes. Several areas can be identified mostly near tune ratios with integer tunes: k_z/k_t=1/3, 1/2, 1 and 2. For reasonably moderate tune depressions ($k_t/k_{t0} > 0.5$), the instability areas are relatively narrow, but as the tune depression becomes stronger, the areas will overlap and no safe regions remain. What these diagrams highlight is the fact that additional safe regions exist outside the EQP line [29].

Motivation and Prior Research

Confirmation of this work has been made possible by means of multiparticle simulations. However, experimental verification remains limited. The most notable evidence comes from a 2009 experiment at UNILAC in GSI in which the heavy ion linac lattice was modified to cross the $k_z/k_t = 1$ resonance. The resulting transverse emittance growth was measured thus giving an indication of a space-charge resonance effect. However, several key differences have to be noted: a heavy ion linac was used rather than a proton linac, with an emittance ratio ϵ_z/ϵ_t of 10 which is much larger than those usually found in proton/H^- linacs where the ratio is closer to 1. The experiment explored only the $k_z/k_t = 1$ resonance and only an increase in transverse emittance was observed [180].

It is therefore imperative that more experimental evidence is gathered that explores

the stability chart further, in conditions relevant for normal linac operations. In 2012, an opportunity arose for a beam study on this subject in the J-PARC linac and an ongoing collaboration was started between RAL and J-PARC. Originally, EQP was adopted as the reference design for the J-PARC linac, in which space-charge driven transverse to longitudinal coupling resonances are suppressed. Because of the recent J-PARC energy upgrade where a triple frequency jump was introduced, to maintain EQP, transverse focussing needs to be increased. However, as was recently identified at SNS, intra-beam stripping is a major cause of beam loss in H^- linacs [181]. The increased particle density caused by remaining EQP, has the unintended consequence of enhancing intra-beam stripping beam loss. Maintaining EQP and reducing intra-beam stripping are two conflicting requirements which have highlighted the necessity to explore the tune space outside EQP such that a new safe operating point can be identified. While this study is certainly relevant for improving the performance of the J-PARC linac, it also opens the possibility of improving the practical design guidelines for high intensity linacs, while benchmarking existing theoretical and simulation work on this subject. It is also interesting to note that such a study is possible at J-PARC owing to the nature of the machine, which uses wide-ranging EMQs throughout the entire linac rather than PMQs, thus enabling flexible tuning of the operating point and testing of different lattices. This experiment would not be possible for many modern linacs (SNS, Linac4, ESS) owing to the nature of their quadrupoles, thus making J-PARC a unique machine for these studies [182], [183].

Experimental Procedure

The J-PARC linac layout is shown in Figure 6.2. At the time the experiment was carried out, the linac consisted of an H^- ion source, a LEBT, a 324 MHz, 3 MeV RFQ and a MEBT line (MEBT1). After the front end, a DTL accelerates the beam to 50 MeV followed by an SDTL up to 181 MeV. A major upgrade took place in the summer of 2013 taking the beam energy to 400 MeV by a series of annular coupled structures operating at 972 MHz. A transport line (L3BT) injects the beam to the RCS.

Four different working points have been tried with temperature ratios of 1.0, 0.9, 0.7 and 0.5 as in Figure 6.3. To avoid any uncertainty from matching into the DTL, only the SDTL

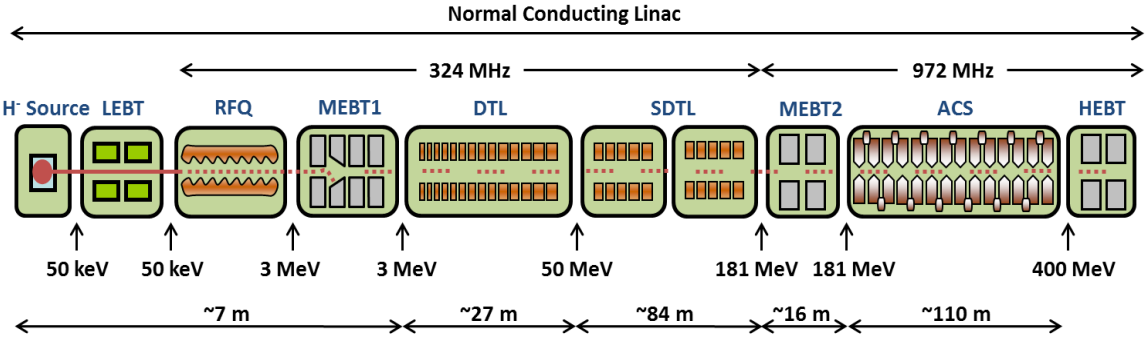

Figure 6.2: Schematic layout of the J-PARC H^- linac.

section has been modified for each test case, by adjusting the quadrupole gradients such that the beam stays on the resonance, thus enhancing the effect. The front end and the DTL settings are kept constant for all measurements. The beam current was set at 15 mA which was the operating value. The design current is 30 mA for the first phase of the project and 50 mA after the energy upgrade.

The experimental procedure follows several steps. First the quadrupole settings in the SDTL section are changed such that the working point is brought to the desired value. Transverse matching is then achieved at the DTL - SDTL transition with an array of wire scanners (WS) and quadrupoles. Next, wire scanners are used to measure the transverse emittance at the ACS entrance. And finally, bunch shape monitors (BSM) are used at the ACS entrance to evaluate the longitudinal emittance. This procedure is repeated for each of the working points.

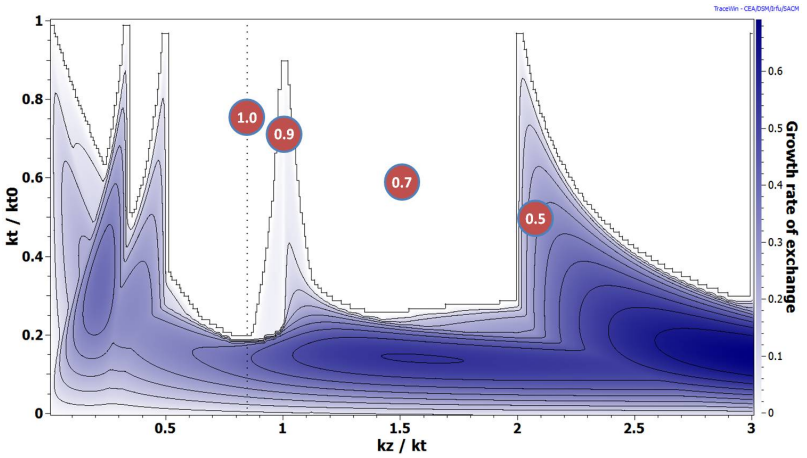

Figure 6.3: J-PARC linac stability chart for an emittance ratio $\epsilon_z/\epsilon_t = 1.2$, showing the four working points tested.

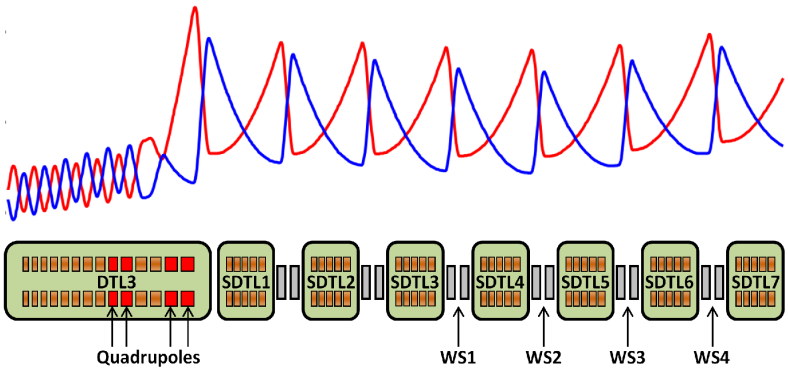

Figure 6.4: Transverse DTL to SDTL matching section, showing the locations of the four tuning quadrupoles and wire scanners, as well as the matched beam envelope.

The DTL-SDTL transition section is shown in Figure 6.4, with details of the matching routine, as well as a matched envelope example. Gradients of four quadrupoles are varied and the beam size is measured with four periodically located wire scanners. Matching involves the use of an envelope code over several quadrupole tuning iterations until the RMS beam widths measured with the wire scanners are equal.

A similar setup exists at the SDTL-ACS transition, used to measure transverse emittance. By knowing the phase advance between the scanners, emittance and Twiss parameters can be obtained by a parameter fitting routine to the measured RMS beam widths. For this, a 3D envelope model of the machine used during operation and developed in Open XAL is being employed [184].

The longitudinal emittance measurement is also performed at the SDTL-ACS transition, using one of the three recently installed BSMs, or sometimes known as Feschenko monitors, developed by INR in Russia [185]. These longitudinal beam profile monitors use a thin target which probes the ion beam. Secondary electrons are emitted and accelerated quickly such that the time structure is kept. An RF deflector system at the same frequency as the ion beam modulates the electron energy, while an additional magnetic field can separate secondary electrons from detached electrons, which is important for halo measurements. The resulting beam profiles measured for the J-PARC linac with BSM1 can be seen in Figure 6.5, showing the bunch length for the entire pulse duration [186].

Details of the SDTL-ACS transition setup are given in Figure 6.6. As there is no information on the longitudinal phase advance between BSMs, the transverse emittance mea-

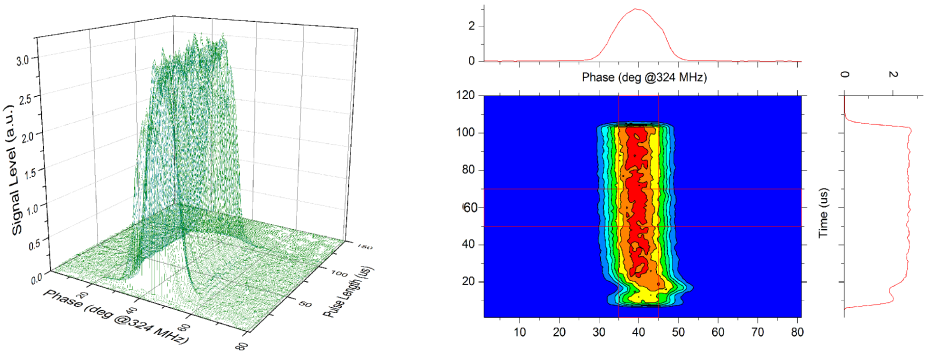

Figure 6.5: Longitudinal beam profile in the J-PARC linac measured with BSM1 for the entire pulse duration. Density scale as in Figure 2.11.

surement technique cannot be applied in this case. Instead, the synchronous phase of tank SDTL15 is set to bunching mode (-90 degrees) and the RMS phase width is measured at the BSMs as a function of the tank amplitude. The emittance and Twiss parameters at SDTL15 are then calculated by doing a 3 parameter scan to fit the measured beam widths. As the distance between SDTL 15 and the BSM location is over 20 m long, the longitudinal emittance growth in this section is not negligible and the envelope model cannot be used. Instead, the fitting is done by particle tracking using IMPACT and assuming a Gaussian distribution at SDTL15. During BSM calibration, a full scan was performed in which the RMS beam width was measured as a function of SDTL15 tank amplitude and then compared with simulations performed with IMPACT and TraceWin. The results for BSM1 which will be further used for the measurement of emittance can be seen in Figure 6.7 where a good agreement between simulation and measurement can be observed. For completeness, the simulation results for BSM2 and BSM3 are also included.

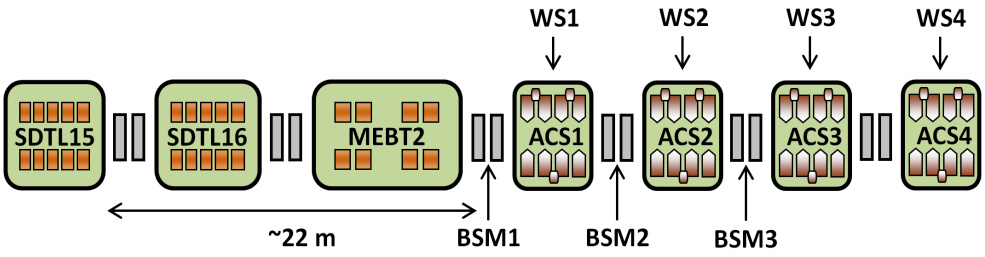

Figure 6.6: SDTL to ACS transition showing the location of the diagnostics devices. At the time the experiment was performed, the ACS modules and their respective quadrupoles were not installed. Also, at SDTL16 position, two debuncher cavities were installed instead.

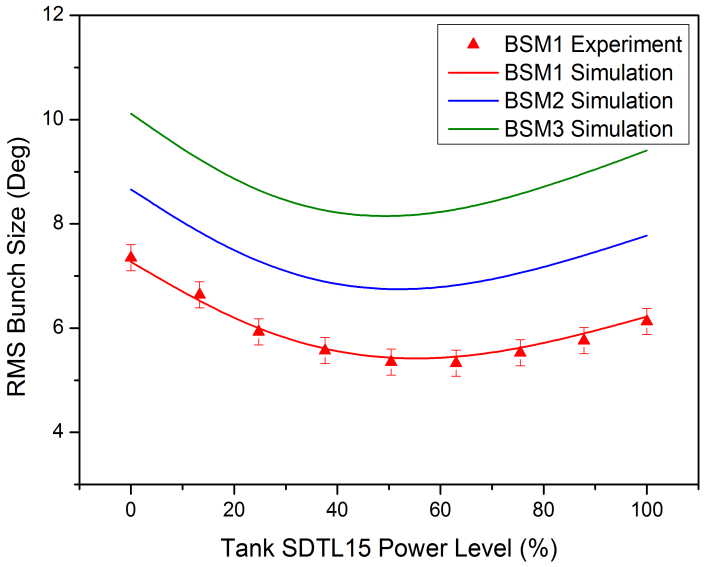

Figure 6.7: Simulated (BSM1, BSM2 and BSM3) and measured (BSM1) RMS bunch length for different power levels at SDTL15.

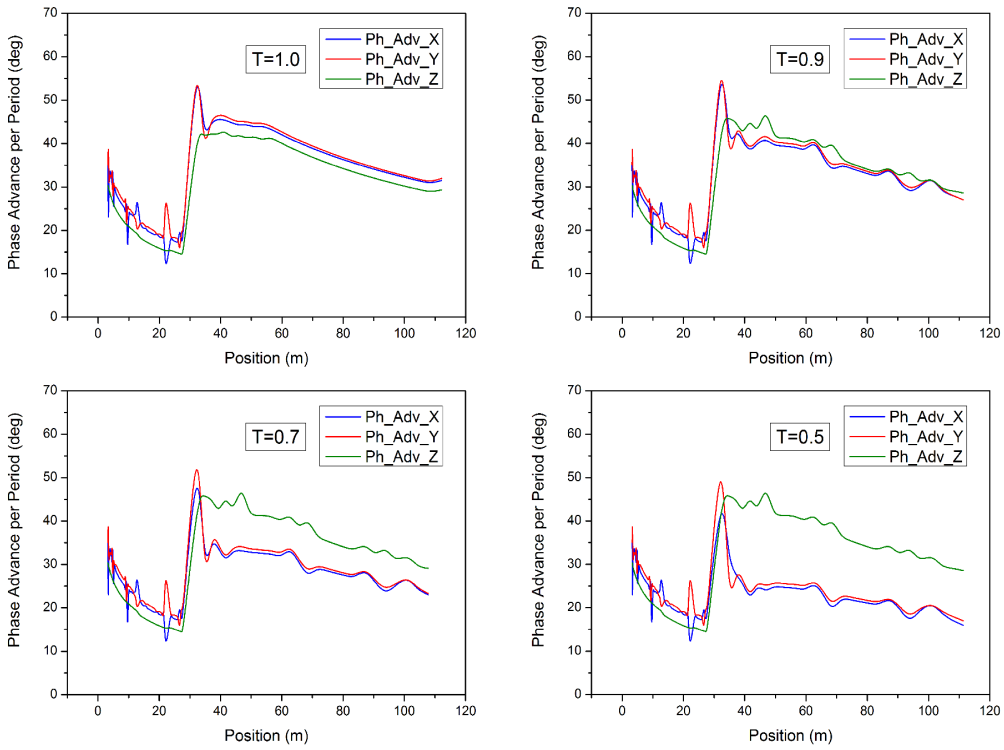

Figure 6.8: Phase advance per period vs. position in the J-PARC linac for the four working points tested.

Simulations

In preparation for the experiment extensive multiparticle simulations have been performed using Tracewin and IMPACT. The results reported here refer to Tracewin only. Impact

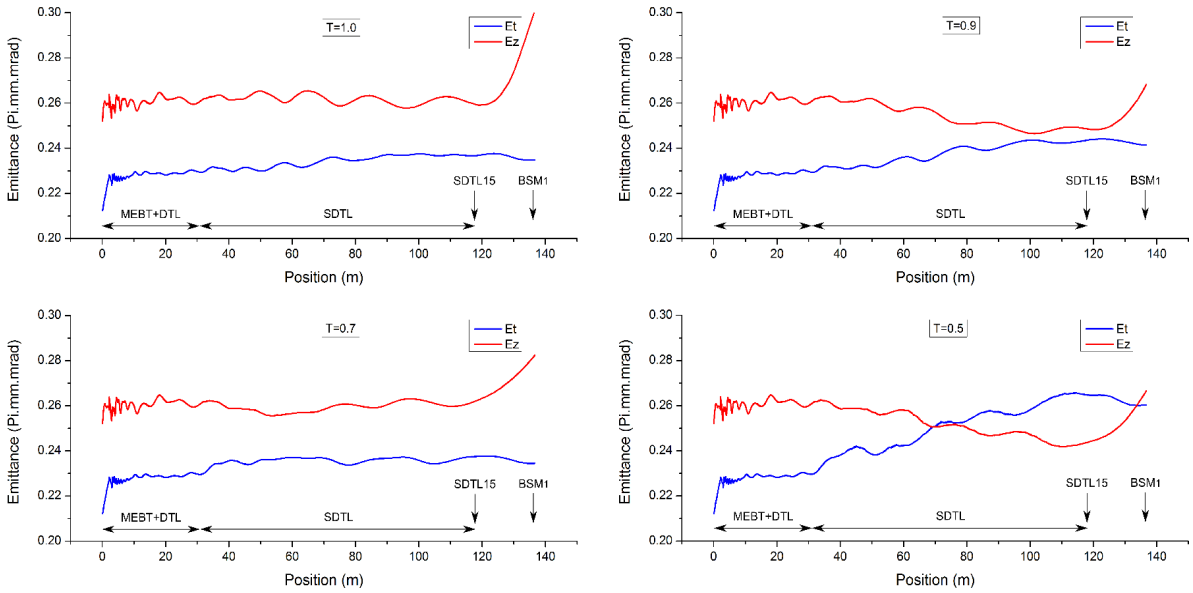

Figure 6.9: Simulated emittance evolution vs. position in the J-PARC linac for the four working points tested.

results however show similar trends and have been used to validate these simulations. The phase advance per period for the four working points can be seen in Figure 6.8, showing a constant longitudinal phase advance and a decreasing transverse phase advance equating with a larger beam size.

The emittance evolution throughout the linac for the four cases can be seen in Figure 6.9 with a summary of the emittance values presented in Table 6.1. The graphical representation seen in Figure 6.10 shows some emittance exchange for case T=0.9 ($k_z/k_t = 1$) and much stronger for T=0.5 ($k_z/k_t = 2$), while cases T=1.0 and T=0.7 show no exchange. It is also interesting to note a strong emittance growth longitudinally between the end of the SDTL (tank SDTL15) and the location of the bunch shape monitors as indicated in Figure 6.9. This is caused by the absence of longitudinal focussing in this section (∼22 m) and is the

T_t/T_z	DTL Output(π.mm.mrad)		SDTL Output(π.mm.mrad)		Emittance Growth (%)	
	ϵ_t	ϵ_z	ϵ_t	ϵ_z	ϵ_t	ϵ_z
1.0	0.229	0.260	0.237	0.261	3.1	0.4
0.9	0.229	0.260	0.243	0.249	5.7	-4.1
0.7	0.229	0.260	0.237	0.260	3.2	0.2
0.5	0.229	0.260	0.266	0.243	15.6	-6.7

Table 6.1: Simulated J-PARC linac emittance values for the four working points tested.

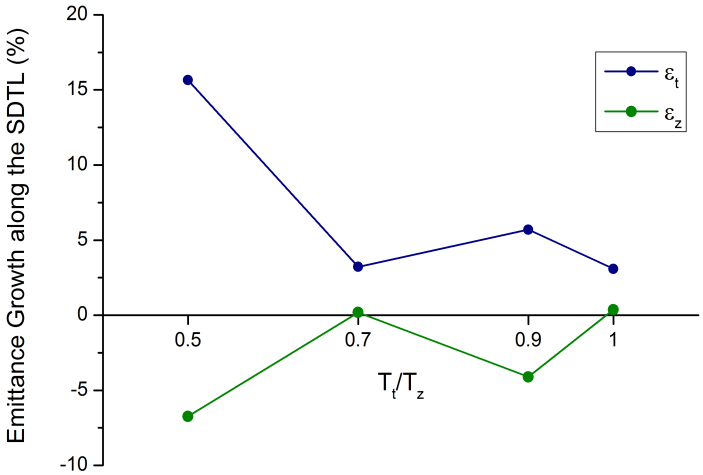

Figure 6.10: Simulated emittance growth in the J-PARC linac for the four working points tested.

reason for needing multiparticle tracking to estimate the emittance.

Experimental Results

As explained above, the SDTL output transverse emittance is measured using a set of wire scanners at the beginning of the ACS section. Typical horizontal and vertical beam profiles for the four working points tested can be seen in Figure 6.11 as measured by one of the wire scanners. The longitudinal emittance is estimated using RMS beam phase lengths measured with BSM1.

The results are summarised in Table 6.2 where the measured emittance values at end of the SDTL are presented. The 3D sum of the emittance for each case is in the range of ±5% suggesting that the 3D emittance is conserved within the accuracy of the measurement. A clear increase in transverse emittance coupled with a decrease longitudinally has been observed for the case 0.5. This is the first experimental observation of emittance exchange in

T_t/T_z	SDTL Output(π.mm.mrad)	
	ϵ_t	ϵ_z
1.0	0.216	0.269
0.9	0.229	0.233
0.7	0.253	0.223
0.5	0.293	0.161

Table 6.2: Measured J-PARC linac emittance values for the four working points tested.

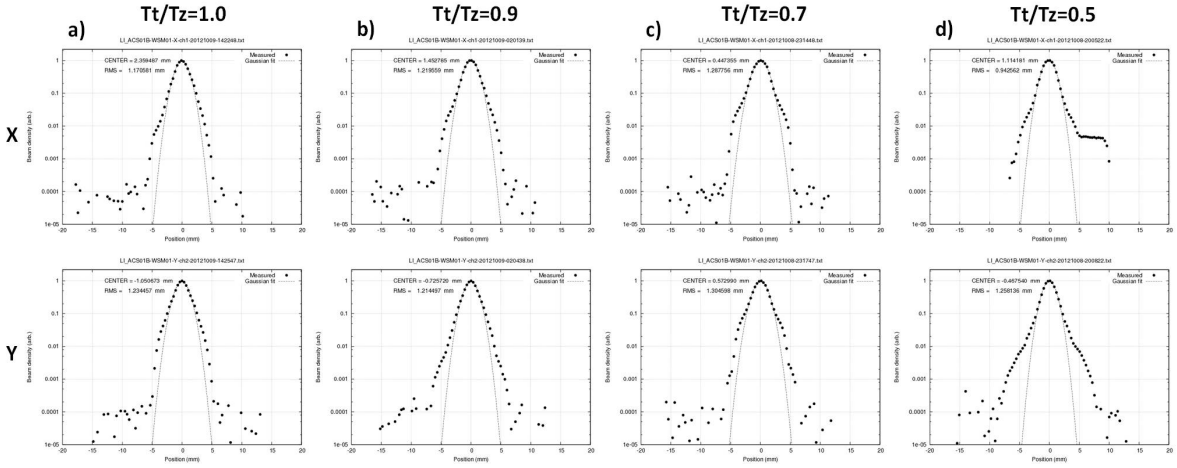

Figure 6.11: Measured transverse beam profiles in the ACS section. The horizontal axis is the measured width (mm) while the vertical is the logarithmic beam density (a.u.). Clear halo can be seen for the case T=0.5.

a linac driven by the $k_z/k_t = 2$ resonance and also the first emittance exchange measurement in a proton linac with emittance ratios close to 1. Nevertheless, the level of exchange is significantly higher than predicted by simulation. Additionally, unexpected halo has been measured transversely as indicated by the long tails in Figure 6.11d.

The measurements for cases 1.0 and 0.9 are both consistent with simulations with some weak exchange observed for 0.9 and no exchange for the EQP case (T=1.0). However, some exchange has also been measured for case 0.7, which is unexpected as it has not been predicted numerically or by theory.

Preliminary Conclusions and Implications for the ISIS Linac Design

While the first experimental evidence for emittance exchange at $k_z/k_t = 2$ in a proton linac with emittance ratios close to 1 is certainly encouraging, question still remain and efforts are still being made to quantify the measurement limitations and fully understand the results. The most puzzling is the unexpected emittance exchange seen at T=0.7. A strong contender for a possible explanation currently being investigated is transverse mismatch observed at SDTL input. Indeed, very recent work presented at the SpaceCharge'15 Workshop in Oxford details the mechanism by which initial mismatch could lead to emittance exchange and suggest that integer and half integer resonances are dominant [187]. However, these preliminary measurements could also indicate that an unrecognised mechanism might be contributing

to the stronger emittance exchange. Amongst the things considered are machine errors and beam size mismatch as well as a large tune-spread footprint which could in reality keep part of the beam on resonance.

For a complete understanding it is hoped that these initial observations will be explained by repeating the experiment after the energy upgrade. This will have the obvious advantage of measuring longitudinal emittance without the significant SDTL15 to BSM1 emittance growth, while the accuracy of both the transverse and longitudinal emittance measurement could be verified.

This brings the discussion back to the choice of a working point (EQP or not) and the use of stability charts in linac design. What this experiment has highlighted is the need to understand the limitations of these design tools, as illustrated by the unexpected emittance growth at T=0.7. Over the last few years, some tendency to use the charts as proof of good beam dynamics design has been observed. In reality however, while these charts are useful guidelines, they cannot substitute a systematic analysis of the influence of mismatch, initial particle distribution, beam tune spread, resonances, errors, etc., supported by thorough self consistent multi-particle computer simulations.

The implications for the ISIS linac design choices are clear. As explained above, with this experiment carried out at J-PARC there is now sufficient experimental as well as theoretical evidence to support the avoidance the $k_z/k_t = 1$ and $k_z/k_t = 2$ stop-bands. It is also clear that an EQP design does not necessarily equate with absence of emittance growth and no halo development and that safe working points do exist outside EQP. For the linac designs to be presented further, a different approach was followed in which rather than having a rigid EQP condition, a flexible working point was chosen which avoids the above mentioned stop-bands and produces smaller beam sizes such that the accelerating structures to be used can be designed with smaller apertures and higher efficiencies. Additionally, the linacs were designed to operate away from resonances not only at the design beam current, but also at smaller beam currents. Employing PMQs in the DTL section of the linac has its advantages, but it also means that the working point will be shifted should the beam current be smaller. During commissioning and operation, the machine will often have to operate at lower intensities and outside the design parameters. Therefore the working point

is not EQP but chosen such that sufficient width is given for alternative running modes. In practice this means that a working point close to the EQP line was generally chosen, while correcting for any possible overlap between the tune footprint and the nearby resonances at $k_z/k_t = 1$, 1/2 and 1/3. For the DTL design, this choice bears no effect on the overall machine cost, as the phase advance requirements in the longitudinal plane do not force the tanks to operate below their capabilities. This is also true for the CCL section and for the superconducting linac. Since a superconducting cavity design with accelerating gradients up to 19 MV/m was adopted, the chosen working region can be retained without the need of crossing the $k_z/k_t = 1$ resonance and without compromising the available voltage budget. Alternative designs are currently being investigated where a higher accelerating gradient is proposed with a working point in the tune diagram outside EQP between the $k_z/k_t = 1$ and $k_z/k_t = 2$ stop-bands (see Figure 6.1). If the preceding normal conducting linac is kept at EQP, the effects of crossing the $k_z/k_t = 1$ resonance need to be investigated as well as the effects of moving the normal conducting linac away from EQP and closer to the SC linac working point.

6.2 The 100 MeV Linac

6.2.1 General Considerations

The first linac design to be presented is a replacement for the current ISIS 70 MeV injector. A full description of the current 202.5 MHz linac was given in Chapter 5 where the need for an increase in reliability was highlighted. A straightforward and by far the most economical upgrade is a new linac in the existing tunnel. By reusing the existing infrastructure, the civil engineering costs are dramatically reduced. However, this poses a length restriction and any linac design would have to fit in the existing tunnel.

The replacement linac would not only improve the machine availability for users, but it could bring the benefit of injecting higher beam currents at a higher energy into the ring, thus allowing slightly higher beam powers. A higher energy is achievable by operating at a higher frequency and redesigning the DTL structure for a higher RF efficiency. Additionally, by adding a MEBT with chopper, the RFQ to DTL mismatch and beam loss experienced

in the current linac would be eliminated, as well as any ring injection losses. Considering that the FETS project is near completion, this works assumes that FETS, or a FETS-like accelerator could be used as the linac front end. As a result, some design parameters are dictated by the FETS parameters. It is hoped that if such an upgrade is planned carefully, installation and commissioning could be completed over a long machine shut down with minimum user disruption.

The four tanks of the current ISIS linac are ∼44 m long including the inter-tank spacing. Upstream of the first DTL tank, the existing front end and the additional space measure ∼6 m. From the end of the last DTL tank to the synchrotron wall an additional 10 m is available. However, due to practical constraints which include a very low ceiling for this tunnel section, installation and maintenance would be very difficult and therefore this segment was considered inadequate. As a result, a total of ∼50 m was considered available for the new linac.

6.2.2 RF Design and Beam Dynamics

The design of the new linac follows the same overall guiding principles as several modern linacs like SNS, J-PARC, Linac4, ESS, etc. It consists of a 3 MeV FETS-like front end followed by a DTL operating at 324 MHz which accelerates the beam up to 100 MeV. The repetition rate is 50 Hz and the peak beam current is 60 mA, a more than double increase from the present linac. With beam pulse lengths between 0.1 and 1 ms, the linac will be capable of providing a range of operating regimes to match the ring injection requirements. Depending on the duty cycle, at the 30% beam chopping rate needed for injection into the ring, the average output beam power is between ∼20 and 200 kW. The layout of the new linac is presented in Figure 6.12 and a summary of the overall parameters is given in Table 6.3.

The front end consists of an H^- ion source, a LEBT, an RFQ and a MEBT line with choppers. The FETS Penning-type surface plasma H^- ion source will be adopted for the new linac. This source is already operating at parameters exceeding those required for the new linac, having been improved over many years in ISIS and FETS. A beam of 65 keV, 2 ms at 50 Hz with beam currents exceeding 60 mA is routinely extracted. A three-solenoid

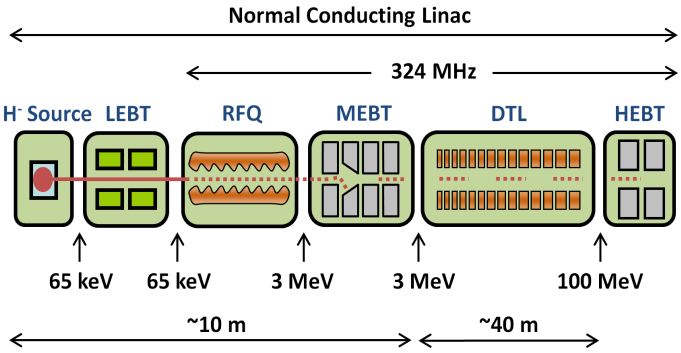

Figure 6.12: General layout of the 100 MeV linac replacement for ISIS.

magnetic LEBT will transport and match the beam from the ion source to the RFQ. A 4 m long, 4-vane RFQ operating at 324 MHz will accelerate the beam up to 3 MeV making use of the available 3 MW Toshiba klystron used at J-PARC. An RMS emittance in the region of 0.27 π.mm.mrad transversely and 0.38 π.mm.mrad longitudinally is expected at the output of the RFQ. The RFQ is followed by the MEBT line. It consists of 11 quadrupoles, 4 re-bunching cavities, a beam chopping system with dedicated beam dumps, collimators for removing beam halo and a comprehensive set of diagnostics. The quadrupole gradients and the voltages in the cavities are variable and will depend on the RFQ output beam. The last 4 quadrupoles and two bunchers form the section matching into the DTL. An in-depth description of each front-end section was given in Chapter 5. Unfortunately, due to the space restrictions imposed for the new linac, the optimal MEBT design with distributed choppers proposed earlier could not be adopted in this case. This is reflected partially in the linac performance in terms of beam dynamics and will be analysed later.

Ion Species	H^-	
Energy	100	MeV
Frequency	324	MHz
Pulse Length	0.1 - 1	ms
Peak Current	60	mA
Repetition Rate	50	Hz
Total Length	50	m
Duty Cycle	0.5 - 5	%
Accelerating Structures	RFQ, DTL	

Table 6.3: General parameters of the 100 MeV ISIS upgrade linac.

The DTL section is ∼40 m long and accelerates the beam to 100 MeV in five tanks. Each tank is fed by a single 3.0 MW peak power Toshiba klystron with output energies of 23.5, 43.9, 63.8, 83.1 and 100.8 MeV. A ∼20% margin has been maintained for the combined structure and beam power for each tank to take into account extra losses and leave sufficient control power. The number of cells in each tank is 57, 32, 26, 23 and 20 respectively.

The RF design optimisation follows the procedure already described in Chapter 4 and involves the optimisation of individual cells, complete tanks and finally the entire linac. Each design choice has been carefully analysed through an iterative process while taking into account RF, beam dynamics and practical requirements. For RF calculations Superfish and CST Microwave Studio have been used, while the linac layout was generated with GenDTL and Parmila. Beam dynamics calculations were performed with several codes. The results presented here are from TraceWin. Figure 6.13 shows the evolution of the geometrical parameters of the cavity through the linac.

The average axial electric field is ramped from 2.9 to 3.3 MV/m in the first tank and then kept constant for the rest of the linac. This is aimed at adiabatically capturing the MEBT beam and reducing the peak fields in the first few linac cells. Also, as a large longitudinal acceptance is needed at the beginning of the DTL to capture the entire beam from the MEBT, the synchronous phase angle is set to -35 degrees in the first few cells. As the beam becomes more bunched, the phase is slowly increased to -25 degrees and then kept constant for the rest of the linac. This is illustrated in Figure 6.14.

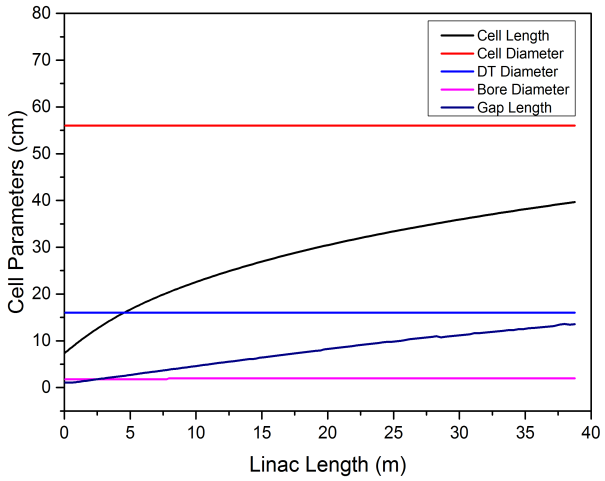

Figure 6.13: Geometrical parameters vs. position in the new ISIS DTL.

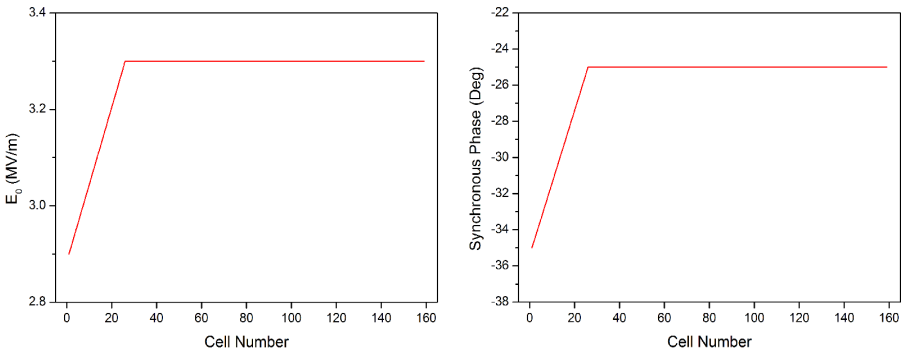

Figure 6.14: Field and phase ramp variation with cell number in the new 100 MeV linac replacement for ISIS.

The resulting electric field map on axis for the entire DTL is shown in Figure 6.15 as calculated by Superfish. Additionally, details of the field profile in individual cells at the low and high energy end are given to illustrate the change in field distribution with the change of cavity geometry.

The small H^- beam expected from FETS allows a DTL design with a small bore radius which increases the transit time factors and the structure efficiency. The diameter is 1.8 cm in the first tank and then kept constant at 2 cm for the rest of the linac. The tank diameter was optimised such that a single value was chosen and kept constant for the entire energy range,

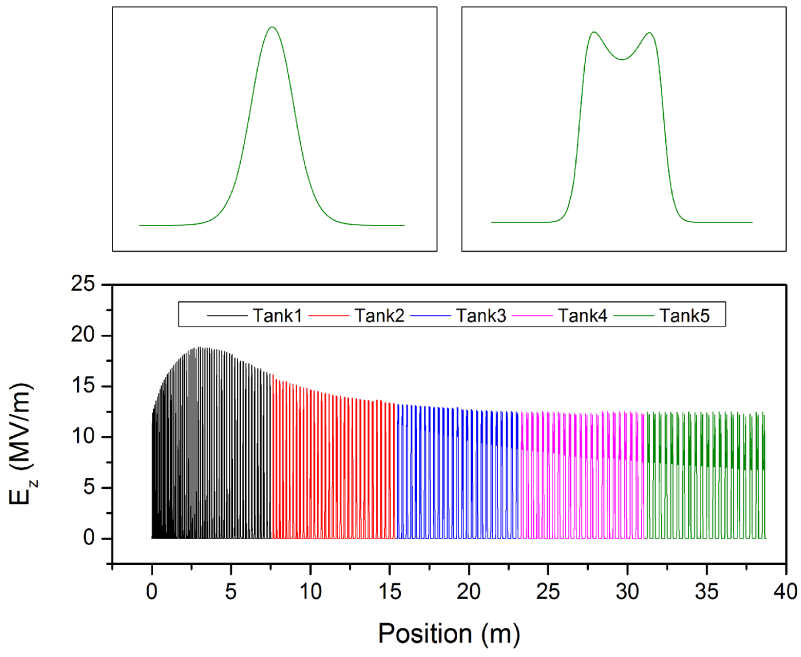

Figure 6.15: Electric field map on axis throughout the DTL (bottom) and details of the field distribution in individual cells at the low (top left) and high (top right) energy ends.

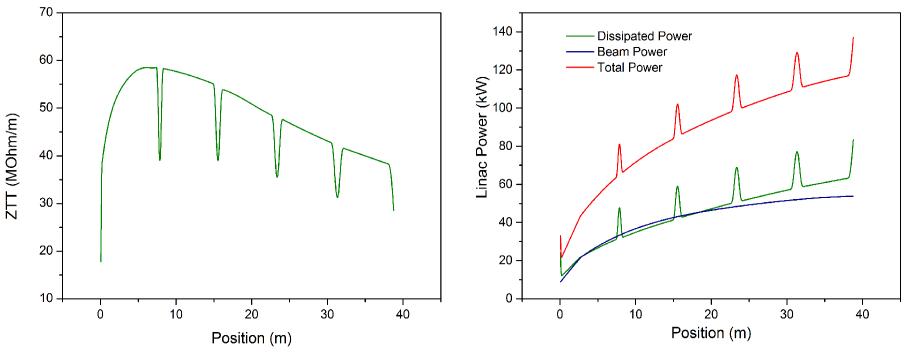

Figure 6.16: Effective shunt impedance per unit length (left) and the dissipated, beam and total power (right) along the new DTL.

thus simplifying overall construction. Due to space limitations, high acceleration efficiency was paramount in the new design. The new linac accelerates an additional 30 MeV in the same tunnel length. This was possible by increasing the RF frequency, by optimising the geometry for higher efficiency and by operating at a higher accelerating gradient. The resulting shunt impedance evolution follows the same curve seen in Chapter 4 and is presented in Figure 6.16 together with the evolution of the peak power (dissipated, beam, total) in each DTL cell. The maximum Kilpatrick factor is kept below 1.8 throughout the linac. Post couplers are envisaged in the five tanks for field stabilisation. A comprehensive list of parameters for each DTL tank is presented in Table 6.4.

		Tank 1	Tank 2	Tank 3	Tank 4	Tank 5
Input Energy	MeV	3.0	23.5	43.9	63.8	83.1
Output Energy	MeV	23.5	43.9	63.8	83.1	100.8
Accelerating Gradient E_0	MV/m	2.9-3.3	3.3	3.3	3.3	3.3
Synchronous Phase	Deg	-35 - -25	-25	-25	-25	-25
Max. Surface Electric Field	Kilp	1.8	1.6	1.6	1.6	1.6
Average ZTT	MOhm/m	53.7	55.7	50.2	44.6	40.4
Dissipated Power	MW	1.27	1.21	1.24	1.28	1.24
Total Power	MW	2.49	2.44	2.43	2.43	2.30
Focussing Scheme			FODO			
Number of Cells		57	32	26	23	20
Tank Diameter	cm	56	56	56	56	56
Drift Tube Diameter	cm	16	16	16	16	16
Aperture Diameter	cm	1.8	2.0	2.0	2.0	2.0
Stems/Cell		1	1	1	1	1
Total Length	m	7.75	7.64	7.79	7.94	7.63

Table 6.4: Main DTL Parameters for the 100 MeV ISIS upgrade linac.

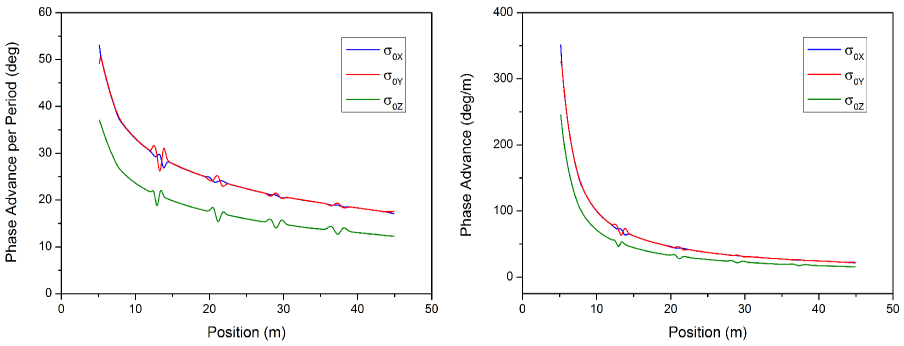

Figure 6.17: Zero current phase advance through the DTL.

From a beam dynamics point of view, the design phase advance ratio between the transverse and the longitudinal energies is obtained in the first tank after the MEBT matching section and is maintained up to 100 MeV by varying the quadrupole settings. A FODO focussing lattice is used throughout the linac which assumes permanent magnet quadrupoles similar to those employed at SNS. The evolution of the zero current phase advance throughout the DTL is shown in Figure 6.17 illustrating the smooth variation philosophy adopted for this design.

Drift spaces between tanks lead to matching errors and it is imperative that these are

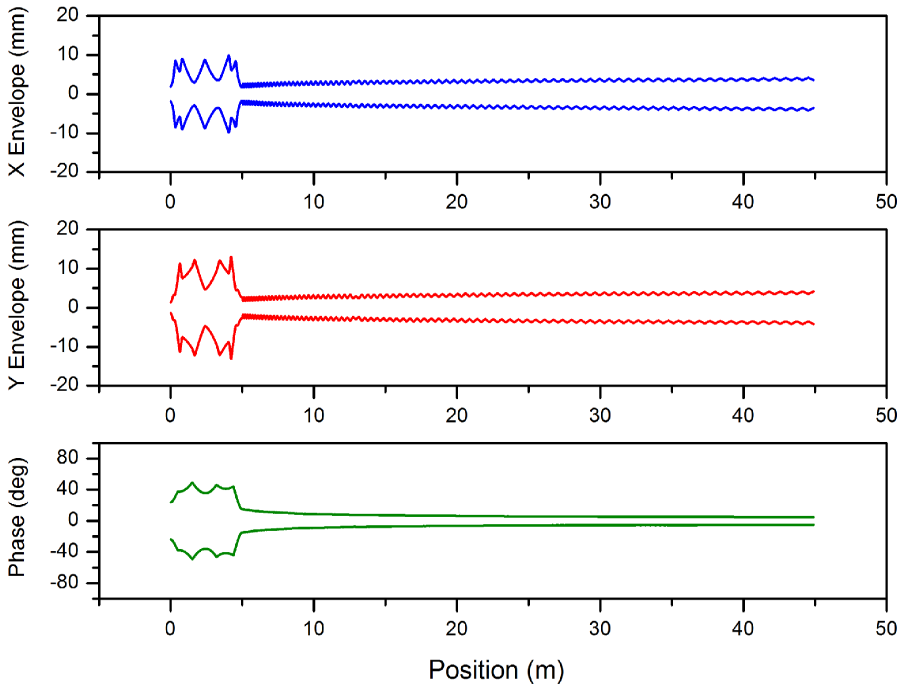

Figure 6.18: 5*RMS emittance beam envelopes evolution with position in the new 100 MeV linac: horizontal (X - top), vertical (Y - middle) and longitudinal (Phase - bottom).

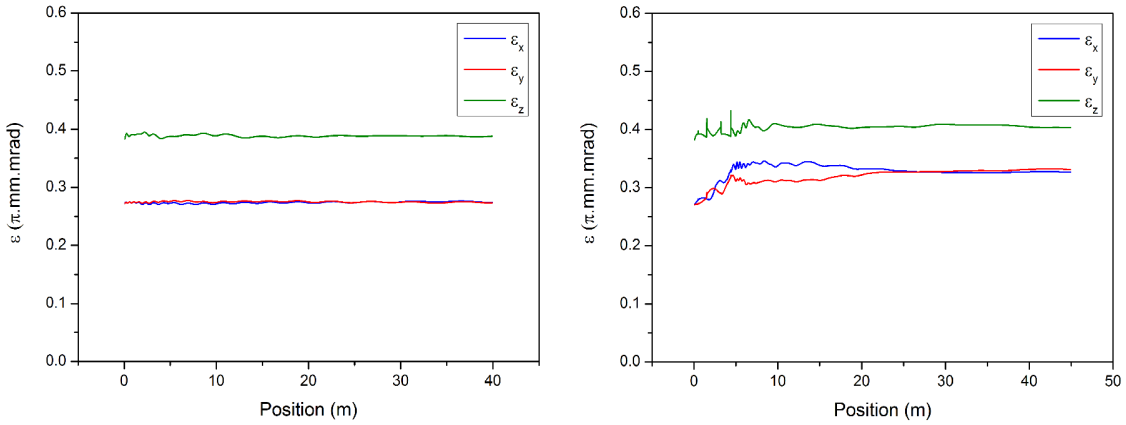

Figure 6.19: RMS emittance evolution through the new linac: DTL only (left) and DTL with MEBT (right).

corrected. Longitudinally, this is achieved by offsetting the synchronous phase in selected cells at the transition between the tanks. In practice this is obtained by moving the accelerating gap. Transversely, inter-tank matching is done with four quadrupoles, which are assumed to be adjustable EMQs. The evolution of the beam envelopes in the matched case when using a input 6D Waterbag distribution is shown in Figure 6.18.

As already mentioned, space restrictions required the use of the FETS MEBT, rather than the more optimal solution proposed in Chapter 4 which requires more space. The consequence is some deterioration in beam quality, illustrated by the evolution of the RMS beam emittance in Figure 6.19 where two cases are compared: the DTL without and with the MEBT. In the first case multi-particle tracking indicates almost no emittance growth ($\Delta\epsilon_x = 0.7, \Delta\epsilon_y = 0.6, \Delta\epsilon_z = 1.3$). When the MEBT is added, the new DTL input beam inherits the traits developed in the MEBT and some beam quality deterioration is visible.

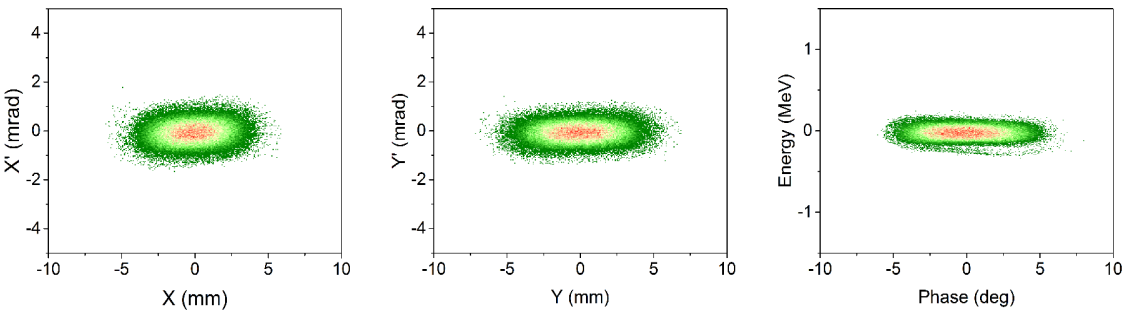

Figure 6.20: 100 MeV linac output distribution when using the MEBT input beam (horizontal, vertical and longitudinal phase-space). Scale as in Figure 2.11.

However, the emittance growth developed in the MEBT is more or less preserved in the DTL and no additional growth is observed ($\Delta\epsilon_x = 20.6, \Delta\epsilon_y = 22.5, \Delta\epsilon_z = 5.5$). The same is true for the halo parameters. This is still a very healthy design. No beam loss has been observed in the DTL, while the MEBT losses are near the measurements limits of modern diagnostics devices used in linacs and have been fully quantified in Chapter 5. The output beam distribution when carrying out an end-to-end simulation is shown in Figure 6.20.

This strong linac design is further illustrated by the evolution of the beam density throughout the linac. While the ratio between the beam pipe and the RMS beam size is generally kept around 8, it is important to identify bottlenecks where the outermost particles could be dangerously close to the vacuum pipe. The radial beam density in Figure 6.21, illustrates that such places do not exist. In addition, the radial beam cross-section is also plotted at the 90%, 99%, 99.9%, 99.99% and 100% density levels as well as longitudinal beam density throughout the linac.

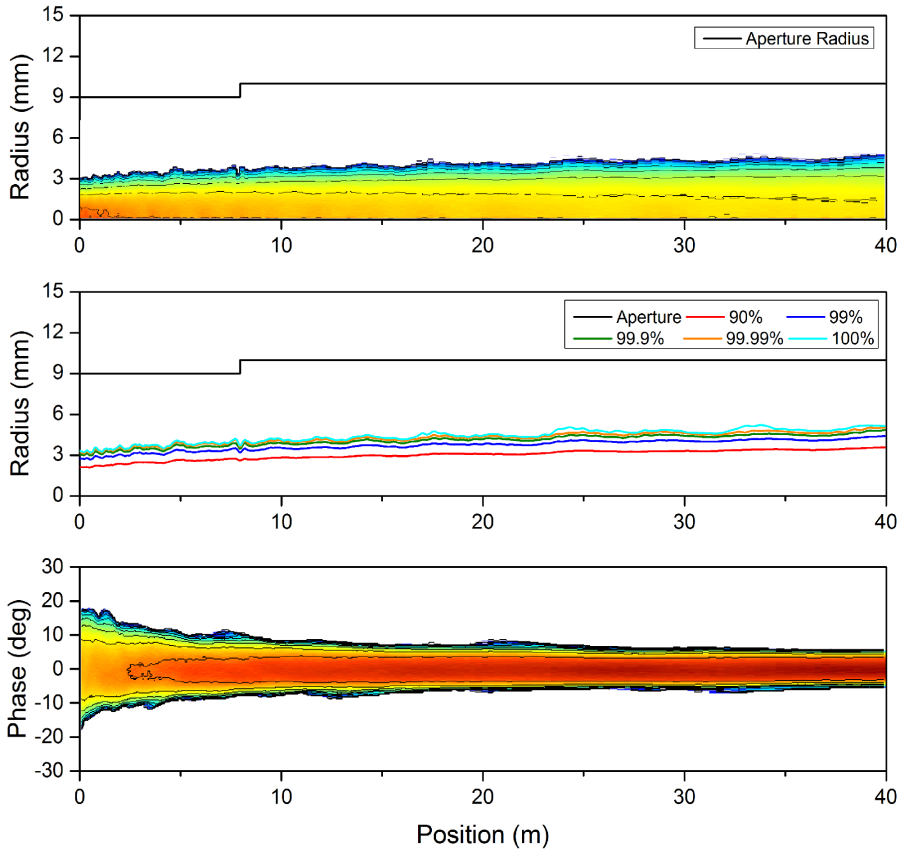

Figure 6.21: Radial beam density (top), and beam cross-section (middle), as well the longitudinal beam density (bottom) evolution throughout the new DTL. Scale as in Figure 5.3

6.3 The 180 MeV Linac

6.3.1 General Considerations

A second linac option under development is a new 180 MeV machine. This solution would require a new linac tunnel, which could be built parallel to the current linac, thus minimising user disruption. By injecting at higher energy into the ISIS synchrotron, 0.5 MW power levels could be achieved, as the reduced space-charge forces (which are proportional to $I/(\beta\gamma)^3$), allow a higher current to be injected. The new linac could also be part of a multi megawatt upgrade scenario in which it is used as the initial stage of an 800 MeV linac which uses the ISIS synchrotron as an compressor ring or is part of a further acceleration chain.

The same linac design could also be part of a proton driver for a neutrino factory in which the high intensity, short duration and small longitudinal emittance bunches needed are achieved via accumulator rings. Simulation studies suggest that optimum injection is at energies around 150 - 200 MeV and hence the 180 MeV linac output energy [188]. More detailed scenarios are discussed in Chapter 1.

The new linac assumes the 100 MeV linac design described in the previous section as the initial stage, with a FETS like front-end and a DTL, and could be adopted as either a stand-alone new linac or as a second stage upgrade to a future 100 MeV linac. One major difference in the new design is the adoption of the distributed chopper MEBT line proposed in this thesis. Above 100 MeV, acceleration is via a CCL structure operating at twice the DTL frequency. The layout of the new linac can be seen in Figure 6.22 and a summary with the main parameters is given in Table 6.5.

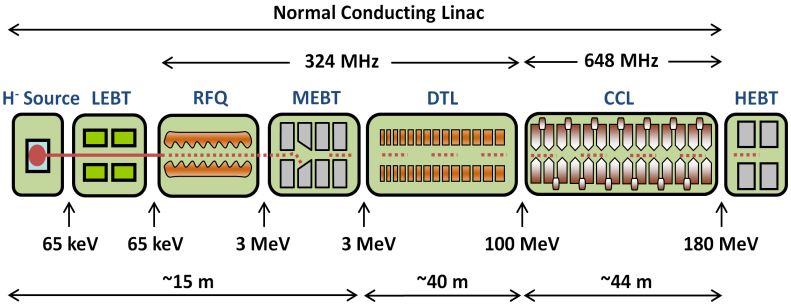

Figure 6.22: General layout of the new 180 MeV linac.

Ion Species	H^-	
Energy	180	MeV
Frequency	324/648	MHz
Pulse Length	0.1 - 1	ms
Peak Current	60	mA
Repetition Rate	50	Hz
Total Length	99	m
Duty Cycle	0.5 - 5	%
Accelerating Structures	RFQ, DTL, CCL	

Table 6.5: General parameters of the 180 MeV linac.

6.3.2 RF Design and Beam Dynamics

The front end uses the same layout as the 100 MeV linac, but is ∼4 m longer. This is because the distributed chopper MEBT is longer than the FETS type MEBT adopted for the lower energy linac. The design of the new MEBT has been described extensively in the previous chapter. It consists of a FODO-type lattice arrangement with distributed choppers separated by 180 degrees in phase advance. This ensures maximum chopping efficiency. To reduce the overall MEBT length, the fast and slow choppers deflect the beam horizontally and vertically. Additionally, the zero current phase advance per cell is close to 90 degrees so that choppers can be placed in every other cell. Over the last three MEBT FODO cells, the phase advanced is adiabatically lowered to ensure a smooth transition into the DTL and a good 6D matching. The impact of the new MEBT is immediately reflected in the overall linac performance when end-to-end tracking studies are carried out. While the emittance growth at the end of the DTL is ∼20% transversely and ∼5% longitudinally when using the FETS MEBT, with the new MEBT it is reduced to ∼8% transversely and ∼4% longitudinally. In addition, the small MEBT beam allows lossless operation, an important requirement for high power operation.

Alternative MEBT solutions were also investigated, while maintaining the fast-slow distributed chopper concept. The transverse phase advance was lowered to ∼60 degrees per cell throughout the entire MEBT, a value near the transverse phase advance in the first DTL cells. Consequently, to keep the deflection mechanism synergetic, the choppers were

positioned every third cell. While the deflection efficiency was maintained, the beam characteristics were also not changed, with the overall transverse emittance growth at the end of the DTL varying by less than 0.5%. This is because the baseline design already avoids sudden jumps in phase advance and includes a smooth transition to the DTL, and therefore any improvement the new lattice brings is marginal. However, as the total number of deflectors was kept the same but more scattered, the overall length of the MEBT increased by a third, which is equivalent with more than 2 m. As the benefits of this overall length increase are rather minor in terms of beam quality, it was decided that such a scheme would be unjustifiable for this application and as such it was not adopted.

After the MEBT, the DTL will accelerate the beam to 100 MeV. The DTL design is unchanged except for small input and transition matching adjustments to accommodate the new MEBT beam. At 100 MeV, the CCL structure is adopted to improve the acceleration efficiency. The CCL operates at twice the DTL frequency with an overall length of 44 m. The CCL design has been optimised to accelerate a high current beam efficiently and the design follows the same procedure as described in Chapter 4. Poisson Superfish is used to optimise the cell geometry for the given frequency and calculate the transit time factors, effective shunt impedance per unit length and cavity dimensions for the entire energy range. These results were then imported into Parmila which was used to design the entire CCL section lattice. Beam optics calculations were further performed with Parmila, Trace3D and TraceWin.

A total of 32 CCL cavities operating at 648 MHz are needed to reach ∼180 MeV. Each cavity consists of eight accelerating cells grouped into the same resonant structure via seven coupling cells. To operate in $\pi/2$-mode (TM_{010}), each accelerating cell is $\beta\lambda/2$ long, while the drifts between cavities can take any integer value of $\beta\lambda/2$. For this case, the drifts were set at $4(\beta\lambda/2)$ to allow sufficient space for diagnostics, correctors and transverse focussing elements.

For each cavity, a symmetric design was adopted rather than a graded-β, normally used in structures at lower energies (DTLs). This means that rather than changing each cell length in the cavity with increasing beam velocity, a local "geometric β" value was chosen and kept constant for each group of eight cells within a cavity and increased for the next. For

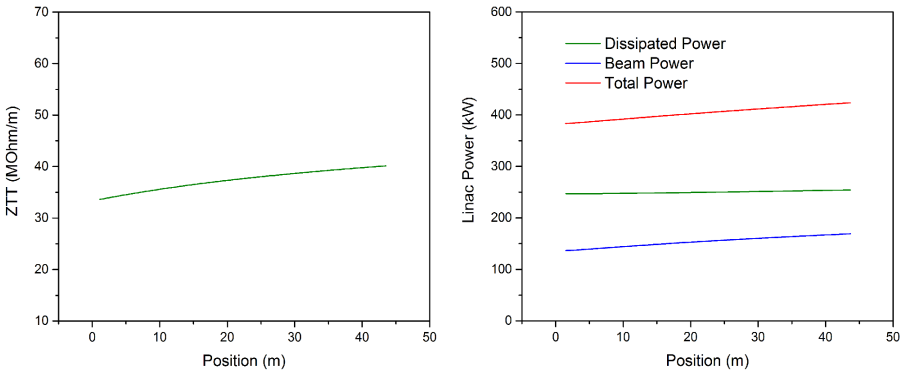

Figure 6.23: Effective shunt impedance per unit length (left) and the dissipated, beam and total power (right) along the CCL section of the linac.

relatively short structures at this energy this approach is preferred as although it generates a small phase shift, it leads to significant savings in cavity design and manufacturing.

The accelerating cell diameter is 34 cm while the aperture is 3.5 cm. The average axial accelerating gradient is kept constant at 3.5 MV/m throughout the entire structure (maximum Kilpatrick of 1), the synchronous phase is -22 degrees and the total dissipated power is 7.2 MW. The evolution of the effective shunt impedance and the dissipated power is shown in Figure 6.23, while a comprehensive list of parameters is presented in Table 6.6.

Assuming a configuration with four neighbouring cavities grouped together via bridge couplers, a total of 8 klystrons operating at 2 MW would be required while maintaining a

		CCL Section
Input Energy	MeV	99.8
Output Energy	MeV	181.6
Accelerating Gradient E_0	MV/m	3.5
Synchronous Phase	Deg	-22
Max. Surface Electric Field	Kilp	1.0
Average ZTT	MOhm/m	37.5
Dissipated Power	MW	7.2
Total Power	MW	12.9
Focussing Scheme		FODO
Number of Cavities		32
Cells per Cavity		8
Cell Diameter	cm	34
Aperture Diameter	cm	3.5
Total Length	m	44

Table 6.6: Main parameters of the CCL section of the 180 MeV ISIS upgrade linac.

20% margin for additional power losses and control. Alternative cavity module arrangements can also be considered for different klystron power ratings. However, this decision has to be taken in the larger international context and after consultation with industry, as klystron development is a lengthy and costly process requiring community agreement on specifications like peak power rating and duty cycle.

The FODO focussing lattice used in the DTL is also adopted here. EM quadrupoles are placed between each cavity module, with the total period length of $6\beta\lambda$. This is illustrated in Figure 6.24. The beam dynamics approach described at the beginning of this chapter is maintained and transverse phase advances are chosen such that the working point in the tune diagram is close to that of the DTL and all integer tune ratios are avoided (k_z/k_t=1/3, 1/2, 1 and 2). This can be seen in Figure 6.25 showing the zero current longitudinal and transverse phase advance evolution throughout the entire linac. The jump in phase advance is at transition between structures where the adoption of the CCL allows higher accelerating gradients.

As the CCL does not have long transitions between tanks, the optics design is relatively straightforward. Particular attention has to be paid to matching the beam from the DTL to the CCL over the double frequency jump. This is achieved by small phase adjustments in the last two DTLs and the first two CCL cells. Transversely, four quadrupoles are needed at transition. The resulting full current envelope evolution for the entire linac can be seen in Figure 6.26, showing a smooth and uniform beam progress thorough the entire linac, without major changes in beam size at any transition.

The careful efforts put into achieving a good initial match, maintaining the correct phase advances and managing transitions swiftly are rewarded when the linac design is analysed

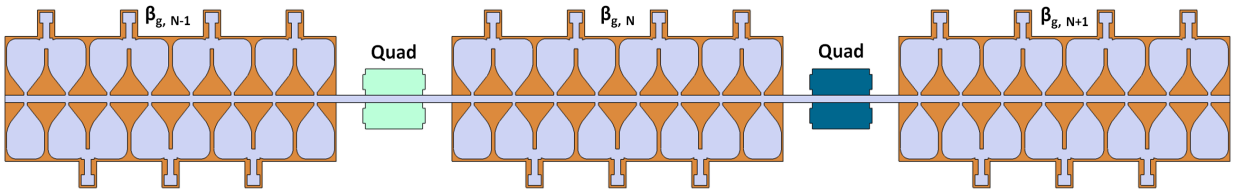

Figure 6.24: Schematic layout of the CCL section configuration showing neighbouring cavity modules of increasing length and quadrupole magnets positioned in the space between cavities.

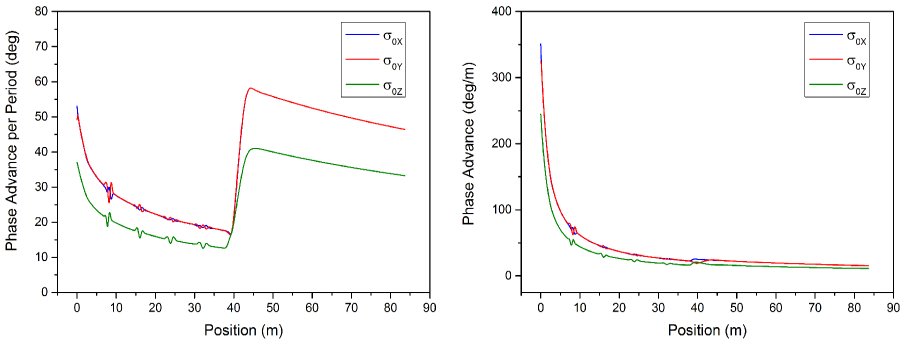

Figure 6.25: Transverse (X and Y) and longitudinal (Z) zero current phase advance vs. position through the DTL and CCL sections of the new 180 MeV linac for ISIS.

by means of multi-particle simulations with 3D space-charge. As in the DTL case, a 6D Waterbag distribution was tracked through the CCL section only to check for any design inconsistencies and bottlenecks followed by a full end-to-end simulation. The results can be seen in Figure 6.27. For the CCL only, the emittance growth is at most 3.1% ($\Delta\epsilon_x = 1.8, \Delta\epsilon_y = 3.1, \Delta\epsilon_z = 1.6$). When the beam is tracked through the DTL and the CCL, the growth is less than 1% ($\Delta\epsilon_x = 0.08, \Delta\epsilon_y = 0.07, \Delta\epsilon_z = 0.6$), while end-to-end tracking including the MEBT shows a maximum growth below 10%($\Delta\epsilon_x = 7.5, \Delta\epsilon_y = 9.3, \Delta\epsilon_z = 4.3$).

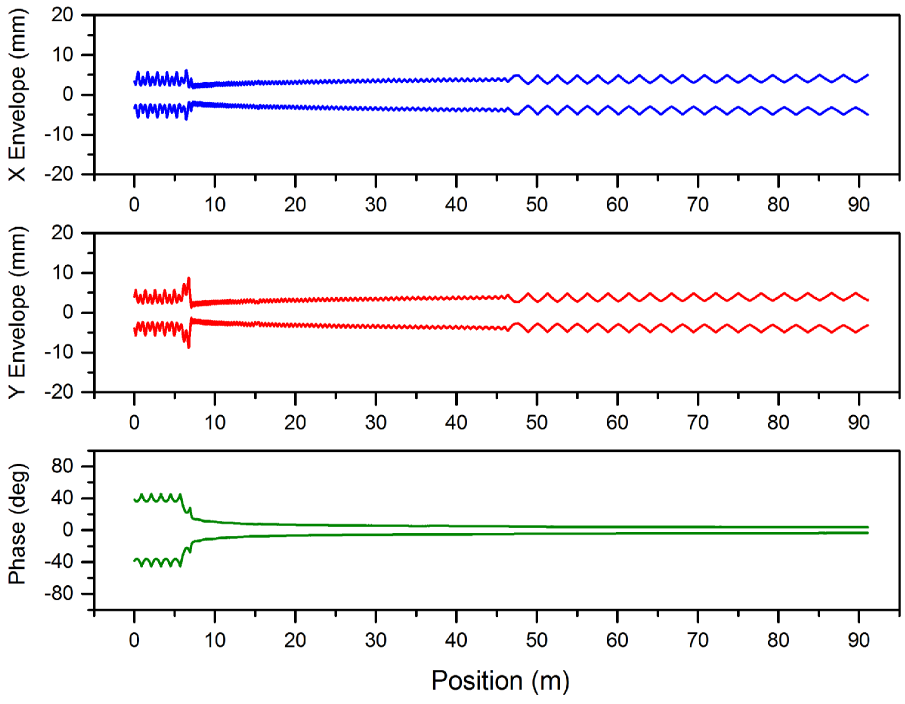

Figure 6.26: 5*RMS emittance beam envelopes evolution with position in the new 180 MeV linac: horizontal (X - top), vertical (Y - middle) and longitudinal (Phase - bottom).

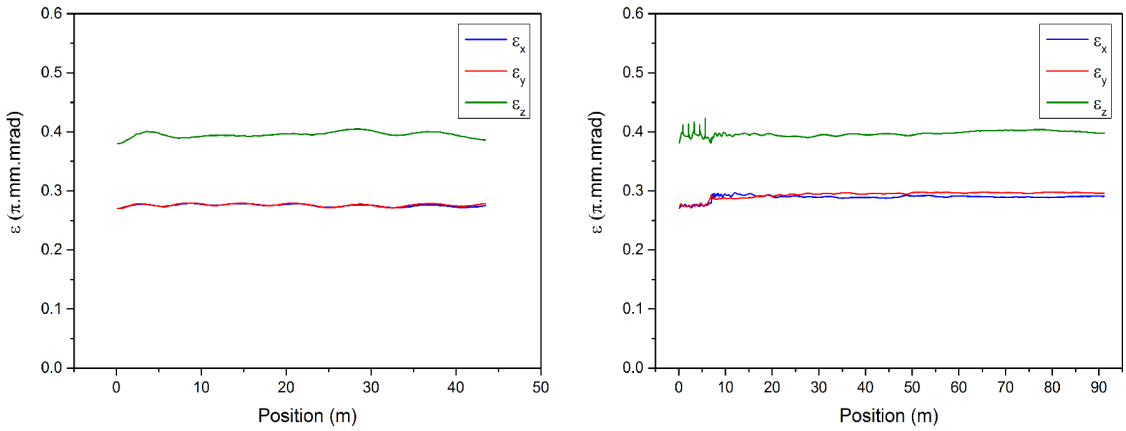

Figure 6.27: RMS emittance evolution through the new 180 MeV linac: CCL only (left) and MEBT+DTL+CCL (right).

This a very robust design, made possible by the adoption of the distributed MEBT design which not only allows fast, bunch by bunch chopping, but greatly reduced initial emittance growth and beam quality deterioration. For comparison, Linac4, ESS, J-PARC, and SNS

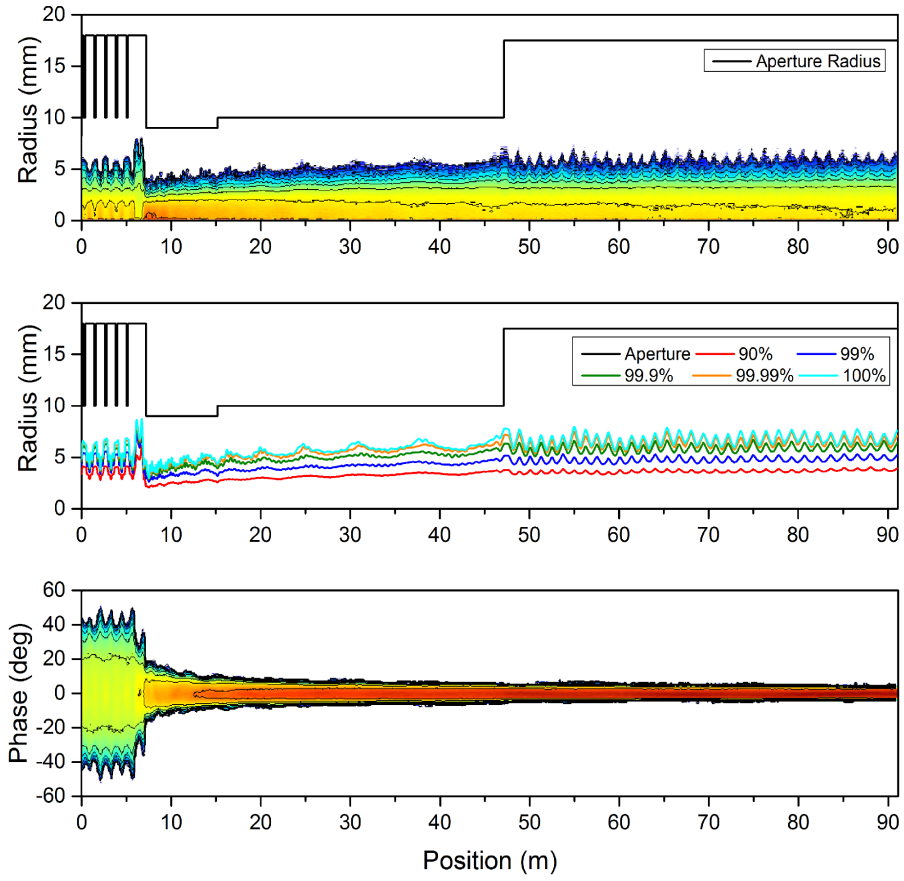

Figure 6.28: Radial beam density (top), and beam cross-section (middle), as well the longitudinal beam density (bottom) evolution throughout the new 180 MeV linac. The upper particle density scale limit is red, while the lower limit is blue.

linac designs have more than 20% growth in the MEBT line alone, consistent with the figures expected for the FETS MEBT.

Regarding the halo development, particular attention was paid to containing halo in view of potential future high power operation. With the adoption of the new MEBT, the halo parameter is reduced to a maximum level of 0.7 (Wangler definition [29]) transversely. A further analysis was carried out using a new halo definition recently proposed by P. Nghiem et al. [189]. To separate the much denser beam core from the external halo, a histogram is calculated for any given spatial or momentum coordinate resulting in a beam density profile. The separation between the core and the halo is therefore the location of the steepest density gradient change. This can be simply found by estimating the maximum of the Laplacian of the density or in 1D by calculating the maximum of the second derivative. This procedure can then be repeated at every time-step. Having defined the separation between the core and the halo, one can now estimate several useful parameters like the percentage of particles in the halo and size of halo compared with the beam size. For the 180 MeV linac, the average percentage of halo particles along the accelerator is 1.5% while the average halo size is 30% of the beam size. This is further illustrated in Figure 6.28, where the beam radial density is plotted at different levels: 90, 99, 99.9, 99.99 and 100%. Good separation between the beam and the vacuum pipe is maintained throughout. The output beam distribution for the end-to-end tracking case is shown in Figure 6.29.

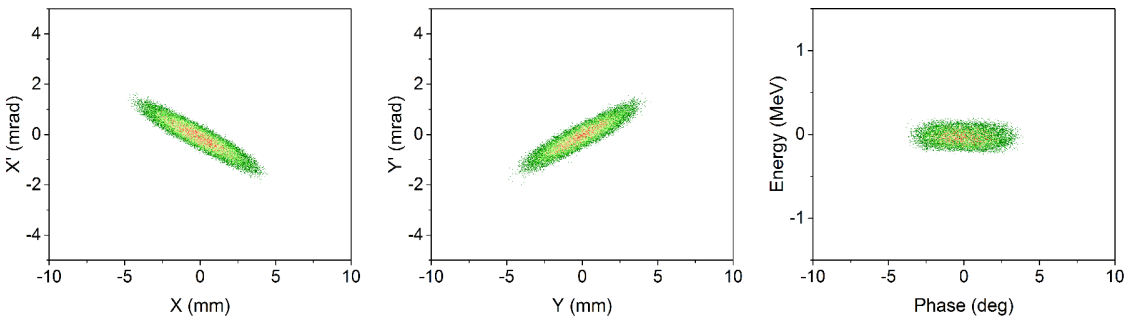

Figure 6.29: Beam distribution at the end of the new 180 MeV linac (horizontal, vertical and longitudinal phase-space). Scale as in Figure 2.11.

6.4 The 800 MeV Linac

6.4.1 General Considerations

The 800 MeV linac is proposed as part of a larger, long term upgrade scenario which would see the replacement of the entire ISIS accelerator chain and the addition of a ∼3.2 GeV synchrotron, opening the possibility of achieving several MW of beam power. The new high power, short pulse facility (ISIS2) would be a complementary addition to the long pulse options to be offered in the next decade to the neutron community by the ESS. Details of this upgrade option are outlined in Chapter 1.

A schematic layout of the new 800 MeV machine is presented in Figure 6.30. It reuses entirely the 180 MeV linac described in the previous section and employs superconducting technology to reach the final energy followed by a ∼87 m long beam line which will transport the beam to a future ring. The assumption here is that such an upgrade could be achieved in several stages where the initial step would see the replacement of the existing 70 MeV linac injector with a new 180 MeV machine, which at a later stage would be further upgraded in energy to 800 MeV as part of the ISIS2 development. This approach would ensure that ISIS is operational for most part throughout construction. An alternative upgrade route would see the current linac upgraded to 100 MeV in the short term, which would then be further upgraded to 180 and 800 MeV in subsequent stages. The obvious disadvantage of both of these staged approaches is the need to relocate an entire linac to a new tunnel and therefore a direct upgrade approach would be preferable [131], [171], [172].

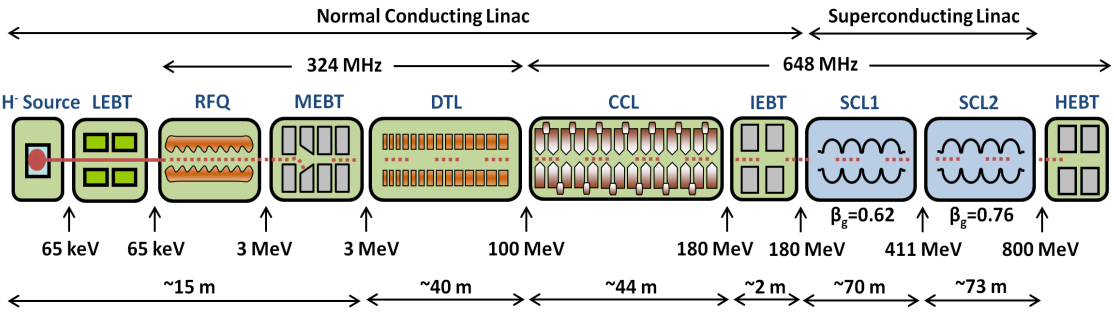

Figure 6.30: General layout of the new 800 MeV linac.

Ion Species	H^-	
Energy	800	MeV
Frequency	324/648	MHz
Pulse Length	0.1 - 1	ms
Peak Current	60	mA
Repetition Rate	50	Hz
Duty Cycle	0.5 - 5	%
Average Beam Power	0.24 - 2.4	MW
Total Length	244	m
Accelerating Structures	RFQ, DTL, CCL	

Table 6.7: General parameters of the proposed 800 MeV linac for ISIS2.

6.4.2 RF Design and Beam Dynamics

The normal conducting section is identical with the 180 MeV linac described above. The FETS-like 3 MeV front end is again employed followed by the DTL and CCL sections. Above 180 MeV superconducting cavities are used to reach 800 MeV. Although high energy normal conducting linacs have been built (LANSCE 800 MeV - CCL, J-PARC 400 MeV - ACS), it was concluded that adopting superconducting cavities at this stage would be a more cost effective solution even when considering the additional capital investment in the cryogenic plant and infrastructure. In addition, they have larger apertures, higher accelerating fields and generally offer a better efficiency due to the absence of ohmic losses. A summary of the main linac parameters is given in Table 6.7.

The superconducting elliptical cavities adopted operate at 648 MHz and have been designed for the same energy gain and beam power per cavity. This approach facilitates cryomodule configuration and klystron development. Consequently, the accelerating gradient

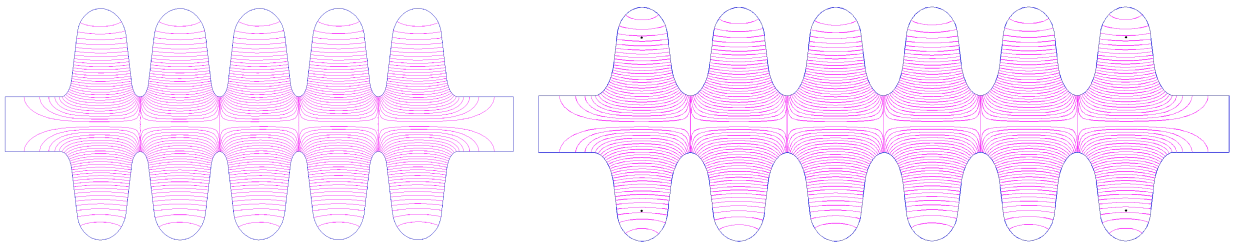

Figure 6.31: Five and six cell superconducting cavities to be employed in the new 800 MeV linac, as modelled by Superfish.

varies between 14 and 19 MV/m due to phase slips when the particle β is different from β_g. Two cavity families are used with β_g=0.62 (SCL1) and 0.76 (SCL2) and a transition energy between the two at 411 MeV. Accelerating cavity design was performed with Superfish and CST MicroWave Studio. An example of a cavity modelled by Superfish is shown in Figure 6.31 which illustrates the cell configuration and the field lines for the TM_{010} accelerating mode. The optimisation procedure aimed at arriving at a robust geometry with minimum peak fields, high quality factors and optimal transit time factors. The results for the two cavity families are two different geometries. A summary with the main geometrical and RF parameters is shown in Table 6.8.

A total of 34, five-cell cavities are needed for SCL1, 33 six-cell cavities for SCL2. The optimal cryomodule configuration has two cavities per cryomodule for SCL1 and three for SCL2. This is illustrated in Figure 6.32. The peak dissipated beam power per cavity assuming a 60 mA beam current is 405 kW for SCL1 and 705 kW for SCL2. A 20% safety margin is then added to account for additional losses and another 30% for control power. This ensures that in the case of cavity failures, a scheme can be implemented in which the

		SCL1	SCL2
Frequency	MHz	648	648
Input Energy	MeV	180	411
Output Energy	MeV	411	800
ΔE	MeV	6.75	11.75
Geometric Beta (β_g)		0.62	0.76
Accelerating Gradient E_0	MV/m	14-17	17-19
Transit Time Factor (T)		0.77	0.76
E_{max}/E_0		1.92	2.00
B_{max}/E_{max}	mT/(MV/m)	1.99	1.59
E_{max}	MV/m	32.6	37.5
B_{max}	mT	65	59.7
Q		1.3×10^{10}	1.5×10^{10}
R/Q	Ω	293	520
Peak Power per Cavity	kW	405	705
Synchronous Phase	deg	-22	-21
Cells per Cavity		5	6
Aperture Diameter	mm	96	100
Total Section Length	m	70	73

Table 6.8: RF and geometrical parameters of the superconducting cavities for the 800 MeV ISIS upgrade linac.

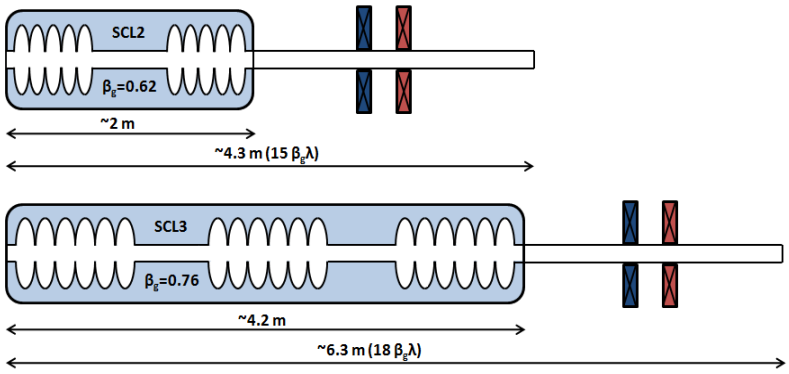

Figure 6.32: Cryomodule configuration for the superconducting section of the new 800 MeV linac for ISIS upgrades.

fields in neighbouring cavities are readjusted and retuned to make up for the off-line cavity. The machine can then continue operating within nominal parameters until the failed cavity can be repaired during a scheduled maintenance period. While this approach has the disadvantage of somehow over-specifying the power requirements for the cavities, it is an important aspect in developing the new generation of high power linacs where reliability and high machine availability are paramount. Assuming 648 MHz pulsed klystrons operating at ∼3 MW, the SCL1 section would be powered by 9 klystrons while SCL2 would need 11. Different configurations could be envisaged based on a different klystron power ratings. The splitting of power from a single klystron to multiple cavities is done using high power vector modulators which allow individual control of amplitude and phase.

From a beam dynamics point of view, the working point established in the upstream section of the linac is also maintained in the superconducting region. This is illustrated in Figure 6.33 where the evolution of the phase advance throughout the linac is shown. The jump in accelerating gradient at the transition between different structures is also reflected here. Transversely, the focussing is done with a FODO doublet quadrupole arrangement located in the room temperature sections at the end of each cell. The six parameter matching between the two SCL stages is found by varying six quadrupole gradients and the cavity phases at each transition region. The synchronous phase is set to -22 degrees in SCL1 and -21 in SCL2.

In SCL1 each lattice focussing period is $15\beta_g\lambda$ long. This includes one cryomodule with two five-cell cavities ($2.5\beta_g\lambda$ each) separated by a $2\beta_g\lambda$ space and a $8\beta_g\lambda$ warm section for

		SCL1	SCL2
Focussing Scheme		FODO	
Focussing Period	$\beta_g\lambda$	15	18
Period Pattern	$\beta_g\lambda$	5×0.5+2+5×0.5+8	6×0.5+1.5+6×0.5+1.5+6×0.5+6
Period Length	m	∼4.3	∼6.3
Quadrupole Length	mm	140	140
Cavities per Period		2	3
Number of Cavities		34	33
Number of Gaps		170	198
Number of Cryostats		17	11
Number of Klystrons		9	11

Table 6.9: Additional parameters of the superconducting section of the 800 MeV linac for ISIS.

quadrupoles and diagnostics. For SCL2, the three six-cell long cavities are each $3\beta_g\lambda$ long and separated by $1.5\beta_g\lambda$ drifts with a longer $6\beta_g\lambda$ long warm section amounting to a total period length of $18\beta_g\lambda$. The total length of the superconducting section is ∼143 m. The general linac configuration is summarised in Table 6.9.

Of particular importance for delivering a high quality beam is the transition between the normal conducting CCL section and the superconducting SCL. Recent experience from SNS as well as J-PARC suggests that diagnostics availability is critical in order to match the beam correctly to the next structure. In addition, the transition section is one of the few opportunities in the linac to fully characterise the beam. Consequently, a small Intermediate Energy Beam Transport Line (IEBT) was designed. It consists of four quadrupoles and two rebunching cavities with ample space for diagnostics and beam scrapers, although the

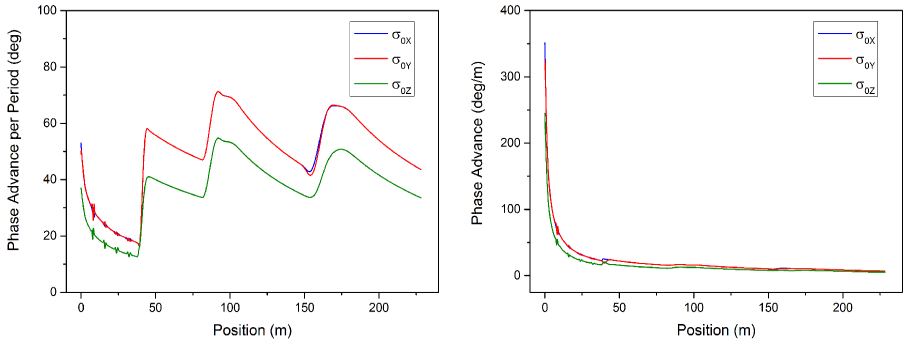

Figure 6.33: Transverse (X and Y) and longitudinal (Z) zero current phase advance through the DTL, CCL and SCL sections of the new 800 MeV linac for ISIS.

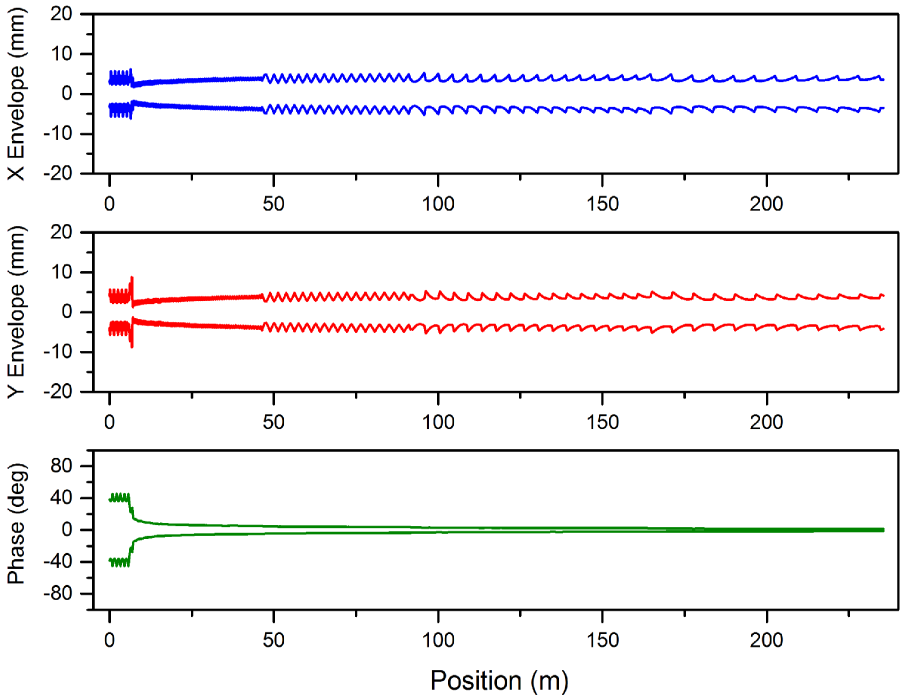

Figure 6.34: 5*RMS emittance beam envelopes evolution with position in the new 800 MeV linac: horizontal (X - top), vertical (Y - middle) and longitudinal (Phase - bottom).

scrapers were not used in the simulations presented here. The matching line allows full 6D matching into the SCL. Alternative matching scenarios were also investigated. A direct CCL to SCL matching is possible by varying quadrupoles and cavity phases at transition, as is proposed for the ESS. This approach however, has the disadvantage of not allowing sufficient space for diagnostics. In one of the earlier designs an alternative more complex IEBT was also studied. It consists of three doublet focussing cells and a 648 MHz rebunching cavity in the first and the third cell. Three dipole magnets are placed in the central cell providing an adjustable orbit bump. The result is that halo and far off-momentum particles are intercepted with stripping foils and loss collectors placed at specific locations between dipoles, thus limiting the losses further downstream. This is a novel method of removing longitudinal halo. However, with the inclusion of the distributed MEBT scheme, the adoption of a smooth phase advance approach and a much more careful matching and overall optics design, it was found that halo development was much slower and the use of such a scheme would not only be costly, but its performance and benefits in terms of improving the beam quality would be unclear and was therefore not included in the baseline design.

As in the 100 and 180 MeV linacs, extensive multi-particle tracking simulations were per-

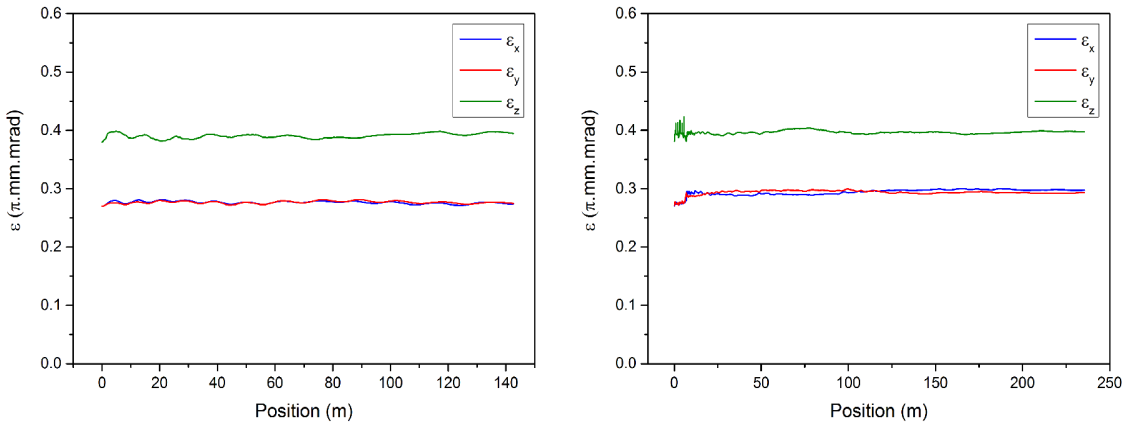

Figure 6.35: RMS emittance evolution through the new 800 MeV linac: SCL only (left) and MEBT+DTL+CCL+SCL (right).

formed aimed at understanding the beam behaviour, validating the design and identifying any potential bottlenecks. Figure 6.34 shows the beam envelope throughout the entire linac. Periodic, smooth oscillations can be observed with a beam size nearly constant throughout the entire 244 m long linac. Avoiding these sudden changes is part of the entire design philosophy adopted here and the analysis of the emittance evolution is a further verification of the design choices adopted here. Figure 6.35 shows the emittance evolution in the SCL section (left) as well as the entire linac including the MEBT, DTL, CCL and SCL. The emittance growth in the SCL section when tracking a 6D WB distribution is below 2% transversely and below 4% longitudinally. The overall linac emittance growth when tracking a beam from the MEBT to the SCL output is below 10% in all planes (SCL only: $\Delta\epsilon_x = 1.3, \Delta\epsilon_y = 1.7, \Delta\epsilon_z = 3.8$, DTL+CCL+SCL: $\Delta\epsilon_x = 2.3, \Delta\epsilon_y = -1.0, \Delta\epsilon_z = 3.9$, MEBT+DTL+CCL+SC: $\Delta\epsilon_x = 9.8, \Delta\epsilon_y = 8.3, \Delta\epsilon_z = 4.3$). The emittance in this machine is incredibly well preserved highlighting a solid and thorough design. To appreciate fully the low level of emittance growth it is sufficient to mention that it is well below the detection capabilities of many modern diagnostic devices. Or in the words of Sir Joseph Whitworth, the famous 19th century British engineer, "you can only make as well as you can measure".

The emittance preservation made possible by this design is an important result, but in view of low loss operation needed for high power machines, an analysis of the halo development is also necessary. The evolution of the beam size is illustrated in Figure 6.36 where the radial and longitudinal beam density is plotted as well as the radial beam size at different

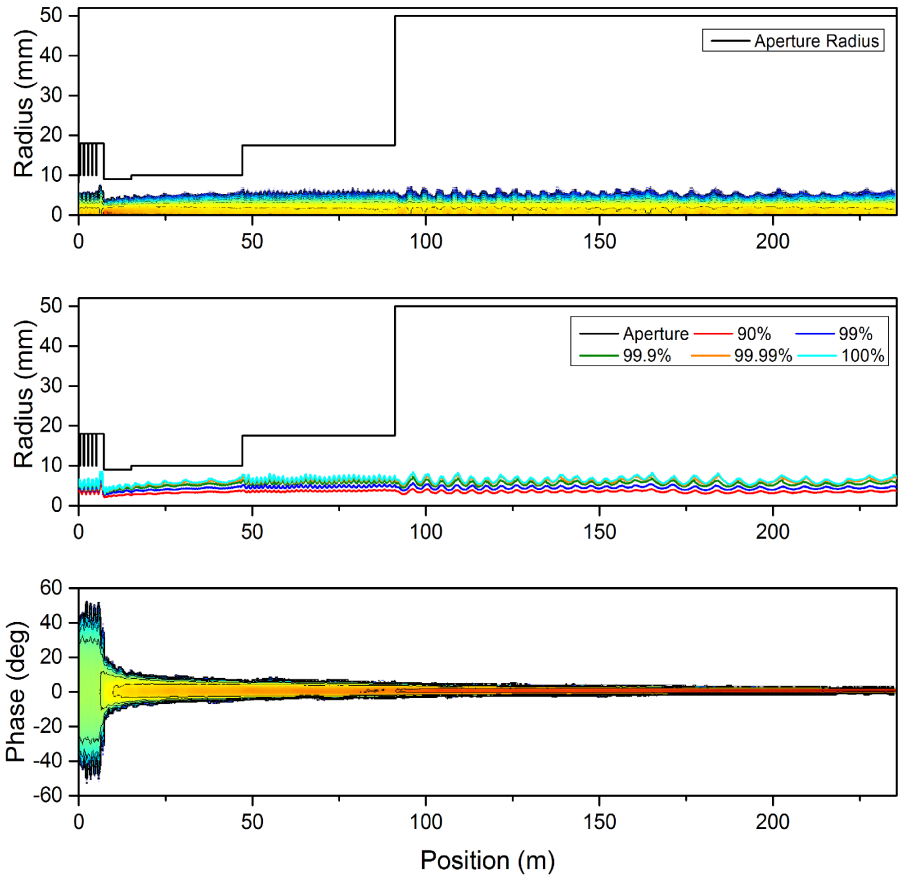

Figure 6.36: Radial beam density (top), and beam cross-section (middle), as well the longitudinal beam density (bottom) evolution throughout the new 800 MeV linac. The upper particle density scale limit is red, while the lower limit is blue.

density levels. It is immediately clear that the size of the beam outside the 99% envelope which might be considered as halo does not grow out of control and the entire beam is well contained within the machine aperture. Furthermore, applying the halo analysis method described above (Nghiem [189]) the percentage of beam halo is more or less preserved at

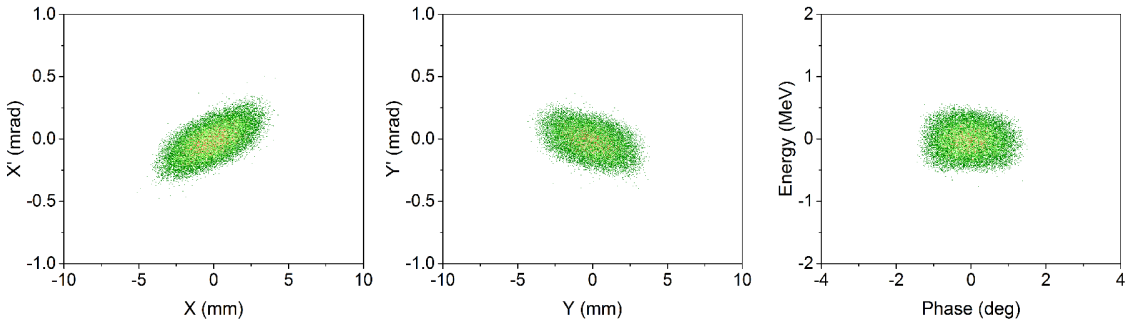

Figure 6.37: Beam distribution at the end of the new 800 MeV linac (horizontal, vertical and longitudinal phase-space). Scale as in Figure 2.11.

$\sim$ 2%, with the average halo size throughout the entire SCL section at $\sim$35%. The output beam distribution is shown in Figure 6.37.

Regarding losses, the current simulations predict no beam loss in the MEBT, DTL, CCL or SCL sections. Of course, in reality machine errors and imperfections will inevitably lead to some loss and are generally part of extensive error studies to understand the potential loss pattern and propose mitigation techniques. However, it is important to highlight that having a baseline design that limits emittance growth and avoids losses from the outset is a key requirement for a high power linac.

6.5 Chapter Summary

In this chapter, design details of three potential ISIS linacs were presented, operating at different energies: 100, 180 and 800 MeV. These machines incorporate the principles of linac design explored by this thesis. Particular attention was paid to choosing the right accelerating structures for the normal conducting section. The working point choice in the tune diagram was such that space-charge resonances, which could potentially lead to emittance growth, halo development and beam loss, are avoided. This choice was backed up by experimental evidence carried out at J-PARC where for the first time emittance exchange driven by $k_z/k_t = 2$ resonance was measured in a proton linac with emittance ratios close to 1.

Additionally, these linac designs show the implementation of the distributed "fast-slow" MEBT scheme proposed in this thesis as a solution for fast chopping and for preventing beam quality degradation at the transition between the RFQ and the DTL. The results are excellent and show no beam loss and an emittance growth below 10% over the entire length for the two linacs (180 and 800 MeV) where the scheme was adopted. The result is encouraging not only for ISIS upgrades in particular, but for potential future high power machines in general in which control of machine activation is paramount.

Chapter 7

Conclusions

At Rutherford Appleton Laboratory, the development of a next generation high power proton accelerator is driven by two important factors: the necessity to upgrade the ageing ISIS Spallation Neutron Source (in the short-medium term) and the requirement of a high intensity proton machine as the driver for a future neutrino factory (in the medium-long term). In this context, this thesis tackles energy and intensity limitations in linear accelerators in general and in normal conducting linacs in particular.

The choice of accelerating cavities and technological solutions play an important role in modern linac designs, as this will influence construction and operational costs as well as machine reliability. The first half of the thesis is dedicated to defining a framework and analysing the range of structures available for normal conducting linacs. It is the first time such a systematic effort was made. The cavities studied are the DTL, SDTL, CH-DTL, CCDTL, CCL, ACS and PIMS and represent the entire family of cavities spanning the full energy spectrum where normal conducting cavities are usually employed (3-400 MeV). The concluding data is not only relevant for ISIS upgrades, but for the wider community.

The second part of the thesis concentrated on intensity limitations in high power linacs and in particular the best approach in designing a MEBT line with choppers such that initial mismatch is avoided and beam quality is preserved in the downstream accelerator. Analysis of several conventional designs from leading proton accelerator laboratories indicated that a different approach was needed. An innovative distributed chopper concept was proposed which uses the "fast-slow" chopping scheme developed for the FETS project. Furthermore,

the limits of high intensity operation were investigated through an experimental campaign at J-PARC where for the first time emittance exchange driven by $k_z/k_t = 2$ resonance was measured in a proton linac with emittance ratios close to 1

Finally, the concepts developed here are applied in the design of a future ISIS linac. The three options developed not only outperform the existing ISIS linac, but are comparable or better than similar projects worldwide, a testament that the linac design principles explored and formulated here are not particular to a certain machine, but generic and universal. In addition, these linac designs are sufficiently versatile such that they can also be incorporated with virtually no modifications in the proton driver design for future, long-term projects like the neutrino factory.

Much of the work presented here had as a starting point the existing ISIS linac. The work presented in Chapter 5 detailing the need of a matching section between the ISIS RFQ and DTL has led to a new internal project to build a MEBT for ISIS which has now started. Similarly, the FETS MEBT design presented in detail here is now being implemented as part of the FETS project.

7.1 Future Work

In terms of further experimental work, beam-time has now been approved by J-PARC to further investigate alternative operation modes and space-charge resonances. This has implications not only for J-PARC's aim of achieving 1 MW or for ISIS upgrades, but for the wider community and in particular ESS which has the challenging aim of delivering 5 MW of beam power in the next decade.

As for ISIS upgrades, this thesis has presented three robust conceptual designs to increase considerably the beam power. Once a political decision has been made about the future of ISIS, significant effort will be needed to deliver a technical design report which would bring the machine a step closer to construction.

Bibliography

[1] H.W. Turnbull et al. "The Correspondence of Isaac Newton", volume 1. Cambridge University Press, Cambridge (1959).

[2] John of Salisbury. "The Metalogicon of John of Salisbury". University of California Press, Berkeley (1955).

[3] W.K.H. Panofsky. *Beam Line*, **27**, 1 (1997) 36–44.

[4] G. H. Rees. *Reviews of Accelerator Science and Technology*, **1**, 43.

[5] M. Lindroos, G. H. Rees et al. "Spallation Sources". In "Elementary Particles - Accelerators and Colliders", volume 21C (2013).

[6] C. Westfall. "How Argonne's Intense Pulsed Neutron Source Came to Life and Gained Its Niche: The View from an Ecosystem Perspective". Technical Report ANL/HIST-5, Argonne, IL, US (2007).

[7] I. Gardner. "ISIS Status Report". In "Proceedings of EPAC'94", pages 3–7. London, UK (1994).

[8] J. Galambos. "SNS Performance and the Next Generation of High Power Accelerators". In "Proceedings of PAC'13", Pasadena, CA, USA (2013).

[9] Y. Yamazaki. "J-PARC Status". In "Proceedings of PAC'09", Vancouver, BC, Canada (2009).

[10] S. Fu et al. "Status of CSNS Project". In "Proceedings of IPAC'13", Shanghai, China (2013).

[11] D. Hagerman. "The Status of LAMPF". In "Proceedings of PLINAC'76", Chalk River, Ontario, Canada (1976).

[12] S. Peggs (ed) et al. "ESS Technical Design Report". Technical Report ESS-DOC-274-V6, Lund, Sweden (2013).

[13] D. Reggiani. "Extraction, Transport and Collimation of the PSI 1.3 MW Proton Beam". In "Proceedings of HB'12", Beijing, China (2012).

[14] C. Prior. "Overview of High Intensity Accelerator Projects". In "Proceedings of HB'10", Morschach, Switzerland (2010).

[15] S. Kim. "SNS Lessons Learned from Design, Integration and Operation". In "Proceedings of SLHiPP4", Geneva, Switzerland (2014).

[16] H. B. Knowles. "Thirty-Five Years of Drift-Tube Linac Experience". Technical Report LA-10138-MS, LANL, NM, US (1984).

[17] A. Sessler & E. Wilson. "Engines of Discovery, A Century of Particle Accelerators". World Scientific (2007).

[18] C. Plostinar. "RF Design Options for a 180 MeV H^- Linac for Megawatt Beam Facilities". In "Proceedings of PAC'07", Albuquerque, NM, USA (2007).

[19] A. Lombardi. "The Radio Frequency Quadrupole (RFQ)". In "Proceedings of CAS 1992", volume CERN-2006-012.201. Zeegse, The Netherlands (2005).

[20] F. Tecker. "CLIC (and room temperature RF)". In "Proceedings of the 6^{th} International Accelerator School for Linear Colliders", Pacific Grove, CA, USA (2011).

[21] P. Ostroumov & F. Gerigk. *Reviews of Accelerator Science and Technology*, **6**.

[22] F. Gerigk. "Cavity Types". In "Proceedings of CAS: RF for Accelerators, 2010", volume CERN-2011-007. Ebeltoft, Denmark (2011).

[23] H. Podlech. "Superconducting versus normal conducting cavities". In "Proceedings of CAS: High Power Hadron Machines, 2011", volume CERN-2013-001.151. Bilbao, Spain (2013).

[24] S. Brooks. "Muon Capture Schemes for the Neutrino Factory". University of Oxford (2010). D.Phil Thesis.

[25] C. Prior. "Proton Drivers Based on Rapid Cycling Synchrotrons". In "Proceedings of NUFACT'05", Frascati, Italy (2005).

[26] C. Plostinar & M. Clarke-Gayther. "Re-bunching RF Cavities and Hybrid Quadrupoles for the RAL Front End Test Stand (FETS)". In "Proceedings of EPAC'06", Edinburgh, UK (2006).

[27] C. Prior. "Updates to the ISIS Spallation Neutron Source". In "Proceedings of APAC'05", Indore, India (2007).

[28] J. Thomason et al. "Megawatt Upgrades for the ISIS Facility". In "Proceedings of HB'08", Nashville, TN, USA (2008).

[29] T. Wangler. "Principles of RF Linear Accelerators". Wiley-VCH (2008).

[30] N. Pichoff. "Introduction to RF Linear Accelerators". In "Proceedings of CAS 2003", volume CERN-2005-04. Zeuthen, Germany (2003).

[31] F. Gerigk. "Introduction to RF Linear Accelerators". In "Proceedings of CAS 2010", Aarhus, Denmark (2010).

[32] M. Vretenar. "Introduction to RF Linear Accelerators". In "Proceedings of CAS 2008", Frascati, Italy (2008).

[33] "CST Studio". `http://www.cst.com`

[34] M. Weiss. "Introduction to RF Linear Accelerators". In "Proceedings of CAS 1992", volume CERN-94-01. Jyväskylä, Finland (1994).

[35] J. Le Duff. "Dynamics and acceleration in linear structures". In "Proceedings of CAS 1992", volume CERN-94-01. Jyväskylä, Finland (1994).

[36] M. Reiser. "Theory and Design of Charged Particle Beams". John Wiley & Sons Inc., New York, NY, USA (1994).

[37] S.Y. Lee. "Accelerator Physics". World Scientific, Singapore (1999).

[38] F. Gerigk. "Beam Halo in High-Intensity Hadron Linacs". Technical University of Berlin, Berlin (2006). Ph.D Thesis.

[39] G. Bellomo et al. "Adiabatic Matching in Periodic Accelerating Lattices for Superconducting Proton Linacs". In "Proceedings of EPAC'02", Paris, France (2002).

[40] K. R. Crandall & D.P. Rusthoi. "Trace 3-D Documentation". Technical Report LA-UR-97-886, Los Alamos, NM, USA (1997).

[41] R. Duperier et al. "CEA Saclay Codes Review for High Intensity Linacs Computations". In "Proceedings of ICCS'02", Amsterdam, Netherlands (2002).

[42] X. Pang. "Advances in Proton Linac Online Modeling". In "Proceedings of IPAC'15", Richmond, VA, USA (2015).

[43] F. Sacherer. *IEEE Transactions on Nuclear Science*, **NS-18**, 3.

[44] V. Vlasov. *Journal of Experimental and Theoretical Physics*, **8**, 3.

[45] C. Prior. "Dynamics of Non-Linear Beams with Space-Charge". In "Proceedings of CAS Course on High Power Hadron Machines", Bilbao, Spain (2011).

[46] Y. Papaphilippou. "Phase Space Concepts". In "Proceedings of USPAS", Cornell University, Ithaca, NY (2005).

[47] I. Kapchinsky & V. Vladimirsky. "Limitations of Proton Beam Current in a Strong Focusing Linear Accelerator Associated with the Beam Space Charge". In "Proceedings of the International Conference on High-Energy Accelerators and Instrumentation", Geneva, Switzerland (1959).

[48] P. Lapostolle & M. Weiss. "Formulae and Procedures Useful for the Design of Linear Accelerators". Technical Report CERN-PS-2000-001 (DR), Geneva, Switzerland (2000).

[49] Y. Batygin. "Space Charge Dominated Beam Transport and Acceleration". In "Proceedings of USPAS", Boston, Massachusetts (2010).

[50] P. Lapostolle. *IEEE Transactions on Nuclear Science*, **NS-18**, 6.

[51] P. Lapostolle. "Effets de la charge d'espace dans un accélérateur linéaire à protons". Technical Report CERN Report AR/Int SG/65-15, Geneva, Switzerland (1965).

[52] A. Lombardi et al. "End-to-end Beam Dynamics for CERN Linac4". In "Proceedings of HB'06", Tsukuba, Japan (2006).

[53] C. Plostinar & G. H. Rees. *Nuclear Instruments and Methods A*, **744** (2014) 48–53.

[54] C. Plostinar & G. H. Rees. "A Linac-Based Approach to Modelling an Orbit Separated Cyclotron". In "Proceedings of LINAC'14", Geneva, Switzerland (2014).

[55] J. Stovall. "Low and Medium Energy Beam Acceleration in High Intensity Linacs". In "Proceedings of EPAC'04", Lucerne, Switzerland (2004).

[56] B. Bonin. "Field Emission in RF Cavities". In "Proceedings of the CERN Accelerator School on Superconductivity in Particle Accelerators, CERN 96-03", Hamburg, Germany (1995).

[57] R. Reid. "Vacuum Science and Technology in Accelerators". In "Cockcroft Institute Lectures", Daresbury, UK (2007).

[58] O. Malyshev. "Introduction to Vacuum Systems for Particle Accelerators". In "Cockcroft Institute Particle Accelerator School", Daresbury, UK (2013).

[59] T. Morishita et al. "Fabrication of the New RFQ for the J-PARC Linac". In "Proceedings of IPAC'10", Kyoto, Japan (2010).

[60] M. Eshraqi. "Beam Physics Design of the Optimus+ SC Linac". Technical Report ESS/AD/0050, ESS, Lund, Sweden (2013).

[61] R. Duperrier et al. *Physical Review Special Topics - Accelerators and Beams*, **10**, 084201.

[62] W. Kilpatrick. *Review of Scientific Instruments*, **28** (1957) 824–826.

[63] S. Wang & G. Loew. "Field Emission and RF Breakdown in High-Gradient Room-Temperature Linac Structures". Technical Report SLAC-PUB-7684, SLAC, Stanford, CA, USA (1997).

[64] R. Garoby. "High Intensity Pulsed Proton Injectors". In "Proceedings of CARE Meeting 2004", DESY - Hamburg, Germany (2004).

[65] C. Plostinar (Ed.). "Comparative Assessment of HIPPI Normal Conducting Structures". Technical Report CARE-Report-2008-071-HIPPI, Geneva, Switzerland (2008).

[66] J. Billen & L. Young. "Poisson Superfish Documentation". Technical Report LA-UR-96-1834, Los Alamos, NM, USA (2006).

[67] C. Plostinar & A. Letchford. "Shunt Impedance Studies in ISIS". In "Proceedings of LINAC'08", Victoria, BC, Canada (2008).

[68] C. Plostinar. "RF Cavity Design with Superfish". University of Oxford (2013). JAI Lecture Notes.

[69] S. Ramberger et al. "Drift Tube Linac Design and Prototyping for the CERN Linac4". In "Proceedings of LINAC'08", Victoria, BC, Canada (2008).

[70] F. Gerigk & M. Vretenar (Ed.). "Linac4 Technical Design Report". Technical Report CERN-AB-2006-084 ABP/RF, Geneva, Switzerland (2006).

[71] F. Gerigk (Ed.). "Conceptual Design Report of the SPL II". Technical Report CERN-2006-006, Geneva, Switzerland (2006).

[72] F. Grespan et al. "ESS DTL Design and Drift Tube Prototypes". In "Proceedings of LINAC'14", Geneva, Switzerland (2014).

[73] R. De Prisco et al. "ESS DTL Status: Redesign and Optimizations". In "Proceedings of IPAC'14", Dresden, Germany (2014).

[74] Y. Yamazaki (Ed.) et al. "Accelerator Technical Design Report for J-PARC". Technical Report KEK-REPORT-2002-13, Tsukuba, Japan (2003).

[75] F. Gerigk. "A New 180 MeV H^- Linac for Upgrades of ISIS". In "Proceedings of EPAC'04", Lucerne, Switzerland (2004).

[76] C. Plostinar. "Progress on the RAL Linac Design". In "Proceedings of HIPPI 2008 Annual Meeting", Geneva, Switzerland (2008).

[77] J. Billen et al. "Room-Temperature Linac Structures for the Spallation Neutron Source". In "Proceedings of PAC'01", Chicago, IL, USA (2001).

[78] A. Lombardi et al. "End-to-End Beam Dynamics for CERN Linac4". Technical Report CERN-AB-2007-001, Geneva, Switzerland (2007).

[79] A. Lombardi et al. "Loss Control and Steering Strategy for the CERN Linac4". Technical Report AB-Note-2007-033-ABP, Geneva, Switzerland (2007).

[80] A. Lombardi et al. "Beam Dynamics in Linac4 at CERN". In "Proceedings of HB'08", Nashville, TN, USA (2008).

[81] S. Ramberger et al. "An Optimised Design for the Linac4 Drift Tube Linac". Technical Report CARE-Report-08-054-HIPPI, Geneva, Switzerland (2008).

[82] F. Gerigk et al. "RF Structures for Linac4". In "Proceedings of PAC'07", Albuquerque, NM, USA (2007).

[83] M. Vretenar et al. "Status of the Linac4 Project at CERN". Technical Report CARE-Conf-08-021-HIPPI, Geneva, Switzerland (2008).

[84] M. Baylac et al. "Statistical Simulations of Machine Errors for Linac4". In "Proceedings of HB'06", Tsukuba, Japan (2006).

[85] J. Billen et al. "A $3\lambda/4$ Post-Coupler for Drift-Tube Linacs". In "Proceedings of PAC'85", Vancouver, BC, Canada (1985).

[86] G. Bellodi et al. "Effects of RF Errors on the Linac4 Performance". In "Proceedings of HIPPI 2008 Annual Meeting", Geneva, Switzerland (2008).

[87] T.Kato. "Proposal of a Separated-type Drift Tube Linac for a Medium-Energy Structure". Technical Report KEK Report 92-10, Tsukuba, Japan (1992).

[88] M. Ikegami. *Prog. Theor. Exp. Phys.*, **02B002**.

[89] S. Wang et al. "Improvements of RF Characteristics in the SDTL of the J-PARC Proton Linac". In "Proceedings of LINAC'04", Lübeck, Germany (2004).

[90] T. Ito et al. "RF Characteristics of the SDTL for the J-PARC". In "Proceedings of LINAC'06", Knoxville, TN, USA (2006).

[91] D. Krämer. "FAIR An International Facility for Antiproton and Ion Research". In "Proceedings of RuPAC'06", Novosibirsk, Russia (2006).

[92] G. Clemente. "The Room Temperature CH-DTL and its Application for the FAIR Proton Injector". Johann Wolfgang Goethe Universität, Frankfurt am Main (2007). Ph.D Thesis.

[93] G.Clemente et al. "Geometrical Optimisation of the 70 mA, 70 MeV CH-Proton Injector Cavity for the FAIR Project". Technical Report GSI Annual Report 2004, GSI, Darmstadt, Germany (2004).

[94] R. Tiede et al. "KONUS Beam Dynamics Design of a 70 mA, 70 MeV Proton CH-DTL for GSI-SIS12". In "Proceedings of LINAC'04", Lübeck, Germany (2004).

[95] K. Crandall & T. Wangler. "PARMTEQ - A Beam Dynamics Code for the RFQ Linear Accelerator". In "AIP Conference Proceedings", San Diego, CA, USA (1988).

[96] G. Clemente et al. "Development of a Normal Conducting CH-DTL". In "Proceedings of PAC'05", Knoxville, TN, USA (2005).

[97] G. Clemente et al. "Beam Dynamics Layout and Loss Studies for the FAIR P-Injector". In "Proceedings of EPAC'08", Genova, Italy (2008).

[98] F. Gerigk & M. Vretenar. "Design Choices for the SPL Normal Conducting Front End (3 - 120 MeV)". Technical Report CERN-NUFACT-NOTE NF-110, CERN, Geneva, Switzerland (2002).

[99] J. Billen et al. "A New RF Structure for Intermediate-Velocity Particles". In "Proceedings of LINAC'94", Tsukuba, Japan (1994).

[100] M. Pasini. "CCDTL Design Update for Linac4". Technical Report CARE-Note-2005-014-HIPPI, CERN, Geneva, Switzerland (2005).

[101] M. Pasini et al. "CCDTL Prototype: Status Report". Technical Report CARE-Note-2006-021-HIPPI, CERN, Geneva, Switzerland (2006).

[102] M. Pasini et al. "CCDTL Prototypes: Test Results". Technical Report CARE-Note-2007-036-HIPPI, CERN, Geneva, Switzerland (2007).

[103] M. Vretenar et al. "CCDTL Section for Linac4". Technical Report CARE-Note-2008-020-HIPPI, CERN, Geneva, Switzerland (2008).

[104] E. Benedico Mora & M. Vretenar. "Design of a Side-Coupled Linear Accelerator Structure for Linac4". Technical Report CARE-Note-2005-015-HIPPI, CERN, Geneva, Switzerland (2005).

[105] M. Vretenar et al. "Design and Development of RF Structures for Linac4". In "Proceedings of LINAC'06", Knoxville, TN, USA (2006).

[106] R. Wegner & F. Gerigk. "A Comparison of Pi/2-Mode Standing Wave Structures for Linac4". Technical Report CERN-AB-Note-2006-049-RF, CERN, Geneva, Switzerland (2006).

[107] J-M. De Conto et al. "Development of Side Coupled Cavities". Technical Report CARE-Note-08-11-HIPPI, CERN, Geneva, Switzerland (2008).

[108] J. Billen et al. "Spallation Neutron Source (SNS) Coupled-Cavity Linac Hot Model". Technical Report SNS 101020000-TR0001 R00, Los Alamos, NM, USA (2002).

[109] N. Bultman et al. "Fabrication and Tuning of the SNS CCL Hot Model". In "Proceedings of PAC'03", Portland, OR, USA (2003).

[110] K. Hasegawa. "Commissioning of Energy Upgraded Linac of J-PARC". In "Proceedings of LINAC'14", Geneva, Switzerland (2014).

[111] H. Ao et al. *Physical Review Special Topics - Accelerators and Beams*, **15**, 051005.

[112] M. Ikegami et al. "Beam Dynamics Design of The Annular-Coupled-Structure Linac and Its Beam Matching Section for The KEK/JAERI Joint Project". In "Proceedings of LINAC'02", Gyeongju, Korea (2002).

[113] N. Hayashizaki et al. "Structure Design of the Annular Coupled Structure Linac for the JAERI/KEK Joint Project". In "Proceedings of LINAC'02", Gyeongju, Korea (2002).

[114] H. Ao & Y. Yamazaki. *Physical Review Special Topics - Accelerators and Beams*, **15**, 011001.

[115] I. Wilson & H. Henke. "The LEP Main Ring Accelerating Structure". Technical Report CERN-Report-89-09, CERN, Geneva, Switzerland (1989).

[116] R. Wegner & F. Gerigk. *Nuclear Instruments and Methods A*, **606**, 3.

[117] "GdfidL". `http://www.gdfidl.de`

[118] E. Sargsyan & A. Lombardi. "Pi-Mode 352 MHz Scaled LEP Cavities as an Alternative Accelerating Structure for the Energy Range of 90 to 160 MeV in CERN Linac4/SPL". Technical Report CARE-Note-2007-003-HIPPI, CERN, Geneva, Switzerland (2007).

[119] R. Wegner. "Pi-Mode Structure (PIMS)". In "HIPPI 2008 Annual Meeting", CERN, Geneva, Switzerland (2008).

[120] P. Bourquin et al. "Development Status of the Pi-Mode Accelerating Structure (PIMS) for Linac4". Technical Report CARE-CONF-08-024-HIPPI, CERN, Geneva, Switzerland (2008).

[121] R. Maier. "High Power Proton Linacs, Applications and Design Concepts". In "Proceedings of EPAC'02", Paris, France (2002).

[122] D. Findlay. "Linacs at Rutherford Appleton Laboratory". Technical Report RAL Internal Report, Harwell, UK (2004).

[123] S. Nath et al. "Comparison of Linac Simulation Codes". In "Proceedings of PAC'01", Chicago, IL, USA (2001).

[124] A. Franchi et al. "Benchmarking Linac Codes for the HIPPI Project". In "Proceedings of HB'04", Bensheim, Germany (2004).

[125] A. Letchford et al. "Testing, Installation, Commissioning and First Operation of the ISIS RFQ Pre-Injector Upgrade". In "Proceedings of PAC'05", Knoxville, TN, USA (2005).

[126] D. Faircloth et al. "The Development of the ISIS H^- Surface Plasma Ion Source at RAL". In "Proceedings of ICANS-XVIII", Dongguan, China (2007).

[127] C. Plostinar et al. "Modelling the ISIS 70 MeV Linac". In "Proceedings of IPAC'12", New Orleans, LA, USA (2012).

[128] J. Lawson. *Journal of Electronics and Control*, **5**, 146 (1958) 146–151.

[129] A. Aleksandrov et al. "Optimal Design of a High Current MEBT with Chopper". In "Proceedings of EPAC'08", Genoa, Italy (2008).

[130] C. Plostinar. "Front End MEBT Studies for a High Power Proton Accelerator". In "Proceedings of PAC'09", Vancouver, BC, Canada (2009).

[131] G. H. Rees. *ICFA Beam Dynamics Newsletter*, **54** (2011) 148–152.

[132] D.-O. Jeon. *Phys. Rev. ST Accel. Beams*, **16**.

[133] J.-F. Ostiguy et al. "Overview of Beam Optics for Project-X CW Linac". In "Proceedings of HB'10", Morschach, Switzerland (2010).

[134] C. Plostinar. "Chopping Options for ESS". Technical Report ESS/AD/0022, Lund, Sweden (2011).

[135] A. Aleksandrov. "Overview and Future Demands of Fast Choppers". In "Proceedings of LINAC'10", Tsukuba, Japan (2010).

[136] M. Clarke-Gayther. "A Two Stage Fast Beam Chopper for Next Generation High Power Proton Drivers". In "Proceedings of IPAC'11", San Sebastian, Spain (2011).

[137] E. Laface et al. "ESS End-to-End Simulations: A Comparison Between Impact and MADX". In "Proceedings of IPAC'12", New Orleans, LA, USA (2012).

[138] C. Plostinar et al. "Modelling of the FETS MEBT Line Using GPT". In "Proceedings of IPAC'11", San Sebastian, Spain (2011).

[139] K. Halbach. *Nuclear Instruments and Methods*, , 187 (1981) 109–117.

[140] M. Bassetti. *Particle Accelerators*, **52** (1996) 221–250.

[141] S. Caspi et al. "An approach to 3D magnetic field calculation using numerical and differential algebra methods". Technical Report LBL-32624, SC-MAG 395, Upton, NY, USA (1992).

[142] G. Leleux. "Compléments sur la physique des accélérateurs". Technical Report CEA/DSM/LNS/86-101, Saclay, France (1986).

[143] H. Enge. *Review of Scientific Instruments*, **35** (1964) 278–287.

[144] F. Méot. "Zgoubi Users' Guide". Technical Report Brookhaven National Laboratory Report C-AD/AP/470, Upton, NY, USA (2012).

[145] S.S. Kurennoy & J.F. Power. "Development of Meander-Line Current Structure for SNS Fast 2.5 MeV Beam Chopper". In "Proceedings of EPAC'00", Vienna, Austria (2000).

[146] R. Hardekopf et al. "Design Construction and Initial Operation of the SNS MEBT Chopper System". In "Proceedings of EPAC'04", Lucerne, Switzerland (2004).

[147] J.W. Staples et al. "Design of the SNS MEBT". In "Proceedings of LINAC'00", Montery, CA, USA (2000).

[148] S. Nath et al. "Beam Behaviour Through the SNS Chopper System". In "Proceedings of LINAC'02", Gyeongju, Korea (2002).

[149] A. Aleksandrov et al. "New Design of the SNS MEBT Chopper Deflector". In "Proceedings of PAC'07", Albuquerque, NM, USA (2007).

[150] S. Fu & T. Kato. *Nuclear Instruments and Methods*, **440** (2000) 296–306.

[151] S. Wang et al. *Nuclear Instruments and Methods*, **547** (2005) 302–312.

[152] F. Caspers et al. "Design of a Chopper Line for the SNS SPL". In "Proceedings of LINAC'02", Gyeongju, Korea (2002).

[153] F. Caspers et al. "The CERN-SPL Chopper Concept and Final Layout". In "Proceedings of EPAC'04", Lucerne, Switzerland (2004).

[154] C. Plostinar & E. Sargsyan. "Comparative Study of Beam Dynamics in Linac4 using CERN and RAL MEBT (Medium Energy Beam Transport) Lines". In "Proceedings of PAC'07", Albuquerque, NM, USA (2007).

[155] R. Miyamoti et al. "Beam Physics Design of MEBT". Technical report, Lund, Sweden (2012).

[156] D. Findlay et al. "The RAL Front End Test Stand". In "Proceedings of NuFact'04", Osaka, Japan (2004).

[157] A. Letchford et al. "Current Status of the RAL Front End Test Stand (FETS) Project". In "Proceedings of LINAC'12", Tel Aviv, Israel (2012).

[158] A. Letchford et al. "Status of the RAL Front End Test Stand". In "Proceedings of IPAC'10", Kyoto, Japan (2010).

[159] M. Clarke-Gayther. "A Fast Beam Chopper for Next Generation High Power Proton Drivers". In "Proceedings of EPAC'04", Lucerne, Switzerland (2004).

[160] M. Clarke-Gayther. "The Development of a Fast Beam Chopper for Next Generation High Power Proton Drivers". In "Proceedings of EPAC'08", Genoa, Italy (2008).

[161] M. Clarke-Gayther. "The Development of a Fast Beam Chopper for Next Generation High Power Proton Drivers". In "Proceedings of IPAC'10", Kyoto, Japan (2010).

[162] M. Clarke-Gayther. "The Development of a Slow-Wave Chopper Structure for Next Generation High Power Proton Drivers". In "Proceedings of PAC'09", Vancouver, BC, Canada (2009).

[163] M. Clarke-Gayther et al. "A Fast Beam Chopper for the RAL Front End Test Stand". In "Proceedings of EPAC'06", Edinburgh, Scotland (2006).

[164] C. Plostinar. "MEBT Design for the RAL Front End Test Stand". In "Proceedings of IPAC'10", Kyoto, Japan (2010).

[165] S. Lawrie. "MEBT Quadrupoles". FETS Internal Report (2013).

[166] C. Plostinar et al. "A Hybrid Quadrupole Design for the RAL Front End Test Stand (FETS)". In "Proceedings of EPAC'08", Genoa, Italy (2008).

[167] C. Plostinar et al. "Design Progress of the Re-Bunching RF Cavities and Hybrid Quadrupoles for the RAL Front End Test Stand". In "Proceedings of LINAC'06", Knoxville, TN, USA (2006).

[168] C. Plostinar et al. "Design Optimisation of the Re-Bunching Cavities for the Front End Test Stand". In "Proceedings of LINAC'10", Tsukuba, Japan (2010).

[169] C. Gabor et al. "Design Report of a Non-destructive Emittance Instrument for Rutherford Appleton Laboratory's Front End Test Stand FETS". In "Proceedings of DIPAC'09", Basel, Switzerland (2009).

[170] P. Krejcik. *IEEE Transactions on Nuclear Science*, **NS-32**, 5 (1985) 3163–3165.

[171] C. Plostinar, C. Prior & G. H. Rees. "Conceptual Design of a New 800 MeV H^- Linac for ISIS Megawatt Developments". In "Proceedings of IPAC'11", San Sebastian, Spain (2011).

[172] C. Plostinar, C. Prior & G. H. Rees. "Beam Dynamics Design Aspects for a Proposed 800 MeV H^- ISIS Linac". In "Proceedings of LINAC'12", Tel-Aviv, Israel (2012).

[173] C. Plostinar et al. "Review of Linac Upgrade Options for the ISIS Spallation Neutron Source". In "Proceedings of IPAC'15", Richmond, VA, USA (2015).

[174] F. Gerigk. "Arguments to choose the Frequency for a new 180 MeV Linac and the associated Front-End Test Stand at RAL". Technical Report RAL Internal Report - FETS-TN-2004-001, RAL, Harwell, UK (2004).

[175] I. Hofmann. *IEEE Transactions on Nuclear Science*, **NS-28**, 3 (1981) 2399–2401.

[176] R. Jameson. *IEEE Transactions on Nuclear Science*, **NS-28**, 3 (1981) 2408–2412.

[177] J-M. Lagniel & S. Nath. "On Energy Equipartition Induced by Space Charge in Bunched Beams". In "Proceedings of EPAC'98", Stockholm, Sweden (1998).

[178] I. Hofmann et al. "Review of Beam Dynamics and Space Charge Resonances in High Intensity Linacs". In "Proceedings of EPAC'02", Paris, France (2002).

[179] I. Hofmann et al. *Phys. Rev. Lett.*, **86**, 2313.

[180] L. Groening et al. *Phys. Rev. Lett.*, **103**, 224801.

[181] M. Plum. "Challenges Facing High Power Proton Accelerators". In "Proceedings of IPAC'13", Shanghai, China (2013).

[182] C. Plostinar. "Measurement of Resonant Spac Charge Effects in the J-PARC Linac". In "Proceedings of IPAC'13", Shanghai, China (2013).

[183] M. Ikegami et al. "Resonance Crossing in Linacs - Recent Measurements on Space Charge Resonances in J-PARC Linac". In "Proceedings of the Space Charge Workshop 2013", CERN, Geneva, Switzerland (2013).

[184] T. Pelaia. "Open XAL Status Report 2013". In "Proceedings of IPAC'13", Shanghai, China (2013).

[185] A. Feschenko. "Technique and Instrumentation for Bunch Shape Measurements". In "Proceedings of RUPAC'12", Saint-Petersburg, Russia (2012).

[186] A. Miura et al. "Bunch Length Measurement of 181 MeV Beam in J-PARC Linac". In "Proceedings of IPAC'13", Shanghai, China (2013).

[187] J-M. Lagniel. "Usefulness and limits of the [α, η, β] charts". In "Proceedings of SpaceCharge'15", Oxford, UK (2015).

[188] C. Prior & G. H. Rees. "RAL Proton Driver Studies for a Neutrino Factory". In "Proceedings of NUFACT'00", Monterey, CA, USA (2000).

[189] P. Nghiem et al. *Applied Physics Letters*, **104**, 074109.